



MINISTÉRIO DAS OBRAS PÚBLICAS, TRANSPORTES E COMUNICAÇÕES

Laboratório Nacional de Engenharia Civil

EULERIAN-LAGRANGIAN ANALYSIS OF TRANSPORT AND RESIDENCE TIMES IN ESTUARIES AND COASTS

Portland, Outubro 1997

Anabela Pacheco de Oliveira

Dissertação apresentada no Oregon Graduate Institute of Science and Technology
para obtenção do grau de Doctor in Philosophy

I&D
TESE
HIDRÁULICA

MINISTÉRIO DO EQUIPAMENTO, DO PLANEAMENTO E DA ADMINISTRAÇÃO DO TERRITÓRIO
Laboratório Nacional de Engenharia Civil

**Departamento de Hidráulica
Núcleo de Estuários**

Processo 604/43

**Oregon Graduate Institute of
Science and Technology**

**Department of Environmental Sciences
and Engineering**

**EULERIAN-LAGRANGIAN ANALYSIS
OF TRANSPORT AND RESIDENCE
TIMES IN ESTUARIES AND COASTS**

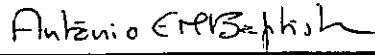
Anabela Pacheco de Oliveira

**Licenciada em Engenharia Civil pelo Instituto Superior Técnico
Mestre em Engenharia e Ciências do Ambiente
pelo Oregon Graduate Institute of Science and Technology**

**Dissertação apresentada ao Oregon Graduate Institute of Science and Technology
para obtenção do grau de Doctor in Philosophy**

Portland, October 1997

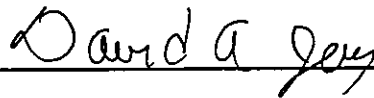
The dissertation "Eulerian-Lagrangian Analysis of Transport and Residence Times in Estuaries and Coasts" by Anabela Pacheco de Oliveira has been examined and approved by the following Examination Committee:



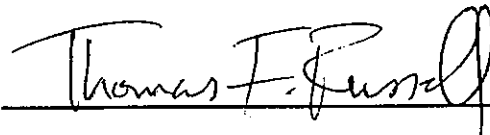
António M. Baptista, Ph.D., Thesis Advisor



William Fish, Ph.D., Associate Professor



David A. Jay, Ph.D., Associate Professor



Thomas F. Russell, Ph.D., Professor, University of Colorado

To my husband, André

ACKNOWLEDGEMENTS

André Fortunato, to whom this thesis is dedicated, has been the best husband, friend and colleague anyone could dream of. He offered me love and encouragement at every corner and was always very proud of my work. He was also very understanding of my need to have pets around me and was a wonderful "daddy" when I left him alone with the "kids" for extensive periods of time. During the last 6 years, André was also my second advisor and this thesis would not have been possible without his many suggestions, insightful advice and constructive criticism.

My cats, Fox and Eddy, have been a constant source of love and delight. They helped me forget every hardship in their special way, and they never complained for my long working hours (except for an occasional peeing outside the litterbox).

The encouragement of my family has helped me immensely during the last six years. The love of my mother have been an invaluable source of strength and motivation during my graduate student years. My brother, sister-in-law and my two wonderful nephews, André and Miguel, were a constant, cheerful source of love and support. My parents-in-law were always there to help me in any possible way.

My friends have made these last six years more bearable. Margarida Cardoso da Silva helped me a lot with her overwhelming good humor. The support of my friends, Margarida, Paula, Madureira, Tiago and Amélia was much appreciated. The help and friendship of Phil and Angela Pearson, and Elvira was invaluable. Ed Meyers and Jeff Darland also helped me a lot with their friendship and for making sure that I would stop working now and then. To all other friends at OGI and LNEC, my whole-hearted thanks.

I have been privileged to have António Melo Baptista as my academic and thesis advisor. I benefited immensely from his scientific knowledge, teaching skills and generous dedication to his students. I am also very grateful for his understanding of the hardships of living away from one's spouse, and thus for allowing me to pursue my Ph.D. in absentia during the last one-and-half years. António and Izi's friendship were a very important source of support during the last 6 years.

I am also grateful to the other members of my thesis committee, Professor Thomas F. Russell, Dr. William Fish and Dr. David Jay, for their suggestions and comments.

A thesis on numerical modeling can hardly succeed without the help of a system administrator. I was lucky to have the help of Paul Turner and Brad Beck at OGI, and João Palha Fernandes at LNEC. I am also very grateful to Daloris Flaming, for taking care of many problems while I was in Portugal and at OGI, and for her friendship.

I would like to acknowledge the financial support of Junta Nacional de Investigação Científica e Tecnológica, through grant BD/2775/93 (Programas Ciência and Praxis XXI). I also acknowledge the support of Laboratório Nacional de Engenharia Civil, in particular the heads of the Hydraulics Department, Jaime M. Baptista, and the Estuaries division, Eduardo M. Oliveira.

TABLE OF CONTENTS

DEDICATION	iii
ACKNOWLEDGEMENTS	iv
TABLE OF CONTENTS	v
LIST OF TABLES	x
LIST OF FIGURES	xi
ABSTRACT	xvi
CHAPTER 1	
Introduction	1
1.1 Modeling transport processes in estuaries and coasts	1
1.2 Objectives and Methodology	4
1.3 Organization.....	6
References	7
CHAPTER 2	
A screening analysis of control volume finite element Eulerian-Lagrangian methods	11
2.1 Introduction	11
2.2 Numerical Properties	12
2.2.1 Comparison of basic properties of accuracy and stability	12
2.2.1.1 One-dimensional truncation error analysis.....	13
2.2.1.2 Two-dimensional numerical experimentation.....	17
2.2 Comparison of CVFE-ELM formulations	20
2.3 Conclusions.....	26
References	27
CHAPTER 3	
On the role of tracking on Eulerian-Lagrangian solutions of the transport equation.	29

3.1	Introduction.....	29
3.2	Context.....	33
3.3	Numerical Formulation.....	42
3.4	Formal analysis	44
3.5	Numerical experimentation.....	47
	3.5.1 Experimental design	47
	3.5.2 Results and discussion	49
	3.5.2.1 Overall impact of tracking errors	49
	3.5.2.2 Mass errors	51
	3.5.2.3 Phase errors	54
	3.5.2.4 Numerical diffusion.....	54
3.6	Final considerations	58
	Appendix A - Review of models TEA-NL and ELA	62
	Appendix B - Tracking techniques	64
	Appendix C - Closure errors	66
	References.....	67
 CHAPTER 4		
	Local Mass Conservation in Finite Element Shallow Water Models	71
4.1	Introduction.....	71
4.2	Experiment set-up	72
4.3	Sources of local mass errors	78
4.4	Effect of grid refinement on mass conservation	80
4.5	Conclusions.....	81
	References.....	82
 CHAPTER 5		
	Mass Conservation of Eulerian-Lagrangian Transport Simulations in Estuaries and Coasts	84
5.1	Introduction	85

5.2	Model Formulations	88
5.2.1	Quadrature-Integration Control Volume Finite Element Eulerian-Lagrangian model (VELA)	89
5.2.2	Quadratic-Interpolation Finite Element Eulerian-Lagrangian model (ELA)	93
5.3	Analysis of Mass Conservation	94
5.3.1	Influence of integration errors at the feet of the characteristic lines	95
5.3.2	Influence of flow mass balance	101
5.3.3	Application to the Tagus estuary	108
5.4	Conclusions.....	119
	References	120
CHAPTER 6		
	Diagnostic Modeling of Residence Times in Estuaries	124
6.1	Introduction.....	124
6.2	Background.....	126
6.3	Method description	128
6.4	Accuracy analysis	130
6.5	Diagnostic characterization of residence times	135
6.5.1	Re-entrant Tracer	135
6.5.1.1	Experiment Set-up.....	135
6.5.1.2	Spatial Variability of Residence Times.....	136
6.5.1.3	Influence of release time (within the tidal cycle and for spring/neap tides)	140
6.5.1.4	Influence of river flow.....	143
6.5.1.5	Integral analysis.....	144
6.5.2	Once-through Tracer.....	145
6.5.2.1	Experiment set-up.....	145
6.5.2.2	Spatial Variability of Residence Times.....	146
6.5.2.3	Influence of release time	150
6.6	Conclusions.....	151
	References.....	152
CHAPTER 7		
	Final Considerations	155

7.1	Major Contributions.....	155
7.2	Directions for future research	158
7.2.1	Mass conservation in flow and transport models	159
7.2.1.1	Influence of inundation.....	159
7.2.1.2	Influence of the vertical dimension	161
7.2.2	Overall accuracy of ELMs	162
7.2.2.1	Three-dimensional finite element ELMs.....	162
7.2.2.2	Adaptive grids	165
7.3	Diagnostic modeling of residence times	166
	References	168

APPENDIX

	VELA, User's manual for a Two-Dimensional Depth-Averaged Transport and Particle Model	171
A.1	Introduction.....	171
A.2	Model Description	172
A.2.1	Transport model	172
A.2.1.1	c formulations.....	173
A.2.1.2	cH formulation.....	181
A.2.2	Particle model	182
A.3	Input Files Structure	186
A.3.1	Transport Grid File	187
A.3.2	Parameter File	187
A.3.3	Boundary Conditions File	189
A.3.4	Flow field File.....	190
A.3.5	Particle initial position File	191
A.3.6	Estuary limits File	191
A.3.7	Concentration initial conditions File	192
A.3.8	Source File	192
A.4	Output Files Structure	193
A.4.1	Particle transport mode	193
A.4.2	Mass transport mode	194
A.5	Examples of Application	195
A.5.1	Pure convection of a rotating Gauss hill	196

A.5.1.1	Definition of the Test	196
A.5.1.2	Input files	197
A.5.1.3	Results	200
A.5.2	Residence Times in the Tagus estuary	201
A.5.2.1	Definition of the Test	201
A.5.2.2	Input files	202
A.5.2.3	Results	206
References	206
VITAE	209

LIST OF TABLES

Table 3.1	2D Error Measures.....	37
Table 3.2	Tracking techniques.....	38
Table 3.3	Definition of particle runs.....	39
Table 3.4	Maximum and (Minimum) closure errors.	40
Table 3.5	1D Error measures.	48
Table 3.6	Parameters for Numerical tests.	49
Table 5.1	Tests parameters	99
Table A.1	Runge-Kutta coefficients	184

LIST OF FIGURES

Figure 2.1	Definition of control volume (shaded area).....	13
Figure 2.2	Effective diffusion numbers: a) comparison of Gauss and subdivision quadrature, for a range of Courant number from 0 to 1; b) variability with the number of subdivision points for a broader range of Courant numbers (similarly to other ELMs, the effective diffusion number of subdivision quadrature CVFE-ELMs is independent of the integer part of the Courant number).....	16
Figure 2.3	Comparison of maximum effective diffusion for several quadrature CVFE-ELMs.	17
Figure 2.4	Domain, flow field and initial conditions for CDF2.....	18
Figure 2.5	Comparison of mass error, peak ratios (maximum concentration in the model, divided by the maximum analytical concentration) and maximum negative concentration for ELA, and VELA with several subdivision levels..	19
Figure 2.6	a) Bathymetry (in meters) and initial conditions for the Polar Quadrant test, b) Bathymetry (in meters and relative to the mean sea level) and initial conditions for the Tagus estuary test.	22
Figure 2.7	a) Snapshot of the flow field for the Polar quadrant test at time = 4.75 hours; b) Snapshot of the flow field for the Tagus estuary test at time = 9 hours.	23
Figure 2.8	Comparison of mass and numerical damping of formulations that evaluate integrals at ξ and at the time $n+1$	24
Figure 2.9	Comparison of conservative and non-conservative formulations in the Polar Quadrant channel.	25
Figure 2.10	Conservative and non-conservative simulations in the Tagus estuary.	26
Figure 3.1	Sources of mass errors in ELMs: a) Backtracking of the characteristic lines: with tracking errors in one characteristic line only, for a Courant number of 1. b) Use of non-conservative flow field. c) Interpolation at the feet of the characteristic lines.	32
Figure 3.2a)	Bathymetry of the Tejo Estuary and location of the particles.	34
Figure 3.2b)	Flow field for $t=0$ s.	35
Figure 3.2c)	Grid and initial conditions for ELA runs.	35
Figure 3.3a)	Flow mass errors over a period of 3 tidal cycles: Maximum local mass errors per second, scaled by the elemental volumes at rest.	36
Figure 3.3b)	Flow mass errors over a period of 3 tidal cycles: Global mass errors per second in percentage, scaled by the volume of the estuary at rest.....	36
Figure 3.4	a) Mass errors for 3 tidal cycles, for Euler and Runge-Kutta tracking, with time steps of 10 and 60 minutes. b) Mass error differences between Euler and Runge-Kutta tracking techniques.....	42

Figure 3.5	Concentration field for $\sigma/\Delta x = 10$ and $Pe = \infty$, after 100 time steps (test 1).	50
Figure 3.6	Time series of error measures: a) Mass errors for several $\epsilon/\Delta x$ ($Cu = 1$) vs maximum mass errors for a simulation without tracking errors ($Cu = 0.5$). (b) 1 st moment for several $\epsilon/\Delta x$ ($Cu = 1$). (c) 2 nd moment for several $\epsilon/\Delta x$ ($Cu = 1$) against maximum 2 nd moment for a simulation without tracking errors ($Cu = 0.5$).....	51
Figure 3.7	Mean mass errors for 12 seeds (circles and dashed line): a) versus $\epsilon/\Delta x$. b) $\sigma/\Delta x$. c) Diffusion number ($D^*=Pe/Cu$).	52
Figure 3.8	Standard deviation of the mean mass errors: a) versus $\epsilon/\Delta x$. b) $\sigma/\Delta x$. c) D^*	53
Figure 3.9	Mean 1 st moment for 12 seeds (circles and dashed line): a) versus $\epsilon/\Delta x$. b) $\sigma/\Delta x$. c) D^*	55
Figure 3.10	Standard deviation of the mean first moment: a) versus $\epsilon/\Delta x$. b) $\sigma/\Delta x$. c) D^*	56
Figure 3.11	Potential for instabilities in presence of tracking errors, for a tracking error of 50%: (a) Concentration field for time steps 0, 11 and 48. (b) L2-norm for pi-ELM and reference ELM: instability generated by the presence of tracking errors.....	57
Figure 3.12	Time series of 2 nd moment with tracking errors scaled by time series of 2 nd moment without tracking errors (both with $Cu = 0.5$).....	58
Figure 3.13	Time series of L2-norm for several $\epsilon/\Delta x$	60
Figure 3.14	Time series of mass errors generated by tracking errors for several integration and interpolation ELMs: ELLAM with Gauss quadrature integration (Celia, 1994), piecewise ELM (Oliveira and Baptista, 1995), and linear interpolator ELM (Baptista, 1987).....	60
Figure 4.1 a)	Tagus estuary: bathymetry.....	73
Figure 4.1 b)	Computational grids: whole grid for source analysis; grid limited by thick line for convergence analysis.....	74
Figure 4.2	Maximum local mass errors for ADCIRC using a fully non-linear run: a) real bathymetry. b) flat bathymetry of 10m.....	76
Figure 4.3	Influence of non-linear terms and bathymetry on the maximum local mass errors for the 2D models: cumulative nodal percentages, which identify, for a specific value of local mass error m_i , the percentage of nodes that have an error equal to or larger than m_i	77
Figure 4.4	Influence of bathymetric slope on local mass errors: a) bathymetric profiles for the test cases; b) flux in the steepest element divided by the flux at the left boundary; c) scaled mass error (defined as the scaled flux minus 1, multiplied by 100) and linear regression (correlation coefficient of 0.999) versus the largest bathymetric slope in each bathymetric profile; d) scaled mass error versus the maximum elevation and velocity gradients.	79

Figure 4.5	Influence of grid refinement on local mass conservation. a) cumulative nodal percentages: 1) TIDE2D; 2) TEA-NL; 3) ADCIRC. b) scaled mass errors for the 1D runs.81
Figure 5.1	a) Definition of the control volume: shaded region. b) Triangles at the feet of the characteristic lines. c) Example of subdivision: 3 levels which leads to 9 integration sub-triangles.91
Figure 5.2	CDF5: Velocity field and concentration initial conditions (maximum concentration of 1). The shaded area indicates a flow cell.96
Figure 5.3	CDF5: Concentration distributions after 9 time steps for ELA and VELA with 7623 nodes (coarsest grid).97
Figure 5.4	CDF5: time series of mass ratios (mass in the model over the initial mass) for VELA and ELA, for several grid refinements.98
Figure 5.5	CDF5: correlation between cell size divided by Δx and maximum absolute mass errors.100
Figure 5.6	CDF5: effect of subdivision on VELA's: a) mass ratio; b) maximum concentration.102
Figure 5.7	Polar Quadrant channel with reverse quadratic bathymetry: Bathymetry, concentration initial conditions and level 0 grid.103
Figure 5.8	Polar channel: time series of mass ratios for VELA and ELA with several grid refinements.104
Figure 5.9	Polar channel: correlation between maximum flow mass errors and standard deviation of transport mass ratios.105
Figure 5.10	Polar channel: influence of the use of the conservative transport equation: a) mass conservation; b) maximum concentration for level 1 grid.107
Figure 5.11	Tagus estuary: a) bathymetry and location of initial position of Gauss plumes.108
Figure 5.11	Tagus estuary: b) Snapshot of flow field at time = 9 hours.109
Figure 5.11	Tagus estuary: c) coarsest grid for VELA.110
Figure 5.12	Tagus estuary: distribution of maximum local flow mass errors (s^{-1}).111
Figure 5.13	Concentration distributions for ELA and VELA 9 hours after release: a) Mouth plume; b) Upstream plume.112
Figure 5.14	Tagus estuary: time series of mass ratios for VELA and ELA for several grids.113
Figure 5.15	Tagus estuary: time series of mass ratios for several subdivision levels.114
Figure 5.16	Effect of bathymetry on mass errors (Tagus estuary): a) time series of absolute mass errors for VELA and ELA for real and constant bathymetry; b) time series of absolute mass errors for VELA with 1 and 8 subdivisions, for constant bathymetry.115

Figure 5.17	Tagus estuary - relationship between absolute mass errors and: a) time step; b) diffusion coefficient.	117
Figure 5.18	Influence of the continuity term (Lagrangian approach), for the mouth plume of the Tagus estuary: a) mass time series. b) maximum concentration time series.	118
Figure 6.1	a) Bathymetry of the Tagus estuary.....	126
Figure 6.1	b) Definition of the control region, release regions and release times for the re-entrant tracer. Particles in each release are distributed in a 50x50 m ² grid, the coarsest distribution leading to converged statistics.....	129
Figure 6.2	Effect of tracking accuracy: a) Statistics of distance between particle positions in real*8 and real*16 runs, for 10 M ₂ cycles. b) Closing errors. ...	131
Figure 6.3	Accuracy analysis - effect of advection for the re-entrant tracer.....	132
Figure 6.4	Accuracy analysis - effect of advection and the shape of the control region: a) reference control region, with advection. b) reference control region, without advection. c) alternative control region.....	133
Figure 6.5	Accuracy analysis - effect of grid refinement for the re-entrant tracer....	134
Figure 6.6	RTs for region 1 and release time 2 for the re-entrant tracer: a) Individual and statistics of RTs. b) Histogram and cumulative histogram of RTs. ...	137
Figure 6.7	Variability of RT in space.....	138
Figure 6.8	Snapshots of the forcing flow field for selected release times: a) release time 1. b) release time 4. c) release time 6. d) release time 11.	139
Figure 6.9	Variability of RT in time for every other release time. a) in region 2 and 4.	141
Figure 6.9	Variability of RT in time for every other release time. b) integrated over all regions.....	142
Figure 6.10	Histograms of RTs for region 1, release time 1, for a spring and a neap tides.....	142
Figure 6.11	Histograms of RTs for a river flow of 40, 400 and 4000 m ³ /s. a) release time 1, for region 5. b) release time 1, for region 6. c) region 1, for release time 8. d) region 1, for release time 12.....	143
Figure 6.12	Comparison of “single number” RT and histogram calculated with RT results at all release times and all regions. a) 4000 m ³ /s. b) 400 m ³ /s. Histograms are multiplied by 5.....	145
Figure 6.13	RTs versus river flow for integral approach using salinity data (adapted from Martins et al. (1984)) and transport model, and statistics of integrated particle model results (calculated with RTs from all release times and all regions).....	146
Figure 6.14	Map of RT for the whole estuary at release time 1.....	147

Figure 6.15	Maps of RT for the channel region: a) release time 1; b) release time 2; c) release time 3; d) release time 4; e) release time 5; f) release time 6.	148
Figure 6.15	Maps of RT for the channel region: g) release time 7; h) release time 8; i) release time 9; j) release time 10; k) release time 11; l) release time 12.	149
Figure 6.16	Maps of RT statistics. a) mean. b) standard deviation.....	150
Figure 7.1	Mass errors in flow and transport simulations in the Tagus estuary, with and without inundation: a) cumulative nodal fractions of maximum flow mass errors (mass errors are calculated with equation (4.2), but the scaling was done using the elemental volume at each time step). b) transport mass errors for a Gauss plume released in the upper Tagus estuary ('dry' nodes are not included in the computations).....	160
Figure 7.2	Domain discretization, control volume definition and subdivision quadrature integration	165
Figure 7.3	Residence times for the re-entrant tracer in region 4 (Figure 6.1b), using particle simulations forced by two flow fields that differ on the handling of the tidal flats.	167
Figure A.1	Control volume (shaded area in space and time), area of influence (Voronoi polygon, dark shaded area) and integration quadrangle at time $n+1$ (dashed area).	177
Figure A.2	a) integration area at the feet of the characteristic lines. b) subdivision of each triangle into sub-triangles: illustrated for 3 subdivision levels.	177
Figure A.3	Mapping of subdivision triangles from time step n to time step $n+1$	179
Figure A.4	Forward tracking of quadrature integration points for 5 subdivision levels at the mouth the Tagus estuary: a) initial positions; b) after 1 hour.	180
Figure A.5	Control region for a Tagus estuary simulation and example of residence time calculation for a re-entrant and once-through tracer.	185
Figure A.6	Geometry and forcings of the test case.	196
Figure A.7	Concentrations after 50 time steps: analytical solution and model represented by lines and filled isolines, respectively.	200
Figure A.8	Error measures a) mass error; b) peak error; c) negative concentrations.	201
Figure A.9	Tagus estuary: limits of control region (thick line) and particle release area (square).	202
Figure A.10	Residence times in the Tagus estuary: individual residence times and histogram analysis.	206

ABSTRACT

Eulerian-Lagrangian Analysis of Transport and Residence Times in Estuaries and Coasts

Anabela Pacheco de Oliveira

Oregon Graduate Institute of Science and Technology, 1997

Supervising Professor: António M. Baptista

Eulerian-Lagrangian methods (ELMs) are increasingly used to simulate groundwater and surface water transport and water quality, largely due to their ability to use large time steps and to formally decouple processes with distinct time scales. Yet, two severe limitations remain: (1) ELMs do not inherently conserve mass, and (2) in multiple dimensions, robust implementations of “higher-order” ELMs are expensive.

Our research focused on the understanding of the main sources of errors in ELMs. We analyzed systematically the impact and relative importance of tracking errors, integration errors and forcing by non-conservative flow fields, on measures of mass conservation, overall accuracy and stability. From this analysis, we propose new methodologies and general guidelines towards mass conservative, globally accurate and stable multi-dimensional ELM transport simulations in estuarine and coastal regions.

We performed a pioneering study of the influence of tracking errors, demonstrating their very strong negative impact on mass conservation, overall accuracy and stability. Low-order tracking methods are strongly discouraged in the presence of complex flow fields, typical of estuaries, because they are too inaccurate to allow overall mass balance and phase preservation, and they lead to potential instability.

We show that the evaluation of the integrals at the feet of the characteristic lines is an important source of mass and overall errors, which can be controlled through grid

refinement. To avoid such errors, we develop a new method that combines the flexibility and local mass properties of control volume finite element methods (CVFE), with a new quadrature integration technique. Subdivision quadrature overcomes stability constraints of traditional quadratures and allows for easy implementation in multiple dimensions. We find subdivision quadrature CVFE-ELMs to be an attractive alternative to current finite element ELMs in estuaries and coasts.

Non-conservative flow fields are the primary concern for estuarine and coastal applications because ELMs cannot mitigate their effect without jeopardizing overall accuracy. We found bathymetric gradients and complex geometry to be the main sources for flow mass errors, and grid refinement to be inadequate to eliminate them. Consequently, mass imbalances in ELM solutions cannot be removed by grid refinement. Control volume finite elements and conservative-equation-based formulations are equally ineffective in the presence of a non-conservative flow. The problem needs to be addressed at the source, i.e., the circulation models that generate the flows.

A detailed analysis of residence times illustrates the importance of improving numerical models, and provides new insights on the variability of residence times in estuarine systems. A new methodology is proposed, which emphasizes the importance of local analysis of residence times to understand the fluxing properties of a complex system, while providing an alternative approach to traditional bulk evaluations of residence times.

CHAPTER 1

Introduction

1.1 Modeling transport processes in estuaries and coasts

Estuaries and coasts are areas of great economic and ecological interest, which balanced management is broadly recognized as necessary for sustainable development. Numerical models are progressively becoming critical tools for optimization of estuarine resources, mostly due to their ability to simulate alternative scenarios at relatively low cost (Salomon and Pommeputy, 1990, Bell et al., 1992, Wu and Tsanis, 1994) and to their flexibility to address simultaneously physical, chemical and biological processes (e.g., Salomon and Pommeputy, 1990, Wood et al., 1995, Skogen et al., 1995, Ng et al., 1996).

The emerging development of nowcast-forecast systems for estuaries and coasts (e.g. CORIE¹, for the Lower Columbia River; CAFE, for Cheasapeake Bay; PORTS systems for Tampa Bay, Houston, New York and New Jersey) has raised new challenges on numerical modeling. Nowcast-forecast systems, which have been successfully used for climate, ocean and lake studies (Kelley et al., 1996; Schmalz, 1996), will require integration of complex real-time data acquisition systems with advanced numerical models to achieve an accurate characterization of both present and future circulation and transport patterns in estuarine and coastal regions (Baptista et al., 1997).

The quality of numerical models simulations is thus a fundamental part for the over-

1. <http://www.ccalmr.ogi.edu/CORIE/>

all success of these projects, in particular when complex problems such as wetting and drying of tidal flats are included. However, two major factors still limit numerical models predicting capabilities for most environmental applications: limited understanding of some processes and errors inherent to the numerical techniques used in the models.

The incomplete understanding of some important estuarine processes (e.g. turbulence) and their interactions (e.g. between physical and biological processes) is an important limitation on the predictive capabilities of numerical models, since models only represent the knowledge that we incorporate in them. However, predictions are not the only useful use of numerical models, which can often be most effectively used to advance our understanding of complex processes, through controlled experiments that target a specific problem (e.g. Wood et al., 1995).

The rapid growth of computational power over the last decades has led to an outburst of new and increasingly more complex numerical models. While relatively little attention has been dedicated to the assessment and intercomparison of model performances (see Lynch and Davies, 1995), accuracy, stability and mass conservation are basic requirements for the success of numerical modeling. In particular, when water quality is the ultimate goal, numerically-generated errors can jeopardize the final output as they propagate from flow to transport simulations.

Transport models, which are the core of most water quality numerical models for estuarine systems, have always been a challenge due to the different nature of the advective and dispersive processes. This dual nature has triggered the development of a multitude of methods including Eulerian-Lagrangian methods, ELMs (Baptista, 1987, Russell, 1989, Celia et al., 1990, Yeh et al, 1992, Healy and Russell, 1993, Oliveira and Baptista, 1995). ELMs combine the convenience of a fixed computational grid with tailor-made techniques for each process: advection is solved by the backward method of the characteristics, while diffusion is solved by finite differences, finite elements or finite volumes. The accuracy and stability of ELMs have been the subject of considerable attention, leading to the development of many distinct formulations (Neuman, 1984, Baptista, 1987, Celia et al., 1990, Yeh et al., 1992, Healy and Russell, 1993, Oliveira and Baptista, 1995).

In spite of their increasing application to a broad range of fields (Sorek, 1988, Binning and Celia, 1996, Hauguel, 1985, Dimou, 1992, Wood et al., 1995, Rasch and Williamson, 1990, Staniforth and Côté, 1991), ELMs remain limited by their inability to inherently conserve mass (Baptista, 1987, Russell, 1989). Transport mass errors can seriously jeopardize long-term simulations of conservative and non-conservative tracers. Mass errors are particularly problematic for multi-component water quality modeling, because they affect not only the global balance of a component species but they also affect all derived species which depend on the mass of the component species. Any mass imbalance introduced artificially by the numerical methods chosen for the solution of the hydraulic transport can thus alter the whole speciation and lead to an incorrect environmental characterization. The negative impact of mass imbalances is particularly strong on long-term simulations, even for conservative tracers.

Mass errors in ELM transport simulations result primarily from: 1) inaccurate tracking of the characteristic lines, 2) errors in the evaluation of the integrals at the feet of the characteristic lines, 3) forcing by a non-conservative flow field, and 4) implementation of boundary conditions. Mass errors generated by implementation of boundary conditions were formally addressed by a new class of ELMs - the Eulerian-Lagrangian Localized Adjoint Methods, ELLAMs (Zisman, 1990, Celia et al., 1990, Russell, 1989, Binning and Celia, 1996), but remain a problem for other ELM formulations. Understanding of the other sources of mass errors, as well as finding solutions to address them, remains an open research topic.

The development of increasingly more accurate numerical transport models is fundamental not only for predictive purposes, but also to help us deepen our understanding on estuarine processes. The conceptual approach, which emphasizes the diagnostic rather than the predictive potential of numerical models, is to use controlled experiments, much like laboratory experiments, to study specific problems. However, diagnostic modeling's representation of the actual system and larger flexibility in accounting for temporal and spatial scales are definite advantages relative to laboratory studies.

Diagnostic analysis, using both full transport models and simpler, particle-tracking

models, has been successfully used in estuaries for a wide variety of purposes such as a comparison of the clean-up properties of different processes (Salomon and Pommepey, 1990), a study of the chaotic dispersion in tidal systems (Fortunato et al., 1997), a study of the effect of physical processes on oyster recruitment (Jacobsen et al., 1990), and an investigation of the role of adsorption kinetics in the variability of the partitioning between the aqueous and solid phases (Wood et al., 1995). Recently, both particle and transport models have started to be used to characterize residence times (Hofmann et al., 1991, Salomon and Pommepey, 1990, Wu and Tsanis, 1990). Residence times are convenient and concise descriptors of the flushing properties of a system and provide a simple indicator for comparison amongst systems. However, past studies of residence times using numerical models focused on localized studies, and often lack a system-wide perspective of their complex spatial and temporal variability.

1.2 Objectives and Methodology

Our ability to simulate transport processes in estuarine systems can be greatly improved by a better understanding of the numerical properties of the models currently used and by avoiding the generation of important errors through appropriate choices in our modeling procedure. To achieve our overall goal of enhanced transport modeling using Eulerian-Lagrangian models, we examined in detail the influence of the tracking, the evaluation of the integrals at the feet of the characteristic lines and the use of non-conservative flows on the mass conservation, and on the overall accuracy and stability of ELMs.

Mass conservation is a basic requirement for accurate water quality modeling. **Our first goal was thus to understand the generation of mass errors in ELM simulations of transport in complex flows, and to propose new methodologies to achieve mass conservation.** These methodologies combine both recommended guidelines to prevent the generation of mass errors and new/adapted methods for the solution of the transport equation that are inherently less affected by the sources of mass errors. We compared the relative importance of each source of mass errors for surface water applications and identified relationships between the magnitude of the source and corresponding ELM mass errors. Since

flow mass errors are generated outside the ELM transport simulation, we also examined in detail the sources of flow mass imbalances in estuarine systems for different flow formulations and tested a model-independent solution.

Although mass conservation is the primary concern for water quality models, it should not be obtained at the expense of either overall accuracy or stability. **Our second goal was thus to combine the methodologies developed to achieve mass conservation in ELMs with techniques that preserve the stability and overall accuracy of the integration FE-ELMs proposed in Oliveira (1994).** Since the exact integration method from Oliveira (1994) is awkward to implement and computationally intensive in two dimensions (Priestley, 1994), we proposed a quadrature integration method that combines good overall accuracy with unconditional stability and simplicity of implementation in multiple dimensions.

Since our ultimate goal was to improve transport simulations for real problems in surface water systems, this research was performed both on simple benchmark problems from the Convection-Diffusion forum (Baptista et al., 1995), on synthetic systems with analytical flow fields (Lynch and Gray, 1978) and on the Tagus estuary. Whenever convenient, formal analysis further supported the numerical experimentation.

Our analysis is conducted on a simplified, two-dimensional, depth-averaged framework. Although the state-of-the-art in ELM transport models is three-dimensional (see for instance, Dimou, 1992, King and DeGeorge, 1996), mass imbalances are associated with the Lagrangian treatment of advection, and therefore are present on both 2D and 3D problems. Two-dimensional transport problems avoid the large computational cost associated with current 3D, finite element ELM models, thus allowing for a more systematic, detailed analysis, while keeping the geometric complexity associated with most estuarine and coastal systems.

Finally, we take advantage of elements of the numerical techniques described above to explore the use of particle tracking to characterize residence time variability in estuarine and coastal systems. Residence times (RTs) have been extensively used in estuarine studies for a variety of purposes (Pilson, 1985, Salomon and Pommepuy, 1990, Jay et al., 1995),

but most past studies overlook spatial and temporal variability of RTs within a given estuary. **Our final goal was to develop methodologies to understand the spatial and temporal variability of residence times for conservative (dissolved) tracers.** The analysis was conducted using particles as conservative tracers, and two different approaches were proposed, to account for different tracers' properties. This analysis constitutes a first step towards a more comprehensive, broader analysis of residence times that addresses non-conservative tracers.

1.3 Organization

This thesis comprises seven chapters (including this Introduction), and one appendix. Chapter 2 analyzes the basic properties of several control volume finite element ELMs (CVFE-ELMs), through a combination of formal analysis and numerical experimentation. CVFE-ELMs are the basis for a new model, VELA, used in Chapters 5 and 6 and described in detail in the Appendix.

Chapters 3 to 6 address the impact of the several sources of errors on ELM transport simulations, and explore the use of particle models for residence time characterization. These chapters were written as stand-alone contributions, which can be read separately. Chapter 3¹ examines the influence of tracking on ELM's mass conservation, stability and overall accuracy through a combination of one-dimensional formal analysis and numerical experimentation. The relative importance of tracking errors as a source of mass errors is assessed in a two-dimensional application to a real system and guidelines are suggested to prevent the generation of tracking errors.

Chapter 4 examines the generation of local flow mass errors in finite element, depth-averaged two-dimensional flow simulations in a real system. The analysis is conducted with three flow models with distinct formulations which are representative of the most popular approaches in estuarine finite element modeling. The use of grid refinement is also tested as a model-independent solution to address this problem.

1. Oliveira and Baptista (1997a).

Chapter 5¹ investigates the generation of ELM transport mass imbalances due to integration errors and to flow mass errors as analysed on Chapter 4. The analysis is carried out both in simple tests and a complex estuary, using two distinct transport models. Solutions and guidelines are proposed to address each problem.

Chapter 6² presents a new methodology for the diagnostic evaluation of residence times in estuaries and coasts, taking advantage of the flexibility of numerical models. The particle mode of VELA is used to investigate the space and time variability of residence times and to illustrate the importance of local residence time analysis, as opposed to traditional bulk, single-value methodologies, for the environmental characterization of estuaries and coasts.

Chapter 7 summarizes the major contributions of this work and suggests some avenues for future research. The Appendix is a synthetic user's manual for VELA.

References

- Baptista, A.M., 1987. *Solution of Advection-Dominated Transport by Eulerian-Lagrangian Methods using the Backwards Method of Characteristics*, Ph.D. Dissertation, Massachusetts Institute of Technology, Cambridge.
- Baptista, A.M., E.E. Adams and P. Gresho, 1995. Benchmarks for the Transport Equation: the Convection-Diffusion Forum and Beyond, in *Quantitative Skill Assessment for Coastal Ocean Models*, D.R. Lynch et al. (editors), American Geophysical Union Estuarine/Coastal Monograph, 47: 241-268.
- Baptista, A.M., M. Wilkin, P. Pearson, C. McCandlish, D. Jay, B.C. Beck, S. Das, J. Hunt, P. Barrett, 1997. Towards a Nowcast-Forecast System for the Columbia River Estuary, in *Proceedings of the 5th International Conference on Estuarine and Coastal Modeling*, M.L. Spaulding et al. (editors), American Society of Civil Engineers, (in press).
- Bell, R.G., D. Munro and P. Powell, 1992. Modelling Microbial Concentrations from Multiple Outfalls Using Time-Varying Inputs and Decay Rates, *Water Science and Technology*, 25(9): 181-188.

1. Prepared for submission to the International Journal for Numerical Methods in Fluids.
 2. Oliveira and Baptista (1997b).

- Binning, P. and M.A. Celia, 1996. A Finite-Volume Eulerian-Lagrangian Localized Adjoint Method for Solution of the Contaminant Transport Equations in Two-Dimensional Multiphase Flow Systems, *Water Resources Research*, 32(1): 103-114.
- Celia, M.A., T.F. Russell, I. Herrera, R.E. Ewing, 1990. An Eulerian-Lagrangian Localized Adjoint Method for the Advection-Diffusion Equation, *Advances in Water Resources*, 13(4): 187-206.
- Dimou, K., 1992. *3-D Hybrid Eulerian-Lagrangian / Particle Tracking Model for Simulating Mass Transport in Coastal Water Bodies*, Ph.D. Dissertation, Massachusetts Institute of Technology, Cambridge.
- Fortunato, A.B., A.M. Baptista and R.A. Luetlich, Jr., 1997. A Three-Dimensional Model of Tidal Currents at the Mouth of the Tagus Estuary (Portugal), *Continental Shelf Research* (in press).
- Hauguel, A., 1985. Numerical modelling of complex industrial and environment flows, in *Proceedings of the 1st International Symposium on Refined Flow Modelling and Turbulence Measurements*, K1-1-K1-25.
- Healy, R.W. and T.F. Russell, 1993. A Finite-Volume Eulerian-Lagrangian Localized Adjoint Method for Solution of the Advection-Dispersion Equation, *Water Resources Research*, 29(7): 2399-2413.
- Hofmann, E.E., K.S. Hedstrom, J.R. Moisan, D.B. Haidvogel and D.L. Mackas, 1991. Use of Simulated Drifter Tracks to Investigate General Transport Patterns and Residence Times in the Coastal Transition Zone, *Journal of Geophysical Research*, 96(C8): 15,041-15,052.
- Jacobsen, T.R., J.D. Milutinovic and J.R. Miller, 1990. Recruitment in Estuarine Benthic Communities: The Role of Physical Processes, in *Residual Currents and Long-Term Transport*, Coastal and Estuarine Studies, R.T. Cheng (editor), American Geophysical Union, 38: 513-525.
- Jay, D., W.R. Geyer and D.R. Montgomery, 1995. An Ecological Approach to Estuarine Classification, in *Estuarine Synthesis*, J. Hobbie (editor), Scientific Committee on the Problems of the Environment, (submitted).
- Kelley, J., D. Welsh, K.W. Bedford, D. Schwab, J.S. Hobgood and B. Hoch, 1996. High-Resolution, Short-Term Lake Forecasts for Lake Erie, in *Proceedings of the 4th International Conference on Estuarine and Coastal Modeling*, M.L. Spaulding and R.T. Cheng (editors), American Society of Civil Engineers, 367-378.

- King, I.P. and J.F. DeGeorge, 1996, Multidimensional modeling of Water Quality using the Finite Element Method, in *Proceedings of the 4th International Conference on Estuarine and Coastal Modeling*, M.L. Spaulding and R.T. Cheng (editors), American Society of Civil Engineers, 340-354.
- Lynch, D.R. and W.G. Gray, 1978. Analytic Solutions for Computer Flow Model Testing, *Journal of Hydraulics Division*, 104(HY10): 1409-1427.
- Lynch, D.R. and A.M. Davies, 1995. Preface, in *Quantitative Skill Assessment for Coastal Ocean Models*, D.R. Lynch and A.M. Davies (editors), American Geophysical Union Estuarine/Coastal Monograph, 47.
- Neuman, S.P., 1984. Adaptive Eulerian-Lagrangian Finite Element Method for Advection-Dispersion, *International Journal for Numerical Methods in Engineering*, 20(2): 321-337.
- Ng, B., A. Turner, A.O. Tyler, R.A. Falconer and G.E. Millward, 1996. Modelling Contaminant Geochemistry in Estuaries, *Water Research*, 30(1): 63-74.
- Oliveira, A., 1994. *A comparison of Eulerian-Lagrangian Methods for the Solution of the Transport Equation*, M.Sc. thesis, Oregon Graduate Institute of Science and Technology, Portland.
- Oliveira, A. and A.M. Baptista, 1995. A Comparison of Integration and Interpolation Eulerian-Lagrangian Methods, *International Journal for Numerical Methods in Fluids*, 21(3): 183-204.
- Oliveira, A. and A.M. Baptista, 1997a. The role of tracking on Eulerian-Lagrangian solutions of the transport equation, *Advances in Water Resources*, (in press).
- Oliveira, A. and A.M. Baptista, 1997b. Diagnostic Modeling of Residence Times in Estuaries, *Water Resources Research*, 33(8): 1935-1946.
- Pilson, M.E., 1985. On the Residence Time of Water in Narragansett Bay, *Estuaries*, 8(1): 2-14.
- Priestley, A., 1994. Exact Projections and the Lagrange-Galerkin Method: A Realistic Alternative to Quadrature, *Journal of Computational Physics*, 112(2): 316-333.
- Rasch, P.J. and D.L. Williamson, 1990. On shape-preserving interpolation and semi-Lagrangian transport, *SIAM Journal of Scientific and Statistical Computing*, 11(4): 656-687.

- Russell, T.F., 1989. Eulerian-Lagrangian Localized Adjoint Methods for Advection-Dominated Problems, in *Numerical Analysis 1989*, Pitman Research Notes, D.F. Griffiths and G.A. Watson (editors), Longman Scientific and Technical, 228: 206-228.
- Salomon, J.C. and M. Pompey, 1990. Mathematical Model of Bacterial Contamination of the Morlaix Estuary (France), *Water Research*, 24(8): 983-994.
- Schmaltz, Jr., R.A., 1996. Southern Boundary Experimental Forecasts with the NOAA East Coast Ocean Model, in *Proceedings of the 4th International Conference on Estuarine and Coastal Modeling*, M.L. Spaulding and R.T. Cheng (editors), American Society of Civil Engineers, 442-453.
- Skogen, M.D., E. Svendsen, J. Berntsen, D. Aksnes, K.B. Ulvestad, 1995. Modelling the Primary Production in the North Sea using a Coupled Three-Dimensional Physical-Chemical-Biological Ocean Model, *Estuarine, Coastal and Shelf Science*, 41(5): 545-565, 1995.
- Sorek, S., 1988. Eulerian-Lagrangian method for solving transport in aquifers, *Advances in Water Resources*, 11(2): 67-73.
- Staniforth, A. and J. Côté, 1991. Semi-Lagrangian Integration Schemes for Atmospheric Models - A review, *Monthly Weather Review*, 119(9): 2206-2223.
- Wood, T.M., A.M. Baptista, J.S. Kuwabara and A.R. Flegal, 1995. Diagnostic Modeling of Trace Metal Partitioning in South San Francisco Bay, *Limnology and Oceanography*, 40(2): 345-358.
- Wu, J. and I.K. Tsanis, 1994. Pollutant Transport and Residence Time in a distorted scale model and a numerical model, *Journal of Hydraulic Research*, 32(4): 583-598.
- Yeh, G.T., J.R. Chang and T.E. Short, 1992. An exact peak capturing and oscillation-free scheme to solve advection-dispersion transport equations, *Water Resources Research*, 28(11): 2937-2951.
- Zisman, S., 1990. *Simulation of Contaminant Transport in Groundwater Systems using Eulerian-Lagrangian Localized Adjoint Methods*, M.Sc. Thesis, Massachusetts Institute of Technology, Cambridge.

CHAPTER 2

A screening analysis of control volume finite element Eulerian-Lagrangian methods

2.1 Introduction

Finite volumes are becoming increasingly popular in Eulerian transport models, mostly due to the local enforcement of mass conservation (Wang et al., 1986, Putti et al., 1990), and have also been successfully combined with Eulerian-Lagrangian methods and structured grids (Roache, 1992, Healy and Russell, 1993, Binning and Celia, 1996). The extension of these methods to unstructured grids by implementing finite volume concepts on a finite element framework (control volume finite element Eulerian-Lagrangian methods, CVFE-ELMs) appear thus a promising avenue for modeling of transport in complex estuarine systems. The use of integration at the feet of the characteristic lines is also attractive, because it provides considerable accuracy gains over the ELMs currently used in engineering models (Oliveira and Baptista, 1995).

The objective of this chapter is to analyze the numerical properties of quadrature integration control volume finite element ELMs. Since control volume finite element ELMs are rather new, an assessment of the basic numerical properties and comparison with reference methods is necessary. Also, many choices can be made in the implementation of CVFE-ELMs. We explore several approaches, with the overall goal of mass conservation, but without overlooking overall accuracy and stability. In particular, we test:

- the use of conservative versus non-conservative formulations, through the introduction of a correcting continuity term;
- the use of the depth-averaged concentration (c) versus the total mass in the water column (cH), as the quantity transported along the characteristic lines;
- the use of direct integration at the feet of the characteristic lines or mapping to the control volume at the head of the characteristic lines.

In this analysis, we use a new two-dimensional, multiple-formulation, quadrature integration CVFE-ELM transport model (VELA). VELA uses subdivision quadrature integration, which keeps the flexibility of traditional quadrature integration methods. Unlike traditional quadratures, though, subdivision quadrature methods are unconditionally stable, as shown in section 2.2.1.1. A detailed description of VELA's formulation, input and output files and two examples of application are presented in the Appendix.

This chapter includes two sections, besides this **Introduction**. The purpose of **Numerical Properties** is two-fold: to compare the basic properties of subdivision quadrature CVFE-ELMs with other formulations, using both 1D formal analysis and a simple 2D benchmark test (Baptista et al., 1995); and to compare several CVFE-ELM formulations using a simple geometry test and a complex estuary. **Conclusions** summarizes the main findings of this chapter.

2.2 Numerical Properties

2.2.1 Comparison of basic properties of accuracy and stability

A combination of truncation error analysis and numerical experimentation is used to assess the stability and overall accuracy of CVFE-ELMs. A 1D truncation error analysis compares the performance of subdivision integration CVFE-ELMs with Gauss and Lobatto integration CVFE-ELMs, and provides a criterion to select the number of subdivision levels in the evaluation of the integrals. Test 2 from the Convection-Diffusion forum (Baptista et al., 1995) extends the conclusions drawn in the formal analysis to two dimen-

sional problems, and compares the performance of CVFE-ELMs with a reference quadratic interpolation FE-ELM (ELA, Baptista et al., 1984).

2.2.1.1 One-dimensional truncation error analysis

We first consider the solution of the simplified, one-dimensional transport equation with constant coefficients in an infinite domain:

$$\frac{Dc}{Dt} = D \frac{\partial^2 c}{\partial x^2} \quad (2.1)$$

where Dc/Dt is the total derivative of the concentration (c), D is the diffusion coefficient, t is time and x is the spatial coordinate.

Equation (2.1) is discretized in time with an α -method leading to:

$$\frac{c^{n+1} - c^\xi}{\Delta t} = \alpha \left(D \frac{\partial^2 c}{\partial x^2} \right)^{n+1} + (1 - \alpha) \left(D \frac{\partial^2 c}{\partial x^2} \right)^\xi \quad (2.2)$$

where ξ denotes the feet of the characteristic lines at time n and Δt is the time step.

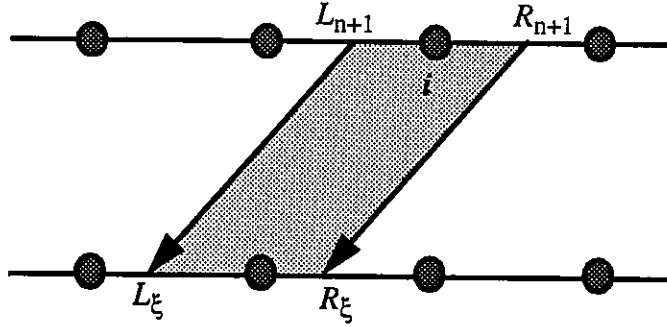


Figure 2.1 Definition of control volume (shaded area).

We integrate equation (2.2) over each control volume (defined in Figure 2.1):

$$\int_{\Omega_{cv}} c^{n+1} d\Omega_{cv} - \int_{\Omega_{cv}} c^\xi d\Omega_{cv} - \alpha \Delta t D \frac{\partial c}{\partial x} \Big|_{R_{n+1}}^{L_{n+1}} - (1 - \alpha) \Delta t D \frac{\partial c}{\partial x} \Big|_{R_\xi}^{L_\xi} = 0 \quad (2.3)$$

where L_i and R_i represent the limiting left and right characteristic lines at time i , respectively.

Using a generic quadrature method to evaluate the integrals at ξ leads to:

$$\begin{aligned} & \frac{\Delta x}{8}(c_{i-1}^{n+1} + 6c_i^{n+1} + c_{i+1}^{n+1}) - \frac{\alpha \Delta t D}{\Delta x}(c_{i-1}^{n+1} - 2c_i^{n+1} + c_{i+1}^{n+1}) = \\ & \frac{\Delta x}{2} \sum_{j=1}^{nqp} w_j \left(\frac{1}{2}(1-\phi)c_{j-\vartheta}^n + \frac{1}{2}(1+\phi)c_{j-\vartheta+1}^n \right) + \\ & (1-\alpha) \frac{\Delta t D}{\Delta x} (c_{j-k''+1}^n - c_{j-k''}^n - c_{j-k'+1}^n + c_{j-k'}^n) \end{aligned} \quad (2.4)$$

where Δx is the grid spacing, nqp is the number of quadrature points, β is the Courant number, and:

$$\begin{aligned} k' &= \text{int}\left(\beta + \frac{1}{2}\right) + 1 \\ k'' &= \text{int}\left(\beta - \frac{1}{2}\right) + 1 \end{aligned} \quad (2.5)$$

$$\left. \begin{aligned} \phi &= 2\left(\vartheta + \frac{r_j}{2} - \beta\right) - 1 \\ \vartheta &= \text{int}\left(\beta - \frac{r_j}{2} + 1\right) \end{aligned} \right\} \quad \text{for } r_j \geq 0$$

$$\left. \begin{aligned} \phi &= 2\left(\vartheta + \frac{r_j}{2} - \beta\right) - 1 \\ \vartheta &= \text{int}\left(\beta - \frac{r_j}{2}\right) + 1 \end{aligned} \right\} \quad \text{for } r_j < 0 \quad (2.6)$$

where r_j are the coordinates of the quadrature points, between -1 and 1. For subdivision quadrature integration, the quadrature weighting factors are defined as:

$$\begin{aligned} w_j &= \frac{1}{nqp-1} \quad \text{for } j = 1 \text{ or } j = nqp \\ w_j &= \frac{2}{nqp-1} \quad \text{other } j \end{aligned} \quad (2.7)$$

Taylor series expansion of equation (2.4) leads to the truncation error:

$$\begin{aligned} \mu = & \left[\frac{\Delta x}{\Delta t} \sum_{j=1}^{nqp} \left(\beta - \frac{r_j}{2} \right) \right] \frac{\partial c}{\partial x} + \\ & + \left[\frac{\Delta x^2}{\Delta t} \left(-\frac{\beta^2}{2} - \frac{1}{8} + \sum_{j=1}^{nqp} \frac{w_j}{8} ((1-\phi)\vartheta^2 + (1+\phi)(1-\vartheta)^2) \right) \right] \frac{\partial^2 c}{\partial x^2} \end{aligned} \quad (2.8)$$

To compare the properties of the different quadrature methods, it is convenient to define the *Effective Diffusion number* associated with the second derivative of concentration:

$$\Upsilon(\beta) = -\frac{\beta^2}{2} - \frac{1}{8} + \sum_{j=1}^{nqp} \frac{w_j}{8} ((1-\phi)\vartheta^2 + (1+\phi)(1-\vartheta)^2) + D \quad (2.9)$$

Effective diffusion numbers, for $D = 0$ and for both Gauss and subdivision quadrature CVFE-ELMs, are presented in Figure 2.2 (where negative values of Υ indicate instability and positive values are a measure of numerical diffusion). Similarly to other quadrature methods (Oliveira and Baptista, 1995), the numerical diffusion of the subdivision CVFE-ELMs depends strongly on the fractional Courant number, with exact solutions when the feet of the characteristic lines falls on top of a node. Unlike Gauss and other quadrature methods (Figure 2.2a), however, subdivision quadrature is unconditionally stable (within the conditions of truncation error analysis, Figure 2.2b), thus removing the major limitation for the application of quadrature methods.

Similarly to other quadratures, the accuracy of the subdivision CVFE-ELMs is strongly dependent on the number of quadrature points. The maximum effective diffusion number was plotted against the number of quadrature points for Gauss, Lobatto and subdivision quadratures (Figure 2.3). Results show that subdivision is the least accurate of the three methods, for an equal number of points. Accuracy becomes very similar for n Gauss points, $n+1$ Lobatto points and $n+2$ subdivision points (Figure 2.3). Previous studies (Oliveira and Baptista, 1995) showed that a large number of quadrature points (on the order of 6-7 Gauss points) is necessary for accurate results with small peak error. Compar-

ison of effective diffusion numbers for Gauss and subdivision methods suggests that at least 8-9 subdivision points are necessary for similar accuracy.

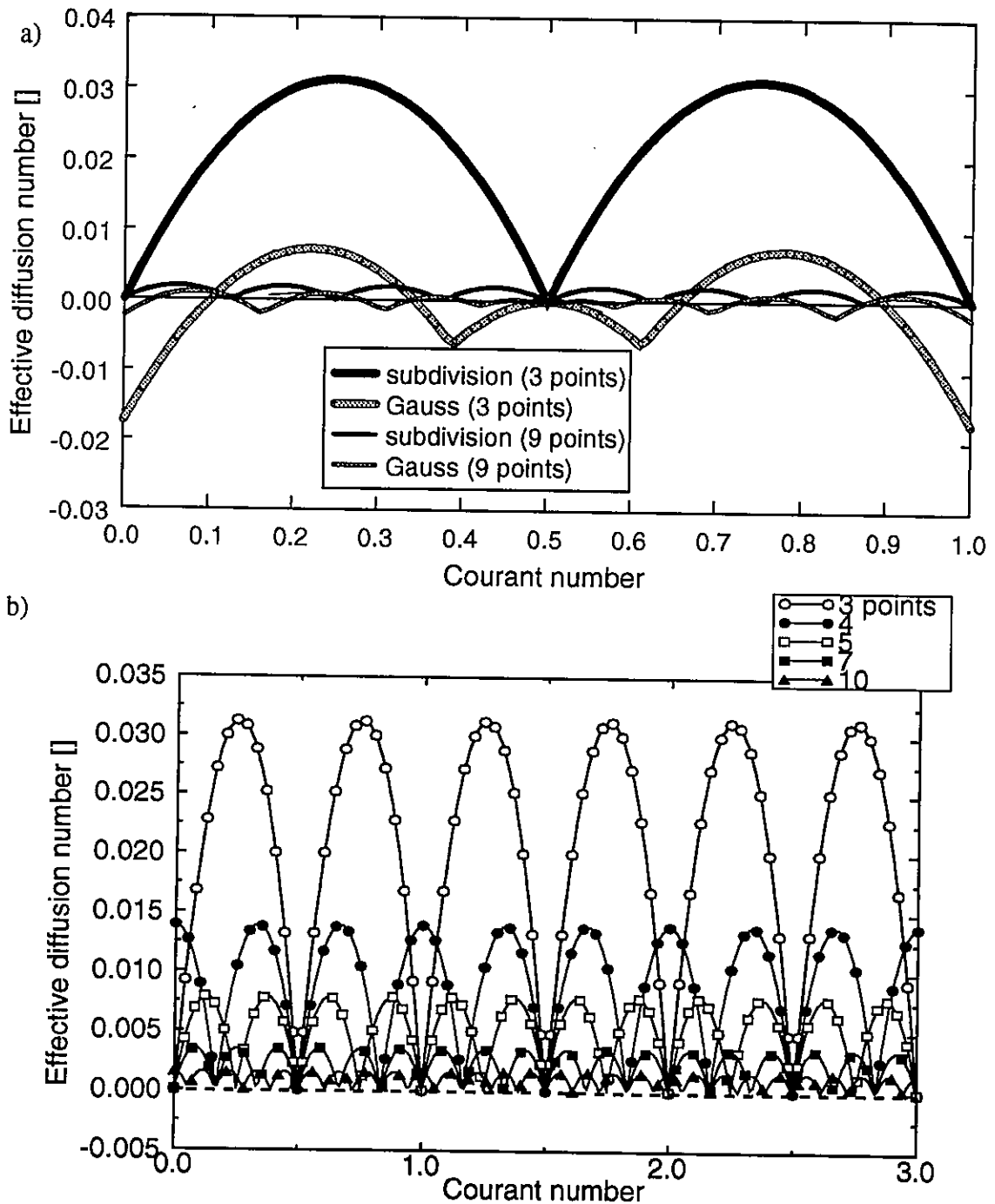


Figure 2.2 Effective diffusion numbers: a) comparison of Gauss and subdivision quadrature, for a range of Courant number from 0 to 1; b) variability with the number of subdivision points for a broader range of Courant numbers (similarly to other ELMs, the effective diffusion number of subdivision quadrature CVFE-ELMs is independent of the integer part of the Courant number).

Our analysis showed that, at least for simple flows, subdivision quadrature is an attractive alternative to the exact-integration method (Oliveira and Baptista, 1995), by combining the flexibility of quadrature methods with unconditional stability. Although subdivision CVFE-ELM is less accurate than other quadratures for the same number of points, the increase in subdivision levels for comparable accuracy is small.

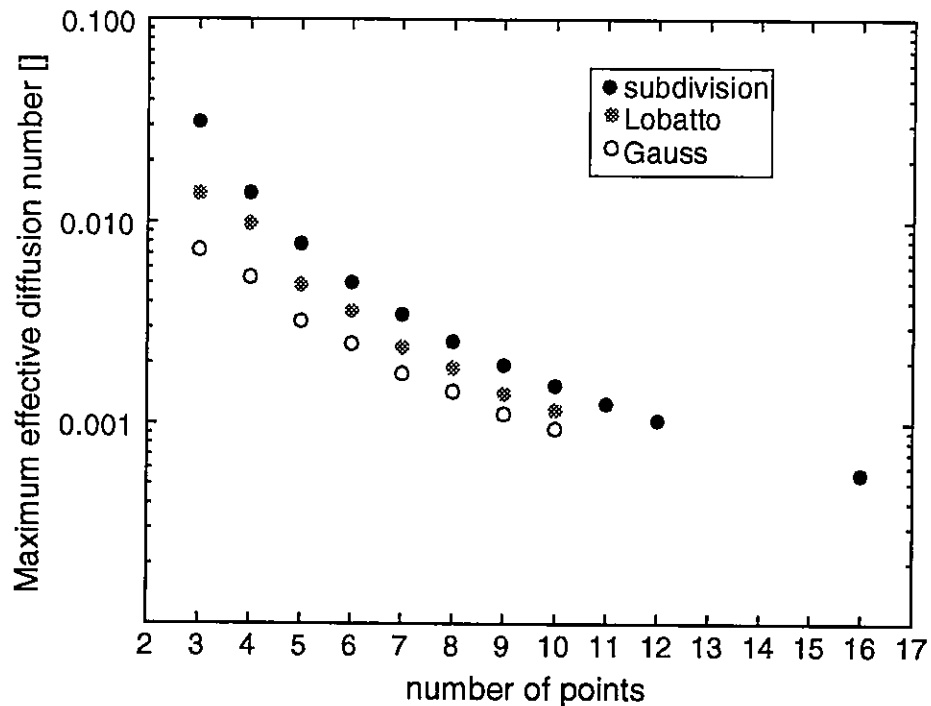


Figure 2.3 Comparison of maximum effective diffusion for several quadrature CVFE-ELMs.

2.2.1.2 Two-dimensional numerical experimentation

This section compares basic overall accuracy and mass conservation of CVFE-ELM, using VELA, with those from a quadratic interpolation FE-ELM (ELA, Baptista et al., 1984). The analysis is conducted using test 2 from the Convection-Diffusion forum (CDF2, Baptista et al., 1995), which represents the pure convection of a rotating Gauss hill. The plume is defined by a standard deviation of 600 m and a maximum concentration of 1 (Figure 2.4). The simulations were performed with two grids for VELA (grid spacing of 200 and 100 m, dimensionless standard deviations of 3 and 6) and one grid for ELA (grid spacing of 100 m and standard deviation of 6). VELA simulations were performed

for 1, 2, 4, 8, and 16 levels of subdivision, for both grids. Simulations were run for 50 time steps, with a time step of 50 s. Comparison between models is based on peak ratios, mass errors, and maximum negative concentrations. All simulations are performed without diffusion.

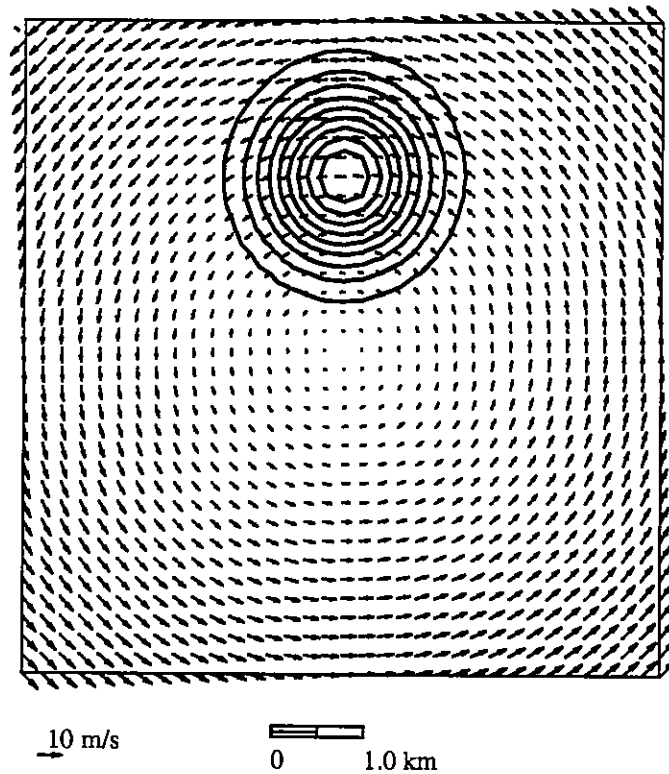


Figure 2.4 Domain, flow field and initial conditions for CDF2.

In close agreement with the formal analysis, the accuracy of VELA is strongly dependent on the number of quadrature points and on grid refinement. Mass conservation is heavily reduced by a larger number of subdivisions and by increased grid refinement (Figure 2.5). Peak errors are also reduced by grid refinement, but differences are diluted with increasing number of subdivision levels: for 16 subdivision levels, the maximum concentrations are very similar for the two grids.

Unlike other error measures, oscillations (measured by maximum negative concentrations) are practically the same for all simulations within each grid, except for a sin-

gle subdivision (Figure 2.5). Increasing grid refinement does not reduce the amplitude of the oscillations, but actually increases them for 2 or more subdivisions. This behavior deserves further investigation, but it is out of the scope of this analysis.

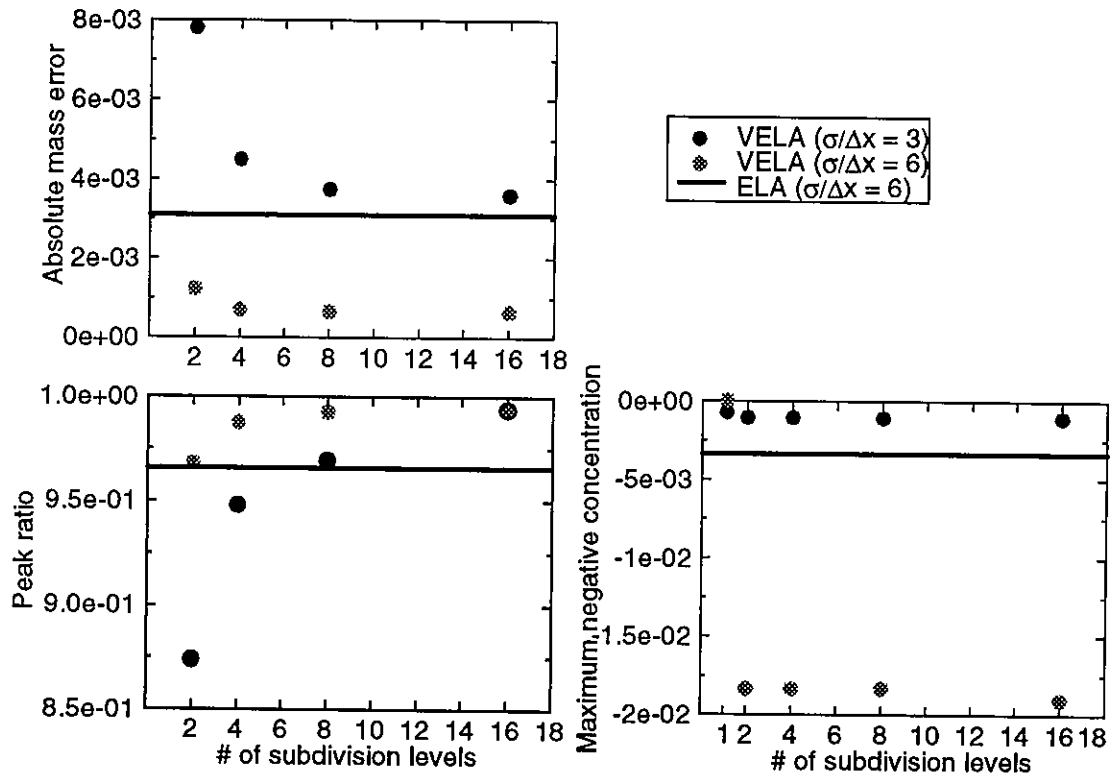


Figure 2.5 Comparison of mass error, peak ratios (maximum concentration in the model, divided by the maximum analytical concentration) and maximum negative concentration for ELA, and VELA with several subdivision levels.

Excessive oscillations can be avoided if distinct subdivisions are used in different areas of the domain, taking advantage of the numerical damping associated with small subdivisions to reduce oscillations. For instance, one subdivision (e.g. linear interpolation in the control volume) can be used in areas of negative concentration, while keeping the necessary number of subdivisions for small numerical damping in regions of positive concentration. This approach was used on VELA's finer grid using 8 subdivision levels everywhere except where concentrations at the feet of the characteristic lines were negative, and reduced maximum negative concentrations from -1.8×10^{-2} to -1.0×10^{-16} .

Comparison of VELA and ELA for the same number of elements ($\sigma/\Delta x = 3$ for VELA and $\sigma/\Delta x = 6$ for ELA) shows that mass errors are slightly larger for VELA, but

differences are considerably reduced if 8 or more subdivision levels are used (Figure 2.5). For an equal number of nodes, VELA's mass errors are much smaller than ELA's, for two or more subdivisions. Numerical damping follows a similar pattern: for the same number of elements, 8 or more subdivision levels are sufficient to guarantee smaller peak errors; for the same number of nodes, VELA's peak errors are always smaller than ELA's.

Our analysis showed that VELA compares favorably with traditional quadratic interpolation FE-ELMs. Mass and peak errors are clearly reduced by the combined use of finite volumes and integration techniques. These results confirm the 1D formal analysis and further suggest that the use of at least 8 subdivisions or increased grid refinement are necessary for accurate mass and small peak errors.

2.2.2 Comparison of CVFE-ELM formulations

Distinct CVFE-ELM formulations can be obtained depending on the time level where integrals are evaluated and on the form of the transport equation. Integrals can be directly evaluated at the feet of the characteristic lines (ξ), or at the time step where concentrations are being evaluated, through mapping of the subdivision points ($n+1$). The transport equation can also be solved in its non-conservative form by transporting the concentration along the characteristic lines (non-conservative c formulation), or on its conservative form, either by including the continuity equation term (conservative c formulation) or by transporting the total concentration in the water column backwards in time (cH formulation). The purpose of this section is to compare each of these options, and select the combination that provides best mass conservation and overall accuracy.

This analysis is conducted using VELA with two tests of increasing complexity: advection of a Gauss hill on the Polar Quadrant channel with reverse quadratic bathymetry (Lynch and Gray, 1978, Chen, 1989) and the Tagus estuary. The purpose of the Polar quadrant test is two-fold: to compare the performance of formulations evaluating integrals at time $n+1$ or ξ , and to analyze the differences between c and cH formulations in mass conservation and peak error. The Tagus estuary is then used to illustrate the stability problems of conservative formulations and integration at ξ in complex systems.

For the Polar quadrant test, a Gauss plume with standard deviation of 5000 m and a maximum concentration of 1, is forced by the analytical flow field from Chen (1989). Bathymetry is reverse quadratic with a minimum of 5 m at the open boundary and a maximum of 154 m at the opposite boundary (Figure 2.6a). Elevation (η) and radial velocity (v) are defined as (Chen, 1989):

$$\eta(r, t) = Re \left\{ \eta_0 \frac{\cos \left[\frac{\beta}{2} (r^2 - r_1^2) \right]}{\cos \left[\frac{\beta}{2} (r_2^2 - r_1^2) \right]} e^{i\omega t} \right\} \quad (2.10)$$

$$v(r, t) = Re \left\{ -\eta_0 r \frac{i\omega \sin \left[\frac{\beta}{2} (r^2 - r_1^2) \right]}{\beta h_0 \cos \left[\frac{\beta}{2} (r_2^2 - r_1^2) \right]} e^{i\omega t} \right\}$$

where ω is the forcing tidal frequency, t is time, r , r_1 and r_2 are defined in Figure 2.6a, depth is defined as $h = h_0 x r^2$, $i = \sqrt{-1}$ and:

$$\beta^2 = \frac{(\omega^2 - i\omega t)}{gh_0} \quad (2.11)$$

where g is the gravity.

The flow field is forced by a M_8 wave (period of 3.1 h) with an amplitude of 1 m (Figure 2.7a). Simulations are performed with 3 grids with increasing refinement, for 100 time steps and using a time step of 900 s. All simulations are performed without diffusion.

Simulations in the Tagus estuary also involve a Gauss plume, released instantaneously close to the mouth. The flow field (Fortunato et al., 1997, Figure 2.7b) was calculated with a wave-equation model (*ADCIRC*, Luettich et al., 1991), with realistic tidal forcing and a grid with 1784 nodes. Bathymetry is complex and ranges from 2.5 to 600 m in our simulations (Figure 2.6b).

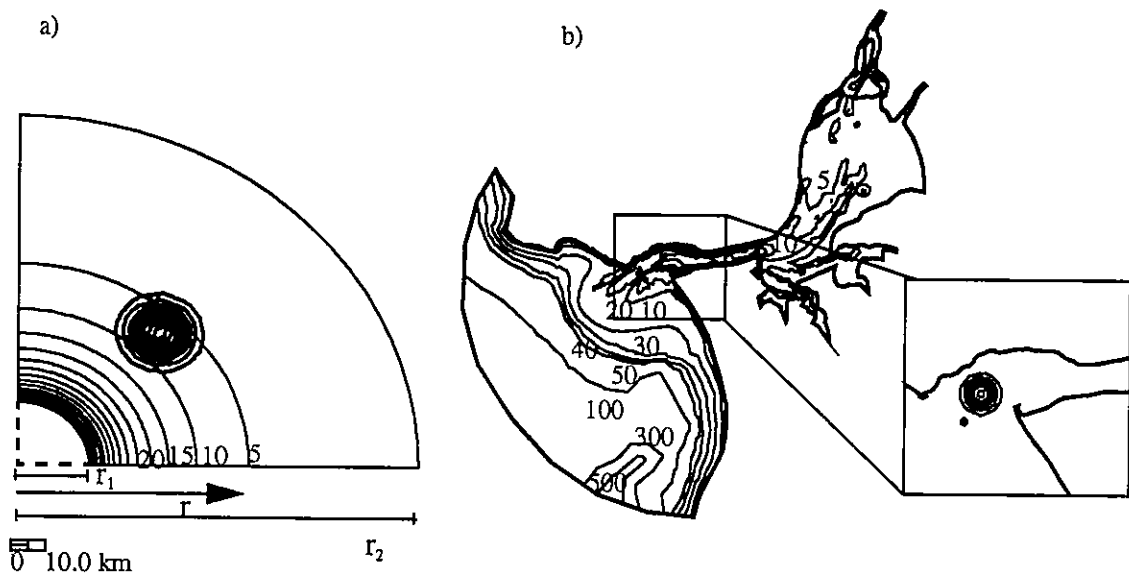


Figure 2.6 a) Bathymetry (in meters) and initial conditions for the Polar Quadrant test, b) Bathymetry (in meters and relative to the mean sea level) and initial conditions for the Tagus estuary test.

Comparison of formulations with distinct integration methods on the polar quadrant channel (Figure 2.8) show that evaluation of integrals at ξ has better mass conservation, but at the expense of other measures of accuracy. Important peak errors, on the order of 15% and with strong time variability, appear for integration at ξ , and are not eliminated by grid refinement. These errors are generated by the deformation of the image of the Voronoi polygon at the feet of the characteristic lines. Evaluating integrals by mapping to the head of the Voronoi polygon at $n+1$ is clearly better for numerical diffusion, but mass errors are slightly larger (up to 15% whereas for ξ integration are on the order of 7%).

The strong time variability of peak concentrations (Figure 2.8) suggests that, in the presence of complex flows, integration at ξ may have stability problems. This hypothesis was confirmed in the Tagus estuary, for which the ξ -based integration led to instability. Evaluation of integrals by mapping to time $n+1$ appears thus superior and is recommended for applications including complex flow fields.

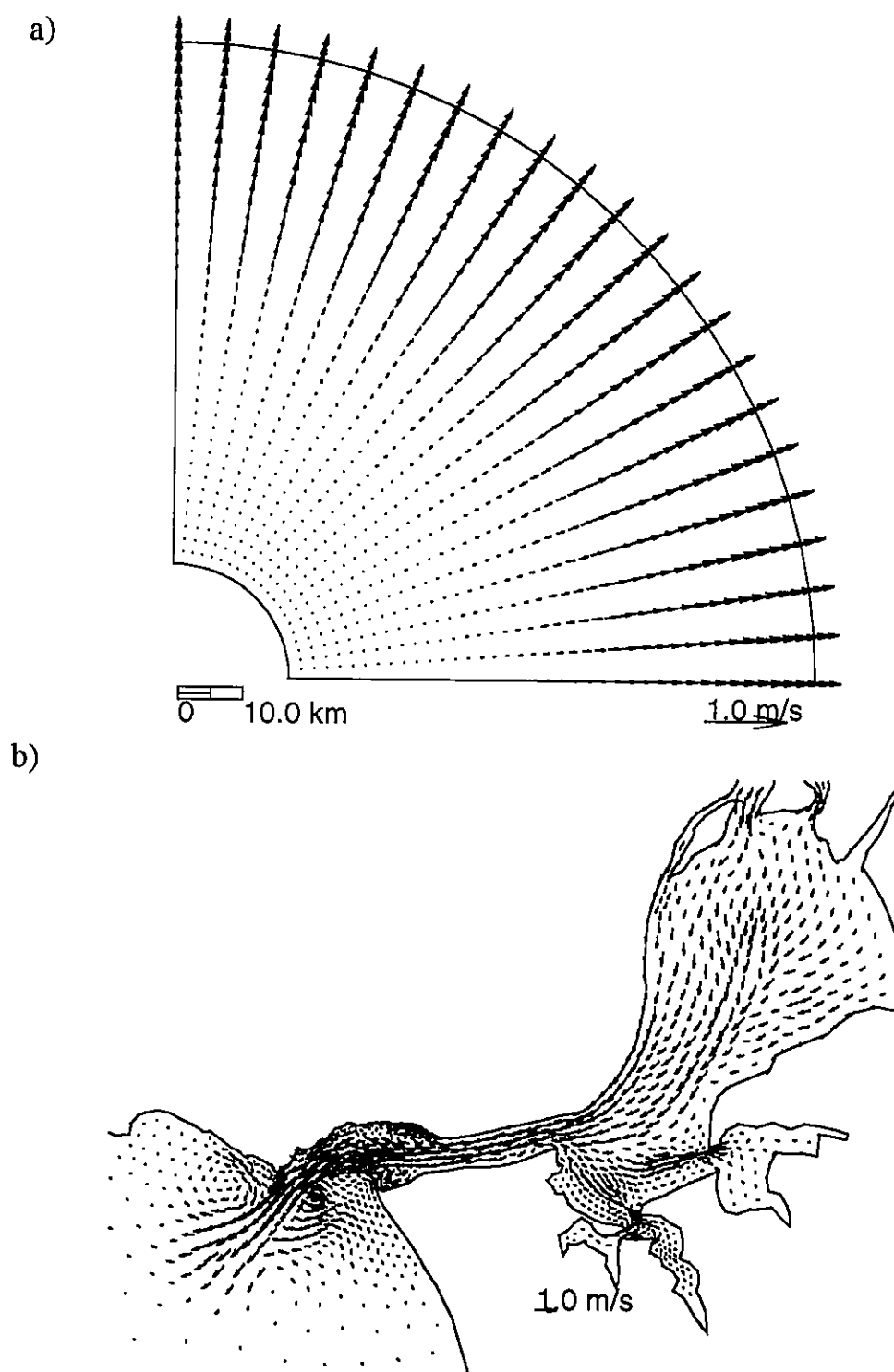


Figure 2.7 a) Snapshot of the flow field for the Polar quadrant test at time = 4.75 hours;
b) Snapshot of the flow field for the Tagus estuary test at time = 9 hours.

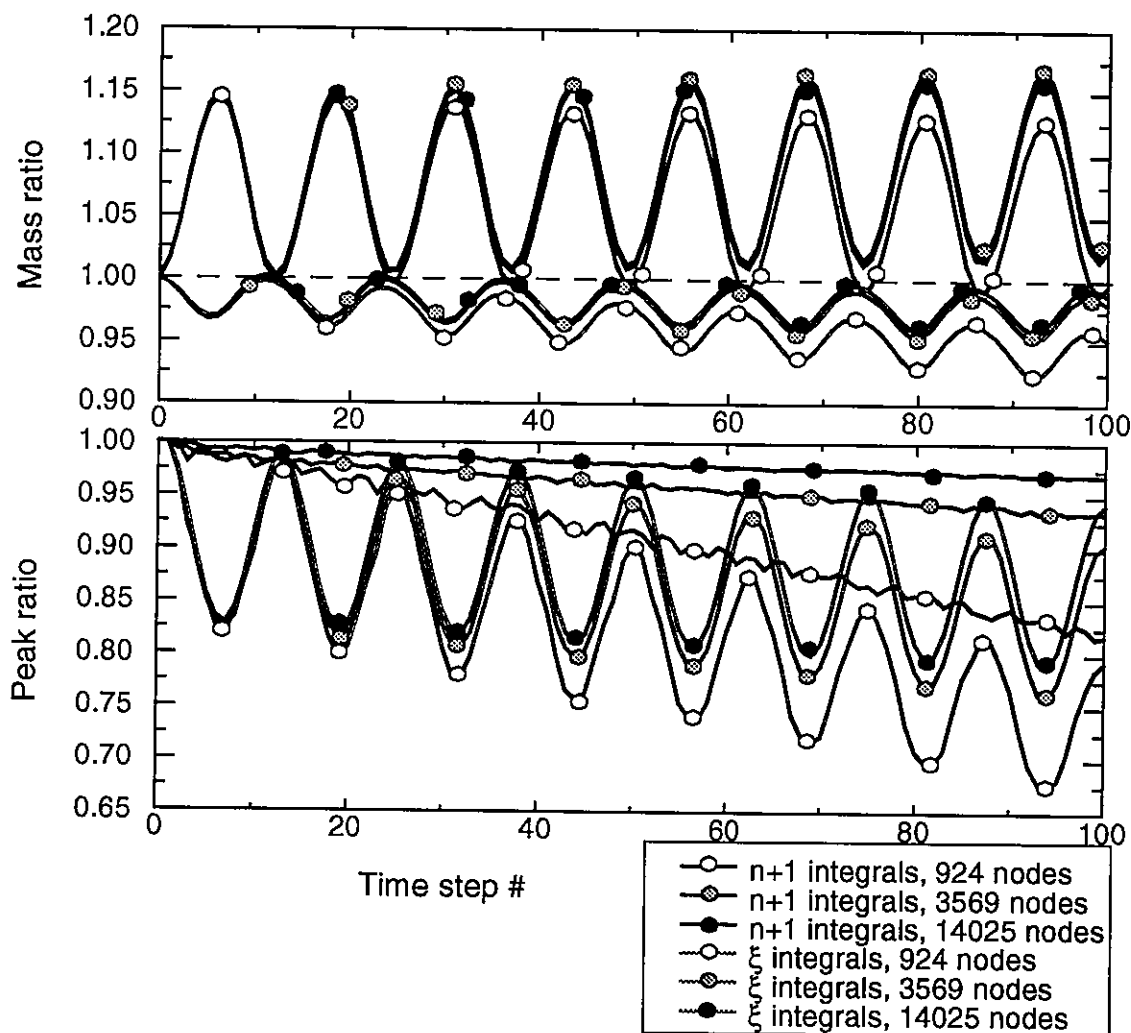


Figure 2.8 Comparison of mass and numerical damping of formulations that evaluate integrals at ξ and at the time $n+1$.

To examine the comparative performance of conservative and non-conservative formulations, we run the polar quadrant test for both conservative c and cH formulations for the coarsest grid. Conservative formulations reduce mass errors considerably relative to non-conservative approaches, in particular if the cH formulation is used (Figure 2.9). However, mass balance is achieved by artificial mass redistribution on both conservative formulations, which lead to strong oscillations over time of the peak concentrations.

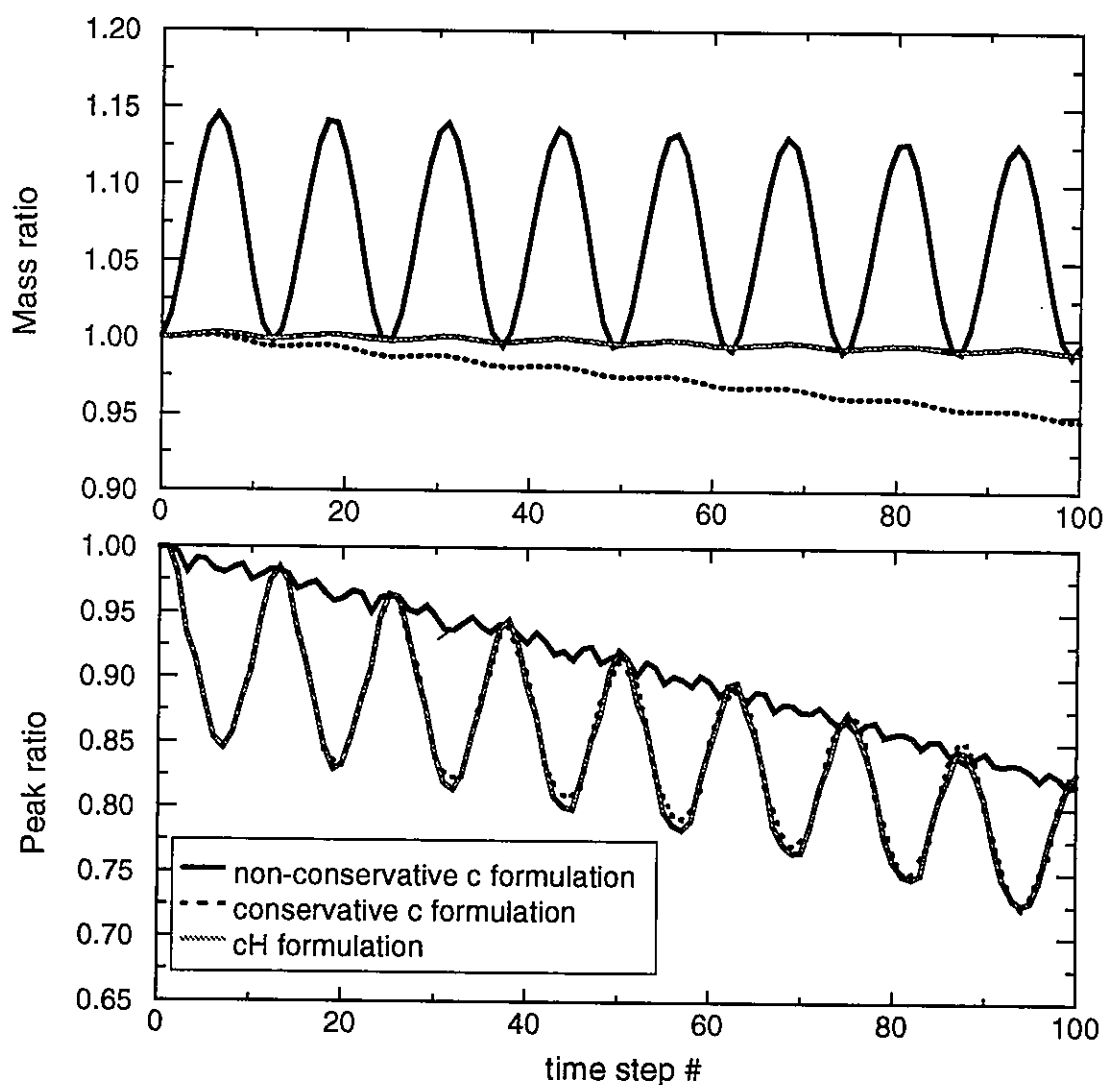


Figure 2.9 Comparison of conservative and non-conservative formulations in the Polar Quadrant channel.

The strong time variability of peak concentrations results from the correction introduced by the continuity equation term: when the fluid mass is decreasing (increasing), conservative formulations increase (decrease) the concentration so that the tracer mass is maintained. For complex, non-conservative flows, this behavior can induce instabilities. We verified this hypothesis on the Tagus and results suggest that both conservative formulations are indeed unstable (Figure 2.10).

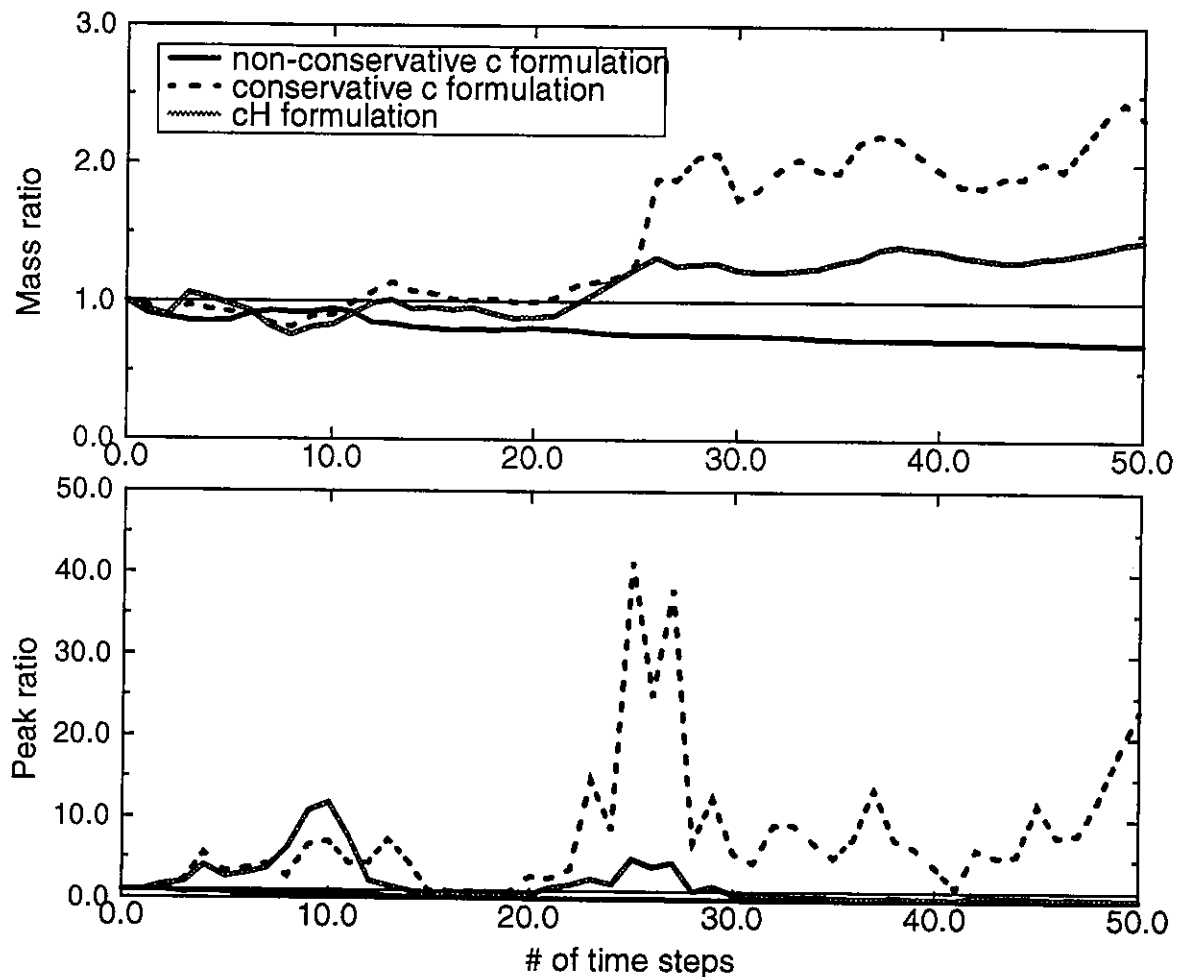


Figure 2.10 Conservative and non-conservative simulations in the Tagus estuary.

2.3 Conclusions

In this chapter, we analyzed the numerical properties of control volume finite element ELMs. The analysis, conducted with a combination of formal analysis and numerical experimentation, showed that:

- subdivision quadrature integration methods are unconditionally stable. Similarly to other quadratures, the accuracy of subdivision integration is dependent on the number of quadrature points and grid refinement;
- conservative formulations, based on the total derivative of the concentration or the total concentration in the water column, lead to instability in presence of complex, non-conservative flows, and therefore should not be used for

coastal applications. The use of the total concentration in the water column as the quantity transported along characteristic lines is thus discouraged, since it requires the use of a conservative transport equation;

- integration at the feet of the characteristic lines can lead to an unstable behavior in the presence of complex flow fields if an effective control of the integration area is not used by mapping the integration points to the control volume at the head of the characteristic lines;
- the combination of finite volumes and quadrature integration leads to a better performance than the reference quadratic interpolation FE-ELMs, on the basis of an equal number of nodes.

References

- Baptista, A.M., E.E. Adams and K.D. Stolzenbach, 1984. *Eulerian-Lagrangian analysis of pollutant transport in shallow water*, Technical Report no. 296, MIT R.M. Parsons, Cambridge.
- Baptista, A.M., E.E. Adams and P. Gresho, 1995. Benchmarks for the Transport Equation: the Convection-Diffusion Forum and Beyond, in *Quantitative Skill Assessment for Coastal Ocean Models*, D. Lynch et al. (editors), American Geophysical Union Estuarine/Coastal Monograph, 47: 241-268.
- Binning, P. and M.A. Celia, 1996. A finite volume Eulerian-Lagrangian localized Adjoint method for solution of the contaminant transport equations in two-dimensional multiphase flow systems, *Water Resources Research*, 32(1): 103-114.
- Chen, C.L. 1989. Analytic Solutions for Tidal Model Testing, *Journal of Hydraulic Engineering*, American Society of Civil Engineers, 115(12): 1707-1714.
- Fortunato, A.B., A.M. Baptista and R.A. Luettich, Jr., 1997. A Three-Dimensional Model of Tidal Currents at the Mouth of the Tagus Estuary (Portugal), *Continental Shelf Research* (in press).
- Healy, R.W. and T.F. Russell, 1993. A Finite-Volume Eulerian-Lagrangian Localized Adjoint Method for Solution of the Advection-Dispersion Equation, *Water Resources Research*, 29(7): 2399-2413.

- Luettich, Jr., R.A., J.J. Westerink and N.W. Sheffner, 1991. *ADCIRC: An Advanced Three-Dimensional Circulation Model for Shelves, Coasts and Estuaries. Report I: Theory and Methodology of ADCIRC-2DDI and ADCIRC-3DL*. Department of the Army, US Army Corps of Engineers.
- Lynch, D.R. and W.G. Gray, 1978. Analytic Solutions for Computer Flow Model Testing, *Journal of Hydraulics Division*, 104(HY10): 1409-1427.
- Oliveira, A. and A.M. Baptista, 1995. A Comparison of Integration and Interpolation Eulerian-Lagrangian Methods, *International Journal for Numerical Methods in Fluids*, 21(3): 183-204.
- Putti, M, W.W.-G. Yeh and W.A. Mulder, 1990. A Triangular Finite Volume Approach with High-Resolution Upwind Terms for the solution of Groundwater Transport Equations, *Water Resources Research*, 26(12): 2865-2880.
- Roache, P.J., 1992. A Flux-Based Modified Method of Characteristics, *International Journal for Numerical Methods in Fluids*, 15(11): 1259-1275.
- Wang, C., N. Sun and W.W.-G. Yeh, 1986. An Upstream Weight Multiple-Cell Balance Finite Element Method for Solving Three-Dimensional Convection-Dispersion Equations, *Water Resources Research*, 22(11): 1575-1589.

CHAPTER 3¹

On the role of tracking on Eulerian-Lagrangian solutions of the transport equation

Abstract

We investigate the effect of tracking errors on the accuracy and stability of Eulerian-Lagrangian methods (ELMs) for the solution of the transport equation. A combination of formal analysis and numerical experimentation demonstrates that the effect is severe. Even moderate tracking errors substantially affect the preservation of the zeroth, first and second moments of concentration (mass, phase and diffusion) and may lead to the instability of otherwise stable and very accurate ELMs. The use of accurate tracking algorithms is strongly recommended for Eulerian-Lagrangian simulations involving complex flows.

3.1 Introduction

Many numerical methods have been proposed to solve the advection-diffusion equation (Vreugdenhil and Koren, 1993). Among the several classes of proposed techniques, Eulerian-Lagrangian methods (ELMs) are generally recognized as very attractive when advection is dominant (Daubert, 1974, Neuman, 1984, Russell, 1985, Hervouet,

1. In press in *Advances in Water Resources*.

1986, Baptista, 1987, Cady and Neuman, 1988, Bentley, 1990, Celia, 1994, Oliveira and Baptista, 1995). The attractive numerical properties of ELMs stem from the adoption of customized techniques for each transport process: typically, advection is solved by the backward method of characteristics, while diffusion is solved by centered finite elements or finite differences. This decoupling strategy eliminates Courant number restrictions associated with Eulerian methods (Daubert, 1974) and provides an efficient way to handle processes with very different time scales (Wood and Baptista, 1993).

In spite of their attractive numerical properties and of their increasing popularity in surface water (Baptista et al., 1984, Cheng et al., 1984, Wang et al., 1988, Barros and Baptista, 1989, Dimou, 1992, Wood and Baptista, 1993) and groundwater (Sorek, 1988, Bentley and Pinder, 1992, Wheeler et al., 1992, Binning and Celia, 1994) applications, the use of ELMs is hindered by the fact that they do not inherently conserve mass, either locally or globally (Baptista, 1987, Russell, 1989, Bentley, 1990, Allen and Khosravani, 1992, Roache, 1992, Healy and Russell, 1993, Binning and Celia, 1994). Mass errors result primarily from: (a) inaccurate tracking of the characteristic lines, (b) use of non-conservative flow fields, (c) errors in the evaluation of conditions at the feet of the characteristic lines, and (d) approximations in the treatment of boundary conditions. Indeed:

- Both inaccurate tracking of characteristic lines and non-conservative flow fields (e.g., flow fields where the continuity equation is not exactly verified due to numerical errors) lead to the incorrect positioning of the feet of characteristic lines (Figures 3.1a-b). On an elemental basis, the consequence is an improper definition of the region where integrals are evaluated at time n ($n+1$ being the current time step) - Binning and Celia (1994). Local mass errors are thus generated and there is no mechanism to compensate for them globally.
- The effect of non-conservative flows is aggravated when, as it is the case for most ELM models, the non-conservative transport equation is used. In order to treat the advective term in its Lagrangian form, these models write the transport equation as:

$$\frac{\partial c}{\partial t} + u_i \frac{\partial c}{\partial x_i} = \frac{\partial}{\partial x_i} \left(D_{ij} \frac{\partial c}{\partial x_j} \right) - \frac{\partial u_i}{\partial x_i} c \quad i = 1, 2, 3 \quad (3.1)$$

where c is the concentration, u_i are the components of velocity in each spatial dimension x_i , D_{ij} is the diffusion coefficient tensor and t is time. Further the models assume that flow continuity is inherently respected, i. e.,

$$\frac{\partial u_i}{\partial x_i} = 0 \quad (3.2)$$

and drop the “source” term that contains the divergence of the flow.

- Errors in the evaluation of concentrations at the feet of the characteristic lines can generate local mass errors, both when interpolation (such as the linear interpolator ELM, as illustrated in Figure 3.1c) or quadrature methods are used (Baptista, 1987, Healy and Russell, 1993). For the transport equation with uniform coefficients and a uniform grid, formal analysis of “interpolation ELMs” shows that these local mass errors do not translate into significant global mass errors, unless significant aliasing occurs at high frequencies (Baptista, 1987). For “quadrature ELMs”, a careful choice of the numerical integration rule is necessary to avoid mass imbalances (Healy and Russell, 1993).
- Incorrect implementation of boundary conditions can lead to significant mass imbalances (Celia, 1994). To minimize this problem Eulerian-Lagrangian Localized Adjoint Methods (ELLAMs - Russell, 1989, Binning and Celia, 1994, Celia, 1994) implement boundary conditions through the use of space-time weighting functions, leading to global mass conservation when other sources of mass imbalances are not present.

Although mass conservation in ELMs has been broadly recognized as a significant problem (Baptista, 1987, Russell, 1989, Bentley, 1990, Roache, 1992, Healy and Russell, 1993, Binning and Celia, 1994), this work represents, to our knowledge, the first systematic investigation of the effect of inaccurate tracking on the numerical properties of ELMs.

We show that tracking errors not only affect mass, but can also introduce significant phase errors and numerical diffusion. Moreover, we show that inaccurate tracking can lead to instability of otherwise stable ELMs.

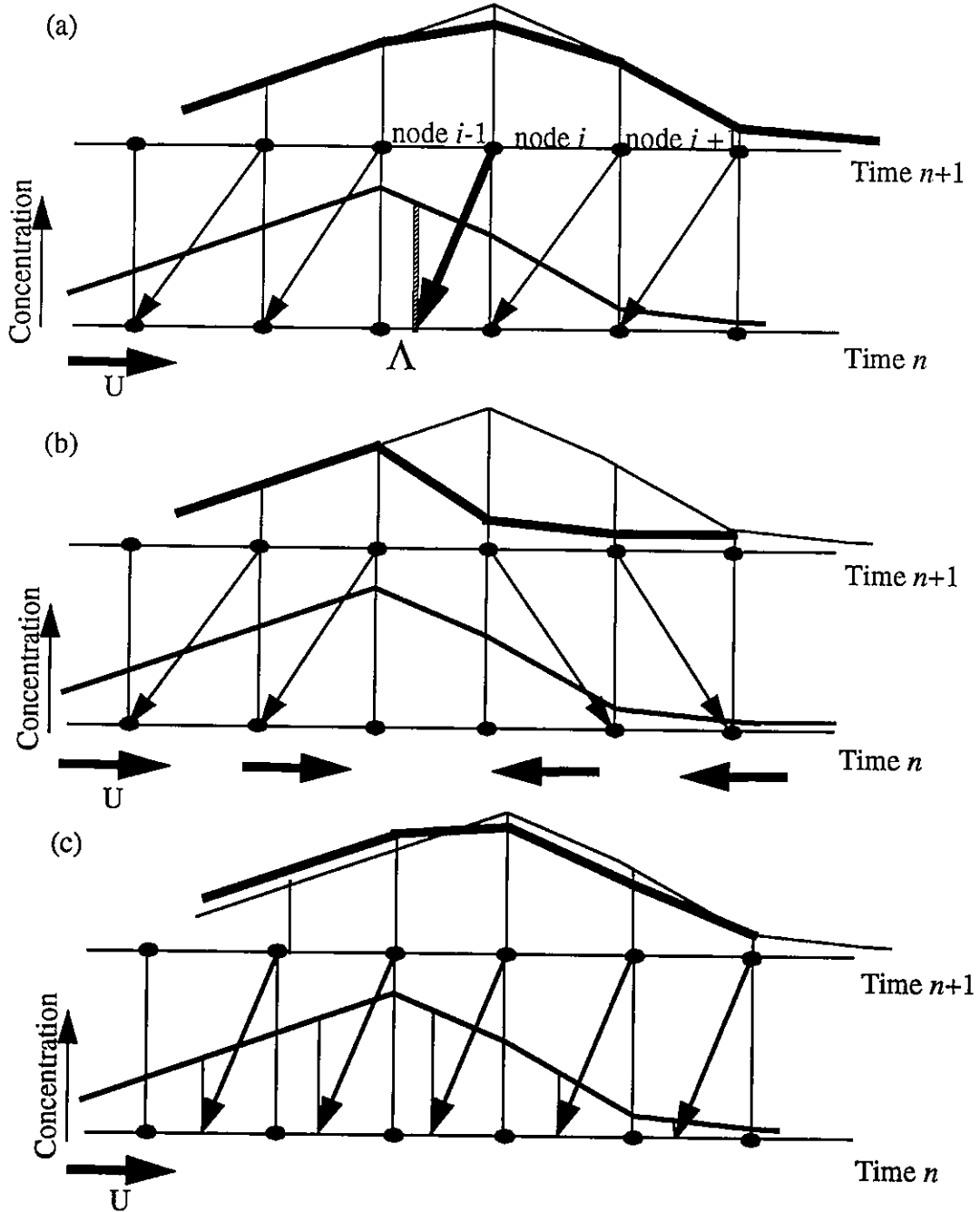


Figure 3.1 Sources of mass errors in ELMs: a) Back-tracking of the characteristic lines: with tracking errors in one characteristic line only, for a Courant number of 1. b) Use of non-conservative flow field. c) Interpolation at the feet of the characteristic lines.

The paper is divided into five sections beyond this introduction. The significance of the tracking errors and resulting mass imbalances in real estuarine systems is illustrated in Section 2, through 2D transport simulations for the Tejo estuary, Portugal. This provides the motivation and context for the remaining sections, which abstract the problem into a simple 1D framework. Section 3 describes the formulation of a reference ELM, including a mechanism to introduce tracking errors. Section 4 uses truncation error analysis to examine the errors introduced or magnified by inexact tracking. The influence of dimensionless parameters on selected numerical properties of solutions with tracking errors is then examined through numerical experimentation (Section 5). Finally, Section 6 summarizes the results and discusses their implications.

3.2 Context

We examine in this section the tracking errors in a complex estuarine system and their impact on the transport of a conservative tracer plume. The Tejo estuary (Figure 3.2a) and the 2D flow and transport models TEA-NL (Westerink et al., 1987, 1988) and ELA (Baptista et al., 1984) are used as reference. The formulation of the two models is briefly reviewed in Appendix A.

The Tejo estuary, located in Portugal, is forced by ocean tides and by regulated river discharges. In combination with a complex geometry and bathymetry, these forcings lead to complicated circulation and flushing patterns (Figure 3.2b). For simplicity, tidal flats were artificially “deepened” in our simulations (Figure 3.2a) and play no role in the conservation errors described herein.

Flow was simulated with model TEA-NL only for the dominant tidal constituent (M_2) and its major harmonics (M_4 , M_6 , M_8 and Z_0). With the exception of advection, all non-linear processes were included. Mass conservation is respected only approximately, both locally and globally (Table 3.1, Figures 3.3a-b), since TEA-NL approximates the continuity equation by finite elements. Maximum global errors are of the order of $2.5 \times 10^{-4} \%/s$ (scaled by the volume of the estuary at rest), while maximum elemental errors are of the order of $0.5 \%/s$ (scaled by the elemental volume).

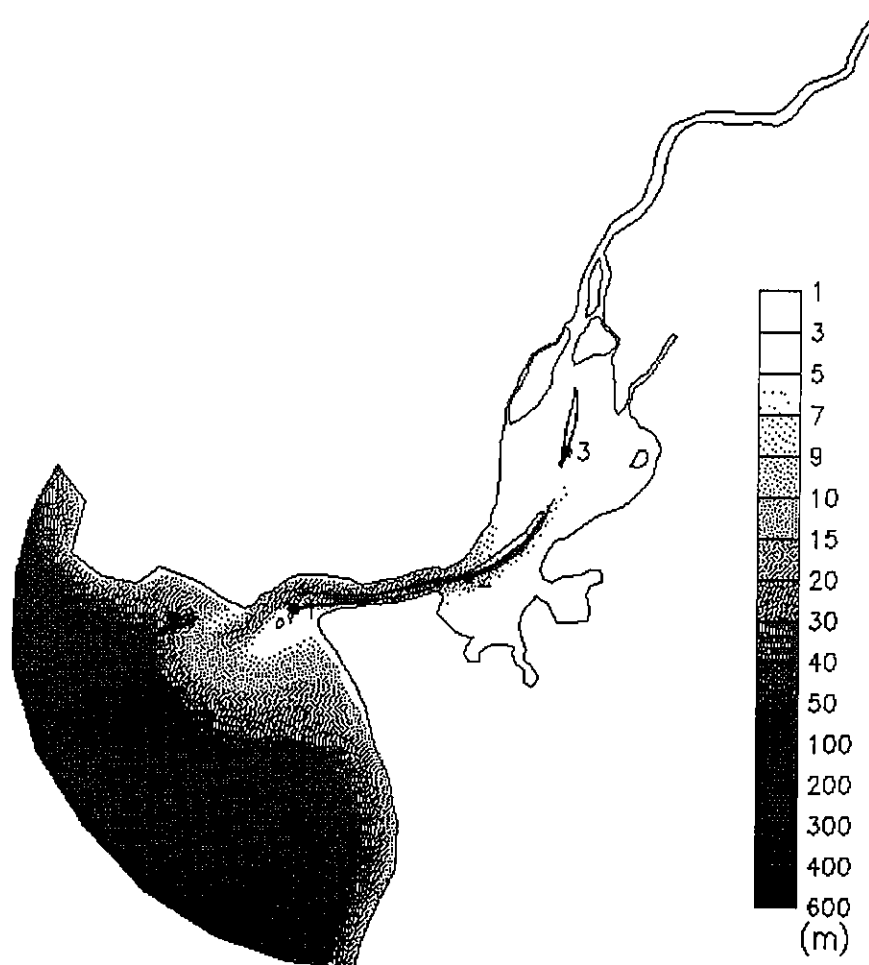


Figure 3.2a) Bathymetry of the Tejo Estuary and location of the particles.

Considerable mass errors occur both at land and ocean boundaries. The treatment of elevation as an essential boundary condition, by dropping the continuity equation and evaluating the velocity using the momentum equations, introduces considerable mass errors at open boundaries (Lynch, 1985), while the treatment of normal flow as a natural boundary condition allows mass imbalances through land boundaries. The generation of mass errors inside the domain is not fully understood yet, but studies conducted for wave continuity equation models suggest that local mass errors are associated with regions of large bathymetric gradients and rapidly changing geometry (Kolar et al., 1994).

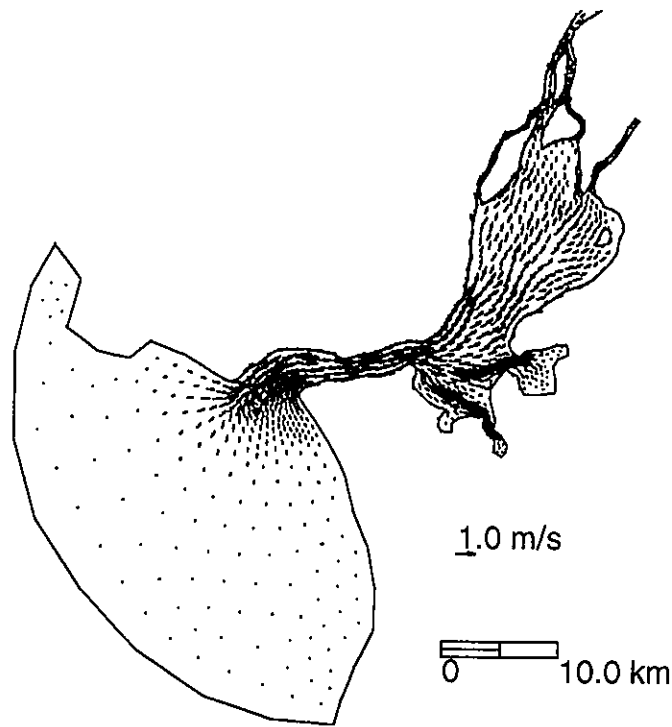


Figure 3.2b) Flow field for $t=0$ s.

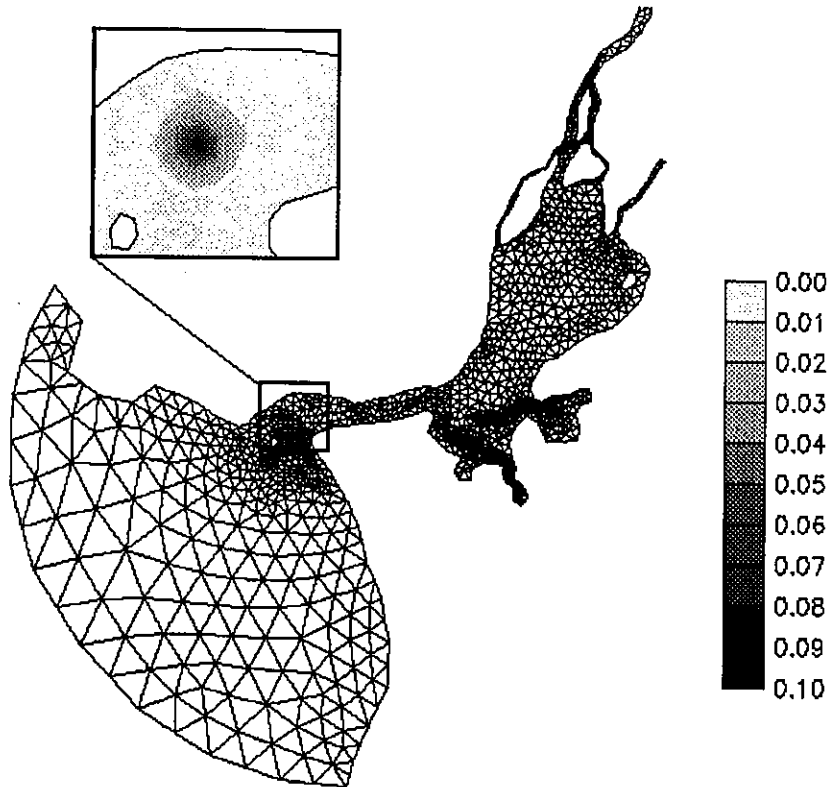


Figure 3.2c) Grid and initial conditions for ELA runs.

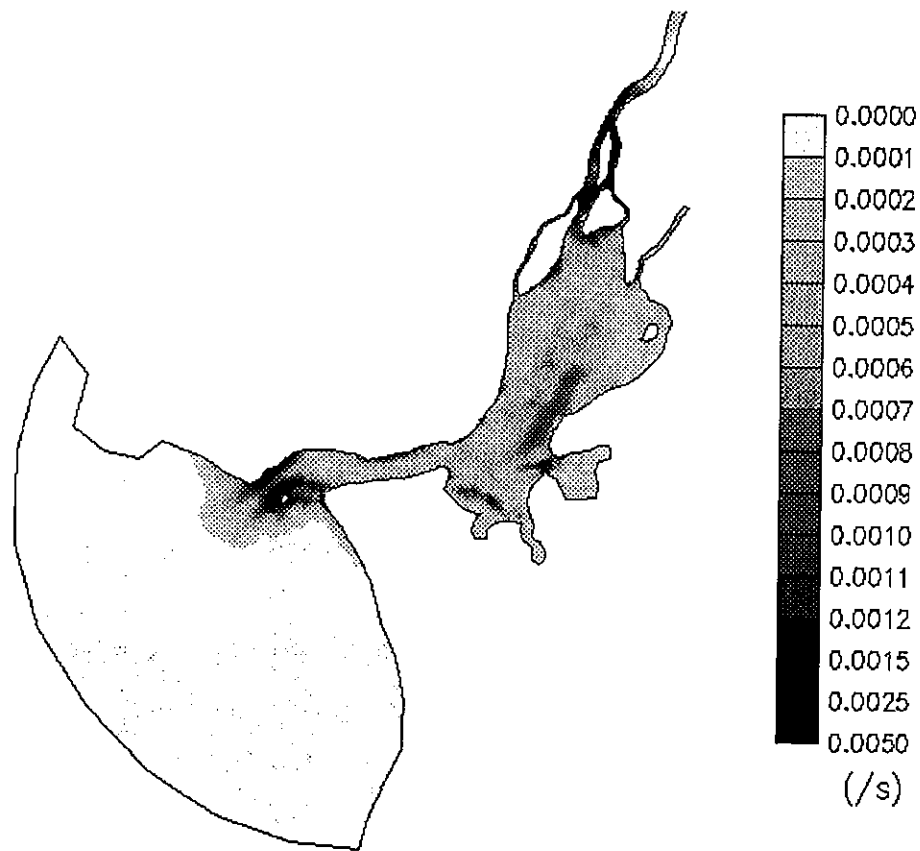


Figure 3.3a) Flow mass errors over a period of 3 tidal cycles: Maximum local mass errors per second, scaled by the elemental volumes at rest.

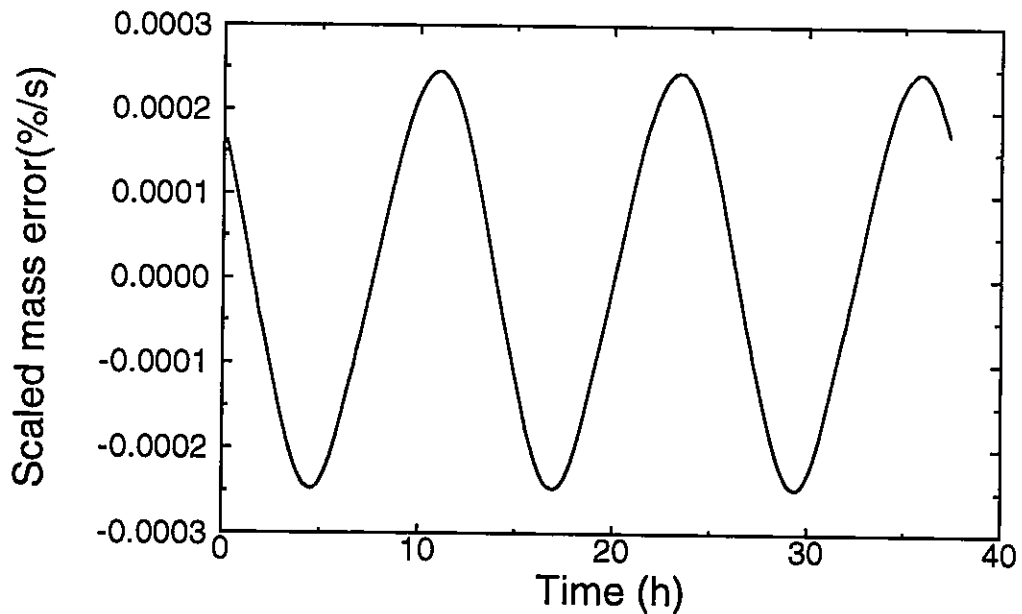


Figure 3.3b) Flow mass errors over a period of 3 tidal cycles: Global mass errors per second in percentage, scaled by the volume of the estuary at rest.

Table 3.1 2D Error Measures

Global Flow Mass Error	$Mf_{global} = \sum_e [\bar{\zeta}_{t+\Delta t}^{(1)} - \bar{\zeta}_t^{(2)}] A_e + \frac{1}{2} [Q_t^{net} + Q_{t+\Delta t}^{net}] \Delta t$ <p>with</p> $Q_t^{net} = \sum_{eb} \frac{w_e^{(3)}}{6} [2H_1 v_{n1}^{(4)} + H_1 v_{n2} + H_2 v_{n1} + 2H_2 v_{n2}]$
Local Flow Mass Error (at element m)	$Mf_m = [\bar{\zeta}_{t+\Delta t} - \bar{\zeta}_t] A_m + \frac{1}{2} [Q_t^{net} + Q_{t+\Delta t}^{net}] \Delta t$ <p>with</p> $Q_t^{net} = \sum_{ebm=1}^3 \frac{w_m}{6} [2H_1 v_{n1} + H_1 v_{n2} + H_2 v_{n1} + 2H_2 v_{n2}]$
Transport Mass Error	$m_{num}(t) = \frac{1}{m_{init}^{(5)}} \int_{\Omega} c_i^{num(6)}(x, y, t) d\Omega$

- (1) $\bar{\zeta}_t$ - arithmetic average of nodal elevation over element e , at time t
- (2) A_e - area of element e
- (3) w_e - length of boundary segment eb
- (4) H_i, v_{ni} - Total depth and normal velocity at node i , of side ebm , of element m
- (5) m_{init} - initially released mass
- (6) c_i^{num} - numerical concentration

ELA (Baptista et al., 1984) is one of the first Eulerian-Lagrangian transport models developed for coasts and estuaries. For this application, ELA was modified to allow for alternative tracking strategies. From the many different techniques (Cheng et al., 1984, Thomas, 1986, Bentley, 1990, Dimou, 1992, Galeati et al., 1992, Allen and Khosravani, 1992, Mitchell and Mayer, 1994, Darmofal and Haines, 1996) that have been considered to perform tracking in transport models, we selected three (Appendix B, Table 3.2):

- one-step backward Euler (BE), where the tracking and diffusion time-steps coincide;
- multi-step backward Euler (MSE), where the tracking time step is a sub-multiple of the diffusion time-step;

- 5th-order Runge-Kutta (RK), where the time-step is dynamically adjusted to meet a user-specified spatial accuracy criterion. This method is constructed from the 4th-order Runge-Kutta displayed in Table 3.2, as discussed in Appendix B.

Table 3.2 Tracking techniques

Method	Position of foot of characteristic line
one-step Euler	$x^\xi = x^{n+1} - u^{n+1} \Delta t$
Multi-step Euler (m steps)	$x^\xi = x_0 - \frac{\Delta t}{m} \sum_{i=0}^{m-1} u(x_i, t_i)$ $x_0 = x^{n+1} \quad x_i = x_{i-1} - \frac{\Delta t}{m} u(x_{i-1}, t_{i-1})$ $t_0 = n + 1 \quad t_i = t_0 - \frac{\Delta t}{m} i$
4 th order Runge-Kutta	$x^\xi = x^{n+1} - \Delta t \left\{ \frac{1}{6} u^n + \frac{1}{3} u \left(\underline{x}^{n+\frac{1}{2}}, t^{n+\frac{1}{2}} \right) + \right.$ $\left. + \frac{1}{3} u \left(\underline{x}^{n+\frac{1}{2}}, t^{n+\frac{1}{2}} \right) + \frac{1}{6} u \left(\underline{x}^{n+1}, t^{n+1} \right) \right\}$ $\underline{x}^{n+\frac{1}{2}} = x^n + \frac{\Delta t}{2} u^n$ $\underline{x}^{n+\frac{1}{2}} = x^n + \frac{\Delta t}{2} u \left(\underline{x}^{n+\frac{1}{2}}, t^{n+\frac{1}{2}} \right)$ $\underline{x}^{n+1} = x^n + \Delta t u \left(\underline{x}^{n+\frac{1}{2}}, t^{n+\frac{1}{2}} \right)$

These schemes are representative of low and high-order integration rules, rather than being intended as optimal accuracy choices. The one-step Euler method (Cheng et al., 1984) is now rarely used, while both the multi-step Euler (Casulli and Cheng, 1992) and

the 5th-order Runge-Kutta methods (Wood and Baptista, 1993) are often used in current practice.

Tracking errors, estimated by closure errors as described in Appendix C, were computed for five particles released at locations with different flow characteristics (Figure 3.2a), using various time steps and lengths of simulation (Table 3.3). Choices of the tracking time steps are loosely representative of those made in published applications (Cheng et al., 1984, Casulli and Cheng, 1992, Galeati et al., 1992, Wood and Baptista, 1993).

Results (Table 3.4) show that while tracking errors can be made quite small (e.g., RK simulations), they are often significant to very large (e.g., BE and most MSE simulations). Efficiency considerations aside, tracking errors depend primarily on the strategy adopted for the tracking sub-time step and on flow character. When the time-step is locally adjusted to control tracking errors, then dependence on flow is reduced or eliminated.

In particular, we note that:

- RK tracking with adjustable time step is very accurate, regardless of the initial location and pathway of the particle;
- Euler methods lead to tracking errors whose magnitude is strongly accentuated by sharp velocity gradients, and which can be very large even for tracking time steps as small as 1 minute;
- Reducing the tracking sub-time step in MSE tracking considerably improves accuracy, but errors in certain regions of the domain remain quite significant even for $\delta t = \Delta t / 10$.

Table 3.3 Definition of particle runs

Run	Time step [minutes]	Simulation length [tidal cycles]
1	1, 5, 15, 30, 60	3
2	10	2, 2.25, 2.5, 2.75, 3

Table 3.4 Maximum and (Minimum) closure errors.

Part icle	Time step analysis (Run 1)			Simulation Length analysis (Run 2)		
	Runge-Kutta	one-step Euler	Multi-step Euler	Runge-Kutta	one-Step Euler	Multi-step Euler
1	0.9E-3 (0.2E-3)	9.57 (2.01)	4.41 (0.16)	0.8E-3 (0.5E-4)	3.41 (2.13)	2.26 (2.01)
2	0.2E-4 (0.7E-5)	5.30 (1.16)	0.59 (0.14)	0.3E-4 (0.3E-5)	1.66 (0.92)	0.30 (0.17)
3	0.4E-4 (0.4E-5)	5.47 (0.87)	2.65 (0.15)	0.3E-4 (0.9E-5)	3.40 (2.72)	0.88 (0.56)
4	0.2E-5 (0.1E-9)	0.63 (0.1E-1)	0.8E-1 (0.1E-2)	0.1E-5 (0.2E-9)	0.13 (0.6E-1)	0.1E-1 (0.6E-2)
5	0.3E-8 (0.8E-14)	1E-1 (0.5E-4)	0.3E-3 (0.5E-5)	0.2E-11 (0.9E-12)	0.9E-2 (0.3E-3)	1E-2 (0.3E-3)

Transport simulations using ELA with RK and MSE tracking were conducted for 3 tidal cycles, with two alternative diffusion time steps ($\Delta t=10$ min and 1 h). The transport problem consists of an instantaneous plume being released during flood at the downstream end of the entrance channel (Figure 3.2c). Mass errors (Table 3.1) are shown in Figure 3.4.

Although RK tracking is very accurate, with negligible closure errors, the associated transport simulation still has mass errors of up to 20% (Figure 3.4a). These transport mass errors are due to a combination of all other effects discussed in section 1. This includes the inability of TEA-NL to preserve the divergence-free characteristics of the flow (Figure 3.4); ELA, which uses a non-conservative form of the transport equation, cannot compensate for this effect.

The tracking part of the transport mass errors, for simulations using MSE methods, can be roughly separated from the total by subtracting the transport mass errors for the corresponding (presumably tracking errors-free) RK simulation. This approach suggests, for example, that MSE tracking increases total transport mass errors by 20% for $\Delta t=10$ min and up to 100% for $\Delta t=1$ h (Figure 3.4b).

The above analysis illustrates the potential for mass imbalances that results from poor tracking. Because this potential is large, there is a clear motivation to search for a better understanding of the influence of the magnitude of the tracking errors on mass conservation and other numerical properties of Eulerian-Lagrangian transport simulations. The following sections abstract the problem to a simple enough level that enables interpretation of cause-effect relationships.

The above analysis also suggests that the use of locally non-conservative flow fields may be an equally important source of transport mass errors. This problem is beyond the scope of this investigation, but will be addressed in future research.

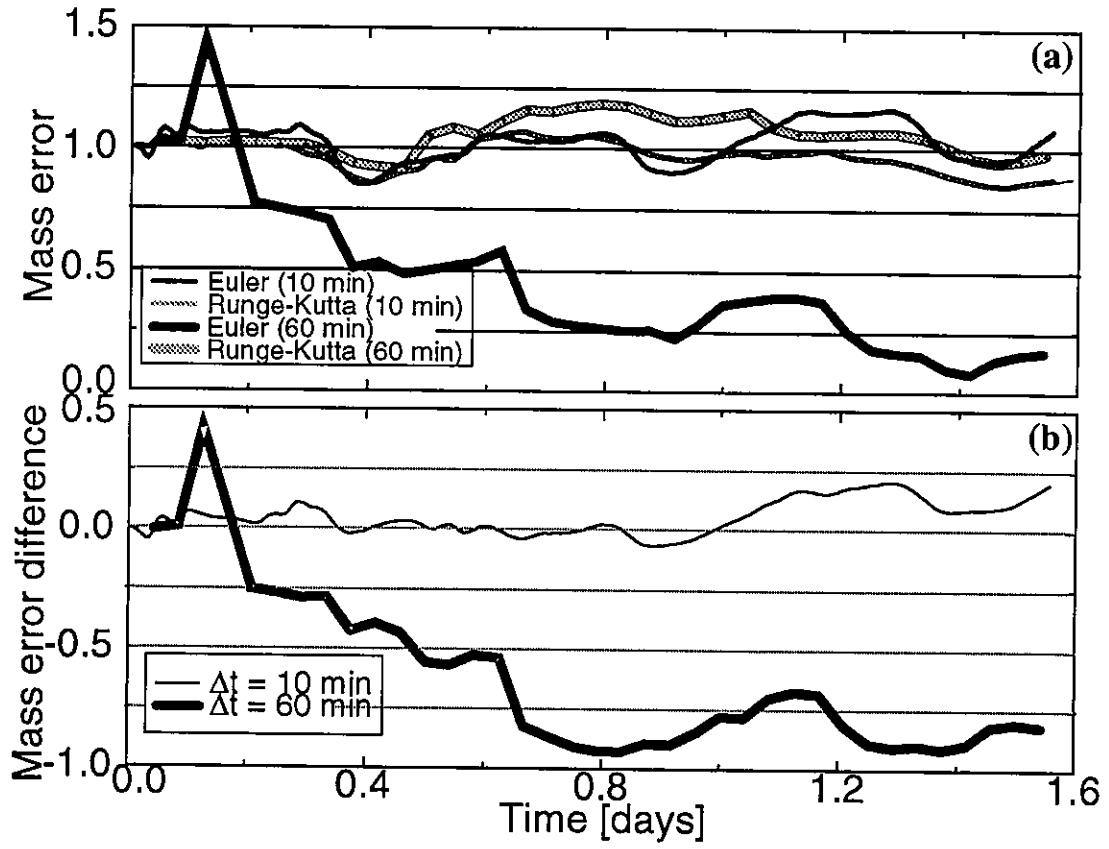


Figure 3.4 a) Mass errors for 3 tidal cycles, for Euler and Runge-Kutta tracking, with time steps of 10 and 60 minutes. b) Mass error differences between Euler and Runge-Kutta tracking techniques.

3.3 Numerical Formulation

As a basis for a systematic analysis of the impact of tracking errors, we now consider the solution of the one-dimensional, simplified form of the transport equation:

$$\frac{Dc}{Dt} = \frac{\partial c}{\partial t} + u \frac{\partial c}{\partial x} = D \frac{\partial^2 c}{\partial x^2} \quad (3.3)$$

where u and D are both positive and constant. Assuming a uniform grid with linear elements, the weighted residual statement for a generic Eulerian-Lagrangian finite element method can be written as:

$$\int_{\Omega} \left\{ \phi_k \frac{c_i^{n+1} - c_i^{\xi}}{\Delta t} + \alpha D \left[\frac{\partial \phi_k}{\partial x} \frac{\partial c}{\partial x} \right]^{n+1} + (1 - \alpha) D \left[\frac{\partial \phi_k}{\partial x} \frac{\partial c}{\partial x} \right]^{\xi} \right\} d\Omega + \Psi = 0 \quad (3.4)$$

where we integrated by parts the diffusion residual and omitted the explicit representation of the resulting boundary terms, Ψ . Linear shape and weighting functions, ϕ_k , are assumed for simplicity. The superscript $n+1$ represents the time level at which concentrations are being evaluated and ξ denotes quantities calculated at the feet of the characteristic lines (at time level n). The time weighting factor, α , was set to 0.5 in all simulations.

Concentrations at the feet of the characteristic lines (c_i^{ξ}) are obtained by linear interpolation:²

$$c_i^{\xi} = \sum_{j=1}^2 \phi_j(\theta_i) c_{i-\sigma_i+j-2}^n = c_{i-\sigma_i}^n - \vartheta_i (c_{i-\sigma_i}^n - c_{i-\sigma_i-1}^n) \quad (3.5)$$

where $\theta_i \in [0,1]$ represents the computed position of the foot of characteristic line for node i within the receiving element, and β_i , σ_i and ϑ_i are the *effective Courant number*, its integer part and its fractional part, respectively:

$$\begin{aligned} \beta_i &= \frac{u\Delta t}{\Delta x} - \Lambda_i = Cu - \Lambda_i \\ \sigma_i &= \text{int}(\beta_i) \\ \vartheta_i &= \beta_i - \sigma_i \end{aligned} \quad (3.6)$$

where Cu is the *Courant number* and Λ_i is a node- and time-dependent tracking error. This tracking error is introduced in the formulation to enable, in later sections, the systematic study of the importance of tracking inaccuracies on the transport simulation.

2. Linear interpolation at the feet of the characteristic lines was selected because it is the simplest method to achieve our purposes. The reader should keep in mind, though, that this method is known to lead to substantial numerical diffusion, and is not a frequent choice in practice (e.g., see discussion in Baptista, 1987).

The finite difference analog of equation (3.4) can be written as:

$$\frac{1}{\delta}(A^{n+1} - A^\xi) = \alpha D^* B^{n+1} + (1 - \alpha) D^* B^\xi \quad (3.7)$$

where $D^* = Cu/Pe$ and:

$$\begin{aligned} A^m &= c_{i-1}^m + 4c_i^m + c_{i+1}^m \\ B^m &= c_{i-1}^m - 2c_i^m + c_{i+1}^m \\ A^\xi &= \left\{ c_{i-1-\sigma_{i-1}}^n + 4c_{i-\sigma_i}^n + c_{i+1-\sigma_{i+1}}^n \right\} - \left\{ \vartheta_{i-1}(c_{i-1-\sigma_{i-1}}^n - c_{i-2-\sigma_{i-1}}^n) \right. \\ &\quad \left. + 4\vartheta_i(c_{i-\sigma_i}^n - c_{i-1-\sigma_i}^n) + \vartheta_{i+1}(c_{i+1-\sigma_{i+1}}^n - c_{i-\sigma_{i+1}}^n) \right\} \\ B^\xi &= \left\{ c_{i-1-\sigma_{i-1}}^n - 2c_{i-\sigma_i}^n + c_{i+1-\sigma_{i+1}}^n \right\} - \left\{ \vartheta_{i-1}(c_{i-1-\sigma_{i-1}}^n - c_{i-2-\sigma_{i-1}}^n) \right. \\ &\quad \left. - 2\vartheta_i(c_{i-\sigma_i}^n - c_{i-1-\sigma_i}^n) + \vartheta_{i+1}(c_{i+1-\sigma_{i+1}}^n - c_{i-\sigma_{i+1}}^n) \right\} \end{aligned} \quad (3.8)$$

3.4 Formal analysis

Taylor series expansion of equation (3.7) leads, after considerable manipulation, to a truncation error, Γ , of the form:

$$\Gamma = \theta \frac{\partial c}{\partial x} + \psi \frac{\partial^2 c}{\partial x^2} \quad (3.9)$$

where:

$$\begin{aligned}\theta &= \left(-\frac{\Lambda_{i-1} + 4\Lambda_i + \Lambda_{i+1}}{6} - (1-\alpha)D^*(\Lambda_{i-1} - 2\Lambda_i + \Lambda_{i+1}) \right) \frac{\Delta x}{\Delta t} \\ \psi &= \left(\frac{Cu^2 - Cu}{2} + \psi_1 \left(\frac{1}{2} - Cu \right) intCu + \psi_2 \frac{(intCu)^2}{2} + \psi_3 \right) \frac{\Delta x^2}{\Delta t}\end{aligned}\quad (3.10)$$

and

$$\begin{aligned}\psi_1 &= \frac{1}{intCu} \left(\frac{\sigma_{i-1} + 4\sigma_i + \sigma_{i+1}}{6} + (1-\alpha)D^*(\sigma_{i-1} - 2\sigma_i + \sigma_{i+1}) \right) \\ \psi_2 &= \frac{2}{(intCu)^2} \left(\frac{\sigma_{i-1}^2 + 4\sigma_i^2 + \sigma_{i+1}^2}{12} + (1-\alpha)D^* \frac{\sigma_{i-1}^2 - 2\sigma_i^2 + \sigma_{i+1}^2}{2} \right) \\ \psi_3 &= \left(\frac{1}{6} + (1-\alpha)D^* \right) \left(\sigma_{i-1} + \frac{3}{2} \right) \Lambda_{i-1} + \left(\frac{4}{6} - 2(1-\alpha)D^* \right) \left(\sigma_i + \frac{1}{2} \right) \Lambda_i + \\ &\quad \left(\frac{1}{6} + (1-\alpha)D^* \right) \left(\sigma_{i+1} - \frac{1}{2} \right) \Lambda_{i+1}\end{aligned}\quad (3.11)$$

Two particular cases are worth considering:

- In the absence of tracking errors, $\theta = 0$, $\psi_1 = 1$, $\psi_2 = 1$ and $\psi_3 = 0$, and truncation errors revert to:

$$\Gamma = \frac{1}{2}(\Phi^2 - \Phi) \frac{\partial^2 c}{\partial x^2} \quad (3.12)$$

where Φ is the fractional part of the Courant number. Equation (3.12) establishes the dependence of the truncation error solely on the fractional part of the Courant number (Baptista, 1987).

- For uniform tracking errors ($\Lambda_i = \Lambda$, $\beta_i = \beta$ and $\sigma_i = \sigma$), equations (3.10) and (3.11) reduce to:

$$\Gamma = (-\Lambda) \frac{\Delta x \partial c}{\Delta t \partial x} + \left(\frac{1}{2}(\Phi^2 - \Phi) + \frac{\sigma^2 + \chi^2}{2} + \frac{\sigma - \chi}{2} + \chi\Phi - \sigma Cu + \left(\sigma + \frac{1}{2}\right)\Lambda \right) \frac{\Delta x^2 \partial^2 c}{\Delta t \partial x^2} \quad (3.13)$$

where χ is the integer part of the Courant number.

Comparison of the above equations shows that tracking errors reduce the order of convergence of the method, introduce phase errors and create an additional source of numerical diffusion. In particular:

- Convergence becomes $O(\Delta x)$ rather than $O(\Delta x^2)$;
- Phase errors, which did not occur in the absence of tracking errors, are now a function of the magnitude and distribution of tracking errors and of the diffusion coefficient;
- Tracking errors create the potential for instability, since the added numerical diffusion can be positive or negative, depending on the specific tracking errors. This problem may be critical when inherently less-diffusive ELMs are used (for instance, integration ELMs - Oliveira and Baptista, 1995).
- Truncation errors are strongly affected not only by the magnitude of the tracking errors, but also by their spatial variability. In particular, errors in the first and second moments depend on the diffusion coefficient only when tracking errors vary in space.
- Uniform tracking errors reduce phase errors to a “rigid-body” shift, but do not eliminate the potential for instability, since the added numerical diffusion can still be negative.

In the presence of tracking errors, different nodes will, in general, have different truncation errors. Differences in nodal errors will generate energy in frequencies that cannot be resolved by the grid. The energy associated with these Fourier components is then folded to the zero-frequency, generating mass errors (Baptista, 1987). The mechanism that

creates mass errors can be examined by considering a simple case, in which only one characteristic line has a tracking error (Figure 3.1a). The concentration field (and the local mass) is exact in all elements except those containing the foot of the characteristic line with the tracking error. Since mass errors in the affected elements cannot compensate each other, the total mass will not be preserved.

3.5 Numerical experimentation

3.5.1 Experimental design

Numerical experimentation provides further insight into the influence of tracking errors on the concentration field. We considered the classical problem of a 1D Gauss hill transported by a uniform steady flow. Tracking errors, characterized by a normal distribution with zero mean and varying standard deviation, were applied at each node at each time step. The dependence of resulting errors on selected dimensionless parameters was then analyzed, using the error measures of Table 3.5. The numerical experiments are organized in three tests (Table 3.6), each examining the influence of a dimensionless parameter: magnitude of the tracking errors ($\epsilon/\Delta x$), Peclet number (Pe) and dimensionless standard deviation of the Gauss hill ($\sigma/\Delta x$), representing the steepness of the concentration gradients.

To study the impact of the magnitude of the tracking errors (test 1), we selected standard deviations between 0 and 100%, well within the range suggested by our 2D analysis for the Tejo estuary (Section 2), where tracking errors even reached 1000% (see Table 3.4, for the one-step Euler tracking). For the study of the effect of the steepness of the concentration gradients (test 2), several standard deviations of the Gauss hill were selected, ranging from poor ($\sigma/\Delta x = 1$) to excellent plume discretization ($\sigma/\Delta x = 20$). Test 3 assesses the importance of diffusion by covering a wide spectrum of diffusion coefficients, ranging from advection-dominated ($Pe = \infty$) to diffusion-dominated transport ($Pe = 0.5$).

Table 3.5 1D Error measures.

Measure of Global Mass (0 th moment)	$m_{num}(t) = \frac{1}{m_{ex}(t)^{**}} \int_{\Omega} c^{num*}(x, t) dx$
Integral measure of phase shift (1 st moment)	$\mu_x(t) = 1 - \frac{\frac{\int_{\Omega} xc^{ex***} dx}{m_{ex}t} - \frac{\int_{\Omega} xc^{num} dx}{m_{num}^{****}t}}{\Delta x}$
Integral measure of numerical diffusion (normalized 2 nd moment)	$\mu_{xx}(t) = \frac{\frac{\int_{\Omega} \left[x - \left(\int_{\Omega} xc^{num} dx \right) / (m_{num}) \right]^2 c^{num} dx}{m_{num}}}{\frac{\int_{\Omega} \left[x - \left(\int_{\Omega} xc^{ex} dx \right) / (m_{ex}) \right]^2 c^{ex} dx}{m_{ex}}}$
Scaled numerical diffusion	$\mu^r = \frac{\left\{ \frac{\int_{\Omega} \left[x - \left(\int_{\Omega} xc^{num} dx \right) / (m_{num}) \right]^2 c^{num} dx}{m_{num}} \right\} \text{with tracking errors}}{\left\{ \frac{\int_{\Omega} \left[x - \left(\int_{\Omega} xc^{num} dx \right) / (m_{num}) \right]^2 c^{num} dx}{m_{num}} \right\} \text{without tracking errors}}$
Discrete L2-norm	$L2(t) = \frac{1}{m_{ex}} \left[\sum_i (c_i^{num} - c_i^{ex})^2 \right]^{\frac{1}{2}}$

* c^{num} - numerical concentration

** m_{ex} - analytical mass

*** c^{ex} - analytical concentration

**** m_{num} - numerical mass

Table 3.6 Parameters for Numerical tests.

Test	Cu	$\lambda(\% \Delta x)$	$\sigma/\Delta x$	Pe
1	1	0,5,10,25,50,75,100	10	∞
1A	0.5	0,5,10,25,50,75,100	10	∞
2	1	25	1,3,6,10,15,20	∞
3	1	25	10	$\infty, 100, 25, 5, 2, 1, 0.5$

All runs were generated with the reference method presented in section 3, for $Cu = 1$. In the absence of tracking errors, the solution of advection is exact, thus minimizing (but not eliminating, since the effective Courant number, β_i , will not be kept at 1) the noise introduced by other sources of errors in ELMs (e.g., interpolation or quadrature errors). A long enough domain was used to prevent boundaries from interfering with the simulation (2301 nodes with a constant grid spacing of 100 meters).

Several “seeds” (initial value used in the generation of the random tracking errors) were considered, in order to provide different distributions of tracking errors, for each standard deviation. The simulations were run for a period large enough (2000 time steps) to provide series of random numbers representative of the chosen statistical distribution.

3.5.2 Results and discussion

Results are shown in Figures 3.5 to 3.14, and consist primarily on time series of error measures and associated statistics.

3.5.2.1 Overall impact of tracking errors

Consistently with our formal analysis, numerical experimentation shows that inexact tracking introduces significant errors on 0th, 1st and 2nd moments of concentration, even in the presence of small tracking errors (Figures 3.5 and 3.6). In addition, tracking errors tend to induce a very distinctive “signature” in the concentration field, characterized by abrupt concentration “bumps” (Figure 3.5) with no apparent spatial or temporal pat-

tern. We interpret these “bumps” as the result of the lack of coherence of the tracking errors in adjacent nodes.

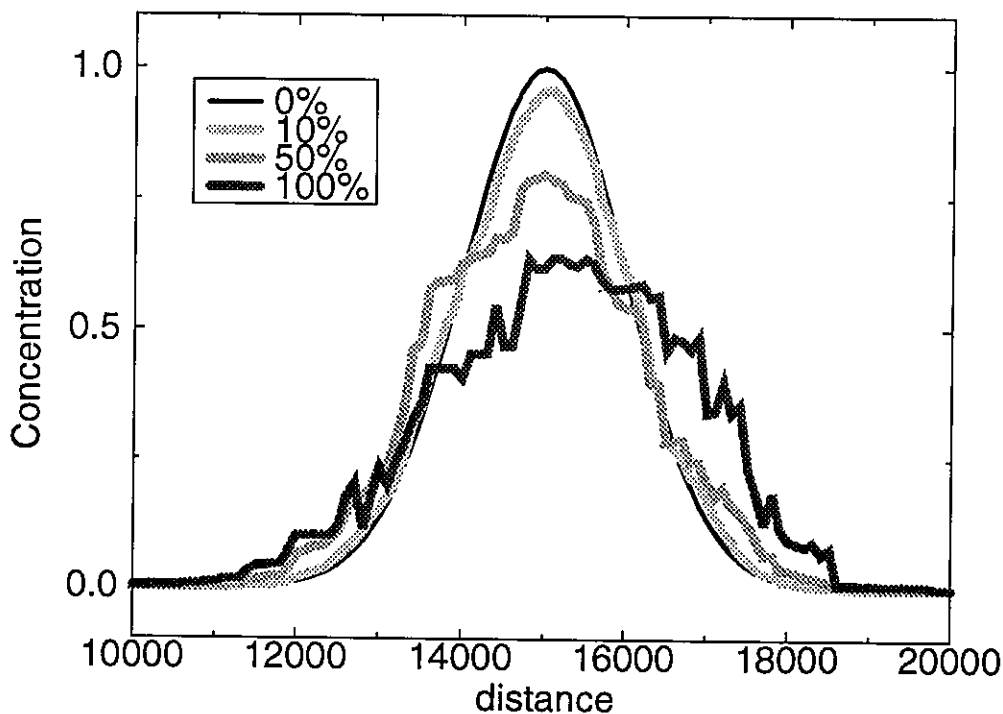


Figure 3.5 Concentration field for $\sigma/\Delta x = 10$ and $Pe = \infty$, after 100 time steps (test 1).

Mass and phase errors vary rather randomly in time (Figures 3.6a-b), which potentially complicates the analysis of their dependence on controlling parameters such as the magnitude of tracking errors. In contrast, numerical diffusion clearly grows with larger tracking errors (Figure 3.6c).

Since the effective Courant number will not be kept at 1 due to the tracking errors, it could be argued that the order of magnitude of the observed errors is due to the specific ELM selected. To analyze this hypothesis, we compare solutions with inexact tracking and a flow-induced Courant number of 1, and solutions without tracking errors but with a Courant number that leads to the maximum numerical diffusion ($Cu = 0.5$, dashed lines in Figure 3.6). Mass and phase errors are both very small when tracking is exact (Figures 3.6a-b). Numerical diffusion, though, can be partially attributed to the selected ELM

(Baptista, 1987): the 2nd moment of solutions with inexact tracking is of the same order of magnitude of the 2nd moment in the absence of tracking errors (Figure 3.6c).

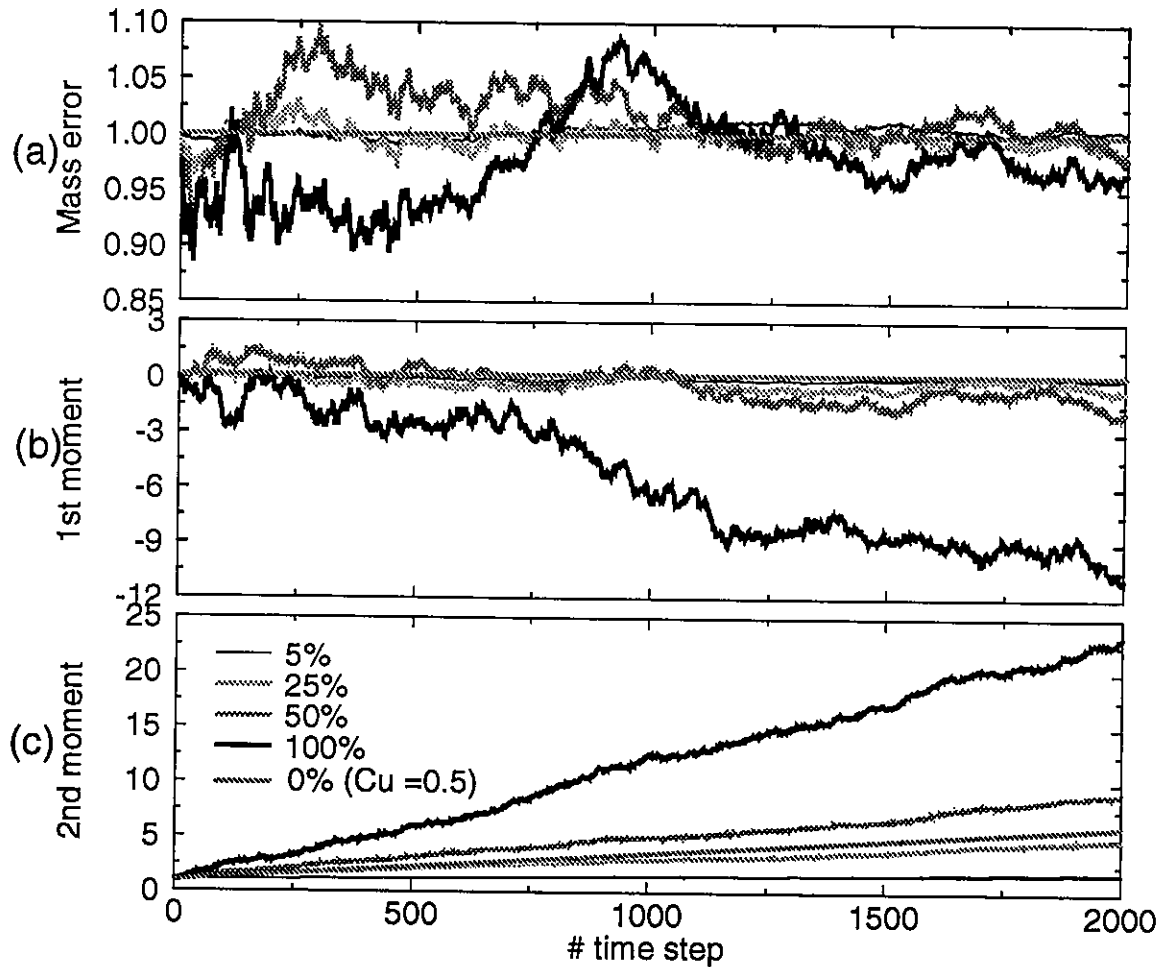


Figure 3.6 Time series of error measures: a) Mass errors for several $\epsilon/\Delta x$ ($Cu = 1$) vs maximum mass errors for a simulation without tracking errors ($Cu = 0.5$). (b) 1st moment for several $\epsilon/\Delta x$ ($Cu = 1$). (c) 2nd moment for several $\epsilon/\Delta x$ ($Cu = 1$) against maximum 2nd moment for a simulation without tracking errors ($Cu = 0.5$)

The next sections discuss the dependence of each error measure - mass, phase and numerical diffusion - on dimensionless parameters.

3.5.2.2 Mass errors

Within a single simulation, the dependence of mass errors on the dimensionless numbers $\epsilon/\Delta x$, $\sigma/\Delta x$ and D^* is mostly inconclusive (dashed lines in Figures 3.7a-c). How-

ever, in the aggregate of several simulations with tracking errors seeded differently, clear patterns of dependency emerge (circles in Figures 3.7a-c). In particular, the likelihood of large mass errors:

- increases significantly with increasing tracking errors (Figure 3.7a), with a quasi-linear variation (Figure 3.8a);
- decreases significantly with increasing refinement (Figure 3.7b), with an almost linear dependence on a log-log scale (Figure 3.8b);
- decreases significantly with the diffusion number (Figure 3.7c), with a quasi-logarithmic variation (Figure 3.8c).

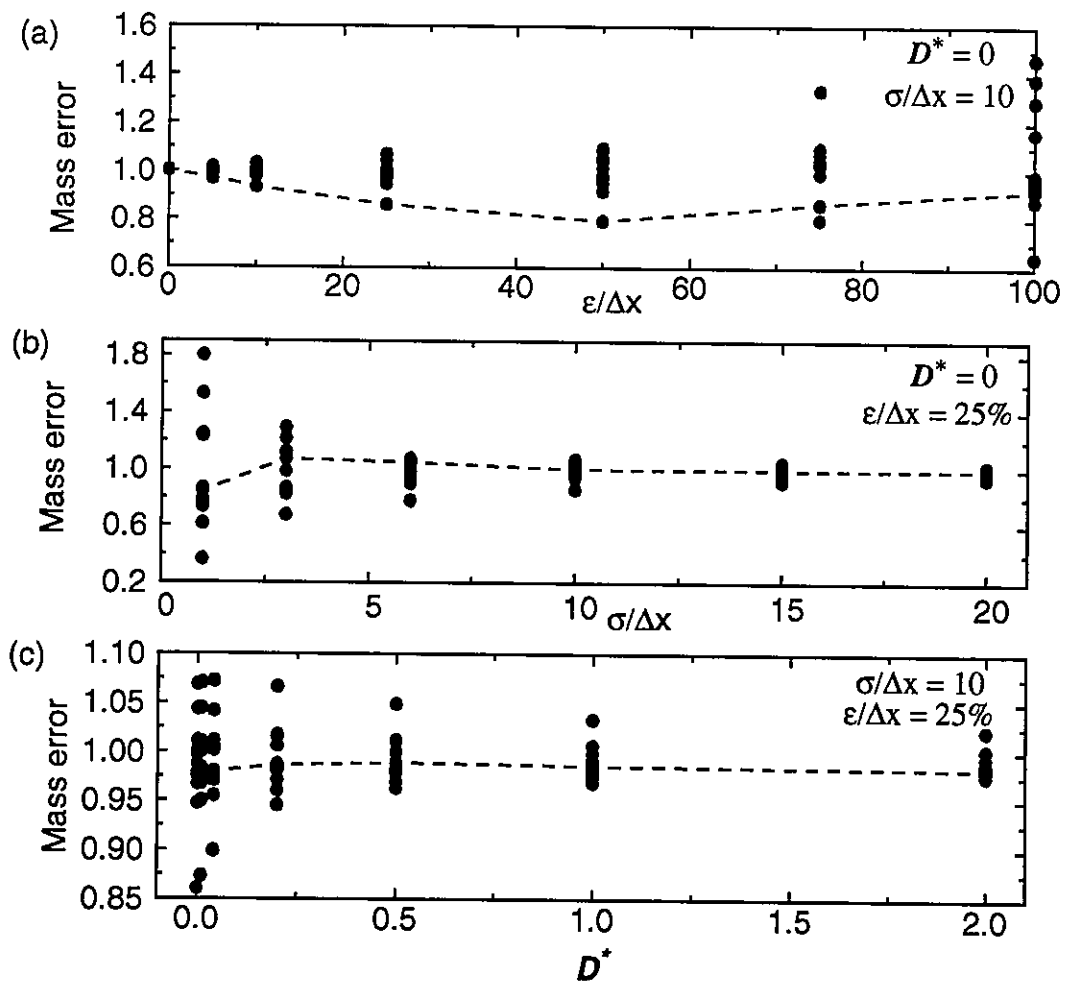


Figure 3.7 Mean mass errors for 12 seeds (circles and dashed line): a) versus $\epsilon/\Delta x$. b) $\sigma/\Delta x$. c) Diffusion number ($D^* = Pe/Cu$).

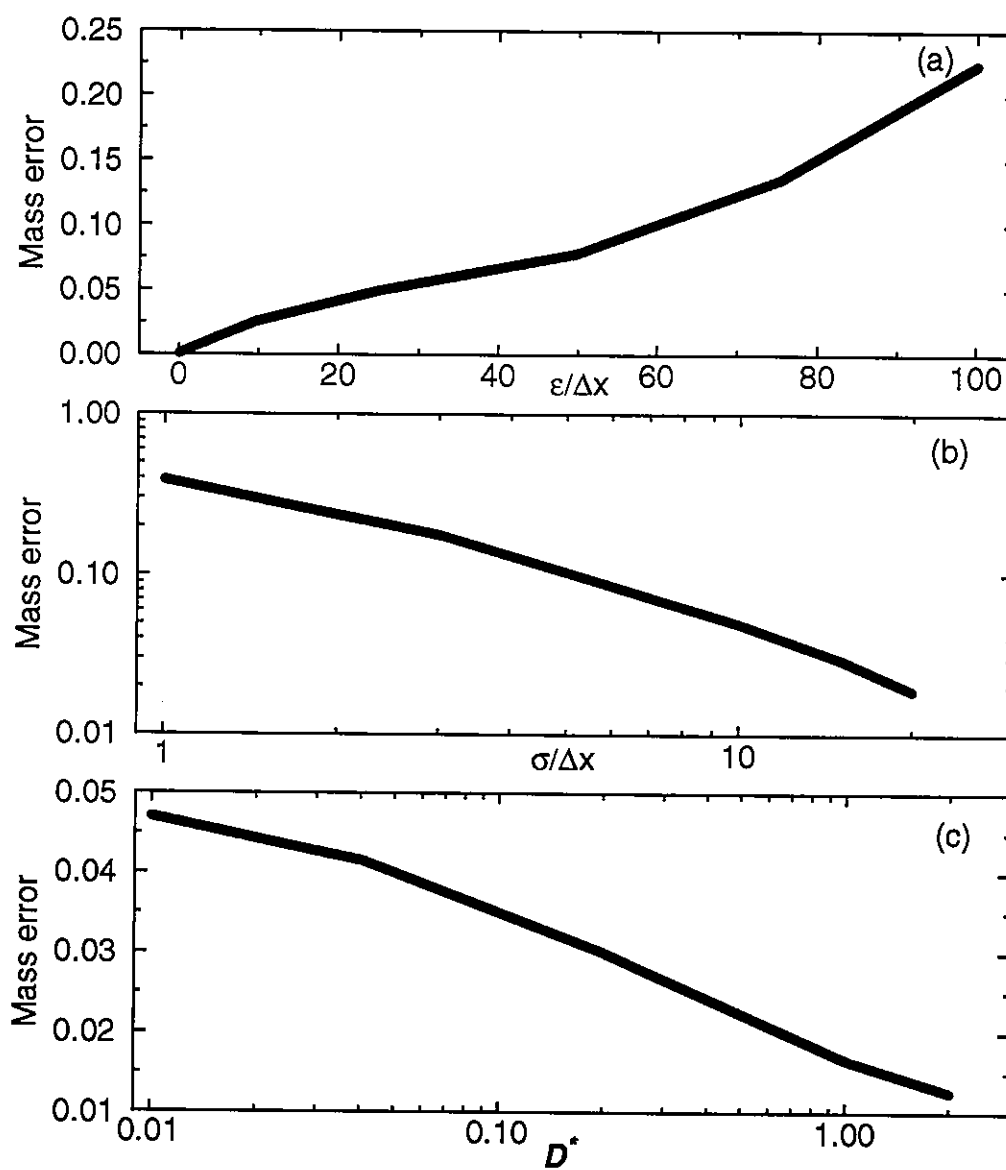


Figure 3.8 Standard deviation of the mean mass errors: a) versus $\epsilon/\Delta x$. b) $\sigma/\Delta x$. c) D^* .

Results clearly suggest that accurate tracking is necessary to obtain conservative transport solutions. Additional grid refinement and added diffusion reduce but do not eliminate mass conservation errors due to tracking.

3.5.2.3 Phase errors

The dependence of phase errors on the dimensionless numbers $\epsilon/\Delta x$, $\sigma/\Delta x$ and D^* is also inconclusive within a single simulation (dashed line in Figures 3.9a-c). However, in the aggregate of several simulations with tracking errors seeded differently, patterns of dependency emerge (circles in Figures 3.9a-c). In particular, the likelihood of large phase errors:

- increases significantly with increasing tracking errors (Figure 3.9a), with a quasi-linear variation (Figure 3.10a);
- decreases significantly with increasing refinement up to $\sigma/\Delta x = 15$, followed by a slight increase for larger values of $\sigma/\Delta x$ (Figures 3.9b and 3.10b);
- decreases significantly with the diffusion number up to $D^* = 1$, with a quasi-logarithmic variation (Figures 3.9c and 3.10c). For diffusion numbers larger than 1, phase errors present an almost-linear increase. This behavior can be explained by the dependence of phase errors on diffusion observed in the truncation error analysis (equation (3.10a)). For $D^* > 1$, simulations are diffusion-dominated, and the first term in equation (3.10a) becomes negligible relative to the second.

Our analysis suggests that accurate tracking is necessary to prevent large phase shifts, of the order of several times the element size. Added diffusion or finer grid resolution do not effectively reduce phase errors.

3.5.2.4 Numerical diffusion

Unlike mass and phase errors, numerical diffusion is practically independent of the specific distribution of tracking errors, thus allowing estimates on the expected 2nd moment. For several solutions with inexact tracking, the normalized 2nd moment can be smaller than 1 over some periods of time. Therefore, tracking errors can introduce negative numerical diffusion, as pointed out by the truncation error analysis. Time varying, potentially negative, numerical diffusion can lead to an unstable behavior, specially if inherently less diffusive ELMs than our reference method are used. In order to illustrate

this possibility, test 1 was repeated, with a tracking error of 50% and a Courant number of 0.5, using a very accurate piecewise ELM Oliveira and Baptista, 1995). This method, which is unconditionally stable in the absence of tracking errors, is even more severely affected by inexact tracking than the linear interpolation ELM (Figure 3.11a), and becomes unstable after a short number of time steps (Figure 3.11b).

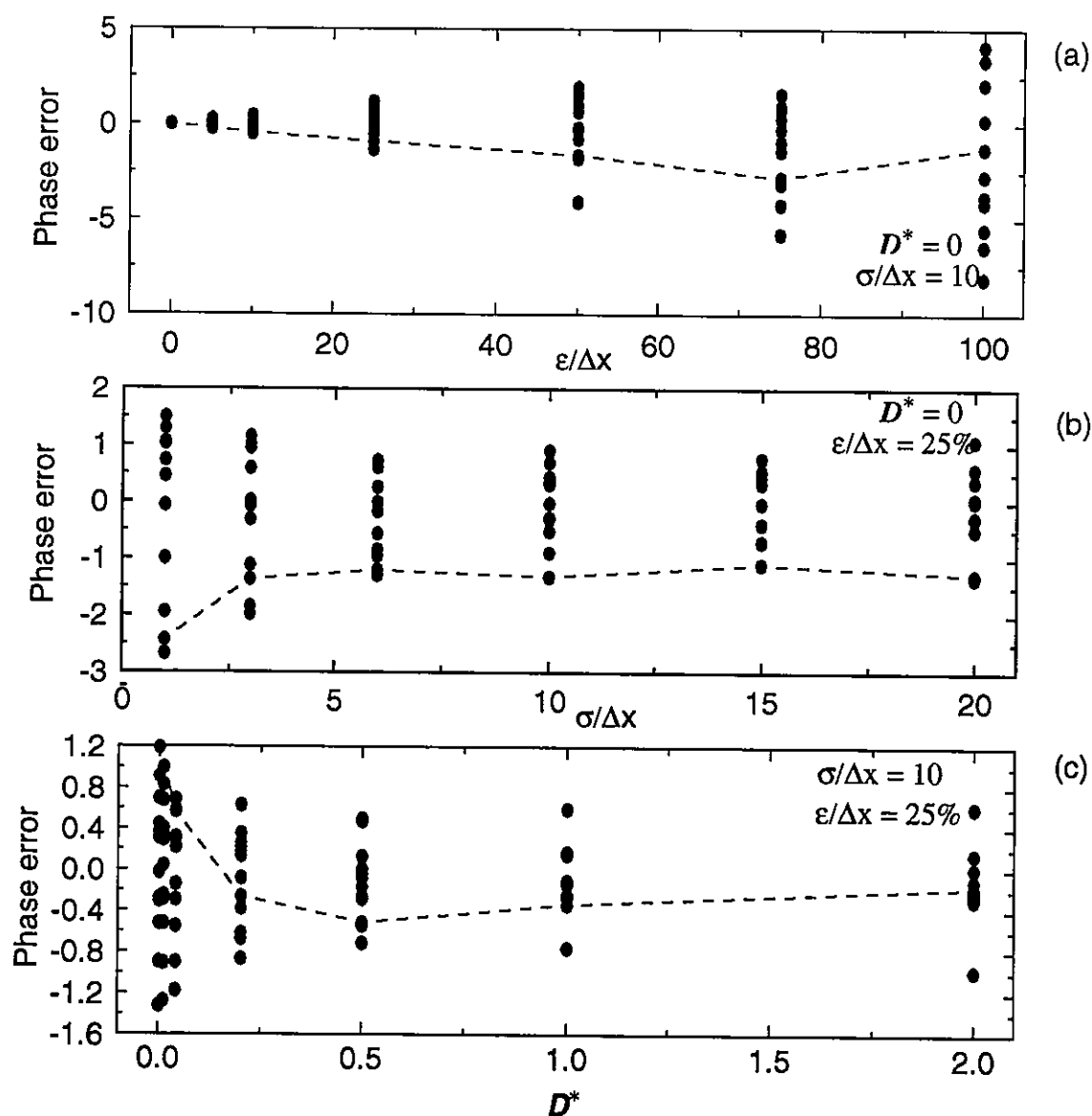


Figure 3.9 Mean 1st moment for 12 seeds (circles and dashed line): a) versus $\epsilon/\Delta x$. b) $\sigma/\Delta x$. c) D^* .

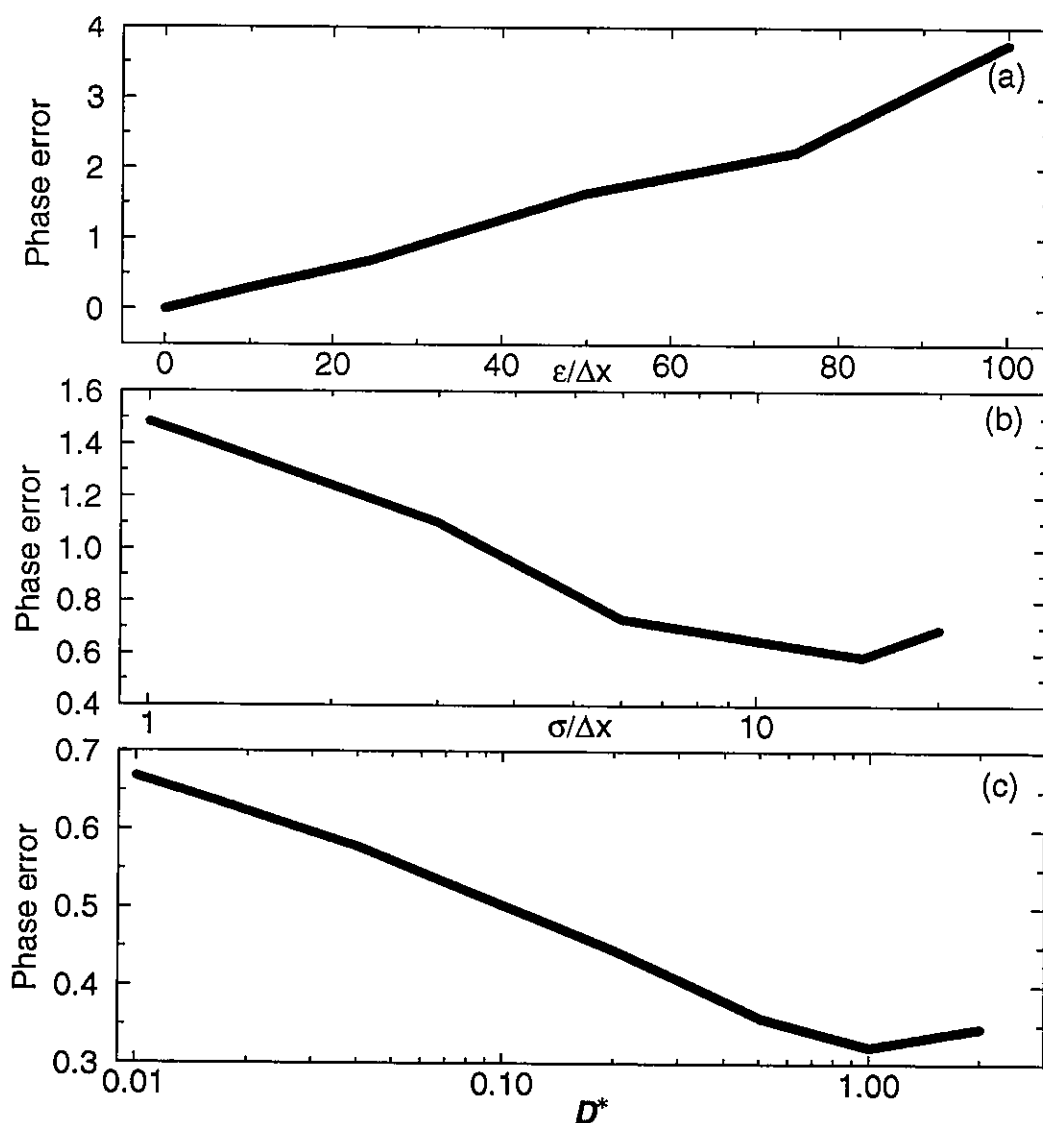


Figure 3.10 Standard deviation of the mean first moment: a) versus $\epsilon/\Delta x$. b) $\sigma/\Delta x$. c) D^* .

Numerical diffusion can also be increased by the presence of tracking errors. However, the numerical diffusion in presence of inexact tracking is of the same order of magnitude of the numerical diffusion without tracking errors and with a Cu of 0.5 (Figure 3.6c). Since the effective Courant number is not kept at 1, the observed 2nd moments of concentration are generated both by tracking errors and by the use of a linear interpolator. In order to allow a meaningful comparison between solutions with and without tracking errors, the runs were repeated for $Cu = 0.5$ (test 1A), which would lead to the maximum numerical diffusion in the absence of tracking errors (Baptista, 1987). The resulting 2nd

moment of concentration was then scaled by the 2nd moment in the absence of tracking errors (Table 3.5).

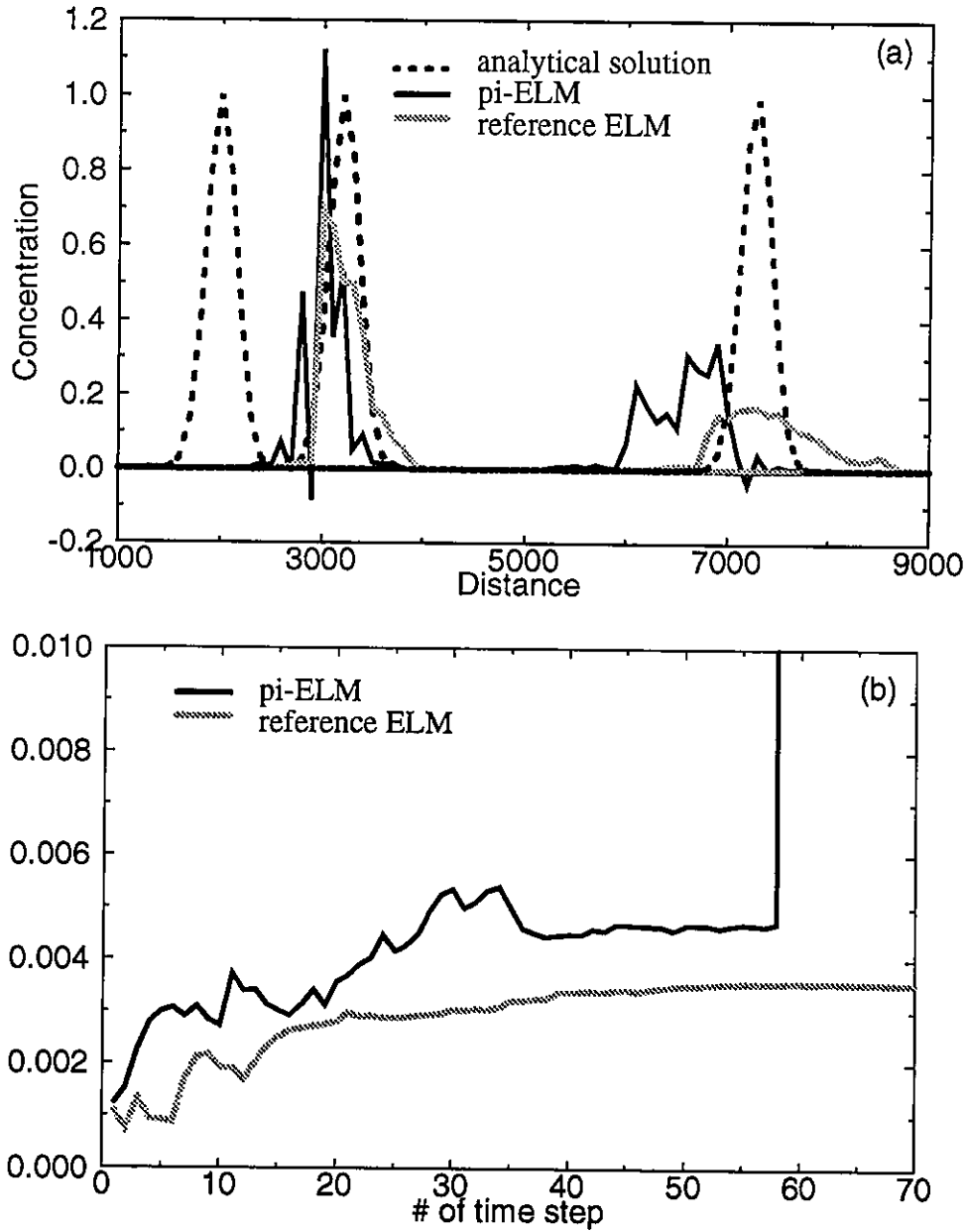


Figure 3.11 Potential for instabilities in presence of tracking errors, for a tracking error of 50%: (a) Concentration field for time steps 0, 11 and 48. (b) L2-norm for pi-ELM and reference ELM: instability generated by the presence of tracking errors.

In general, larger tracking errors lead to an increased numerical diffusion, which can reach significant values: up to 3 times its value without tracking errors, after a short number of time steps (Figure 3.12).

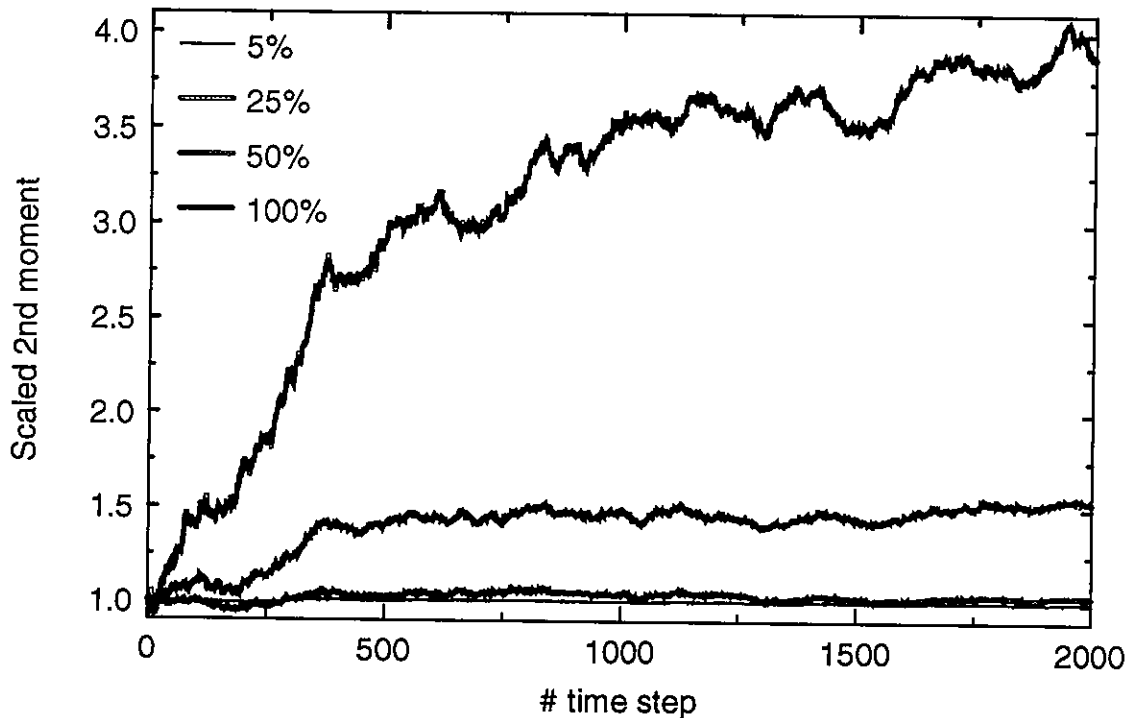


Figure 3.12 Time series of 2nd moment with tracking errors scaled by time series of 2nd moment without tracking errors (both with $Cu = 0.5$).

3.6 Final considerations

This paper addressed the impact of inexact tracking on Eulerian-Lagrangian solutions of the transport equation, through a combination of formal analysis and numerical experimentation. The accuracy (Figure 3.13) and the stability of ELMs (Figure 3.11) were shown to be severely compromised by tracking errors, re-enforcing the need for an accurate tracking. Different scenarios result from specific tracking errors distributions, thus preventing accurate estimates of the effect of inexact tracking in a real system. Still, some

important features can be identified that recommend the use of accuracy controlled tracking techniques:

- In presence of complex flows, considerable tracking errors can be generated in surface water simulations if low order tracking methods are used. Conversely, accuracy-controlled techniques allow for very small tracking errors, regardless of the complexity of the flow pattern or the geometry of the domain.
- Increasing tracking errors lead to wider ranges of both mass and phases errors. For large tracking errors, mass imbalances can be quite significant (Figure 3.6a). Similarly, large artificial phase shifts, of the order of several times the grid spacing, can be generated.
- Both negative numerical diffusion and excessive positive numerical diffusion can result from the presence of tracking errors. Negative diffusion can lead to instability, in particular when otherwise very accurate ELMs are used. The positive numerical diffusion associated with large tracking errors can be several times larger than that of the linear interpolation ELM, thus severely hampering the accuracy of the simulations and the usefulness of ELMs for practical purposes.
- Large diffusion coefficients and grid refinements, usual “fixes” for numerical problems, may be ineffective for simulations with significant tracking errors. Additional grid refinement and added diffusion tend to reduce mass errors but are unable to fully eliminate them. Phase errors are not consistently reduced by larger plume discretization or larger diffusion coefficients.
- Tracking errors affect both interpolation and integration finite element ELM formulations, even otherwise very accurate methods such as the piecewise ELM (Oliveira and Baptista, 1995) and the ELLAMs (Celia, 1994, Figure 3.14).

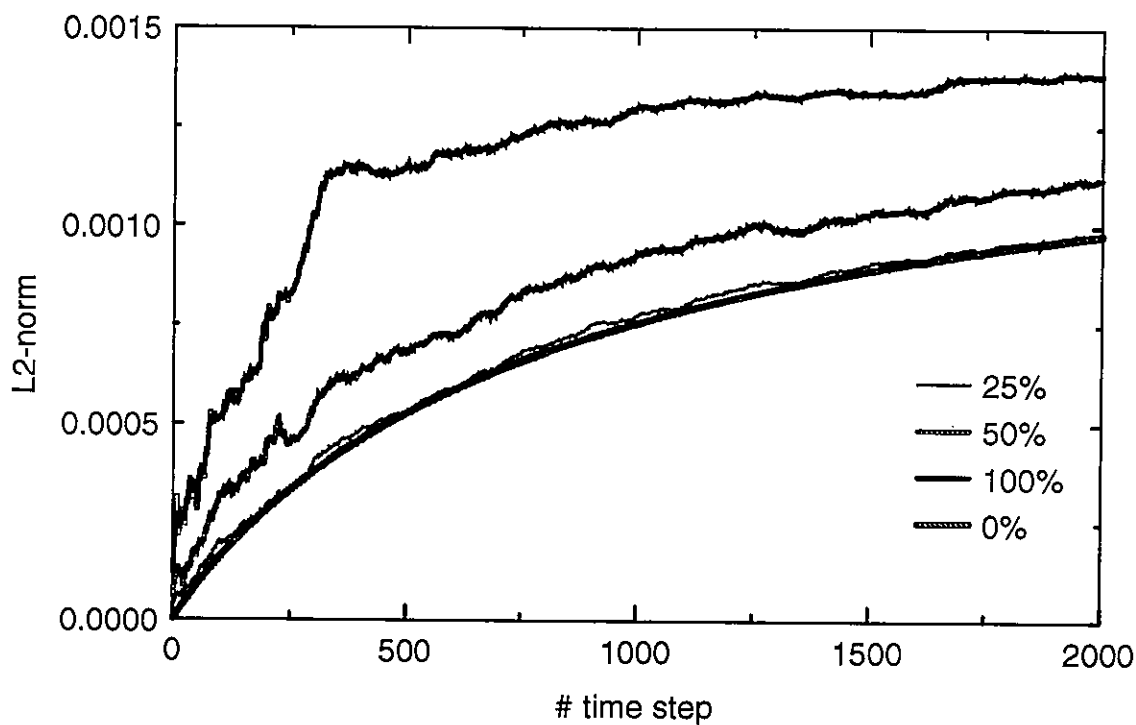


Figure 3.13 Time series of L2-norm for several $\epsilon/\Delta x$.

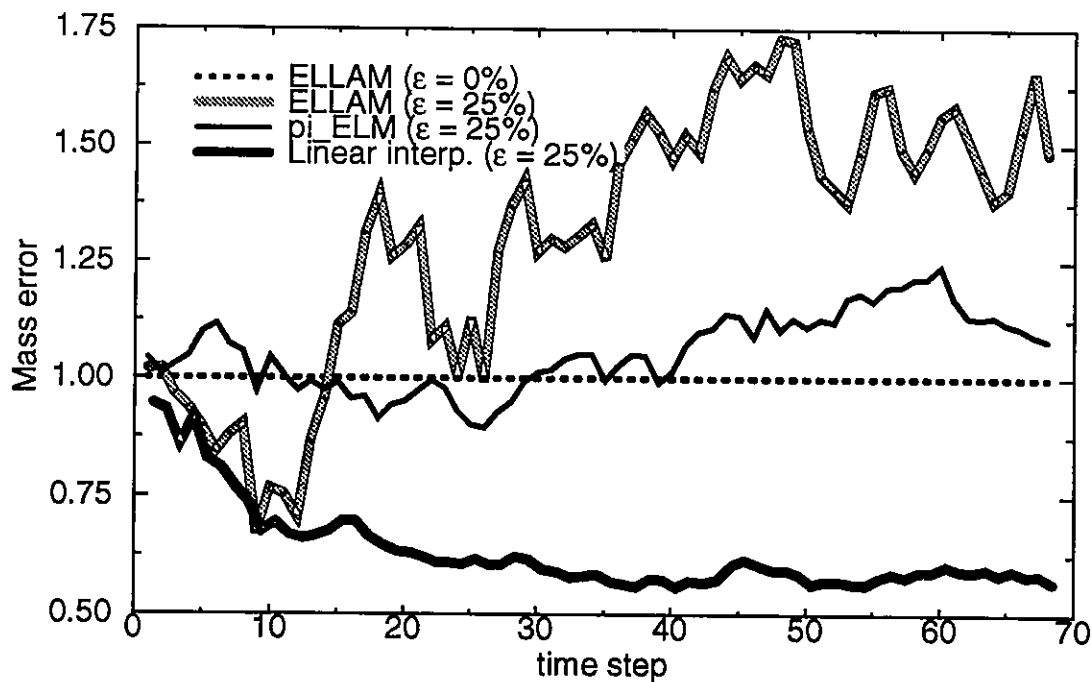


Figure 3.14 Time series of mass errors generated by tracking errors for several integration and interpolation ELMs: ELLAM with gauss quadrature integration (Celia, 1994), piecewise ELM (Oliveira and Baptista, 1995), and linear interpolator ELM (Baptista, 1987).

Mass imbalances, generated either by a poor tracking or by a non-conservative flow field, limit the use of ELMs for general applications, in particular when transformation processes are present. While tracking errors can be kept at acceptable levels by accuracy-controlled tracking techniques, mass errors from non-conservative flows pose a difficult, and interesting, challenge.

Several solutions, which resort to conservative forms of the transport equation, have been proposed to address this problem. For models that use the non-conservative transport equation, a simple solution is to approximate the neglected continuity equation term (Cady and Neuman, 1988). Another solution is the use of an ELLAM formulation with a finite element framework (Russell, 1989; Celia et al., 1990; Celia, 1994), which has the potential advantage of using, *a priori*, a conservative form of the transport equation. However, these two alternatives can only address part of the mass problem in ELMs: neither of them can handle the mass errors that result, on an elemental basis, from errors introduced by non-conservative flows on the tracked image of the element (Binning and Celia, 1994; Celia, 1994).

Recently, Eulerian-Lagrangian concepts within a finite volume framework have shown promise for local mass conservation (Roache, 1992; Healy and Russell, 1993; Celia, 1994; Binning and Celia, 1994; Arbogast and Wheeler, 1995). In particular, the finite volume ELLAM of Healy and Russell (1993) and the flux-based ELM of Roache (1992) have been shown to preserve mass globally, even with inexact tracking. However, inexact tracking and non-conservative flow fields will still lead to local mass imbalances and oscillations.

A potentially more robust and complete solution to the mass conservation problem in ELMs may require the use of very fine grids to reduce flow mass errors. Since grid generation is controlled by different processes in flow and transport, separate grids can be used, thus avoiding unnecessary computational effort in the transport simulation. Further research is still necessary, though, to study and compare these different approaches and provide an Eulerian-Lagrangian formulation that guarantees mass conservation.

Appendix A - Review of models TEA-NL and ELA

Model TEA-NL (Westerink et al., 1987 and 1988) solves the fully non-linear primitive shallow water equations in the frequency domain. The non-linear terms are treated iteratively and a linear friction term is added to both sides of the momentum equations to provide iterative stability and improve convergence. The governing equations are:

$$\begin{aligned} \frac{\partial \eta}{\partial t} + \frac{\partial}{\partial x}(uh) + \frac{\partial}{\partial y}(vh) &= -\frac{\partial}{\partial x}(u\eta) - \frac{\partial}{\partial y}(v\eta) \\ \frac{\partial u}{\partial t} + g\frac{\partial \eta}{\partial x} - fv + \lambda u &= \left[\lambda - c_f \frac{(u^2 + v^2)^{1/2}}{(h + \eta)} \right] u - u\frac{\partial u}{\partial x} - v\frac{\partial u}{\partial y} \\ \frac{\partial v}{\partial t} + g\frac{\partial \eta}{\partial x} + fu + \lambda v &= \left[\lambda - c_f \frac{(u^2 + v^2)^{1/2}}{(h + \eta)} \right] v - u\frac{\partial v}{\partial x} - v\frac{\partial v}{\partial y} \end{aligned} \quad (3.14)$$

where u and v are the depth averaged components of velocity, η is the surface elevation relative to mean sea level, h is the depth relative to mean sea level, g is the acceleration due to gravity, f is the Coriolis factor, c_f is the bottom friction coefficient and λ is the linearized friction factor.

Equations (3.14) are then reduced to their harmonic form by assuming that η , u , v and the right hand side non-linear terms may be expressed as Fourier series. This leads to N_f sets of time independent equations of the form:

$$\begin{aligned} iw\hat{\eta}_j + \frac{\partial}{\partial x}(\hat{u}_jh) + \frac{\partial}{\partial y}(\hat{v}_jh) &= P_{\eta_j}^{nl} \\ iw\hat{u}_j + \frac{\partial}{\partial x}(g\hat{\eta}_j) - f\hat{v}_j + \lambda\hat{u}_j &= P_{u_j}^{nl} \\ iw\hat{v}_j + \frac{\partial}{\partial y}(g\hat{\eta}_j) + f\hat{u}_j + \lambda\hat{v}_j &= P_{v_j}^{nl} \end{aligned} \quad (3.15)$$

where w_j is the j^{th} frequency of the spectrum; $P_{\eta_j}^{nl}$ is the j^{th} harmonic component of the continuity equation non-linear terms, $P_{u_j}^{nl}$ and $P_{v_j}^{nl}$ are the j^{th} harmonic component of the x- and y-momentum non-linear terms, respectively; $\hat{\eta}_j$, \hat{u}_j and \hat{v}_j are the complex elevation

and velocity amplitudes of the j^{th} component of $\eta(t)$, $u(t)$ and $v(t)$, respectively; N_f is the number of frequencies and $i = (-1)^{1/2}$.

Equations (3.15) are spatially discretized using linear finite elements. A weak residual statement is developed by allowing a residual error on the normal flux boundaries, and by integrating the continuity equation residual error by parts. Elevation boundaries are thus strictly enforced while flux boundaries are relaxed and treated as natural boundary conditions.

Model ELA (Baptista et al., 1984) solves the non-conservative depth-averaged transport equation for a passive tracer:

$$\frac{\partial c}{\partial t} + u_i \frac{\partial c}{\partial x_i} = \frac{1}{h} \frac{\partial}{\partial x_i} \left(D_{ij} h \frac{\partial}{\partial x_j} (c) \right) + Q \quad i = 1, 2 \quad (3.16)$$

where c is depth-averaged concentration, h is the flow depth, u_i are the velocity components, D_{ij} is the diffusion coefficient tensor and Q represents internal sources and sinks and vertical fluxes through the bottom and surface of the flow.

ELA decouples advection and diffusion by breaking equation (3.16) into two simpler equations:

$$u_i = \frac{dx_i}{dt} \quad (3.17)$$

$$\frac{Dc}{Dt} = \frac{1}{h} \frac{\partial}{\partial x_i} \left(D_{ij} h \frac{\partial}{\partial x_j} (c) \right) + Q \quad (3.18)$$

The tracking equation (3.17) is solved once at each node for each time step. The original ELA, which solves this equation using a 5th-order Runge-Kutta method, was modified to allow for one-step backward Euler and Multi-step backward tracking (see Appendix B).

The dispersion equation (3.18) is solved using a weak Galerkin weighted residual finite element formulation, over quadratic elements. Concentration-imposed boundaries are strictly enforced as essential boundary conditions while flux boundaries are relaxed and treated as natural boundary conditions.

Because land boundaries are usually enforced as natural boundary conditions in flow models, leading to non-zero normal velocities, special procedures are necessary in the transport model to prevent characteristic lines from crossing these boundaries. Rather than stopping the tracking at the boundary, ELA allows the tracking to continue within a small “slippery region,” defined as a thin layer along the boundary.

Appendix B - Tracking techniques

Tracking of characteristic lines in transport models requires solving (shown in 1D, for simplicity):

$$\frac{dx}{dt} = u \quad (3.19)$$

where $u(t,x)$ is the velocity, t is time and x is the spatial coordinate.

Several methods have been used in the past to solve (3.19), ranging from low order backward Euler methods (Cheng et al., 1984; Allen and Khosravani, 1992) to the high order Runge-Kutta methods (Baptista et al., 1984; Dimou, 1992) (other methods using semi-analytical tracking (Pollock, 1988; Lu, 1994) have also been proposed, but cannot be applied when velocity components depend on nodal velocities in all coordinate directions). The concept behind the derivation of Euler and Runge-Kutta methods is the same: the numerical solution approximates the exact solution by a Taylor series (Thomas, 1986):

$$x(t^n) = x(t^{n+1}) + \Delta t \frac{dx}{dt}(t^{n+1}) + \frac{\Delta t^2}{2!} \frac{d^2x}{dt^2} + \dots + \frac{\Delta t^k}{k!} \frac{d^kx}{dt^k} \quad (3.20)$$

where $\Delta t = t^n - t^{n+1}$.

If we substitute (3.19) into (3.20) and truncate the series after the second term, we obtain the first order, one-step Backward Euler (BE-Table 3.2). The Multi-Step Backward Euler improves the accuracy of the BE by dividing the time step in sub-steps (MSE-Table 3.2). The tracking in the MSE is done by applying the BE sequentially in each sub-step.

The Runge-Kutta methods (RK) eliminate high-order error terms by combining several “trial” steps, which involve the evaluation of velocity at intermediate points between t^n and t^{n+1} . The general expression for RK tracking is:

$$x(t^n) = x(t^{n+1}) + \Delta t \sum_{j=1}^q a_j k_j \quad (3.21)$$

$$\text{with } k_j = u \left(t^{n+1} + c_j \Delta t, x(t^{n+1}) + \Delta t \sum_{m=1}^{j-1} b_{jm} k_m \right)$$

where q is depends on the order of the method and is equal to 6 for a 5th-Runge-Kutta method and equal to 4 for a 4th-order Runge-Kutta. Many sets of coefficients a_j , b_{jm} and c_j have been proposed, generating several types of RK methods (Thomas, 1986; Press et al., 1992).

Unlike Euler methods, the time step for the RK tracking is dynamically adjusted to meet a user-specified accuracy criterion. This adaptive control can done by step-doubling techniques, where the position after one full time step is compared with the position computed using two half-steps, or by embedded RK formulas, where the position computed using a n order RK is compared with the position using a $n+1$ RK formula. This way, RK tracking automatically adjusts to the local complexity of the flow field through an effective control of the truncation error.

The traditional 5th-order RK with a step-doubling accuracy control, was used in this analysis. It was obtained by adding the truncation error to the traditional 4th-order RK defined in Table 3.2.

In our simulations, the number of intermediate time steps in the multi-step Euler tracking was set equal to the first guess of the time step for the Runge-Kutta tracking (δt , taken as 1/10 of the diffusion time step), in order to provide a fair comparison between the two methods. Given the complexity of the chosen flow field and the Courant numbers well above 1, an update of the tracking velocity was also performed for both Euler methods when a characteristic line crossed an element boundary, to improve their performance. These updates on velocity were not necessary for the RK runs, because accuracy was controlled by the spatial criterion (θ), which was set to 10^{-3} m.

Since the output from flow model TEA-NL is in the frequency domain, the evaluation of velocity at intermediate points between time n and $n+1$ can be accurately evaluated by a harmonic synthesis. In space, velocities are interpolated linearly within each element.

Appendix C - Closure errors

Tracking errors were estimated through the evaluation of closure errors for several simulations, with distinct time steps and simulation lengths. To assess the expected range of tracking errors, several particles were released in different regions of the estuary, forward-tracked for the total time of the simulation and then backward-tracked to the initial time. The displacement between release and final location (tracking error), scaled by the equivalent diameter of the average visited element, was evaluated as:

$$E_c = \frac{\sqrt{(x_f - x_r)^2 + (y_f - y_r)^2}}{D_{aver}} \quad (3.22)$$

where (x_r, y_r) and (x_f, y_f) are the release and final locations. D_{aver} is the equivalent diameter of the average visited element:

$$D_{aver} = 2 \times \sqrt{\frac{\left(\sum_{i=1}^m A_i \right) / m}{\pi}} \quad (3.23)$$

where A_i is the area of each of the m elements visited during the tracking.

References

- Allen, M.B. and A. Khosravani, 1992. Solute transport via alternating-direction collocation using the modified method of characteristics, *Advances in Water Resources*, 15(2): 125-132.
- Arbogast, T., and M.F. Wheeler, 1995. A Characteristics-Mixed Finite Element Method for Advection-Dominated Transport Problems, *SIAM Journal of Numerical Analysis*, 32(2): 404-424.
- Baptista, A.M., 1987. *Solution of Advection-Dominated Transport by Eulerian-Lagrangian Methods using the Backwards Method of Characteristics*, Ph.D. Dissertation, Massachusetts Institute of Technology, Cambridge.
- Baptista, A.M., E.E. Adams, and K.D. Stolzenbach, 1984. *Eulerian-Lagrangian analysis of pollutant transport in shallow water*, Technical Report no. 296, MIT R.M. Parsons Laboratory, Cambridge.
- Barros, A.P. and A.M. Baptista, 1989. An Eulerian-Lagrangian Model for Sediment Transport in Estuaries, in *Estuarine and Coastal Modeling*, M.L. Spaulding (editor), American Society of Civil Engineers, 102-112.
- Bentley, L., 1990. *The Eulerian-Lagrangian Least Squares Collocation Method for solving the transport equation*, Ph.D. Dissertation, Princeton University, Princeton.
- Bentley, L. and G.F. Pinder, 1992. Eulerian-Lagrangian Solution of the Vertically Averaged Groundwater Transport Equation, *Water Resources Research*, 28(11): 3011-3020.
- Binning, P. and M.A. Celia, 1994. Two-Dimensional Eulerian-Lagrangian Localized Adjoint Methods for the Solution of the Contaminant Transport Equation in the Saturated and Unsaturated Zones, in *Proceedings of the 10th International Conference on Computational Methods in Water Resources*, A. Peters et al. (editors), Kluwer Academic Publishers, 165-172.

- Cady, R. and S.P. Neuman, 1988. Three-Dimensional Adaptive Eulerian-Lagrangian Finite Element Method for Advection-Dispersion, in *Proceedings of the 7th International Conference on Computational Methods in Water Resources*, M.A. Celia et al. (editors), 183-193.
- Casulli, V. and R.T. Cheng, 1992. Semi-implicit finite difference methods for three-dimensional shallow water flow, *International Journal for Numerical Methods in Fluids*, 15(6): 629-648.
- Celia, M.A., 1994. Eulerian-Lagrangian Localized Adjoint Methods for Contaminant Transport Simulations, in *Proceedings of the 10th International Conference on Computational Methods in Water Resources*, A. Peters et al. (editors), Kluwer Academic Publishers, 207-216.
- Celia, M.A., T.F. Russell, I. Herrera, R.E. Ewing, 1990. An Eulerian-Lagrangian Localized Adjoint Method for the Advection-Diffusion Equation, *Advances in Water Resources*, 13(4): 187-206.
- Cheng, R.T., V. Casulli, and S.N. Milford, 1984. Eulerian-Lagrangian Solution of the Convection-Dispersion Equation in natural Coordinates, *Water Resources Research*, 20(7): 944-952.
- Darmofal, D.L. and R. Haimes, 1996. An Analysis of 3D Particle Path Integration Algorithms, *Journal of Computational Physics*, 123(1): 182-195.
- Daubert, O., 1974. *Programme HYP1, Rapport C41/74/12*, Laboratoire National D'Hydraulique, Chatou, France.
- Dimou, K., 1992. *3-D Hybrid Eulerian-Lagrangian / Particle Tracking Model for Simulating Mass Transport in Coastal Water Bodies*, Ph.D. Dissertation, Massachusetts Institute of Technology, Cambridge.
- Galeati, G, G. Gambolati and S.P. Neuman, 1992. Coupled and Partially Coupled Eulerian-Lagrangian Model of Freshwater-Seawater Mixing, *Water Resources Research*, 28(1): 149-165.
- Healy, R.W. and R.F. Russell, 1993. A Finite-Volume Eulerian-Lagrangian Localized Adjoint Method for Solution of the Advection-Dispersion Equation, *Water Resources Research*, 29(7): 2399-2413.
- Hervouet, J.M., 1986. *Remarques sur la convection faible et son application à l'hydraulique, Rapport HE41/86.09*, Laboratoire National D'Hydraulique, Chatou, France.

- Kolar, R.L., J.J. Westerink, M.E. Cantekin and C.A. Blain, 1994. Aspects of nonlinear simulation using shallow water models based on the wave continuity equation, *Computers and Fluids*, 23(3): 523-538.
- Lu, N., 1994. A semianalytical method of path line computation for transient finite-difference groundwater flow models, *Water Resources Research*, 30(8): 2449-2459.
- Lynch, D.R., 1985. Mass balance in shallow water simulations, *Communications in Applied Numerical Methods*, 1(4): 153-159.
- Mitchell, R.J. and A.S. Mayer, 1994. A Modified Method of Characteristics Technique for Simulating Contaminant Transport in Variably-Saturated Porous Media, in *Proceedings of the 10th International Conference on Computational Methods in Water Resources*, A. Peters et al. (editors), Kluwer Academic Publishers, 505-512.
- Neuman, S.P., 1984. Adaptive Eulerian-Lagrangian Finite Element Method for Advection-Dispersion, *International Journal for Numerical Methods in Engineering*, 20(2): 321-337.
- Oliveira, A. and A.M. Baptista, 1995. A comparison of integration and interpolation Eulerian-Lagrangian methods, *International Journal for Numerical Methods in Fluids*, 21(3): 183-204.
- Pollock, D.W., 1988. Semianalytical computation of path lines for finite difference models, *Groundwater*, 26(6): 743-750.
- Press, W.H., S.A. Teukolsky, W.T. Vetterling and B.P. Flannery, 1992. *Numerical Recipes in Fortran*, Cambridge University Press.
- Roache, P.J., 1992. A Flux-Based Modified Method of Characteristics, *International Journal for Numerical Methods in Fluids*, 15(11): 1259-1275.
- Russell, T.F., 1985. Time Stepping along characteristic with incomplete iteration for a Galerkin approximation of Miscible Displacement in Porous Media, *SIAM Journal of Numerical Analysis*, 22(5): 970-1013.
- Russell, T.F., 1989. Eulerian-Lagrangian Localized Adjoint Methods for Advection-Dominated Problems, in *Numerical Analysis 1989*, Pitman Research Notes, D.F. Griffiths and G.A. Watson (editors), Longman Scientific and Technical, 228: 206-228.
- Sorek, S., 1988. Eulerian-Lagrangian method for solving transport in aquifers, *Advances in Water Resources*, 11(2): 67-73.
- Thomas, B., 1986. The Runge-Kutta methods, *Byte Mag.*, 11(4?): 191-210.

- Vreugdenhil, C.B. and B. Koren (editors), 1993. Numerical Methods for Advection-Diffusion Problems, *Notes on Numerical Fluid Mechanics*, Vieweg, 45.
- Wang, J.D., S.V. Cofer-Shabica, and J. Chin-Fatt, 1988. Finite Element Characteristic Advection Model, *Journal of Hydraulic Engineering*, American Society of Civil Engineers, 114(9): 1098-1114.
- Westerink, J.J., J.J. Connor, K.D. Stolzenbach, 1987. A Primitive Pseudo Wave Equation Formulation for Solving the Harmonic Shallow Water Equations, *Advances in Water Resources*, 10(4): 188-199.
- Westerink, J.J., J.J. Connor, K.D. Stolzenbach, 1988. A Frequency-Time Domain Finite Element Model for Tidal Circulation Based on The Least-Square Harmonic Analysis Method, *International Journal for Numerical Methods in Fluids*, 8(7): 813-843.
- Wheeler, M.F., K.R. Roberson, and A. Chilakapati, 1992. Three-Dimensional Bioremediation Modeling in Heterogeneous Porous Media, in *Proceedings of the 9th International Conference on Computational Methods in Water Resources*, T.F. Russell et al. (editors), Computational Mechanics Publ., Denver, USA, 299-312.
- Wood, T.M. and A.M. Baptista, 1993. A Model for Diagnostic Analysis of Estuarine Geochemistry, *Water Resources Research*, 29(1): 51-71.

CHAPTER 4

Local Mass Conservation in Finite Element Shallow Water Models

Abstract

We examine empirically the local mass conservation properties of finite element shallow water models and identify major sources of error. We find that local mass conservation errors are generated mainly over strong bathymetric gradients and along complex boundaries. Non-linear processes play only a relatively minor role. Grid refinement appears ineffective as a mechanism to enhance local mass conservation for refinement levels that lead to otherwise acceptable numerical solutions. Results are largely model independent for the sample of three distinct models used in our research.

4.1 Introduction

Although finite element (FE) shallow water models are becoming reliable tools for interpretation and prediction of estuarine and coastal flows (Westerink et al., 1996), mass conservation remains a concern. In particular, local flow mass balance has a strong impact on the overall accuracy and conservation of tracer transport, when non-conservative flow models are used as drivers (Oliveira and Baptista, 1997). In spite of its importance, the investigation of local flow mass conservation has lagged behind that of other accuracy and stability issues.

It has been generally accepted that flow mass conservation depends largely on the treatment of boundary conditions (Lynch, 1985, Kolar et al., 1994, Kolar et al., 1996). In particular, global mass is not preserved when the continuity equation is not explicitly included in the treatment of boundary conditions (Lynch, 1985). Approaches to avoid these global errors include discarding the momentum equation normal to the boundary, rather than the continuity equation (Lynch, 1985), or introducing an additional unknown rather than discarding an equation (Kolar et al., 1996). Non-linear processes have also been suggested to generate local mass errors even when global mass is conserved (Kolar et al., 1994).

The present paper focuses specifically on local mass conservation issues. In an earlier work (Fortunato, 1996) we observed that strong local mass errors could be generated internally to the domain, in a simple one-dimensional system. Those errors appear unrelated to initial and boundary conditions and weakly related to non-linearities. We now seek to understand the extent of the problem and to identify the specific generation mechanisms for such local errors. In particular, we will show that, in both one-dimensional and two-dimensional domains: a) significant local mass errors may occur even when global mass is preserved; and b) sharp topological changes (bathymetric gradients, complex boundary topology) are primarily responsible for such local mass errors.

Our present results also suggest that grid refinement may be ineffective in addressing local mass errors.

4.2 Experiment set-up

The 2D analysis was performed on the Tagus estuary, Portugal (Figure 4.1a), whose complex geometry and bathymetry generate strong non-linear processes (Fortunato et al., 1997). Tidal simulations were computed with three two-dimensional, depth-averaged models, which are representative of wave-equation formulations, both in the frequency (TIDE2D, Walters, 1987) and in the time domains (ADCIRC, version 26.7 -

Luettich et al., 1991), and primitive equation formulations in the frequency domain (TEANL, Westerink et al., 1988).

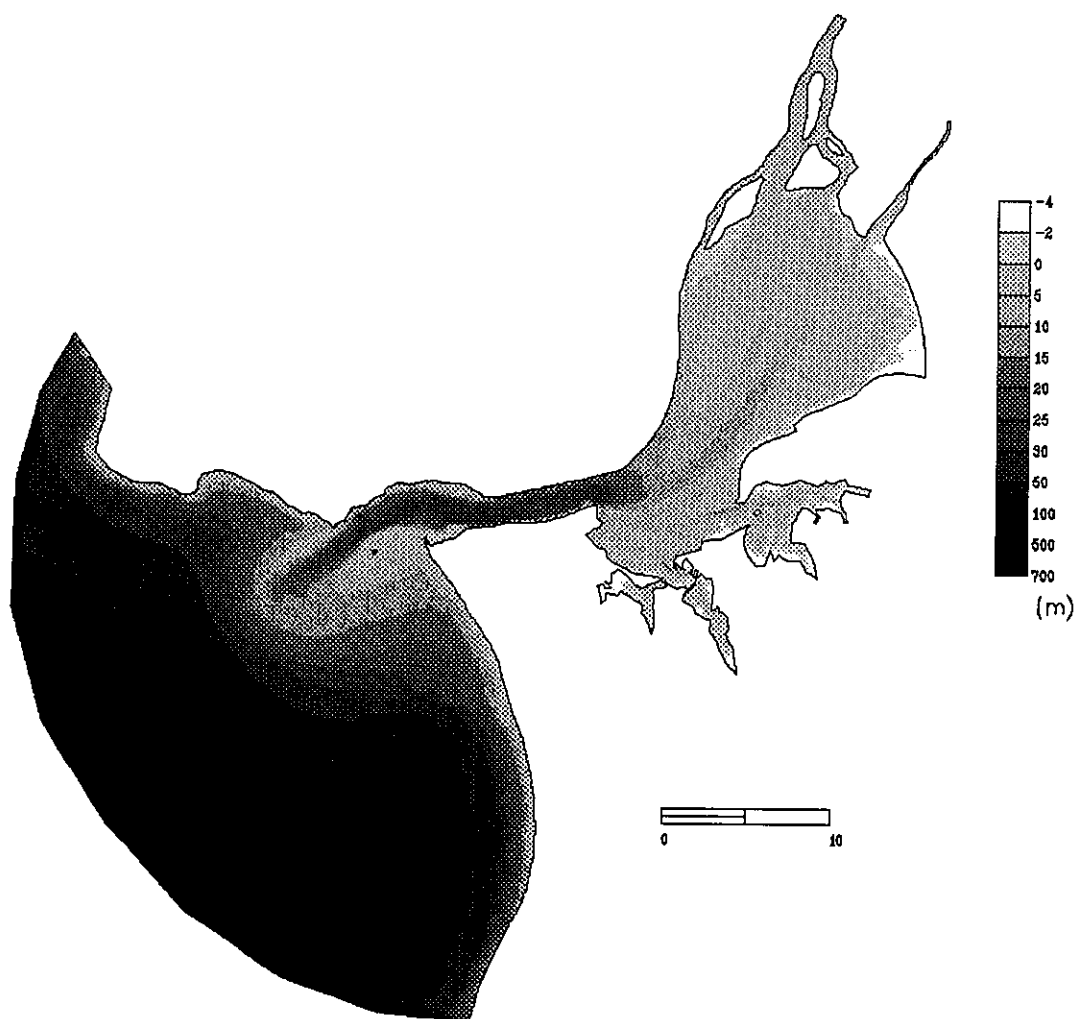


Figure 4.1 a) Tagus estuary: bathymetry.

The 2D analysis of local mass error generation was performed using the computational grid from Figure 4.1b. For the convergence analysis, the computational domain was restricted to the mouth area (Figure 4.1b). Except where otherwise noted, ADCIRC simulations included all non-linear terms, and used a diffusion coefficient and a wave equation coefficient of $10 \text{ m}^2/\text{s}$ and 0.0025 s^{-1} , respectively (Fortunato et al., 1997). Results were harmonically analyzed for the eleven frequencies used in TIDE2D and TEANL. Since

TIDE2D and TEANL do not have horizontal diffusion terms, they could not handle advection in this system.

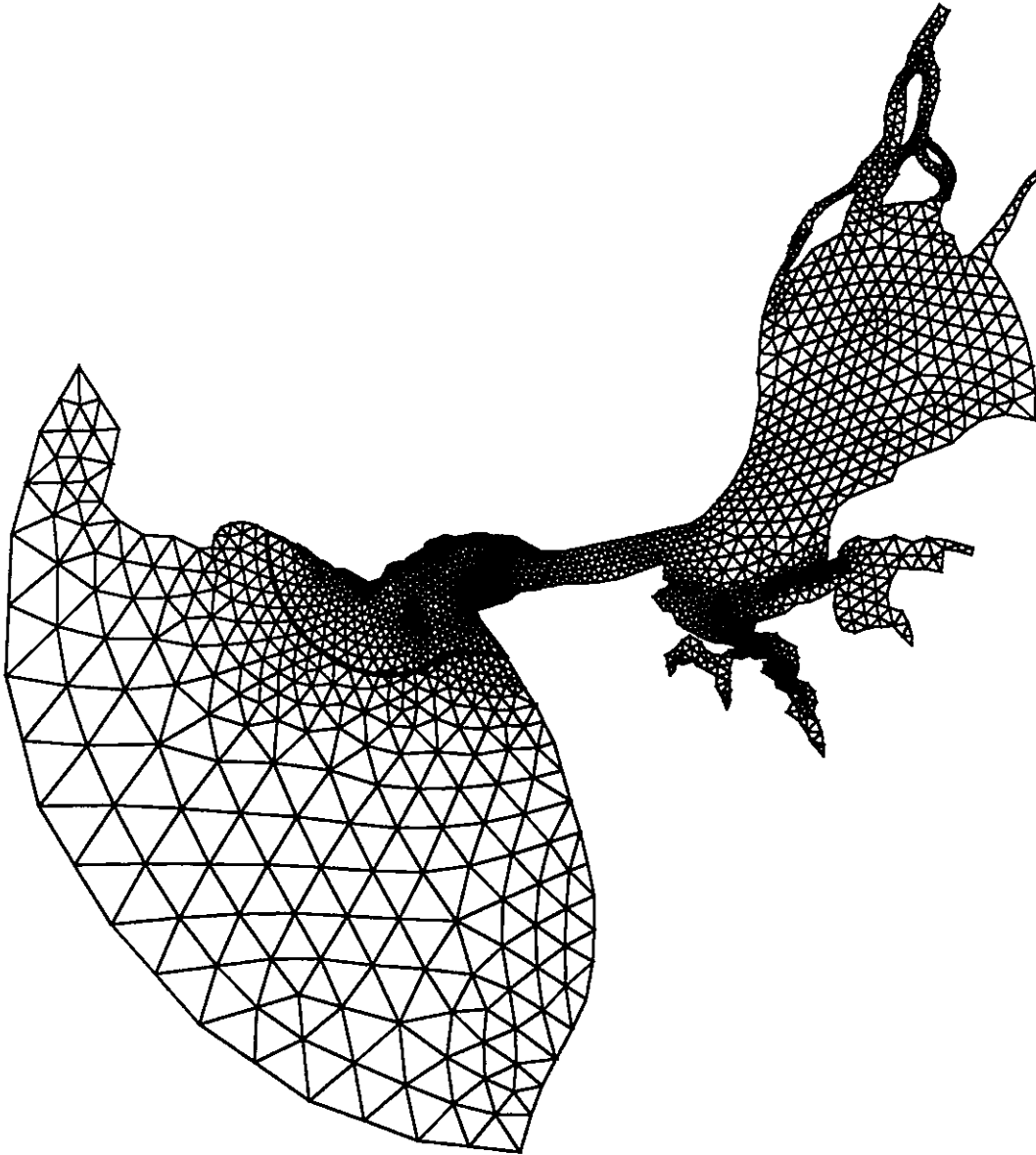


Figure 4.1 b) Computational grids: whole grid for source analysis; grid limited by thick line for convergence analysis.

Local mass errors between consecutive time steps were computed following Kolar et al. (1994), adapted for local conservation over individual elements. We start by integrating the continuity equation in space and time:

$$\int_{t_k}^{t_{k+1}} \int_{\Omega_e} \left[\frac{\partial \eta}{\partial t} + \nabla(Hv) \right] d\Omega_e dt = 0 \quad (4.1)$$

The first term in equation (4.1) is integrated in time and the divergence theorem is applied to the second term. Elemental mass errors (m_e), scaled by the elemental volume at rest (V_e), are defined as:

$$m_e = \left\{ \int_{\Omega_e} (\eta_{t_{k+1}} - \eta_{t_k}) d\Omega_e + \int_{t_k}^{t_{k+1}} \left(\int_{\partial\Omega_e} Hv \cdot \mathbf{n} d(\partial\Omega_e) \right) dt \right\} / (V_e \Delta t) \quad (4.2)$$

where \mathbf{v} are the velocities, \mathbf{n} is the unit outward normal, and $\eta_{t_{k+1}}$ and η_{t_k} are the elevations at time t_{k+1} and t_k , respectively. A small time step ($\Delta t = 1$ min) was selected to accurately represent the time variability of the mass errors. Evaluating the integrals in (4.2) exactly, leads to:

$$m_e = \left\{ [\bar{\eta}_{t_{k+1}} - \bar{\eta}_{t_k}]_e A_e + \sum_{e_b=1}^3 \frac{w_{e_b}}{6} [2H_1 v_{n1} + H_1 v_{n2} + H_2 v_{n1} + 2H_2 v_{n2}] \right\} / (V_e \Delta t) \quad (4.3)$$

where A_e is the elemental area, w_{e_b} is the length of each side of element e , $v_n = \mathbf{v} \cdot \mathbf{n}$ and the subscripts 1 and 2 refer to the nodes in side e_b , and $\bar{\eta}_{t_{k+1}}$ and $\bar{\eta}_{t_k}$ are the element-averaged elevations. Results were then integrated for each node as:

$$m_i = \left[\sum_{e=1}^{ne} m_e \right] / (ne) \quad (4.4)$$

where ne is the number of elements that share node i .

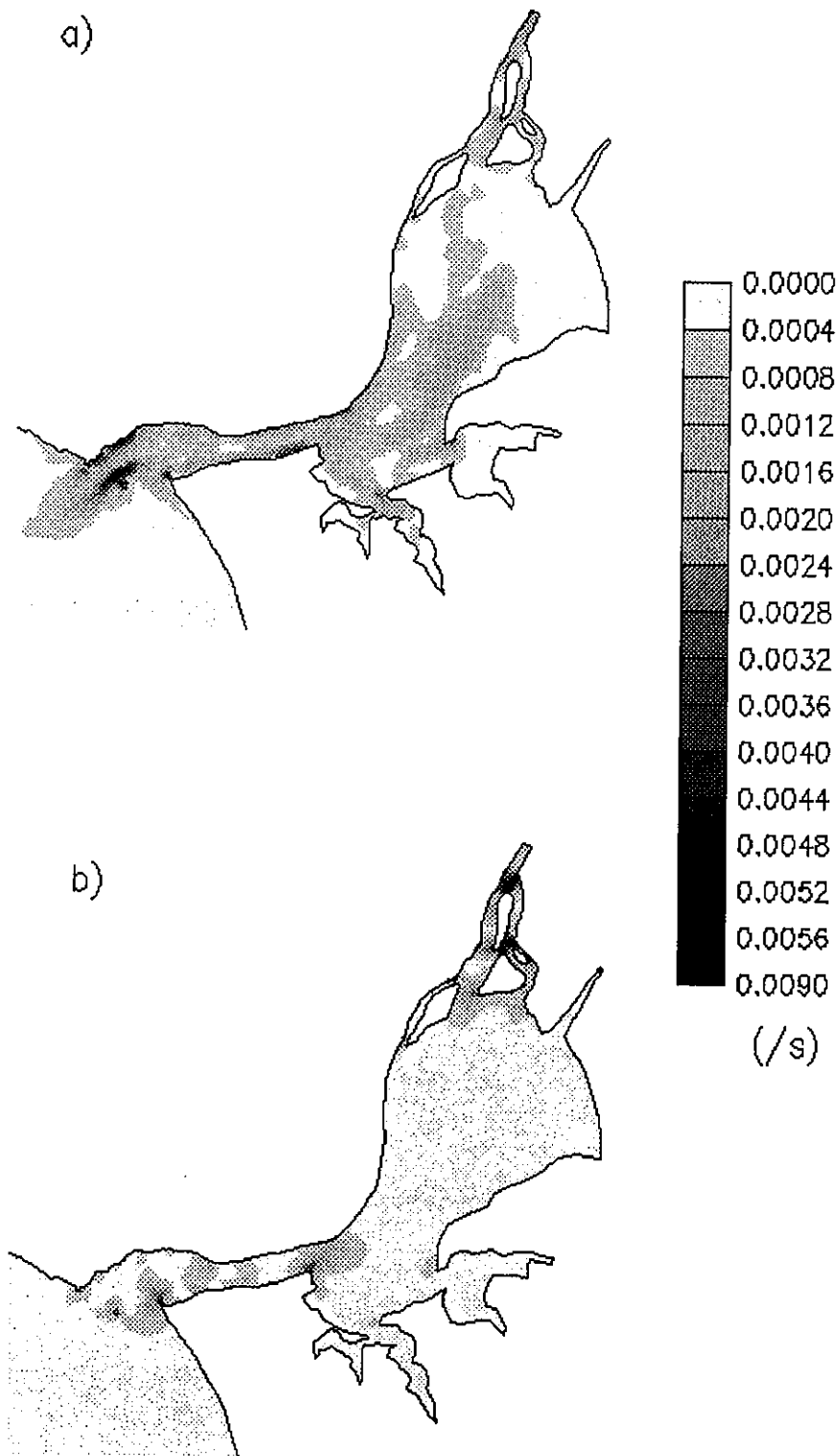


Figure 4.2 Maximum local mass errors for ADCIRC using a fully non-linear run: a) real bathymetry. b) flat bathymetry of 10m.

Statistics of nodal mass errors were then used to generate maps of local mass errors (Figure 4.2) and cumulative nodal percentages (Figure 4.3).

The two-dimensional analysis was complemented by a simple geometry test (Fortunato, 1996), using a one-dimensional model (RITA_{2v}, Fortunato, 1996). A constant elevation of 0.1 m was imposed at the left boundary (Figure 4.4) and mass errors were defined as deviations from the flow at that boundary.

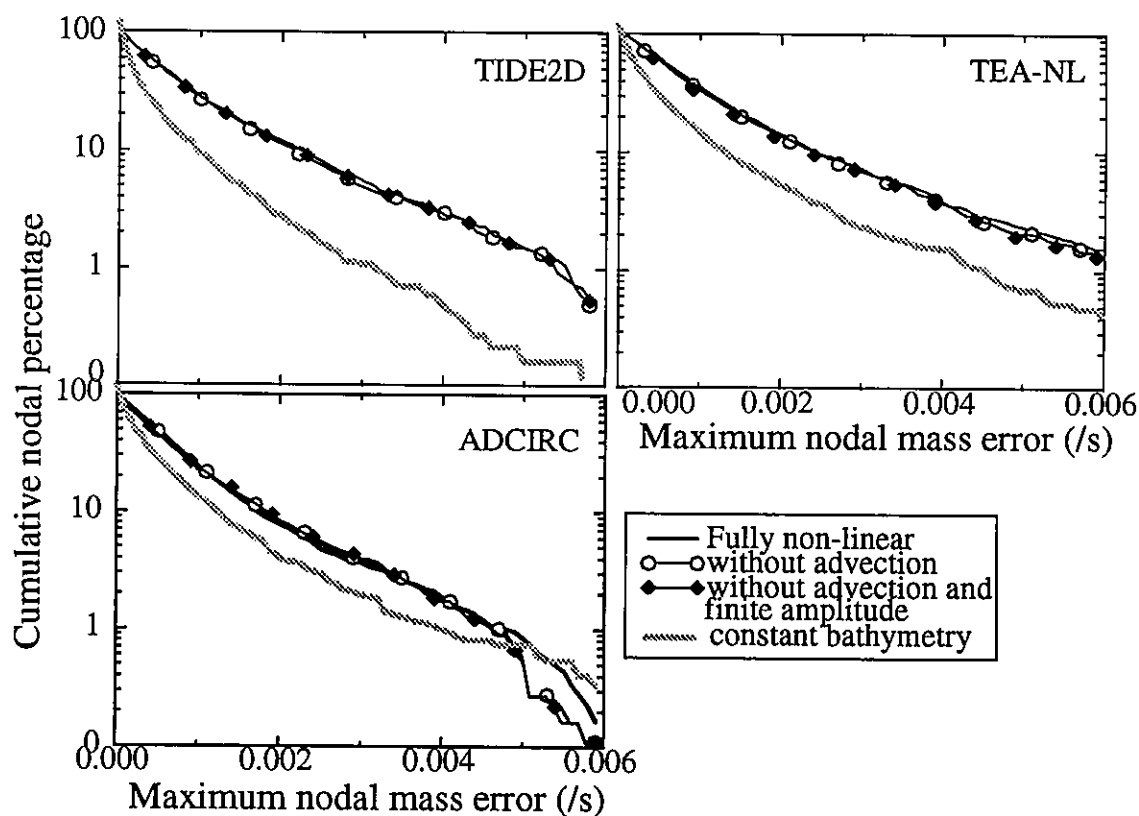


Figure 4.3 Influence of non-linear terms and bathymetry on the maximum local mass errors for the 2D models: cumulative nodal percentages, which identify, for a specific value of local mass error m_i , the percentage of nodes that have an error equal to or larger than m_i .

4.3 Sources of local mass errors

Several numerical tests were carried out in the Tagus estuary, starting with a fully non-linear simulation for ADCIRC and non-linear simulations without advective acceleration terms for the other two models (reference runs). Very large local mass errors, with maxima of $0.7\% \text{ s}^{-1}$, appear in all models. The patterns of spatial variability of the statistics of local mass errors are similar for all models, with largest errors occurring near areas of strong bathymetric gradients, or close to complex boundaries (illustrated in Figure 4.2, for ADCIRC). These results confirm that important mass errors can be generated inside the domain, and suggest that mass error generation in FE models is not related to a specific type of formulation. Global mass preservation is obtained for all models.

The importance of non-linearities on local mass generation was investigated by neglecting one non-linear term at a time in the reference runs: first advection (only for ADCIRC) and then finite amplitude (for all models). Mass errors were only slightly reduced (Figure 4.3), showing that non-linear terms are not the main source of local mass errors.

Concentration of mass errors around complex boundaries and steep bathymetric gradients suggested that geometric changes are an important source of local mass errors. To assess the influence of the bathymetric gradients on mass balance, we repeated the reference runs using a constant depth of 10m in the whole grid. A mass error reduction on the order of 50% was achieved for all models (Figures 4.2b and 4.3). Furthermore, mass errors became confined to areas of complex geometry (Figure 4.2b). Our results also show that mass errors generated at the boundaries were propagated into the domain, but were quickly dissipated. This is consistent with the findings of Kolar et al. (1994).

A search for a direct correlation between bottom slopes and statistics of mass errors in each element proved inconclusive, possibly due to the combined effect of bathymetry and lateral constrains. We thus simplified our analysis to the one-dimensional test from Fortunato (1996) (Figure 4.4), to examine the generation of mass errors due to bathymetric changes only. This test represents a permanent flow over a schematic conti-

mental slope, with constant width. The effect of abrupt geometric changes was elucidated by varying the bathymetric slopes, revealing an almost linear relationship between local mass errors and gradients of bathymetry (Figure 4.4c). Similar patterns were obtained by changing abruptly the width of a channel, while keeping the bathymetry constant (results not shown). Therefore, geometric variability is an important source of mass errors in FE flow simulations.

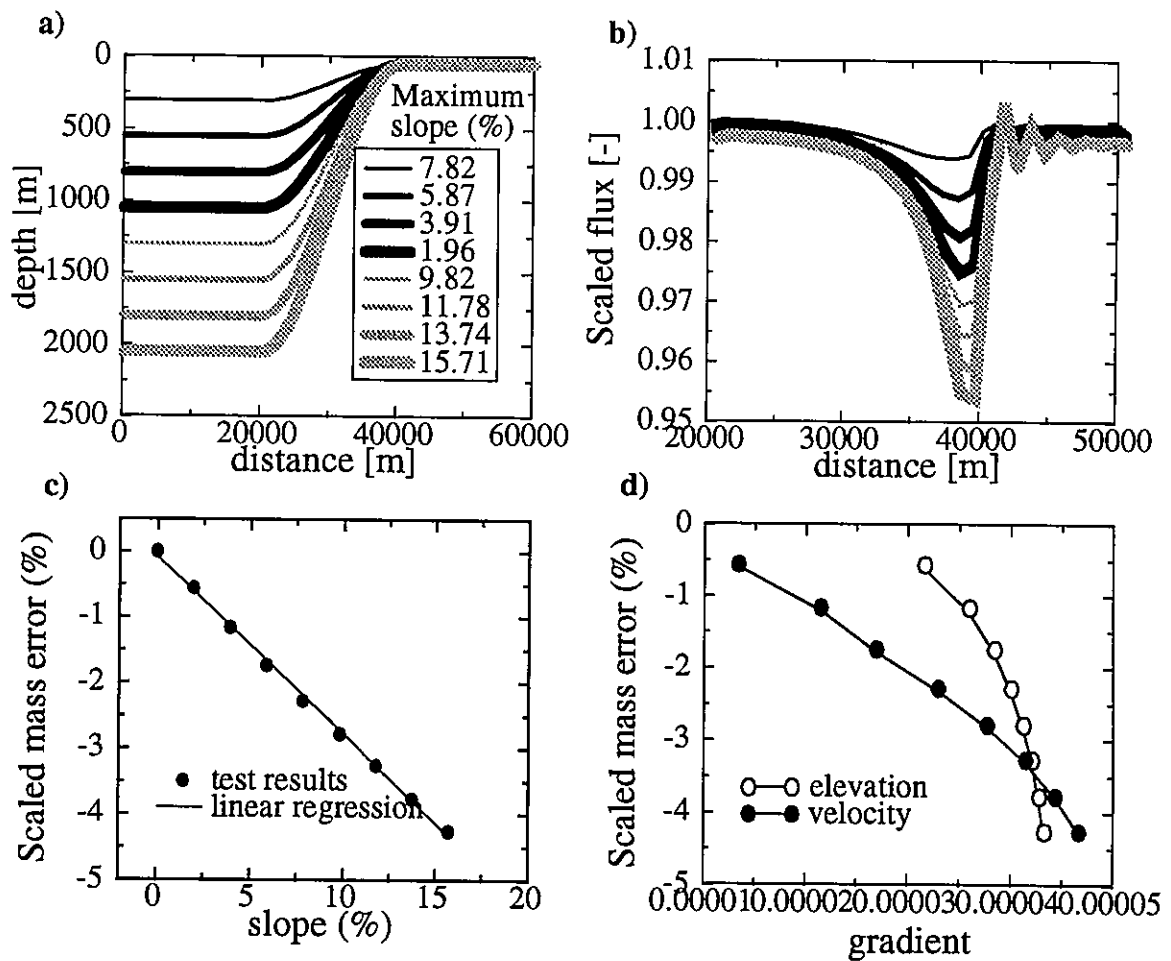


Figure 4.4 Influence of bathymetric slope on local mass errors: a) bathymetric profiles for the test cases; b) flux in the steepest element divided by the flux at the left boundary; c) scaled mass error (defined as the scaled flux minus 1, multiplied by 100) and linear regression (correlation coefficient of 0.999) versus the largest bathymetric slope in each bathymetric profile; d) scaled mass error versus the maximum elevation and velocity gradients.

Noting that a strong geometric change leads to an abrupt spatial variation in either elevation or velocity, and the strong correlation between the spatial gradients of both elevation and velocity and scaled mass errors (Figure 4.4d), our analysis fuels speculation that the generation of local mass errors may result from abrupt spatial variations in either elevation or velocity. Hence, important mass errors could conceivably appear also when sharp flow gradients develop without mediation of topological changes. Of particular interest would be the case of interfaces (e.g. in stratified flows or in the bottom boundary layer).

4.4 Effect of grid refinement on mass conservation

Since all models showed similar mass errors, we tested grid refinement as a model-independent solution for local mass conservation. The analysis was conducted for the mouth area of the Tagus estuary (Figure 4.1.b), using three grid levels for TIDE2D and two-level verification with TEA-NL and ADCIRC, and for the 1D test, using three grid levels.

For the 2D analysis, cumulative nodal percentages show that refining the grid does not reduce statistics of local mass errors: maximum nodal mass errors are practically unchanged for all models (Figure 4.5a). However, mass error convergence was obtained in the 1D test (Figure 4.5b). These results suggest that non-scaled mass errors depend on Δx^2 , which is consistent with the truncation error analysis for the momentum equation (Hagen et al., 1997). Therefore, mass errors in two-dimensions do not converge because they are scaled by the element area. In the 1D test, mass errors are scaled by the element length, and thus converge with Δx .

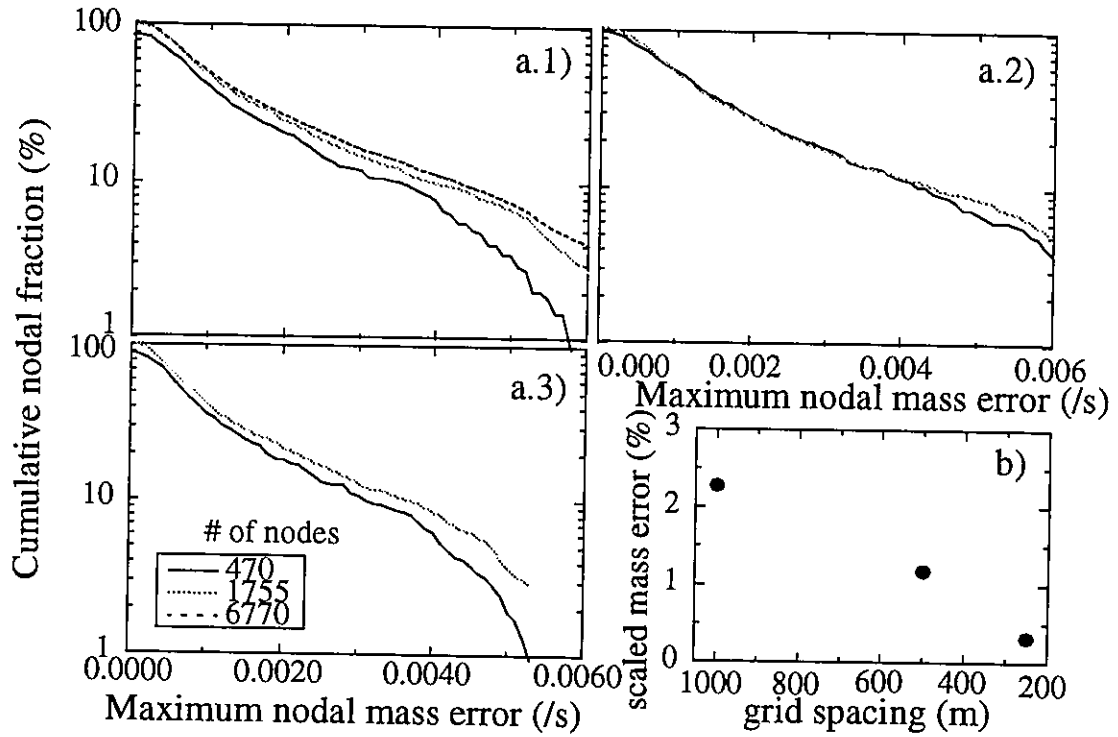


Figure 4.5 Influence of grid refinement on local mass conservation. a) cumulative nodal percentages: 1) TIDE2D; 2) TEA-NL; 3) ADCIRC. b) scaled mass errors for the 1D runs.

4.5 Conclusions

We showed that, for a range of FE shallow water models:

- important local mass errors are generated when both wave-equation and primitive equations formulations are used, even when global mass is preserved;
- local mass balance depends heavily on geometric changes such as bathymetric gradients and domain complexity.
- non-linear terms are not the dominant source of local mass errors in a system with complex geometry and bathymetry;

Results also indicated that grid refinement may not be effective as a mechanism to reduce local mass errors in 2D models.

References

- Fortunato, A.B., 1996. *Three-Dimensional Modeling of Coastal Flows Using Unstructured Grids*, Ph.D. Dissertation, Oregon Graduate Institute of Science and Technology, Oregon.
- Fortunato, A.B., A.M. Baptista and R.A. Luettich, Jr., 1997. A Three-Dimensional Model of Tidal Currents at the Mouth of the Tagus Estuary (Portugal), *Continental Shelf Research* (in press).
- Hagen, S.C., J.J. Westerink and R.L. Kolar, 1997. Finite Element Grids Based on a Localized Truncation Error Analysis, *International Journal for Numerical Methods in Fluids*, (in press).
- Kolar, R.L., J.J. Westerink, M.E. Cantekin and C.A. Blain, 1994. Aspects of Nonlinear Simulations Using Shallow Water Models Based on the Wave Continuity Equation, *Computers and Fluids*, 23(3): 523-538.
- Kolar, R.L., W.G. Gray and J.J. Westerink, 1996. Boundary Conditions in Shallow Water Models - an Alternative Implementation for Finite Element Codes, *International Journal for Numerical Methods in Fluids*, 22(7): 603-618.
- Luettich, Jr., R.A., J.J. Westerink and N.W. Sheffner, 1991. *ADCIRC: An Advanced Three-Dimensional Circulation Model for Shelves, Coasts and Estuaries. Report 1: Theory and Methodology of ADCIRC-2DDI and ADCIRC-3DL*. Department of the Army, US Army Corps of Engineers, Washington, D.C.
- Lynch, D.R., 1985. Mass Balance in Shallow Water Simulations, *Communications in Applied Numerical Methods*, 1(4): 153-159.
- Oliveira, A. and A.M. Baptista, 1997. On the Role of Tracking on Eulerian-Lagrangian Solutions of the Transport Equation, *Advances in Water Resources*, (in press).
- Walters, R.A., 1987. A Model for Tides and Currents in the English Channel and Southern North Sea, *Advances in Water Resources*, 10(3): 138-148.
- Westerink, J.J., J.J. Connor and K.D. Stolzenbach, 1988. A Frequency-Time Domain Finite Element Model for Tidal Circulation Based on the Least-Squares Harmonic Analysis Method, *International Journal for Numerical Methods in Fluids*, 8(7): 813-843.

Westerink, J.J., R.A. Luettich, Jr. and R.L. Kolar, 1996. Advances in Finite Element Modeling of Coastal Ocean Hydrodynamics, in *Proceedings of the 11th Conference on Computational Methods in Water Resources*, A.A. Aldama et al. (editors), Computational Mechanics Publications, 313-322.

CHAPTER 5

Mass Conservation of Eulerian-Lagrangian Transport Simulations in Estuaries and Coasts

Abstract

We investigate the effect of non-conservative flow fields and integration errors on the mass conservation properties of Eulerian-Lagrangian methods (ELMs) for the two-dimensional, depth-averaged transport equation. The analysis is performed with two simple tests and a complex estuary, using both control volume finite element and finite element ELM methods. Experiments show that both small flow mass errors and errors in the evaluation of the integrals at the feet of the characteristic lines can generate important mass errors in ELM transport simulations. The combination of quadrature integration and finite volume concepts leads to better mass conservation than the more traditional interpolation finite-element ELMs.

While the effect of integration errors can be removed with grid refinement, mass errors due to non-conservative flows persist in spite of the use of finite volumes, accurate integration at the feet of the characteristic lines and grid refinement. Conservative formulations improve drastically mass conservation in simple tests, but at the expense of the overall accuracy. Moreover, compensation for flow mass errors generates spatial redistribution of mass which leads to oscillations and instabilities in presence of complex flows, thus discouraging the practical use of conservative formulations. Mass-conservative flow fields and careful grid refinement are therefore necessary for mass conservative Eulerian-

Lagrangian transport simulations in complex flows.

5.1 Introduction

The popularity of Eulerian-Lagrangian methods (Baptista et al., 1984, Sorek, 1988, Rasch and Williamson, 1990, Staniforth and Côté, 1991, DeGeorge and King, 1994, Binning, 1994, Wood et al., 1995) is mostly due to the adoption of customized techniques for different transport processes, which allows for the use of Courant numbers larger than one, and to the convenience of a fixed computational grid: typically advection is solved by the backward method of the characteristics, while diffusion is solved by finite elements, finite differences or finite volumes. Recent development of ELMs led to a multitude of methods with increased accuracy and theoretic unconditional stability (Celia et al., 1990, Yeh et al., 1992, Bentley and Pinder, 1992, Healy and Russell, 1993, Oliveira and Baptista, 1995).

In spite of the good performance of ELMs, mass conservation remains a concern both at global and local levels (Sorek, 1988, Roache, 1992, Healy and Russell, 1993, Binning, 1994, Oliveira and Baptista, 1997a). Mass conservation performance is seldom reported, but the available references suggest that the problem is severe (DeGeorge and King, 1994, Janin, 1995, Oliveira and Baptista, 1997a).

ELM mass errors result primarily from: 1) inaccurate tracking of the characteristic lines; 2) incorrect implementation of the boundary conditions; 3) evaluation of the integrals at the feet of the characteristic lines; and, 4) coupling between flow and transport (Baptista, 1987, Sorek, 1988, Russell, 1989, Celia et al., 1990, Healy and Russell, 1993, Oliveira and Baptista, 1997a). The effect of tracking errors can be eliminated with accuracy-controlled, adaptive tracking techniques that specify the tracking time step according to the complexity of the flow (Oliveira and Baptista, 1997a). Mass errors introduced by inaccurate implementation of boundary conditions are one of the drawbacks of ELMs relative to Eulerian methods. These errors were formally addressed by the Eulerian-Lagrangian Localized Adjoint Methods (ELLAMs - Russell, 1989, Celia et al., 1990), a

conceptually attractive, yet complex to implement, alternative to conventional ELM formulations. ELLAMs preserve mass in simple tests (Celia et al., 1990, Healy and Russell, 1993, Binning, 1994), but they can limit traditional ELM's flexibility in incorporating transformation processes with very different time scales. Indeed, by transporting the weighting function, rather than the concentration, along the characteristic lines, current ELLAM formulations address transformation terms through modifications in the weighting function (Zisman, 1990), which makes their application conceptually difficult to complex reactive problems.

The definition of the initial conditions for the diffusion equation can be an important source of accuracy and mass conservation errors (Sorek, 1988, Russell, 1989, Yeh et al., 1992, Oliveira and Baptista, 1995). This potential has motivated the recent development of many ELMs, which either replace conventional interpolation functions to define the concentration between feet of characteristic lines by integration methods (Yeh et al., 1992, Healy and Russell, 1993, Oliveira and Baptista, 1995), or resort to a combination of low- and high-order interpolation methods to improve mass conservation while taking also into account monotonicity (Priestley, 1993, Gravel and Staniforth, 1994). Integration ELMs explicitly recognize the discontinuities of the concentration gradients within the area limited by the feet of the characteristic lines, and define the initial conditions for the diffusion step using either quadrature (Healy and Russell, 1993, Oliveira and Baptista, 1995) or piecewise techniques (Yeh et al., 1992, Oliveira and Baptista, 1995). While both integration and low/high order interpolation ELMs present in general good properties of mass conservation for simple tests (Yeh et al., 1992, Healy and Russell, 1993, Priestley, 1993, Oliveira and Baptista, 1995), a systematic analysis of the importance of the evaluation of integrals at the feet of the characteristic lines on mass conservation has not been done yet.

The forcing of ELM transport simulations by non-conservative flow fields is perhaps the most important source of mass errors in coastal applications. Large flow mass errors are generated in presence of complex bathymetry and domain geometry (Chapter 4), and therefore important transport mass errors are to be expected. While it would be desirable to address mass conservation directly in the flow simulations, the use of grid

refinement has failed to eliminate local mass errors for a range of alternative finite element circulation models (Chapter 4).

Solutions for the effect of non-conservative flow fields generally involve using the conservative, rather than the non-conservative form of the transport equation, either by using space-time weighting functions (ELLAMs) or by including explicitly the flow continuity equation (Janin, 1995, Tang and Adams, 1996). However, ELLAMs based on backward tracking can only address part of the mass problem, since they cannot account for the deformation of the image of the tracked element at the feet of the characteristic lines (Binning, 1994), and the introduction of the continuity equation can bring additional accuracy problems (Janin, 1995, King and DeGeorge, 1996).

Recently, the success of the finite volume concepts in Eulerian models motivated their adoption in ELM models (Roache, 1992, Healy and Russell, 1993, Binning, 1994). Finite volumes enforce mass conservation locally in Eulerian models and allow for a simple accommodation of the boundary conditions (Patankar, 1980, McCormick, 1992). The combined use of ELM and finite volume concepts has been successfully applied in ELLAM models for structured grids (Healy and Russell, 1993, Binning, 1994). Finite Volume ELLAMs preserve mass in simple tests, even in the presence of tracking errors (Healy and Russell, 1993), but oscillations can appear because conservation is achieved by mass re-distribution in space. The combination of finite volume ELMs and unstructured grids (control volume finite element ELMs - CVFE-ELMs) appears thus as a conceptually attractive solution for mass balance in estuarine and coastal transport modeling.

In spite of the multitude of solutions, though, the influence of flow mass errors on ELM transport mass errors is still poorly understood. A few studies have been performed under very simple conditions (Janin, 1995, Tang and Adams, 1996), but the relationships between flow and transport mass errors and the generation of mass errors in complex, real systems have not been addressed yet.

In this paper, we analyze the influence of two major sources of ELM mass errors: the forcing of transport simulations by non-conservative flow fields and the inaccurate evaluation of integrals at the feet of the characteristic lines. Each problem is addressed

separately in simple tests, and relationships between the magnitude of the sources and mass errors are sought. We also analyze the ability of a combination of finite volumes and integration techniques, grid refinement and conservative formulations to eliminate ELM mass errors. Conclusions are then verified in a complex estuary with a realistic flow field.

For generality, the analysis is conducted using two different ELM models: VELA (Oliveira and Baptista, 1997b) and ELA (Baptista et al., 1984). VELA is a new model that combines finite volumes in a finite element framework, with quadrature integration techniques at the feet of the characteristic lines, and ELA is a quadratic-interpolation finite-element model. Although ELA is no longer state-of-the-art from a numerical analysis perspective, it still represents a practical ELM standard (Baptista et al., 1984, Dimou, 1992, Wood and Baptista, 1995, King and DeGeorge, 1996).

The paper is divided in 3 sections, besides this *Introduction*. *Model formulations* gives a brief description of the two models. *Analysis of Mass Conservation* is divided as follows: *Influence of the integrals at the feet of the characteristic lines* examines the impact of integration errors on mass and overall accuracy, using problem 5 of the Convection-Diffusion Forum (Baptista et al., 1995); *Influence of flow mass balance* examines the effect of forcing ELM transport simulation with non-conservative flow fields, using the Polar Quadrant Channel test (Lynch and Gray, 1978, Chen, 1989); and *Application to the Tagus estuary* verifies, for a complex system, the conclusions drawn in the previous, simpler, tests. *Conclusions* summarizes major findings and discusses their implications for estuarine transport modeling.

5.2 Model Formulations

We start with the conservative form of the two-dimensional, depth-averaged transport equation:

$$\frac{\partial}{\partial t}(cH) + \frac{\partial}{\partial x_i}(Hu_i c) = \frac{\partial}{\partial x_i} \left(D_{ij} H \frac{\partial c}{\partial x_j} \right) \quad (5.1)$$

where c is the concentration, t is time, x_i are the space coordinates, u_i is the velocity along direction i , D_{ij} is the diffusion tensor and H is the total depth (defined as the sum of the elevation, η , and the water depth, h).

Expanding the left hand side of equation (5.1) and dividing by H , we get:

$$\frac{D(c)}{Dt} + c \left(\frac{1}{H} \frac{D(H)}{Dt} + \frac{\partial}{\partial x_i} (u_i) \right) = \frac{1}{H} \frac{\partial}{\partial x_i} \left(D_{ij} H \frac{\partial c}{\partial x_j} \right) \quad (5.2)$$

where the second term in the *LHS* of (5.2) is the flow continuity equation multiplied by c/H . Distinct approaches are now used for each model.

5.2.1 Quadrature-Integration Control Volume Finite Element Eulerian-Lagrangian model (VELA)

Equation (5.2) is divided into three simpler equations:

$$u_i = \frac{dx_i}{dt} \quad (5.3)$$

$$\frac{D(c)}{Dt} = K_1 c \quad (5.4)$$

$$\frac{D(c)}{Dt} = K_2 c + \frac{1}{H} \frac{\partial}{\partial x_i} \left(D_{ij} H \frac{\partial c}{\partial x_j} \right) \quad (5.5)$$

Equation (5.3) is solved by the backward method of characteristics using an adaptive, embedded 4th order Runge-Kutta method (Press et al., 1992) and equation (5.4) is solved with an α -method along the characteristic lines. Equation (5.5) is solved by node-centered finite volumes (Healy and Russell, 1993), while using a finite element framework to define concentrations, depth and velocity within each element. For the continuity equation term, two approaches are used: a *mixed approach* where the first part is evaluated along the characteristic lines and the second part by an Eulerian method:

$$K_1 = -\frac{\partial}{\partial x_i}(u_i) \quad K_2 = -\frac{D(\ln H)}{Dt} \quad (5.6)$$

and a *Lagrangian approach* where the whole term is evaluated along the characteristic lines:

$$K_1 = -\frac{D(\ln H)}{Dt} - \frac{\partial}{\partial x_i}(u_i) \quad K_2 = 0 \quad (5.7)$$

Note that in equations (5.6) and (5.7) $\frac{D(\ln H)}{Dt}$ is used instead of $\frac{1}{H} \frac{D(H)}{Dt}$ to avoid an approximation of the $1/H$ factor along the characteristic lines.

Following Baptista et al. (1984), equations (5.4) and (5.5) are then discretized in time with an α -method:

$$c^{m+1} - c^m = \alpha(\Delta t') K_1^{m+1} c^{m+1} + (1-\alpha)(\Delta t') K_1^m c^m \quad (5.8)$$

$$\frac{c^{n+1} - c^\xi}{\Delta t} = \alpha \left[\frac{1}{\bar{H}} \frac{\partial}{\partial x_i} \left(D_{ij} H \frac{\partial c}{\partial x_j} \right) + K_2 c \right]^{n+1} + (1-\alpha) \left[\frac{1}{\bar{H}} \frac{\partial}{\partial x_i} \left(D_{ij} H \frac{\partial c}{\partial x_j} \right) + K_2 c \right]^\xi \quad (5.9)$$

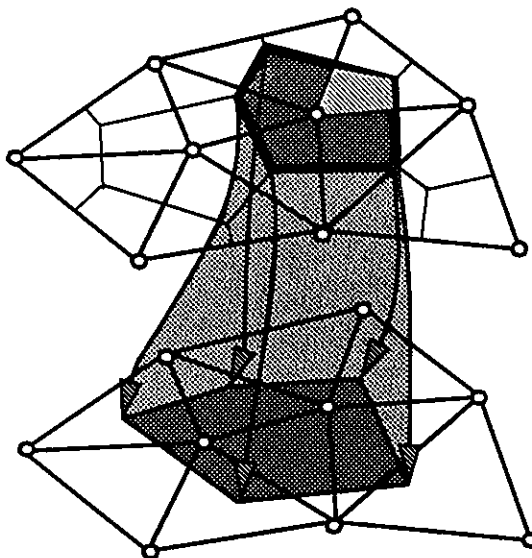
where ξ denotes the feet of the characteristic lines at time n , Δt is the time step between time instants n and $n+1$, and $m+1$ and m denote time instants between n and $n+1$, separated by the sub-time step $\Delta t'$. Integration of equation (5.9) over the control volume (defined as the space-time volume limited by the characteristic lines of the corners of the Voronoi polygon, or area of influence, of each node - Figure 5.1a) leads to:

$$\begin{aligned} \int_{\Omega_{cv}} c^{n+1} d\Omega_{cv} - \int_{\Omega_{cv}} c^\xi d\Omega_{cv} - \frac{\alpha \Delta t}{\bar{H}} \int_S \left(D_{ij} H \frac{\partial c}{\partial x_j} \right) \cdot \hat{n} \Big|^{n+1} dS + \alpha \Delta t \int_{\Omega_{cv}} K_1 c^{n+1} d\Omega_{cv} \\ - \frac{(1-\alpha) \Delta t}{\bar{H}} \int_S \left(D_{ij} H \frac{\partial c}{\partial x_j} \right) \cdot \hat{n} \Big|^\xi dS + (1-\alpha) \Delta t \int_{\Omega_{cv}} K_1 c^\xi d\Omega_{cv} = 0 \end{aligned} \quad (5.10)$$

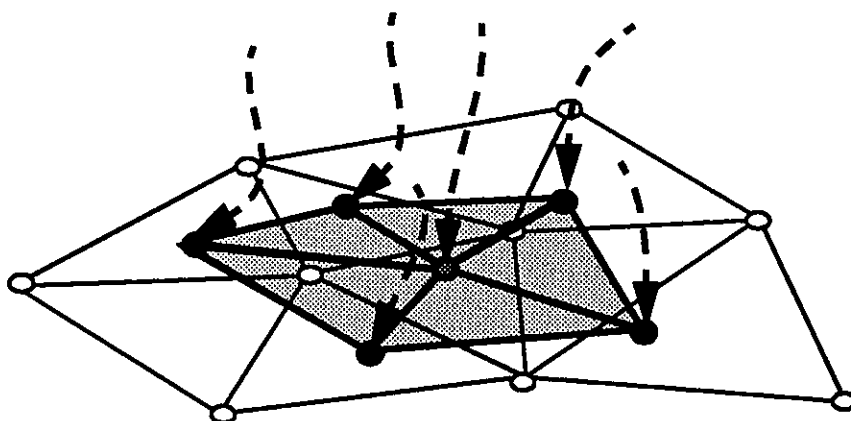
where Ω_{cv} is the control volume, \bar{H} is the average depth in the control volume, S is the

boundary of Ω_{cv} and \vec{n} is the outward unit normal on S . Concentrations and total depths are defined by linear shape functions in each element.

a)



b)



c)

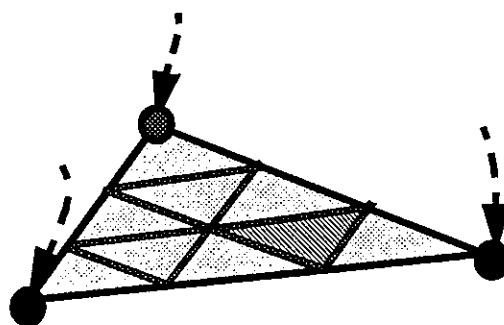


Figure 5.1 a) Definition of the control volume: shaded region. b) Triangles at the feet of the characteristic lines. c) Example of subdivision: 3 levels which leads to 9 integration sub-triangles.

The area integrals at time $n+1$ are evaluated analytically in each quadrangle (dashed area in Figure 5.1a). The area integrals at the feet of the characteristic lines are evaluated by subdivision quadrature (Oliveira and Baptista, 1997b): each triangle formed by the foot of the nodal characteristic line and two sequential corners of the tracked image of the Voronoi polygon (Figure 5.1b) is divided in a user-specified number of sub-triangles (Figure 5.1c). Concentrations and depths are interpolated at each sub-triangle corner and then assumed linear within each sub-triangle (Figure 5.1b). This quadrature integration method leads to very good accuracy provided enough subdivision is used, (Oliveira and Baptista, 1997b) without the computational demand associated with exact-integration methods (Yeh et al., 1992, Oliveira and Baptista, 1995). Unlike other quadrature methods (Oliveira and Baptista, 1995), the proposed approach is also unconditionally stable, at least within the limits of truncation error analysis (Oliveira and Baptista, 1997b).

The continuity equation term (equations (5.6) and (5.7)) requires the evaluation of spatial gradients of velocity. Since tracking sub-time steps vary for each characteristic line in a distinct way, this term is approximated by the gradients along the nodal characteristic line. A similar approach is used to evaluate the logarithm of H on equation (5.7). For the Lagrangian approach, time discretization of equation (5.4) between two tracking sub-time steps becomes:

$$\begin{aligned} \frac{c^{n+1} - c^\xi}{\Delta t} + (\alpha c^{n+1} + (1 - \alpha)c^\xi) \frac{(\ln H^{n+1} - \ln H^\xi)}{\Delta t} + \\ \alpha c \frac{\partial u_i}{\partial x_i} \Big|^{n+1} + (1 - \alpha)c \frac{\partial u_i}{\partial x_i} \Big|^\xi = 0 \end{aligned} \quad (5.11)$$

Integration of equation (5.11) in the control volume leads to:

$$\begin{aligned}
& \int_{\Omega_{cv}} c^{m+1} (d\Omega_{cv}) + \alpha (\overline{\ln H^{m+1}} - \overline{\ln H^m}) \int_{\Omega_{cv}} c^{m+1} d\Omega_{cv} + \alpha \overline{\frac{\partial u_i^{m+1}}{\partial x_i}} \int_{\Omega_{cv}} \Delta t c^{m+1} d\Omega_{cv} + \\
& - \int_{\Omega_{cv}} c^m d\Omega_{cv} + (1 - \alpha) \overline{\frac{\partial u_i^m}{\partial x_i}} \int_{\Omega_{cv}} \Delta t c^m d\Omega_{cv} + (1 - \alpha) (\overline{\ln H^{m+1}} - \overline{\ln H^m}) \int_{\Omega_{cv}} c^m d\Omega_{cv} = 0
\end{aligned} \tag{5.12}$$

where the overbar indicates quantities averaged over the control volume.

Combining equation (5.12) for all intermediate sub-time steps leads to:

$$c^{n+1} = c^\xi \prod_{i=1}^{n \text{ track steps}} \frac{\left(1 - (1 - \alpha) \left(\Delta t_i \overline{\left(\frac{\partial u_j}{\partial x_j} \right)^i} + (\ln H)^{i+1} - (\ln H)^i \right) \right)}{\left(1 + \alpha \left(\Delta t_i \overline{\left(\frac{\partial u_j}{\partial x_j} \right)^{i+1}} + (\ln H)^{i+1} - (\ln H)^i \right) \right)} \tag{5.13}$$

For consistency, K_1 is evaluated using the gradients of depth at the head and feet of the nodal characteristic line in the mixed approach.

5.2.2 Quadratic-Interpolation Finite Element Eulerian-Lagrangian model (ELA)

Since ELA and variants are described in detail elsewhere (Baptista et al., 1984, Wood, 1993), we simply summarize here its main characteristics. This model assumes that the flow continuity equation is satisfied and neglects the second term on the *LHS* of equation (5.2). This equation is then discretized in time as:

$$\frac{c^{n+1} - c^\xi}{\Delta t} = \alpha \left[\frac{1}{H} \frac{\partial}{\partial x_i} (D_{ij} H \frac{\partial c}{\partial x_j}) \right] \Bigg|^{n+1} + (1 - \alpha) \left[\frac{1}{H} \frac{\partial}{\partial x_i} (D_{ij} H \frac{\partial c}{\partial x_j}) \right] \Bigg|^\xi \tag{5.14}$$

Standard application of a weak Galerkin finite element formulation in equation (5.14) leads to:

$$\begin{aligned}
& \sum_{e=1} \left(\int_{\Omega_e} \psi c^{n+1} d\Omega_e - \alpha \Delta t \int_{\Omega_e} D_{ij} \frac{\partial \psi \partial c}{\partial x_i \partial x_j}^{n+1} d\Omega_e - \right. \\
& \quad \left. - (1 - \alpha) \Delta t \int_{\Omega_e} D_{ij} \frac{\partial \psi \partial c}{\partial x_i \partial x_j}^{\xi} d\Omega_e - \int_{\Omega_e} \psi c^{\xi} d\Omega_e - \right. \\
& \quad \left. - \int_{\Omega_e} \psi \frac{\partial c}{\partial x_j}^{\xi} \left(\alpha \Delta t \left(\frac{D_{ij} \partial H}{H \partial x_i} \right)^{n+1} + (1 - \alpha) \Delta t \left(\frac{D_{ij} \partial H}{H \partial x_i} \right)^{\xi} \right) d\Omega_e \right) + BT = 0
\end{aligned} \tag{5.15}$$

where ψ are the weighting functions and BT represent the boundary terms. The domain is then discretized using quadratic elements. The evaluation of the integrals in ξ is based on quadratic interpolation of the concentrations at the feet of the characteristic lines and on quadratic shape functions to define the concentration within the tracked image of each element. The tracking of the characteristic lines is performed with a step-doubling, adaptive, 5th order Runge-Kutta method (Baptista et al., 1984).

5.3 Analysis of Mass Conservation

The purpose of this section is two-fold: to analyze the influence of the evaluation of the integrals at the feet of the characteristic lines and non-conservative flow fields on ELM transport mass balance; and to search for methodologies to achieve mass conservation. We start with two simple tests chosen to address each source of mass errors separately. Test conditions are defined to minimize the presence of other sources of mass errors: domains are considered large enough to prevent open boundary effects, and tracking errors are minimized with a stringent closure error of 10^{-3} m. Results are then confirmed on a real system with complex flow field, geometry and bathymetry, where multiple sources of mass errors are present.

Three levels of grid refinement are used for each test and for both models. Each grid level is obtained from the previous by dividing each element by four and interpolating both the flow field and the concentration initial conditions from the coarsest grid. To avoid ambiguous comparisons of CPU times, we compare results between the two models for an equal number of nodes or elements.

Since sources and sinks are not considered in our analysis, and domains are large enough to prevent any mass from leaving or entering through open boundaries, mass ratios are computed as the mass in the model at each time step scaled by the initial mass and absolute mass errors are computed as the absolute difference between the initial mass and the mass in the model at each time step, also scaled by the initial mass.

5.3.1 Influence of integration errors at the feet of the characteristic lines

We chose problem #5 from the Convection-Diffusion forum (CDF5, Baptista et al., 1995), which represents the convection of concentration-hills within closed streamlines (Figure 5.2), to analyze the effect of integration errors on mass conservation. Although an analytical solution is not available for the concentrations, CDF5 is a stringent test due to its complex forcing flow field (Figure 5.2). Since the flow field is strictly conservative, boundary effects negligible, and tracking very accurate, the evaluation of the integrals at the feet of the characteristic lines is the primary source of mass errors.

Three regular grids are used in the simulations, with the same number of nodes for the two models, starting at a nodal spacing of 100m. Open boundary conditions were specified as zero concentration and depth was set to 10 m. Details of the simulations are summarized in Table 5.1.

CDF5's complex forcing flow field leads to significant stretching of the concentration plume (Figure 5.3), increasing the concentration gradients over time: thus, increasing mass errors due to the integration at the feet of the characteristic lines are to be expected. Mass errors are rather large for ELA, in particular for the coarser grid (~20%), while VELA's mass errors are quite small (Figure 5.4). Refining the grid improves mass conservation considerably: maximum absolute mass errors are reduced from 0.13% to 0.05% for VELA and from 20% to 2.2% for ELA in a single level of refinement (i.e., approximately four times more nodes). For the finest grids, differences between methods are practically inexistent (Figure 5.4).

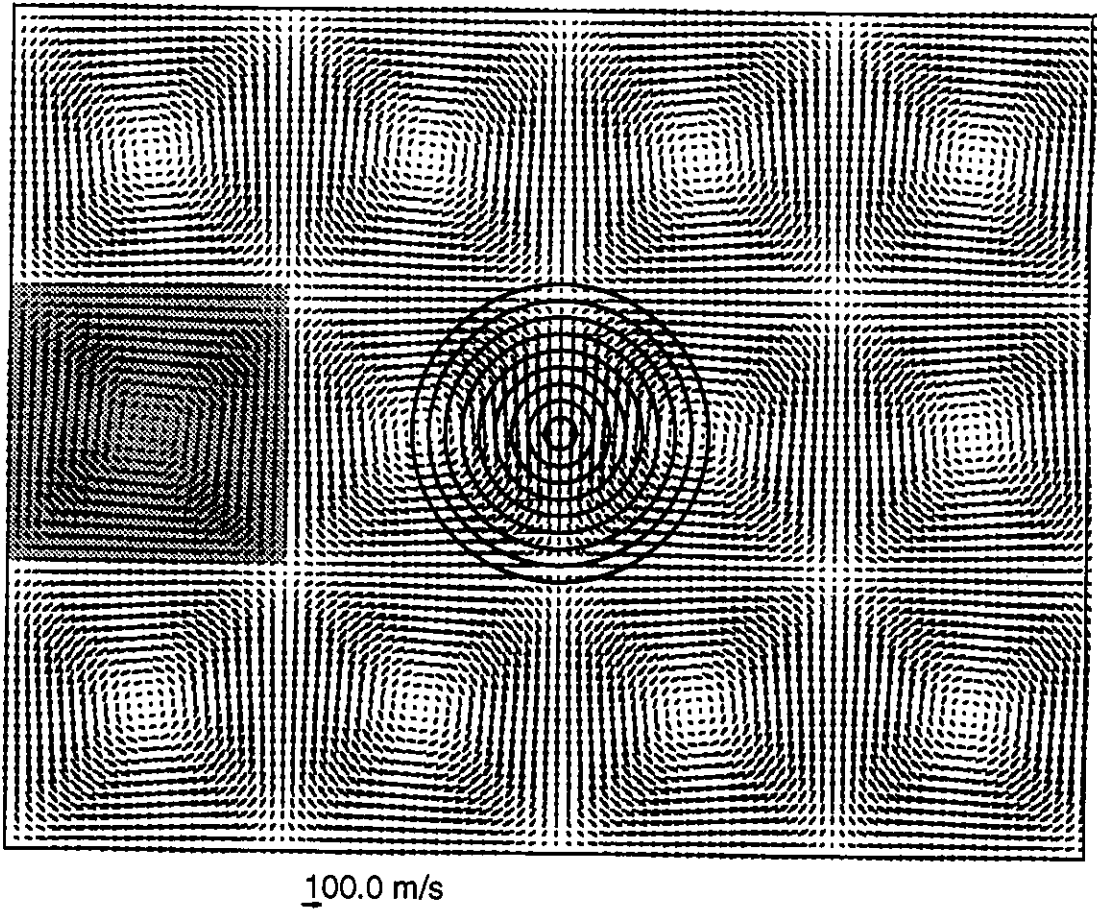


Figure 5.2 CDF5: Velocity field and concentration initial conditions (maximum concentration of 1). The shaded area indicates a flow cell.

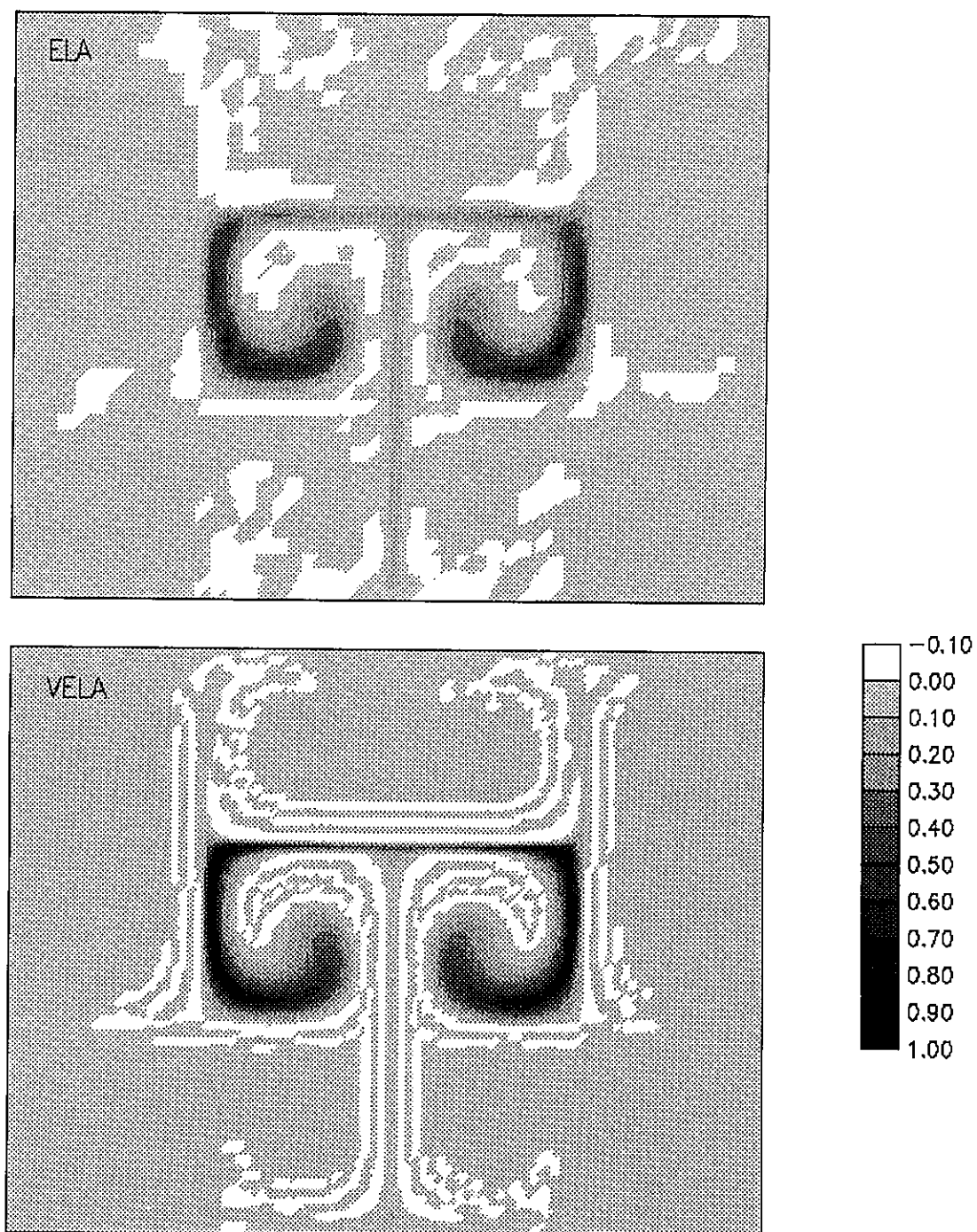


Figure 5.3 CDF5: Concentration distributions after 9 time steps for ELA and VELA with 7623 nodes (coarsest grid).

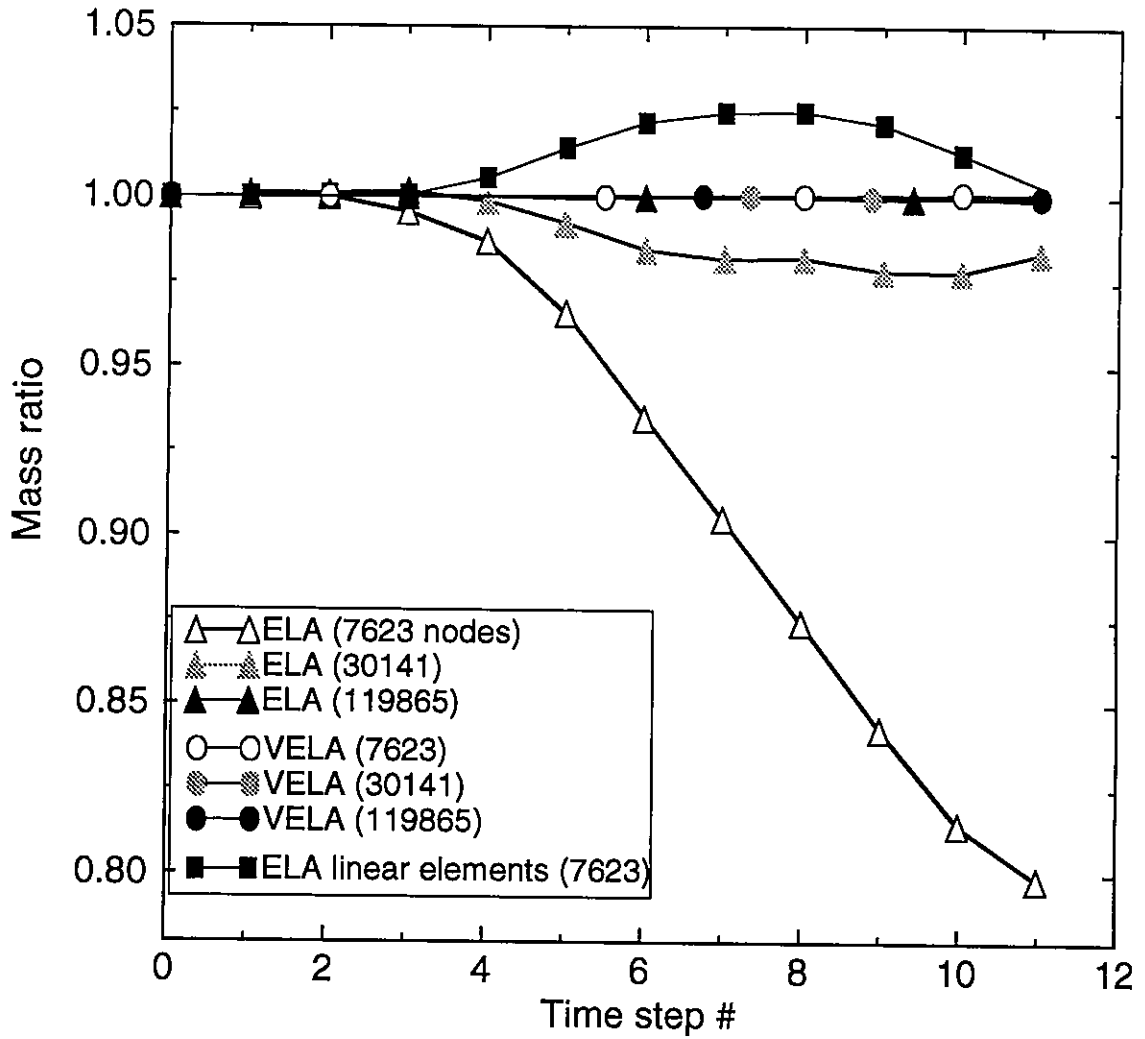


Figure 5.4 CDF5: time series of mass ratios (mass in the model over the initial mass) for VELA and ELA, for several grid refinements.

Table 5.1 Tests parameters

Test	CDForum 5	Polar Quadr.	Tagus estuary
initial time (s)	0	0	0
time step (s)	6	900	3600
number of time steps	12	100	48 (mouth) 72 (upstream)
standard deviation (m)	-	5000	1500 (mouth), 1000 (upstream)
maximum concentration [-]	1, 0.75, 0.5, 0.25	1	1
base radius (m)	0.15	-	-
Forcing wave amplitude (m)	-	0.1, 0.5, 1, 2	(see text)
number of nodes for ELA	7623, 30141, 119865	3569, 14025, 55601	6649, 25610, 100456
number of nodes for VELA	7623, 30141, 119865	924, 3569, 14025	1784, 6649, 25610

To provide a general guidance on the refinement level necessary for accurate results, we now seek a relationship between grid resolution and absolute mass errors. Comparison of mass error statistics for the several grid levels shows quasi-linear correlations on a log-log scale between the nodal spacing scaled by the size of each flow cell (taken as a measure of grid refinement for a specific flow complexity, Figure 5.2) and the maximum absolute mass errors for both models (Figure 5.5). Increasing grid refinement has distinct effects on VELA and ELA, since regression slopes on Figure 5.5 are quite different (4.0 for ELA and 1.5 for VELA), but convergence rates are still quite large for both models. Increasing grid refinement appears thus to be an attractive solution to avoid this source of mass errors since a small increase in grid refinement results in a large reduction in mass errors.

The large mass error difference between ELA and VELA for the coarser grids is largely justified by the different nature of their elements: ELA uses quadratic elements, while VELA is based on linear elements. Differences in corner and middle nodes' trunca-

tion errors generates a non-linear mechanism of energy transfer to frequencies that cannot be resolved by the computational grid (Baptista, 1987). The energy associated with these Fourier components is then folded to the zero-frequency, generating mass errors. As we increase grid refinement, differences in truncation errors are reduced, leading to an overall mass improvement. Formulations based on linear elements, hence, with a single type of nodes, do not have the potential for these errors.

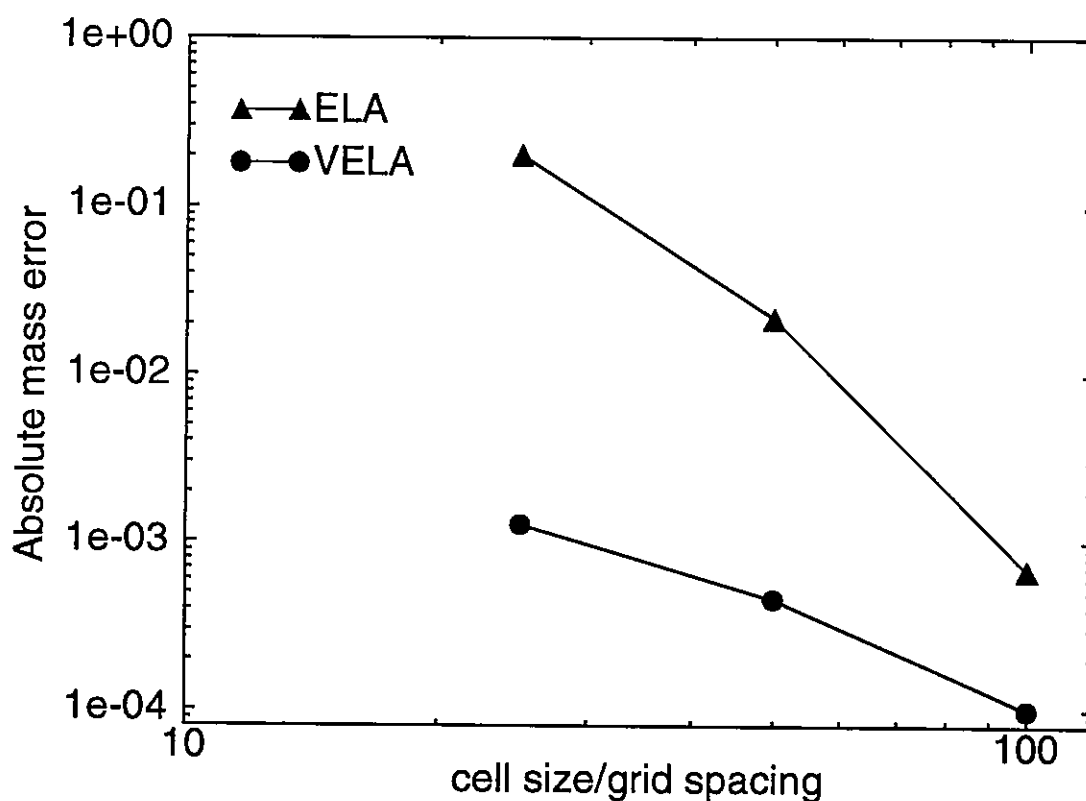


Figure 5.5 CDF5: correlation between cell size divided by Δx and maximum absolute mass errors.

Mass errors should also be smaller for finite volume than for finite element frameworks. Indeed, finite volumes tend to preserve the quantity integrated in the control volume, and for constant depth, mass coincides with the integral of the concentration, making equation (5.10) a statement of mass conservation. To compare effectively the performances of finite element and finite volume-based formulations, we avoided errors due to quadratic interpolation by using a linear interpolation finite element method on the reference run. Results (Figure 5.4) show that finite volume formulations preserve mass much

better than those based on finite elements: the linear interpolation FE-ELM leads to a maximum mass error which is an order of magnitude larger than VELA's. Comparison of mass ratios for the linear and quadratic finite element methods further confirms the effect of the non-linear transfer of energy to unresolved frequencies due to the two type of nodes on quadratic formulations: maximum errors for ELA are an order of magnitude larger than those for the linear interpolation method.

The number of subdivision levels on VELA appears to have a relatively minor impact on mass conservation. We repeated the coarsest grid simulation with 1, 2, and 4 subdivisions, and mass errors are still very small, though larger than with 8 subdivisions (Figure 5.6a). However, the number of subdivisions affects strongly the numerical damping of the model (Figure 5.6b), thus making a larger number of subdivisions necessary for accurate simulations.

Our analysis showed that the evaluation of the integrals at the feet of the characteristic lines can generate important mass errors in the presence of complex flow fields, but these errors can be effectively reduced with grid refinement. The use of careful grid refinement is thus recommended for coastal applications where complex geometry and bathymetry lead in general to complex flow fields.

5.3.2 Influence of flow mass balance

To examine the generation of ELM transport mass errors by non-conservative flow fields, we forced an artificial Gauss plume (Figure 5.7) with the analytical flow from the "Polar Quadrant channel with Reverse Quadratic bathymetry" test (Lynch and Gray, 1978, Chen, 1989). Since the analytical solution for the flow field is obtained for the linearized shallow water equations, the continuity equation is thus defined as:

$$\frac{\partial \eta}{\partial t} + \frac{\partial}{\partial x_i}(hu_i) = 0 \quad (5.16)$$

Since the non-linear continuity equation appears in the conservative transport equation (second term in the LHS of equation (5.2)), imposing equation (5.16) does not

fully eliminate the source-like term in (5.2). The remaining error (ϵ_{flow}) constitutes a controlled source of mass errors, dependent on the non-linearity of the flow field, which allows us to study the effect of flow mass errors in the transport equation:

$$\epsilon_{flow} = \frac{c}{H} \left(\frac{\partial}{\partial x_i} (\eta u_i) \right) \quad (5.17)$$

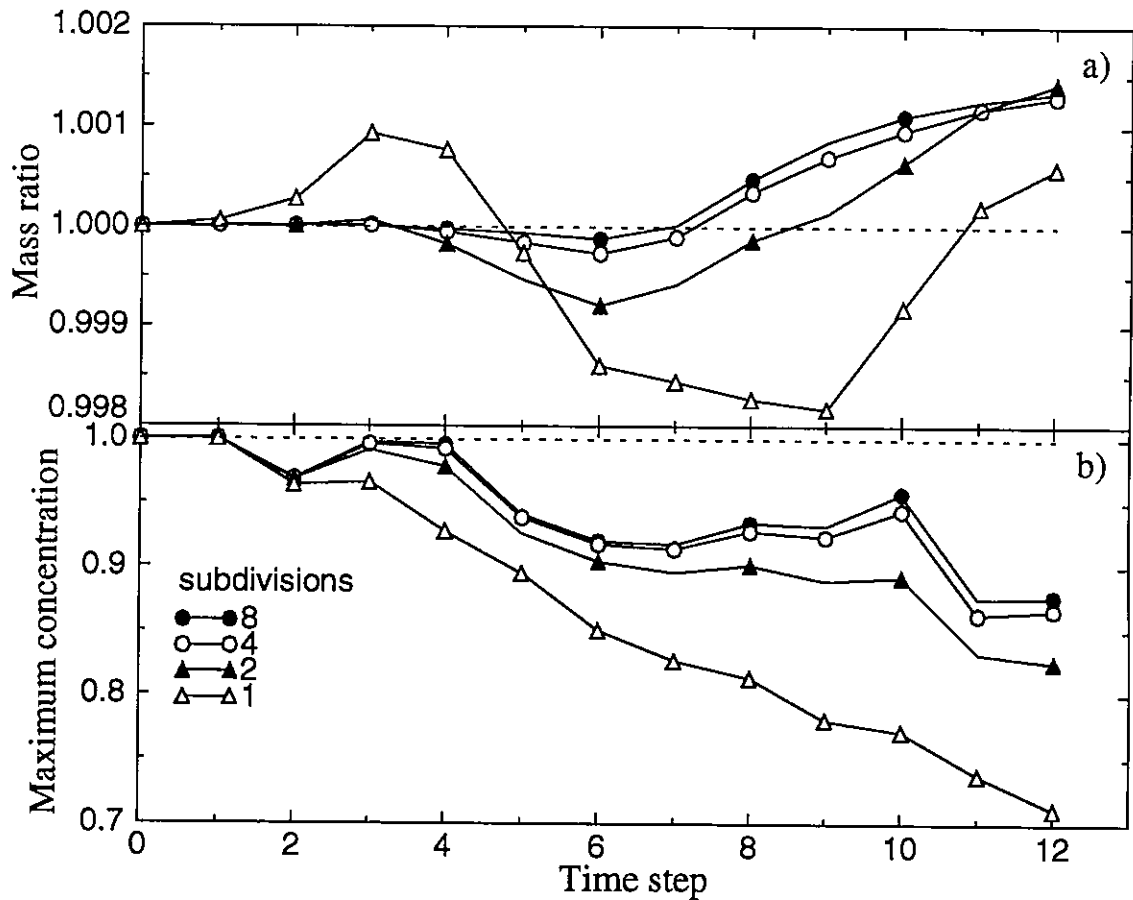


Figure 5.6 CDF5: effect of subdivision on VELA's: a) mass ratio; b) maximum concentration.

The flow field was forced by a periodic wave with period 3.1 h (M_8). Three grids were used in the transport simulations, with the same number of elements for both models. Zero concentration was imposed at the open boundary. VELA's simulations were performed with 8 subdivision levels. Additional details on the simulations are presented in Table 5.1.

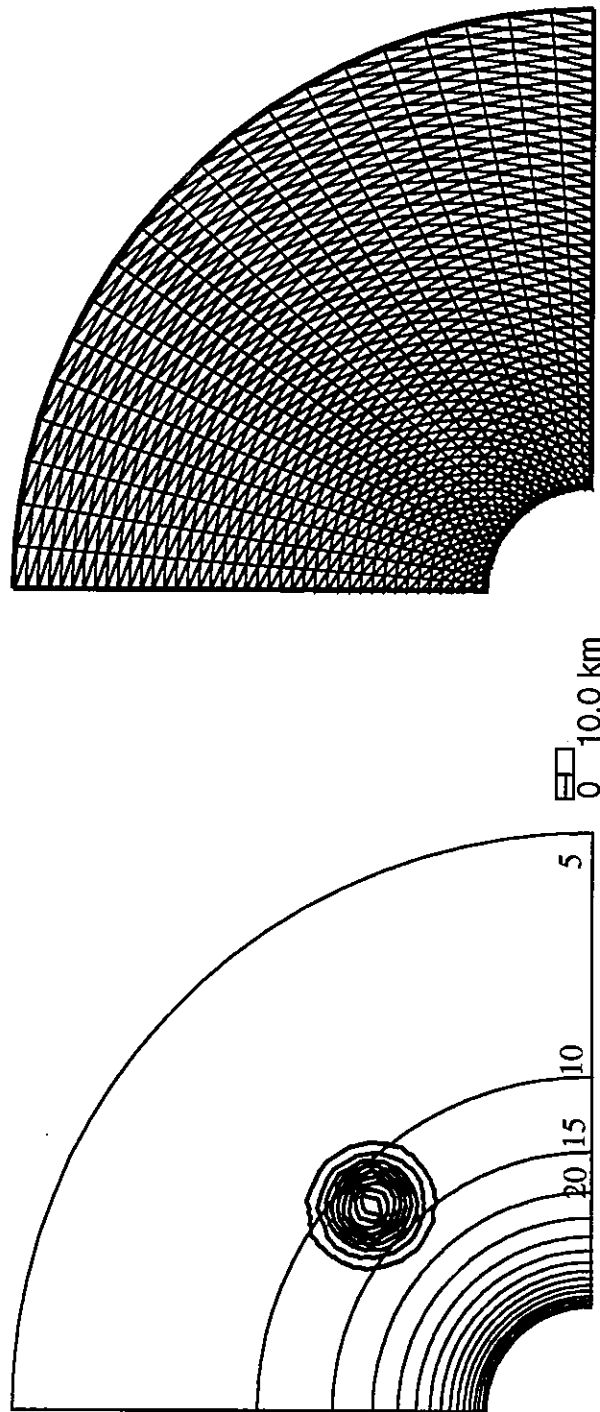


Figure 5.7 Polar Quadrant channel with reverse quadratic bathymetry: Bathymetry, concentration initial conditions and level 0 grid.

Mass ratios are similar in trend and magnitude for both ELA and VELA's non-conservative formulation (Figure 5.8). Mass errors are quite large (up to 15%) and present a clear correlation with the forcing wave. Increasing grid refinement does not reduce the influence of flow mass errors on mass, but eliminates the minor mass errors associated with the integration at the feet of the characteristic lines.

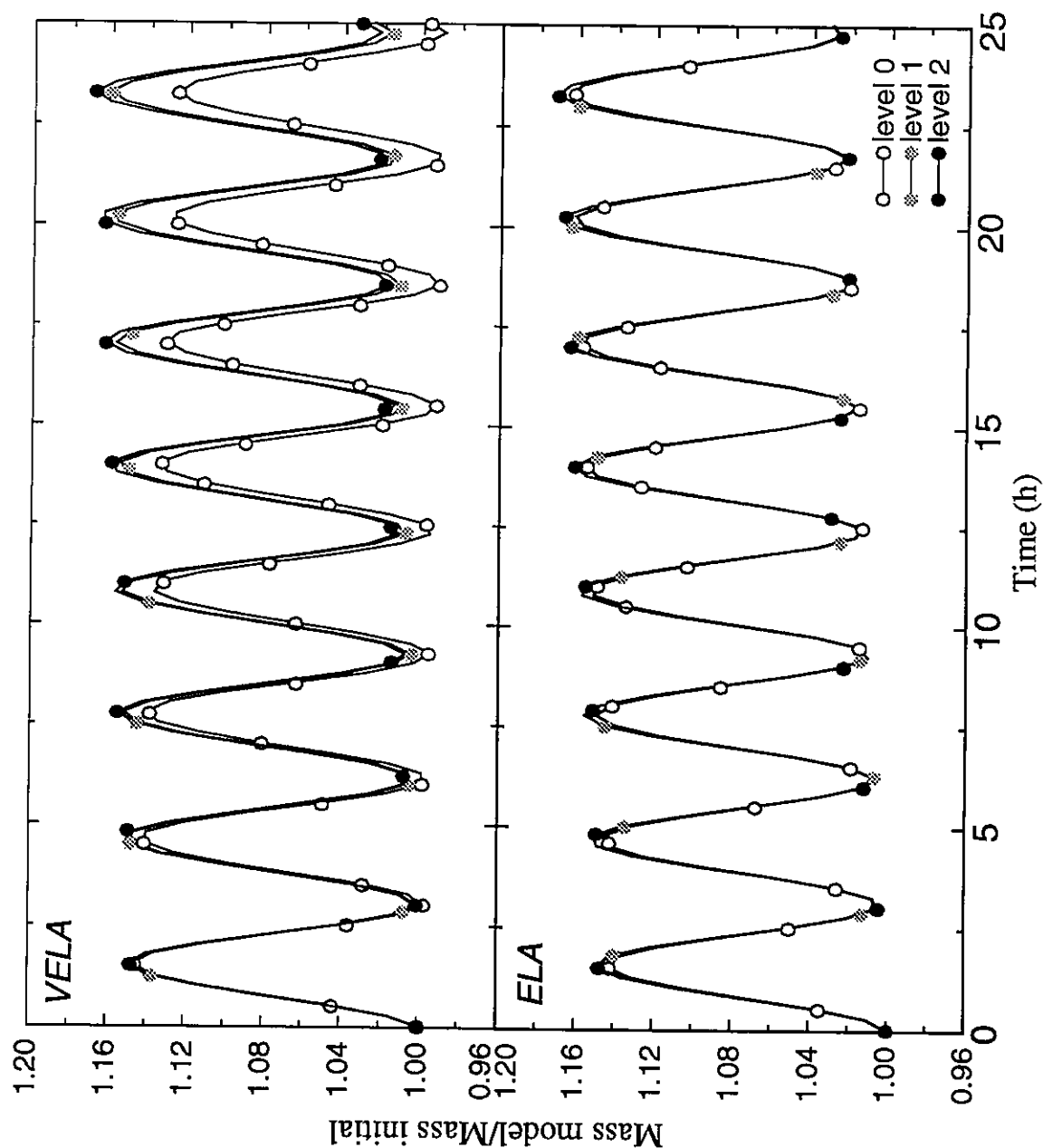


Figure 5.8 Polar channel: time series of mass ratios for VELA and ELA with several grid refinements.

To search for relationships between flow and transport mass errors, we created distinct non-conservative flow fields by varying the amplitude of the forcing wave (Table 5.1). These flow fields were then used to force transport simulations using the second grid (level 1), for which integration mass errors are negligible. Statistics of local flow mass errors (Kolar et al., 1994) were calculated (Chapter 4) for the non-linear continuity equation, thus considering equation (5.17) as a flow mass error.

Results show a quasi-linear correlation between flow and transport mass balances: larger standard deviations of flow mass errors lead to larger standard deviations of transport mass errors (Figure 5.9). This correlation can have an important effect on estuarine water quality modeling, for the coupling of physical and transformation processes, since mass errors cannot be differentiated from chemical and biological changes. Since large flow mass errors have been found for several types of finite element circulation models (Chapter 4), the problem is generalized, thus jeopardizing FE/CVFE-ELM's applicability for water quality modeling.

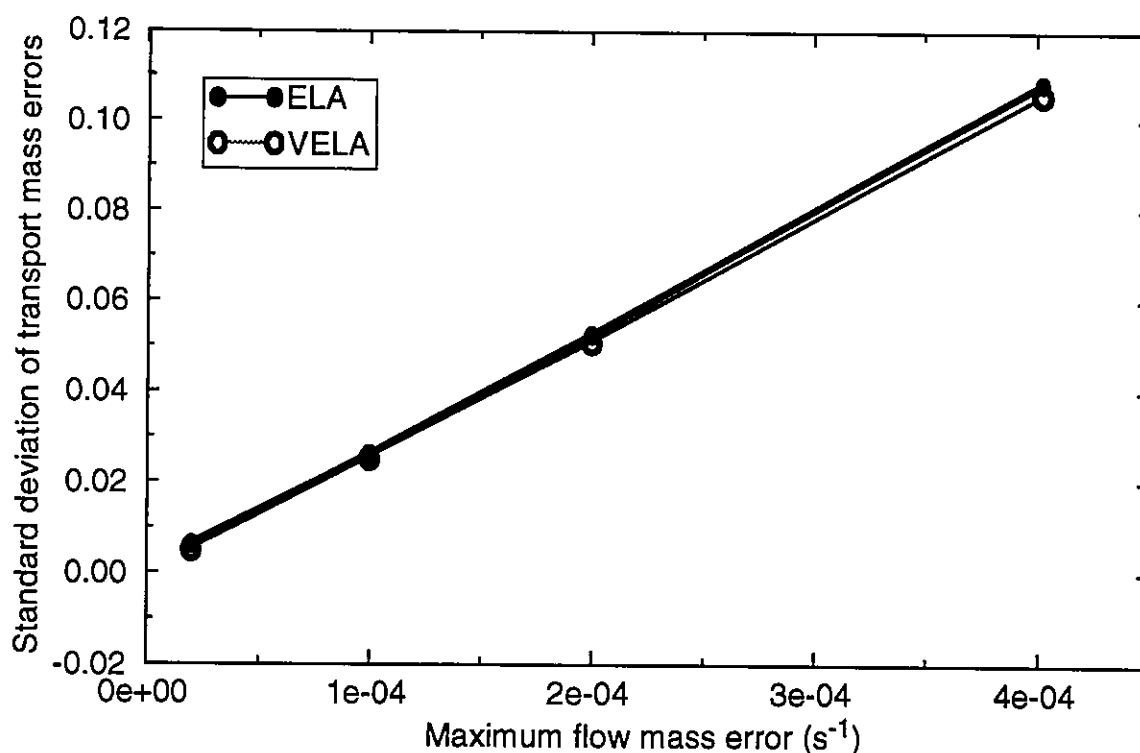


Figure 5.9 Polar channel: correlation between maximum flow mass errors and standard deviation of transport mass ratios.

While this problem should ideally be addressed at its source (i.e., the flow simulation), most current finite element flow formulations have not been able to eliminate it (Chapter 4). Therefore, we search for ways to minimize its effect on the transport simulations. Flow mass errors affect ELM transport simulations in two ways: by misplacing the location of the feet of the characteristic lines (Bentley and Pinder, 1992, Binning, 1994) and by making the source-like term in equation (5.2) non negligible (Baptista, 1987). The former is similar to the effect of tracking errors and conceptually cannot be addressed in the transport equation in an accurate way. Here we concentrate on the latter: flow mass errors related to the source-like term can conceptually be addressed by the use of the conservative transport equation.

We tested two conservative formulations in VELA, by solving the continuity source term along the characteristic lines (Lagrangian approach, equation (5.7)) or using a mixed approach (equation (5.6)). Mass errors were almost eliminated for both approaches (maximum absolute mass errors were reduced from 16% to 1% for conservative formulation with mixed continuity approach, and from 16% to 1.8% for the Lagrangian approach - Figure 5.10a). A similar analysis was performed for the constant bathymetry, rectangular channel forced by a periodic wave (Lynch and Gray, 1978) and also improved mass conservation considerably.

Mass improvement through the use of the conservative formulation, however, is obtained at the expense of overall accuracy. To compensate for lack of continuity within a control volume, VELA changes the concentration accordingly: when the fluid mass is decreasing (increasing), conservative formulations increase (decrease) the concentration so that the tracer mass is maintained (Figure 5.10b). However, for real systems and in presence of complex flows, conservative formulations can have serious drawbacks. On the one hand, they can generate excessive numerical damping, which may be unacceptable for most purposes. On the other hand, they have the potential for unstable behavior as the numerical diffusion can be either positive or negative.

This analysis showed that important mass errors can be generated by flow mass errors, with a direct correlation between the amplitudes of both errors. We also showed

that, in simple tests, the use of the conservative equation improves considerably mass conservation, but introduces considerable numerical diffusion and oscillations. Therefore, conservative formulations based on the total derivative of the concentration should not be used, since they limit our ability to check the quality of our results through mass balances.

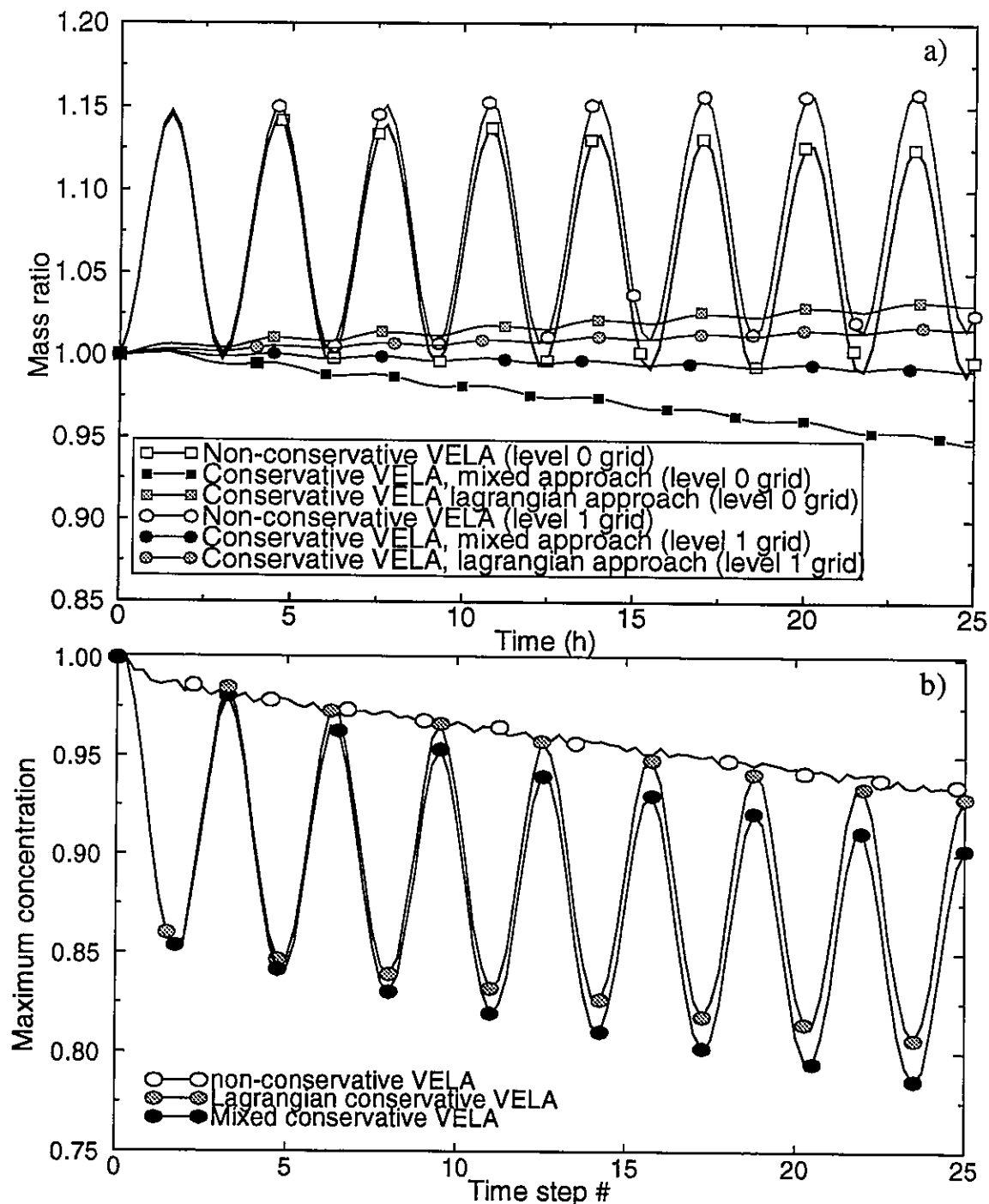


Figure 5.10 Polar channel: influence of the use of the conservative transport equation: a) mass conservation; b) maximum concentration for level 1 grid.

5.3.3 Application to the Tagus estuary

We selected the Tagus estuary, Portugal, for our estuarine test site because of its complex geometry and bathymetry, and associated complex flow field (Figure 5.11). Objectives are: i) to test the conclusions and solutions proposed in the previous tests on an complex estuarine system with multiple sources of mass errors; and ii) to estimate the magnitude and relative importance of integration errors and non-conservative flow fields in the generation of transport mass errors in a real system.

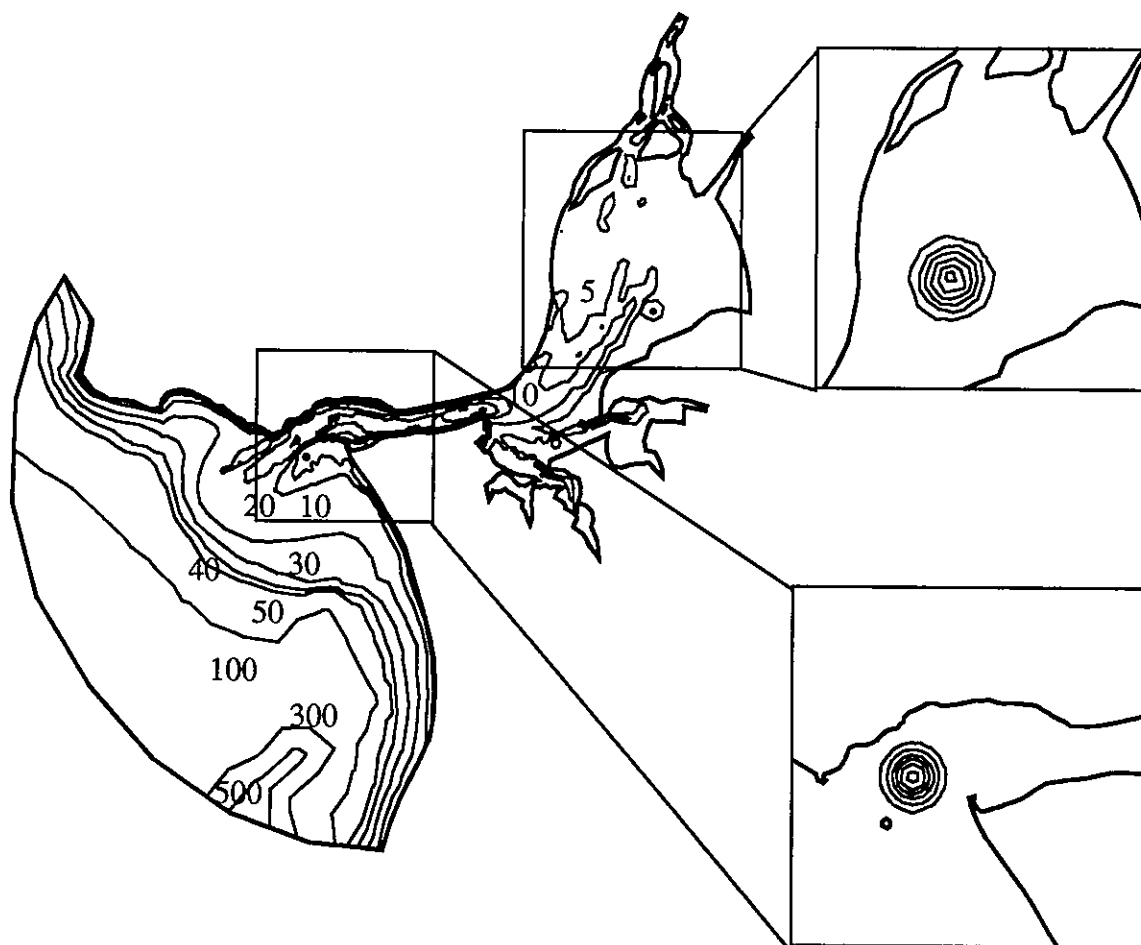


Figure 5.11 Tagus estuary: a) bathymetry and location of initial position of Gauss plumes.

Unlike the previous tests, the transport models were forced with a realistic flow field (Fortunato et al., 1997), calculated with a two-dimensional, depth-averaged wave-equation model (ADCIRC, Luettich et al., 1991). The flow simulation was forced by 11 tidal constituents, and compared acceptably with available field data (Fortunato et al., 1997). Continuity is, however, preserved poorly (Figure 5.12), mainly due to the Tagus complex bathymetry and geometry (Chapter 4). The potential exists then for important transport mass errors. A more complete flow simulation, accounting for the vertical dimension and inundation, can further increase the magnitude of flow mass errors and consequently aggravate transport mass balance.

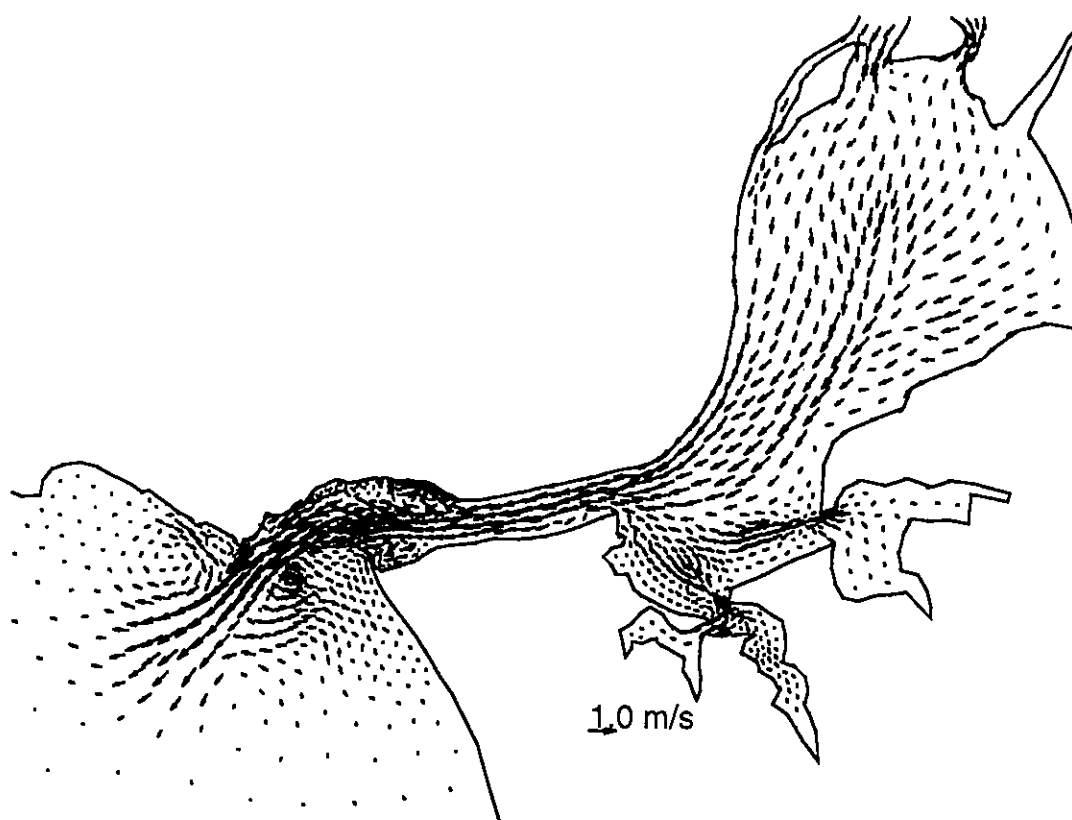


Figure 5.11 Tagus estuary: b) Snapshot of flow field at time = 9 hours.

Since the flow field in the Tagus is very complex (Figure 5.11b), two instantaneous Gauss plumes were released in areas of the estuary with distinct flow characteristics (Figure 5.11a): the plume at the mouth is released in an area of complex bathymetry and boundaries, while the upstream plume is hardly affected by boundary effects but is

released in an area of large flow mass errors, resulting from strong bathymetric gradients. Three grids are used for both models, the coarsest of which (Figure 5.11c) was deemed reasonably accurate for tidal flow simulations (Fortunato et al., 1997).

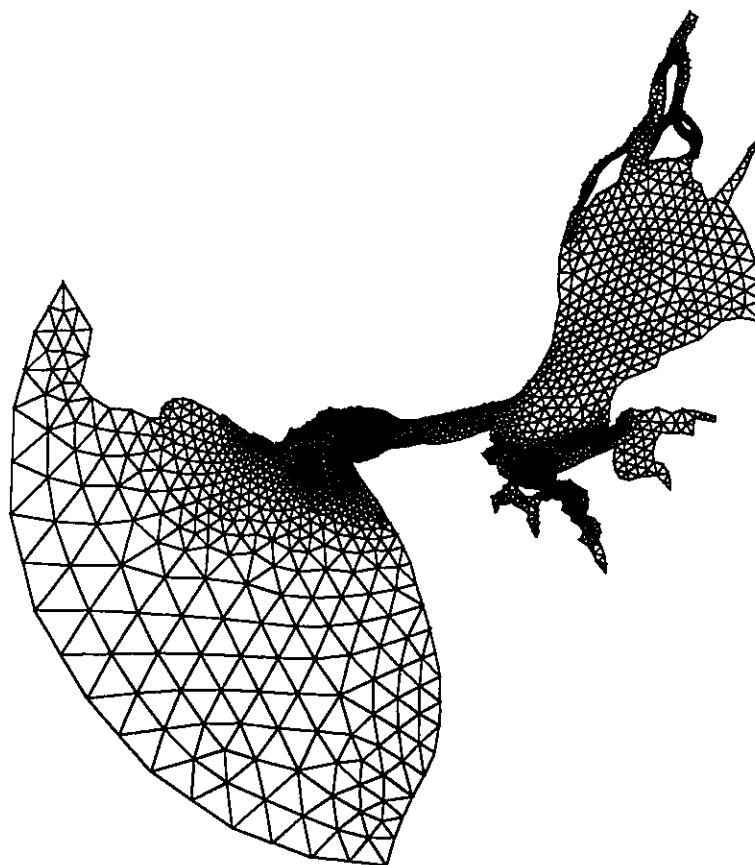


Figure 5.11 Tagus estuary: c) coarsest grid for VELA.

We start with simulations of ELA and VELA's non-conservative formulation, using 8 subdivision levels (reference runs). Due to the strong flow-generated mixing, the plumes are quickly distorted and extend over increasingly larger parts of the domain (Figure 5.13). Considerable mass errors are generated in both models for both plumes (Figure 5.14). Similarly to CDF5, VELA leads to better mass conservation than ELA for an equal number of elements, in particular for the upstream plume.

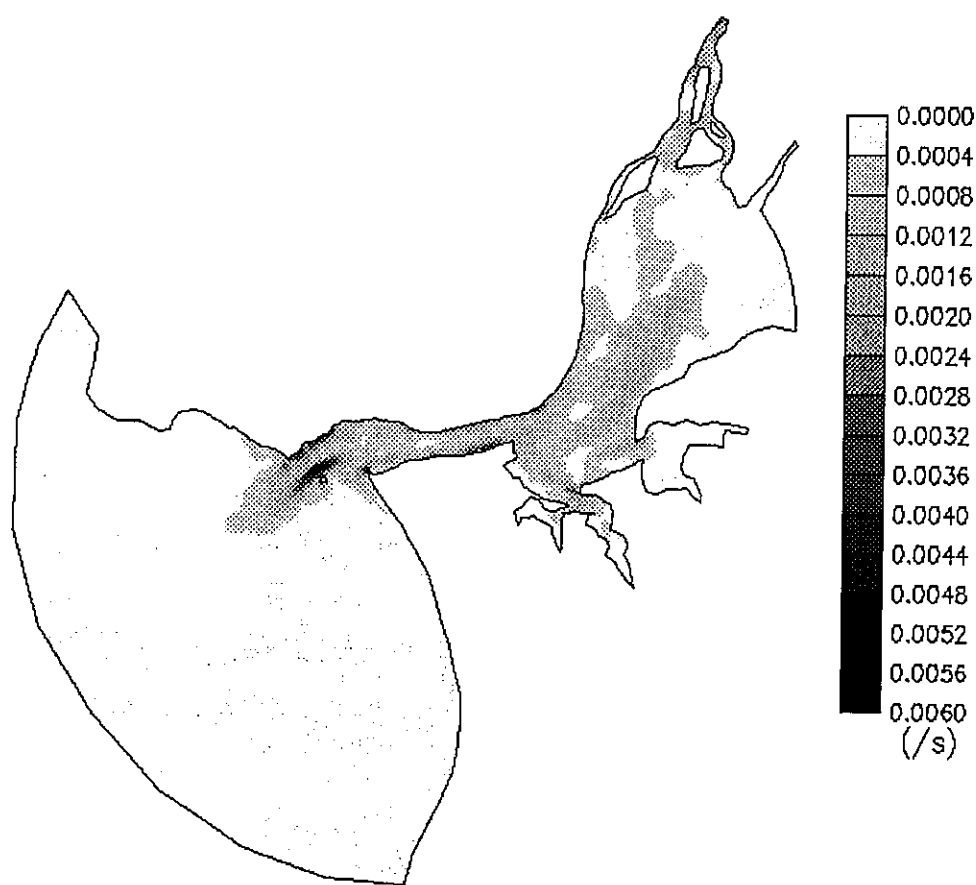


Figure 5.12 Tagus estuary: distribution of maximum local flow mass errors (s^{-1}).

Unlike in the previous tests, the number of subdivisions in VELA is rather important in the mass balance of the Tagus plumes. Time series of mass ratios for several subdivisions show a clear trend in both plumes, with mass errors converging for subdivisions of approximately 8 levels or more (Figure 5.15). However, a larger number of subdivision levels does not always lead to smaller mass errors, which suggests that flow-induced mass errors are being compensated for those generated by integration errors. Likely justifications for this behavior, which was not observed in the previous tests, are the strong distortion of Voronoi integration areas at the feet of the characteristic lines due to the complexity of the flow field, and perhaps more importantly, the strong spatial variability of flow mass errors. The latter effect may be primarily responsible for better mass balances being obtained with a smaller, rather than larger, number of subdivision levels, since less subdivisions reduces the number of concentration interpolation points and therefore reduces the influence of flow mass errors on concentrations.

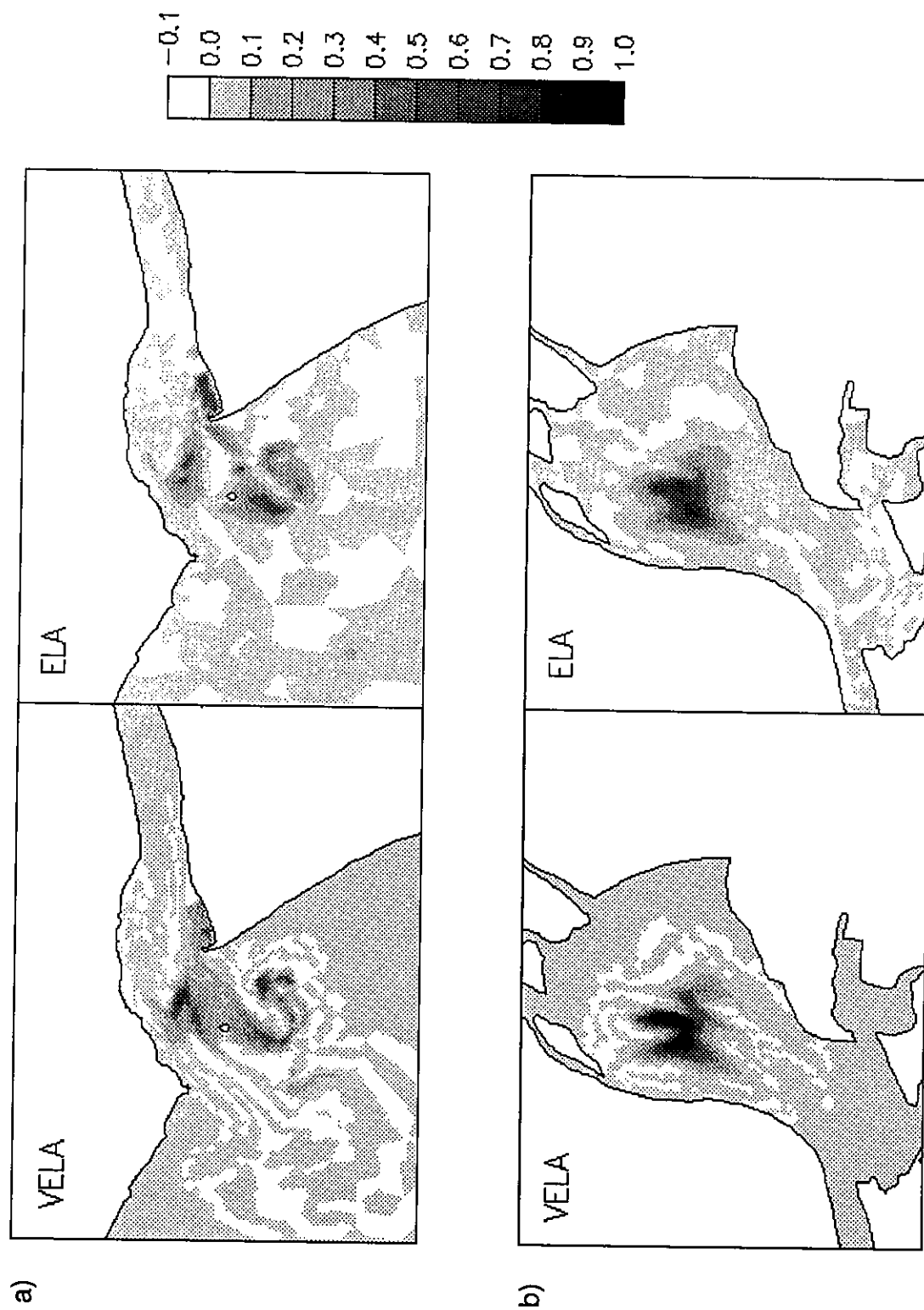


Figure 5.13 Concentration distributions for ELA and VELA 9 hours after release: a) Mouth plume; b) Upstream plume.

Removal of integration errors by increasing grid refinement improves ELA's mass balance considerably, but important mass errors remain (Figure 5.14). Similarly to an increase in subdivision levels, grid refinement does not always improve VELA's mass balance. Therefore, grid refinement is not an overall solution for ELM mass balance in complex systems, since large mass errors remain for both models (Figure 5.14).

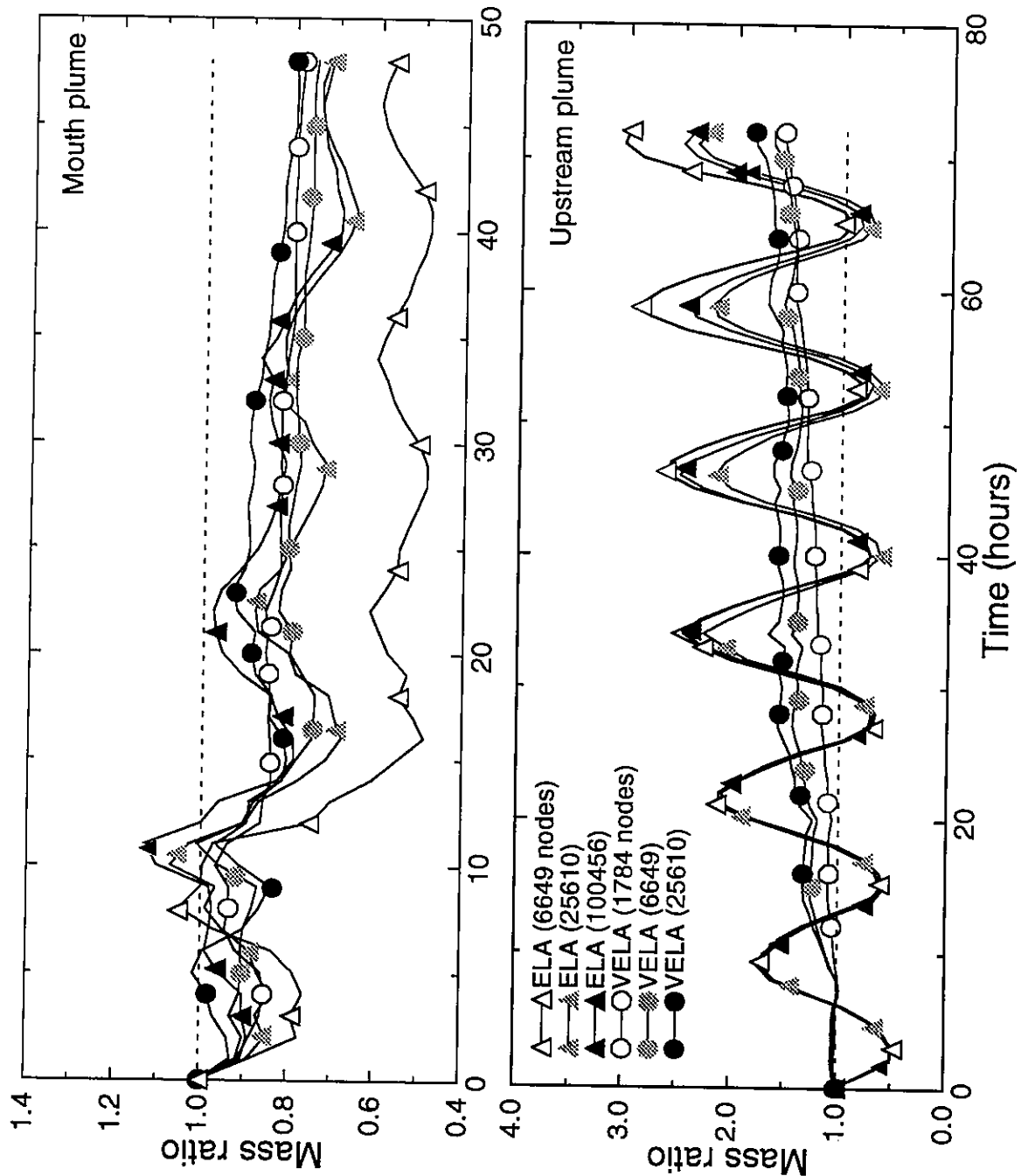


Figure 5.14 Tagus estuary: time series of mass ratios for VELA and ELA for several grids.

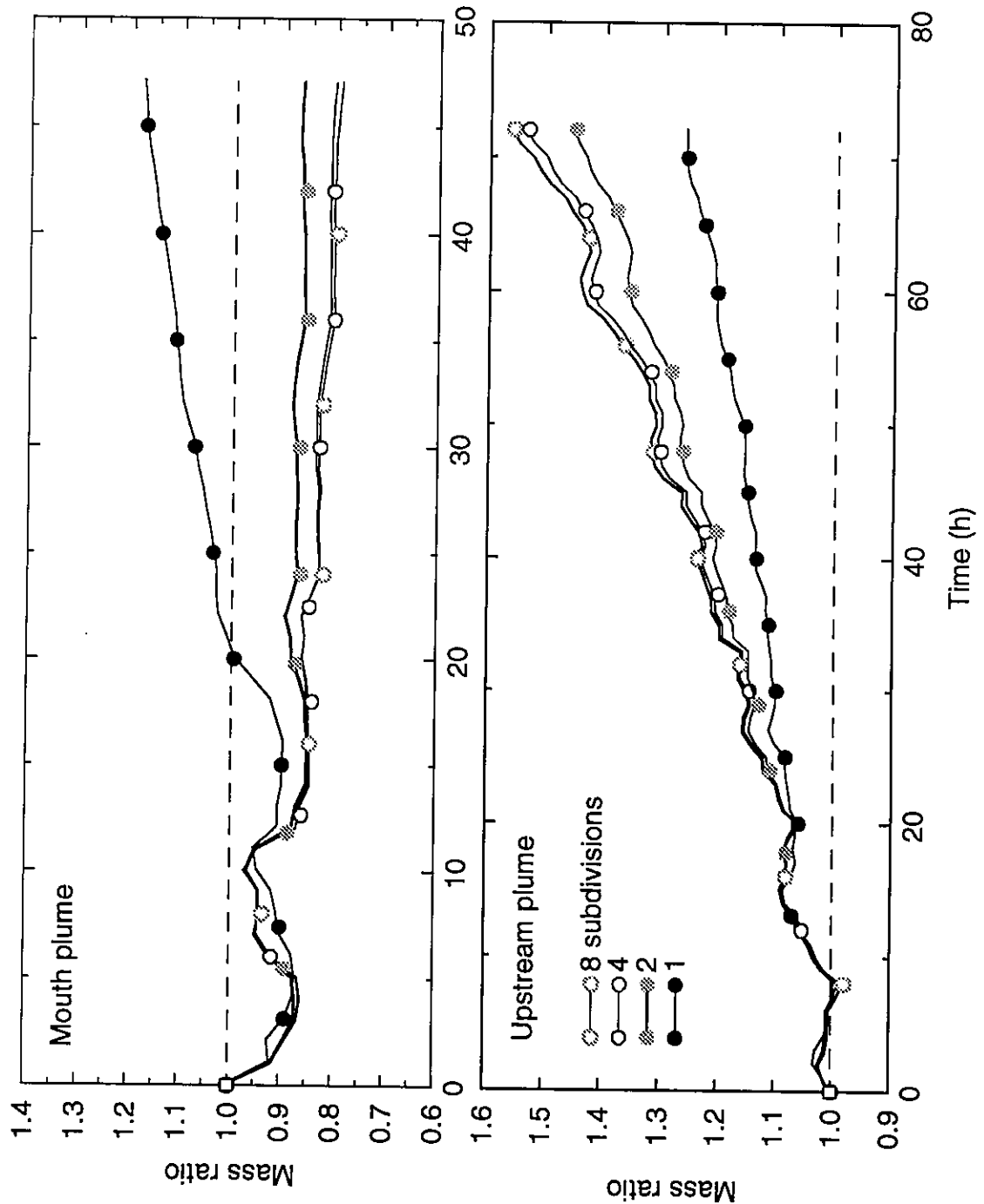


Figure 5.15 Tagus estuary: time series of mass ratios for several subdivision levels.

To compare the importance of flow-induced and integration transport mass errors, we set the bathymetry to 50 m in the whole domain. One of the main source of flow mass errors, bathymetric gradients (Chapter 4), is thus removed from our simulations. ADCIRC simulations were repeated for the constant bathymetry domain and new transport simulations were forced with these flow fields, using the reference run settings. Mass errors were almost eliminated for VELA and considerably reduced for ELA (Figure 5.16a). Differences between models are mainly due to the finite volume ability to preserve the quantity in the control volume, since, similarly to CDF5, mass coincides with the integral of the concentration in the constant bathymetry Tagus, and to generation of mass errors due to the non-linear mechanism of energy transfer to unresolved frequencies associated with quadratic elements in ELA. For ELM transport simulations forced by strongly non-conservative flow fields, flow-generated transport mass errors are thus dominant over those generated by integration errors.

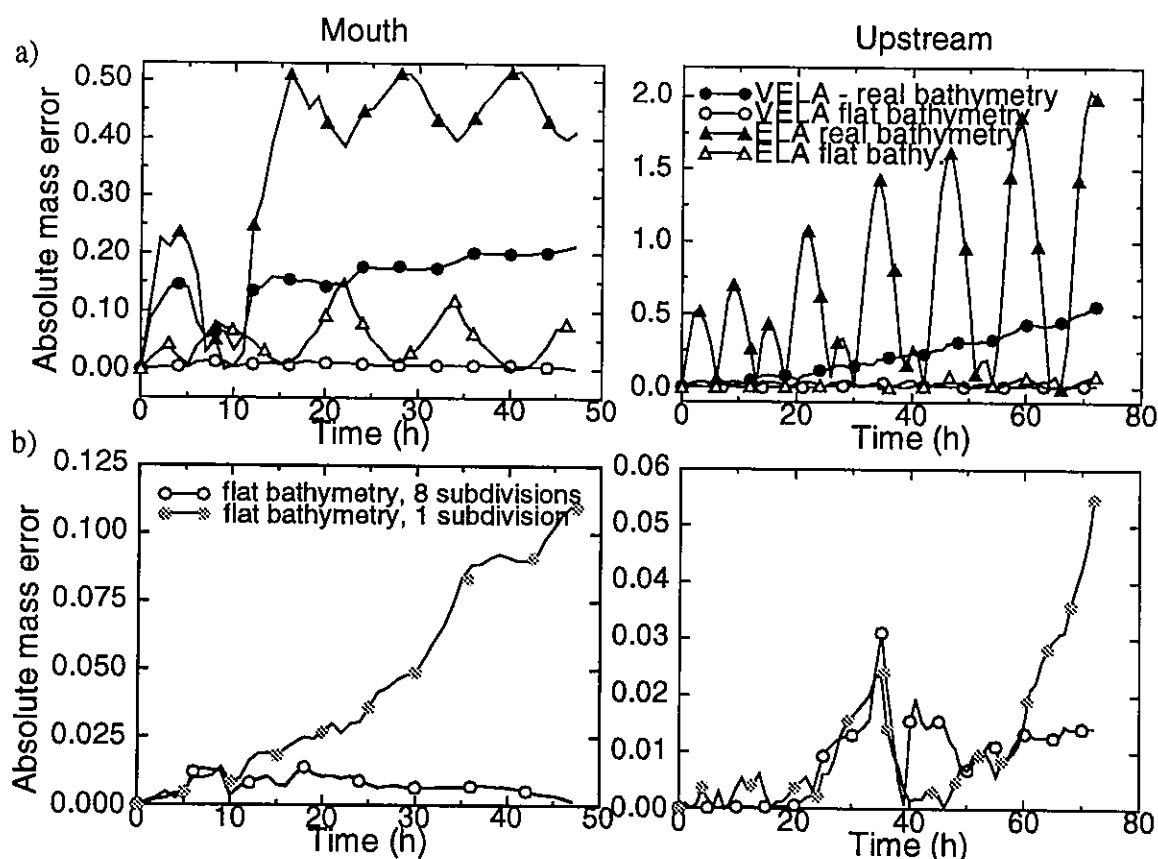


Figure 5.16 Effect of bathymetry on mass errors (Tagus estuary): a) time series of absolute mass errors for VELA and ELA for real and constant bathymetry; b) time series of absolute mass errors for VELA with 1 and 8 subdivisions, for constant bathymetry.

For the constant bathymetry case, smaller mass errors are obtained for a larger number of subdivision levels (Figure 5.16b). These results further suggest that the less-intuitive increase of mass errors with larger subdivision levels on the reference run (Figure 5.15) is generated by a larger number of concentration interpolations in areas with strong variability of flow mass errors. When bathymetry gradients are removed, flow mass errors are very small and vary mildly in the interior of the domain (Oliveira and Baptista, 1997), thus having a minor effect on transport mass balance.

We now examine the dependence of ELM transport mass errors on the time step and diffusion coefficient for the real bathymetry case. The reference runs were repeated for time steps of 15, 30 and 45 min, leading, in general, to smaller mass errors for both models (Figure 5.17a). The decrease of mass errors is larger for ELA, in particular for the upstream plume, where it reduces maximum errors on the order of 200% to about 100% when the time step is reduced to 15 min, while VELA's mass balance is only marginally improved. However, reducing the time step does not lead to mass balance, since important mass errors remain even with a time step as small as 15 min. Introducing an increasing diffusion coefficient, up to 10 m²/s, has similar effects: mass balance improves for larger diffusion coefficients, but important mass errors are still present (Figure 5.17b).

To test the ability of the continuity equation term (equations (5.6) and (5.7)) to reduce the impact of non-conservative flows, VELA was run using both conservative formulations (mixed and Lagrangian approaches). However, numerical oscillations leading to instabilities developed quickly (Figure 5.18). Introduction of a diffusion coefficient up to 5 m²/s and reduction of the diffusion time step in the simulations proved ineffective.

Our results confirm that ELM formulations based on the conservative form of the transport equation have the potential for instability, in the presence of complex systems. The changes in concentration to compensate for the lack of continuity within a control volume in this complex system generate sharp negative and positive peaks, which lead to an unstable behavior in few time steps.

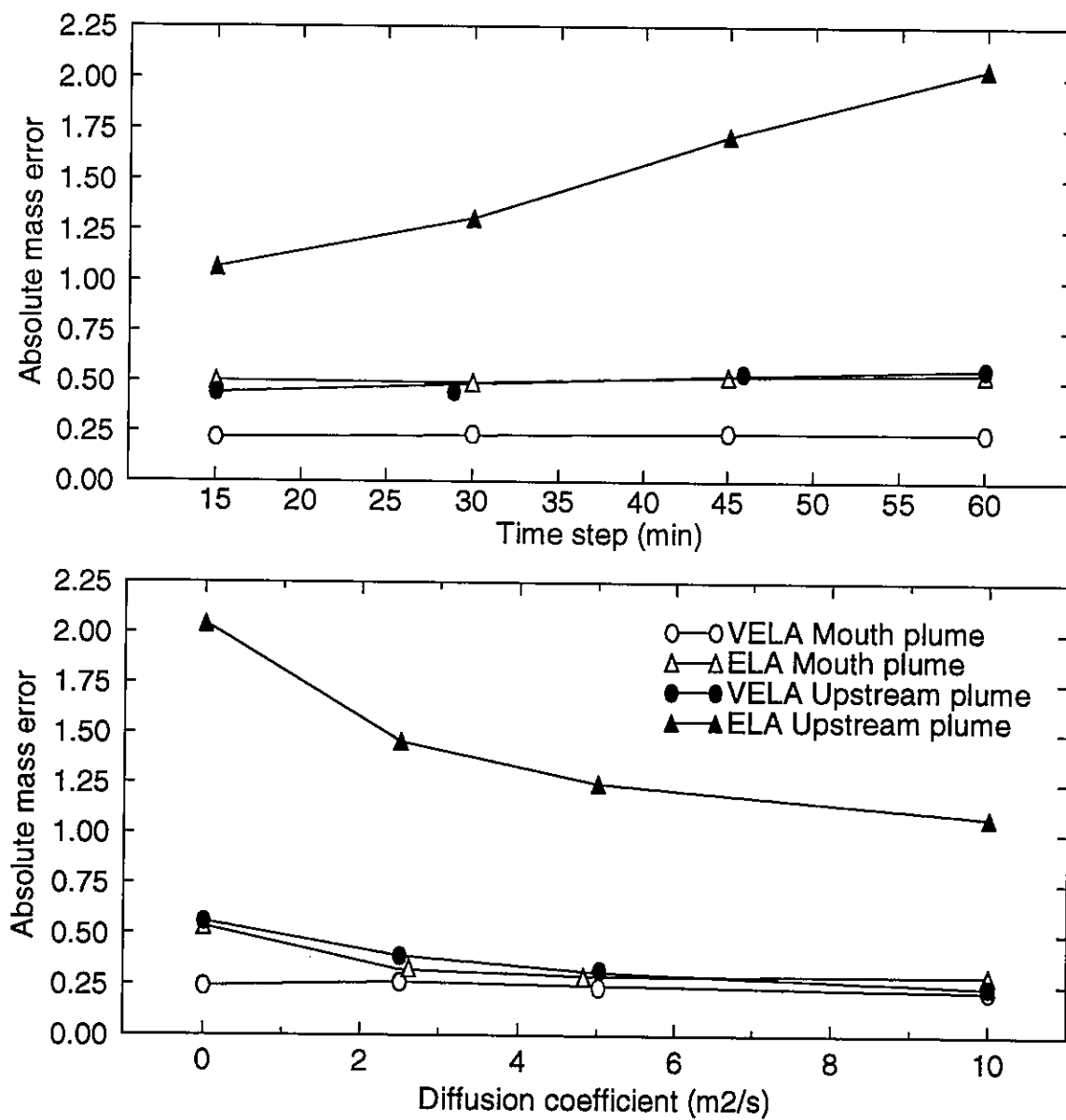


Figure 5.17 Tagus estuary - relationship between absolute mass errors and: a) time step; b) diffusion coefficient.

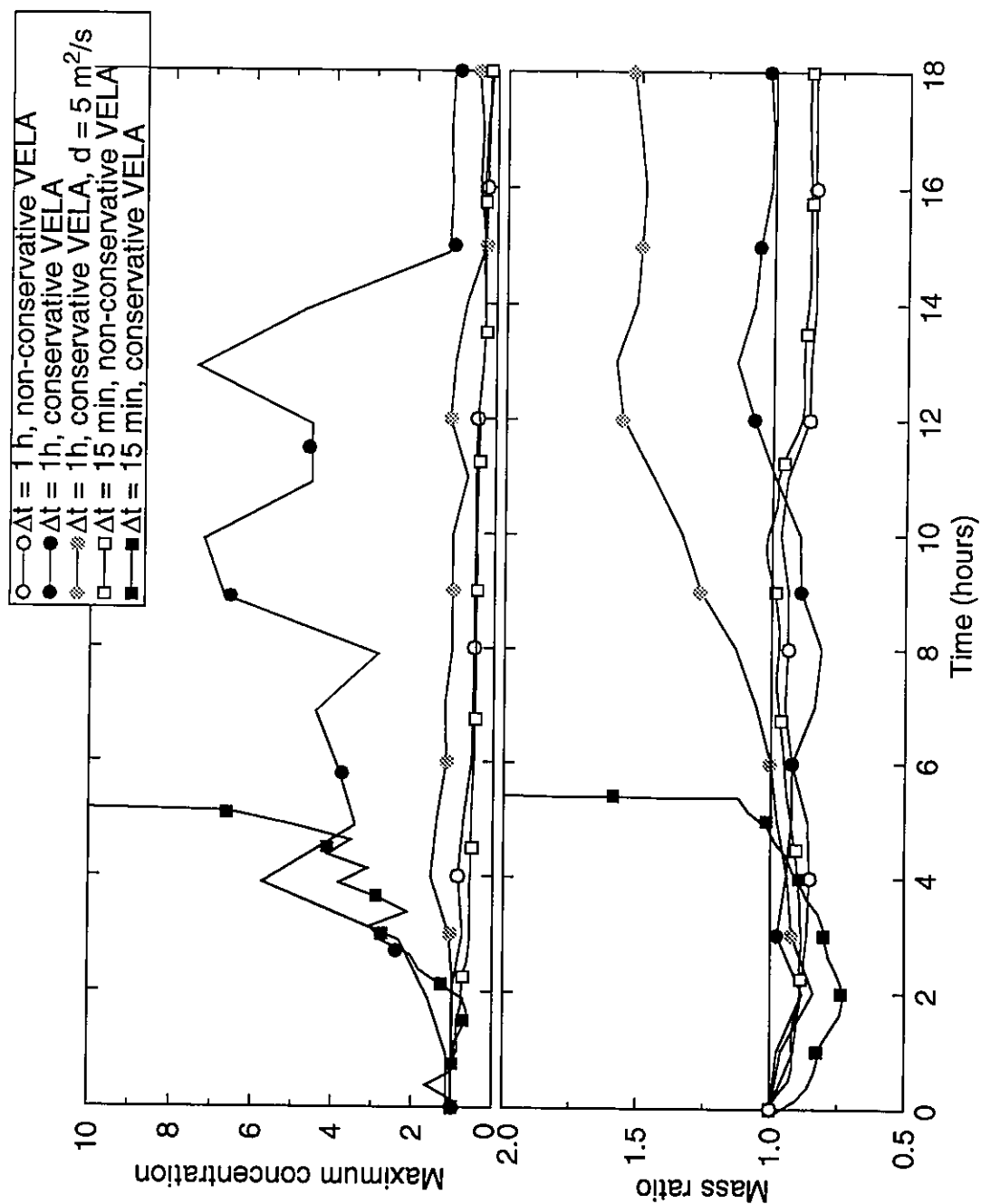


Figure 5.18 Influence of the continuity term (Lagrangian approach), for the mouth plume of the Tagus estuary: a) mass time series. b) maximum concentration time series.

5.4 Conclusions

This paper addressed the impact of integration errors and non conservative flow fields on the mass conservation of Eulerian-Lagrangian transport models. The analysis was conducted using a finite element quadratic interpolation ELM (Baptista, et al., 1984) and a new ELM model that combines control volume finite element concepts with quadrature integration methods. Simple, targeted tests were used to assess the impact of each source of mass errors, with conclusions being further verified in a complex estuary. Some important features were identified that recommend the use of mass-conservative flow fields and careful refinement for estuarine transport simulations:

- both non-conservative flows and errors in the integration at the feet of the characteristic lines can lead to important transport mass errors, in particular for complex systems;
- transport and flow mass errors are directly correlated, both on tidal and long term scales. Since large flow mass errors were found for several models in estuarine simulations, important transport mass errors are expected which may jeopardize the use of ELMs in applications involving non-conservative tracers as well as long term simulations.

While the effect of the integration errors can be substantially reduced by grid refinement, the impact of flow mass imbalances has proved harder to eliminate. Solutions attempted and proved ineffective include:

- conservative formulations based on the total derivative of the concentration, which improve considerably mass conservation in simple tests, but at the expense of overall accuracy: these formulations lead to excessive numerical damping, oscillations, and eventually instability when complex flow fields are present;
- increased grid refinement;
- control volume finite element integration formulations, although they are less sensitive to flow mass errors and integration errors, thus leading to better mass conservation than interpolation FE methods, for an equal number of nodes.

Our analysis recommends thus control volume finite element integration ELMs based on non-conservative forms of the transport equation for practical estuarine applications.

While strategies for minimizing flow mass balance effects on ELM transport could be of practical relevance, this problem should be addressed directly at its source (i.e., the flow simulation). The effect of non-conservative flows on ELM transport can be further aggravated if three-dimensional flow models are used or tidal flats are taken into account. The solution of the 3D continuity equation has the potential to generate mass errors because it is a first-order equation with two boundary conditions (Lynch and Naimie, 1993, Fortunato, 1996). Some solutions have been proposed (Mucino et al., 1994, Janin, 1995), but have not been systematically tested in complex systems. Tidal flats can also generate important flow mass errors, in particular at the wetting and drying interface (Janin, 1995), but solutions to this problem have not been proposed yet.

References

- Baptista, A.M., 1987. *Solution of Advection-Dominated Transport by Eulerian-Lagrangian Methods using the Backwards Method of Characteristics*, Ph.D. Dissertation, Massachusetts Institute of Technology, Cambridge.
- Baptista, A.M., E.E. Adams and K.D. Stolzenbach, 1984. *Eulerian-Lagrangian analysis of pollutant transport in shallow water*, Technical Report no. 296, MIT R.M. Parsons, Cambridge.
- Baptista, A.M., E.E. Adams and P. Gresho, 1995. Benchmarks for the Transport Equation: the Convection-Diffusion Forum and Beyond, in *Quantitative Skill Assessment for Coastal Ocean Models*, D. Lynch et al. (editors), American Geophysical Union Estuarine/Coastal Monograph, 47: 241-268.
- Bentley, L. and G.F. Pinder, 1992. Eulerian-Lagrangian Solution of the Vertically Averaged Groundwater Transport Equation, *Water Resources Research*, 28(11): 3011-3020.
- Binning, P., 1994. *Modeling Unsaturated Zone Flow and Contaminant Transport in the Air and Water Phases*, Ph.D. Dissertation, Princeton University, Princeton.

- Celia, M.A., T.F. Russell, I. Herrera, R.E. Ewing, 1990. An Eulerian-Lagrangian Localized Adjoint Method for the Advection-Diffusion Equation, *Advances in Water Resources*, 13(4): 187-206.
- Chen, C.L., 1989. Analytic Solutions for Tidal Model Testing, *Journal of Hydraulic Engineering*, 115(12): 1707-1714.
- DeGeorge, J.F. and I.P. King, 1994. A Multi-Dimensional Transport Model Utilizing a Characteristic-Galerkin Approach, in *Estuarine and Coastal Modelling III*, M.L. Spaulding et al. (editors), American Society of Civil Engineers, 407-421.
- Dimou, K., 1992. *3-D Hybrid Eulerian-Lagrangian / Particle Tracking Model for Simulating Mass Transport in Coastal Water Bodies*, Ph.D. Dissertation, Massachusetts Institute of Technology, Cambridge.
- Fortunato, A.B., 1996. *Three-Dimensional Modeling of Coastal Flows Using Unstructured Grids*, Ph.D. Dissertation, Oregon Graduate Institute of Science and Technology, Oregon.
- Fortunato, A.B., A.M. Baptista and R.A. Luettich, Jr., 1997. A Three-Dimensional Model of Tidal Currents at the Mouth of the Tagus Estuary (Portugal), *Continental Shelf Research* (in press).
- Gravel, S. and A. Staniforth, 1994. A Mass-Conserving Semi-Lagrangian Scheme for the Shallow Water Equations, *Monthly Weather Review*, 122(1): 243-248.
- Healy, R.W. and T.F. Russell, 1993. A Finite-Volume Eulerian-Lagrangian Localized Adjoint Method for Solution of the Advection-Dispersion Equation, *Water Resources Research*, 29(7): 2399-2413.
- Janin, J.M., 1995. *Conservativité et Positivité dans un module de transport de scalaire écrit en éléments finis - Application a Telemac-3D*, Rapport HE-42/95/054/A, Département Laboratoire National d'Hydraulique, Chatou, France.
- King, I.P. and J.F. DeGeorge, 1996, Multidimensional modeling of Water Quality using the Finite Element Method, in *Proceedings of the 4th International Conference on Estuarine and Coastal Modeling*, M.L. Spaulding and R.T. Cheng (editors), American Society of Civil Engineers, 340-354.
- Kolar, R.L., J.J. Westerink, M.E. Cantekin and C.A. Blain, 1994. Aspects of Nonlinear Simulations Using Shallow Water Models Based on the Wave Continuity Equation, *Computers and Fluids*, 23(3): 523-538.

- Lynch, D.R. and W.G. Gray, 1978. Analytic Solutions for Computer Flow Model Testing, *Journal of Hydraulics Division*, 104(HY10): 1409-1427.
- Lynch, D.R. and C.E. Naimie, 1993. The M2 Tide and Its Residual on the Outer Banks of the Gulf of Maine, *Journal of Physical Oceanography*, 23(10): 2222-2253.
- Luettich, Jr., R.A., J.J. Westerink and N.W. Sheffner, 1991. *ADCIRC: An Advanced Three-Dimensional Circulation Model for Shelves, Coasts and Estuaries*. Report 1: Theory and Methodology of ADCIRC-2DDI and ADCIRC-3DL. Department of the Army, US Army Corps of Engineers.
- McCormick, S., 1992. Finite Volume Element and Multilevel Adaptive Methods, in *Proceedings of the 9th International Conference on Computational Methods in Water Resources*, T.F. Russell et al. (editors), Computational Mechanics Publications, 539-553.
- Mucino, J.C., W.G. Gray and M.G.G. Foreman, 1994. Calculation of Vertical Velocity in a 3D Model Using a Least Squares Approach, in *Proceedings of the 10th International Conference on Computational Methods in Water Resources*, A. Peters et al. (editors), Kluwer Academic Publishers, 1105-1112.
- Oliveira, A. and A.M. Baptista, 1995. A comparison of integration and interpolation Eulerian-Lagrangian methods, *International Journal for Numerical Methods in Fluids*, 21(3): 183-204.
- Oliveira, A. and A.M. Baptista, 1997a. On the Role of Tracking on Eulerian-Lagrangian Solutions of the Transport Equation, *Advances in Water Resources*, (in press).
- Oliveira, A. and A.M. Baptista, 1997b. VELA User's Manual. A Two-Dimensional Depth-Averaged Transport and Particle Model, (in preparation).
- Patankar, S.V., 1980. *Numerical Heat Transfer and Fluid Flow*, Hemisphere, New York.
- Press, W.H., S.A. Teukolsky, W.T. Vetterling and B.P. Flannery, 1992. *Numerical Recipes in Fortran*, Cambridge University Press, 704-716.
- Priestley, A., 1993. A Quasi-Conservative Version of the Semi-Lagrangian Advection Scheme, *Monthly Weather Review*, 121(2): 621-629.
- Rasch, P.J. and D.L. Williamson, 1990. On shape-preserving interpolation and semi-Lagrangian transport, *SIAM Journal of Scientific and Statistical Computing*, 11(4): 656-687.

- Roache, P.J., 1992. A Flux-Based Modified Method of Characteristics, *International Journal for Numerical Methods in Fluids*, 15(11): 1259-1275.
- Russell, T.F., 1989. Eulerian-Lagrangian Localized Adjoint Methods for Advection-Dominated Problems, in *Numerical Analysis 1989*, Pitman Research Notes, D.F. Griffiths and G.A. Watson (editors), Longman Scientific and Technical, 228: 206-228.
- Sorek, S., 1988. Eulerian-Lagrangian method for solving transport in aquifers, *Advances in Water Resources*, 11(2): 67-73.
- Staniforth, A. and J. Côté, 1991. Semi-Lagrangian integration schemes for atmospheric models - A review, *Monthly Weather Review*, 119(9): 2206-2223.
- Tang, L. and E.E. Adams, 1996. Effect of Divergent Flow on Mass Conservation in Eulerian-Lagrangian Transport Schemes, in *Proceedings of the 4th International Conference on Estuarine and Coastal Modeling*, M.L. Spaulding and R.T. Cheng (editors), American Society of Civil Engineers, 106-113.
- Wood, T.M., 1993. *Numerical Modeling of Estuarine Geochemistry*, Ph.D. Dissertation, Oregon Graduate Institute of Science and Technology, Portland.
- Wood, T.M., A.M. Baptista, J.S. Kuwabara and A.R. Flegal, 1995. Diagnostic Modeling of trace metal partitioning in south San Francisco Bay, *Limnology and Oceanography*, 40(2): 345-358.
- Yeh, G.T., J.R. Chang and T.E. Short, 1992. An exact peak capturing and oscillation-free scheme to solve advection-dispersion transport equations, *Water Resources Research*, 28(11): 2937-2951.
- Zisman, S., 1990. *Simulation of Contaminant Transport in Groundwater Systems using Eulerian-Lagrangian Localized Adjoint Methods*, M.Sc. Thesis, Massachusetts Institute of Technology, Cambridge.

CHAPTER 6¹

Diagnostic Modeling of Residence Times in Estuaries

Abstract

The variability of estuarine residence times is elucidated through accurate, diagnostic numerical tracking of a large number of particles, complemented with statistical analysis. Residence times are shown to have strong spatial and temporal variability, which is accentuated by exchanges between the estuary and the coastal ocean due to chaotic stirring at the mouth. The concept of a single residence time per estuary, while convenient from both ecological and engineering viewpoints, is therefore shown to be an oversimplification. Maps of residence times and cumulative histograms are examined as alternatives. The former are attractive only for once-through tracers, while the latter appear useful over a broader range of tracer characteristics.

6.1 Introduction

Residence times are broadly recognized as important descriptors of estuarine behavior (Pilson, 1985, Takeoka, 1984, Zimmerman, 1988, Salomon and Pommepuy, 1990, Delesalle and Sournia, 1992), and are a likely element of any extension of classic estuarine classifications such as Pritchard (1967) and Fairbridge (1980). Yet, no real con-

1. In *Water Resources Research*, 33(8):1935-1946, 1997.

sensus exists on the definition of “residence time”. This is partially because the definition of residence time (hereafter denoted as RT) is largely “operational”, i.e., inherently linked to the method chosen for its evaluation. Traditionally, a single value has been used to define the RT of an estuary. This “bulk” approach is extremely useful for comparative analysis between estuaries and for engineering and ecological studies, but is potentially very misleading. Indeed, RTs clearly vary with river discharge, tidal coefficients, location and time of release during the tidal cycle, among other factors.

Prompted by two workshops of the National Science Foundation Land-Margin Ecosystems Research Program on residence times in estuaries, we have investigated the general question of the variability of RTs in space and time and with environment characteristics, and the issue of whether a single RT may be used to characterize a whole estuary. The analysis is conducted for two different types of tracers: the first is allowed to re-enter the estuary with the tide while the second is not. Neither tracer is allowed to transform within the estuary.

Our investigation is diagnostic, based on accurate numerical tracking of a large number of particles in a reference estuary, for several environmental and release conditions. The Tagus estuary, Portugal (Figure 6.1a) was chosen for its complex geometric and bathymetric features and associated strong non-linear processes (Fortunato et al., 1997). While the forcing circulation was simplified here to the level of description of a depth-averaged barotropic shallow water model, it retains enough complexity for a useful analysis of RT variability.

This paper is divided in 6 sections, besides this *Introduction*. *Background* summarizes the methodologies that have been used to address RTs in estuaries. *Method description* presents our proposed methodology and introduces the two types of tracers used in the analysis. Sources of errors in our method are investigated in *Accuracy analysis*. *Diagnostic characterization of residence times* explores new approaches to characterize RTs. *Conclusions* summarizes our findings and identifies needs for further research.

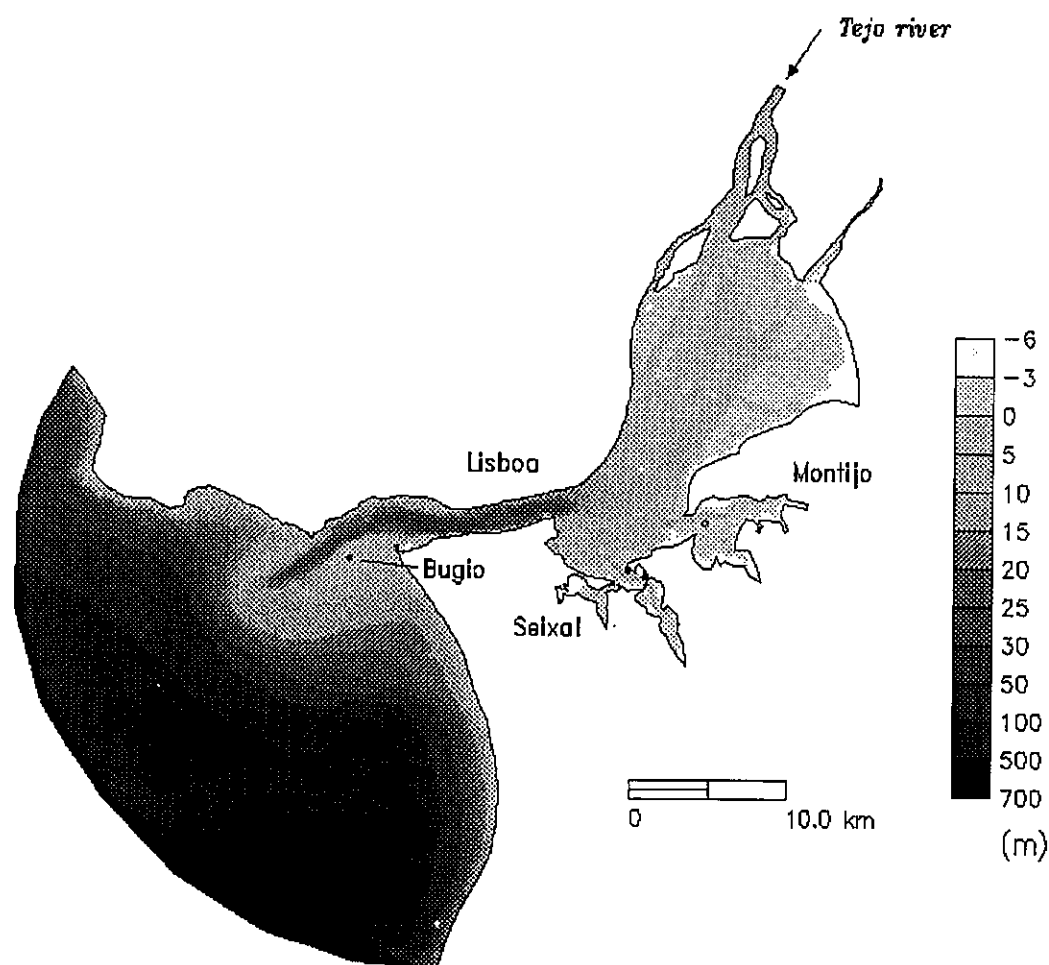


Figure 6.1 a) Bathymetry of the Tagus estuary.

6.2 Background

Most traditional approaches to RT evaluation in estuaries take an integral perspective, suggesting a single value to characterize the whole system (Zimmerman, 1988, Officer and Kester, 1991). The use of a single RT for an estuary is attractive and has been used for various purposes such as establishing comparisons among systems (Jay et al., 1995) and estimating important ecological quantities (Delasalle and Sourmia, 1992). However, integral formulations are typically based on assumptions of steady-state and well-mixed or regionally well-mixed systems, and thus cannot take into account the space and time variability of RT. Among these formulations, those based on salinity data have been extensively applied, as they only require salinity surveys and knowledge of river discharge

rates (Martins et al., 1984, Pilson, 1985, Officer and Kester, 1991). For integral approaches, RT is defined as the total mass of the material within the system, divided by the input fluxes:

$$RT = \frac{\iiint C dx dy dz}{\oint_l Q_{input} dl} \quad (6.1)$$

where C is the concentration and Q_{input} are the input fluxes. For freshwater, equation (6.1) simplifies to (Pilson, 1985):

$$RT = \frac{S_0 - \bar{S}}{S_0} \times \frac{V}{Q} \quad (6.2)$$

where S_0 is the salinity of the ocean water, \bar{S} is the volume-averaged salinity of the system, Q is the total freshwater input and V is the volume of the estuary. The average salinity, a necessarily ambiguous concept, is often calculated based on “representative” salinity measurements that preferably extend over a range of environmental conditions.

Other integral methods use tidal prisms to evaluate RTs (Zimmerman, 1988, Van de Kreeke, 1988). These methods tend however to underestimate RTs (Pilson, 1985, Zimmerman, 1988).

The limitations of integral approaches and the need for local assessments of RTs have been recognized and discussed (Zimmerman, 1988). Local analysis is necessary to address important ecological problems that occur locally (e.g. contact rate between organisms) or that result from local physical processes (e.g. turbidity maximum). Time variability of the environmental forcings also makes RTs strongly dependent on the release time.

Simple RT estimates can be improved by integrating locally the spatial and temporal variability of salinity using multi-box models (Officer, 1980, Zimmerman, 1988, Jay, 1994) or using analytical models (Takeoka, 1984). However, these formulations also tar-

get a single RT for the whole system (or for large sub-regions) and therefore cannot characterize the variability of RTs with tides, time and space below sub-region scale.

To further address these limitations, numerical models have started to be used in RT calculations (Salomon and Pommepey, 1990, Hofman et al., 1991, Wu and Tsanis, 1994). They explicitly recognize tidal effects and take into account the space and time variability of RTs, and can also address RTs of materials that have distinct RTs than the water in which they are suspended. Unlike traditional methodologies, numerical methods do not require scaling with regard to the main riverine source, thus extending the range of applicability to problems with multiple riverine inputs or with non-point sources, and to systems without river forcing (e.g. lagoons). Two different methods have been applied, using particle models (Hofman et al., 1991) and transport models (Salomon and Pommepey, 1990, Wu and Tsanis, 1994). The success of particle models in understanding relevant quantities with strong time and space variability in estuarine and coastal systems (Salomon and Pommepey, 1990, Signell and Geyer, 1990, Foreman et al., 1992, Fortunato et al., 1997) has prompted their use in our present analysis of RTs.

6.3 Method description

We use flow fields generated by numerical models to drive highly-accurate numerical simulations of the release of large numbers of particles. These particles, which represent a parcel of water driven exclusively by advection, are released at key places in the system, at several instants in time. However, extension to include dispersion through random walk presents no conceptual difficulty (see for instance Dimou and Adams, 1989).

Residence times for each particle are measured on the basis of their permanence in a control region (e.g., Figure 6.1b). The definition of permanence is tracer-specific. In this paper, we investigate two contrasting cases. For *re-entrant* tracers, particles are allowed to move in and out of the control region with the tidal forcing. Individual RTs are defined as the time taken for the particle to leave the control region without returning at a later phase of the tide or at a later tidal cycle. For *once-through* tracers, which represent materials

whose properties are considerably changed when outside the control region, individual RTs are defined as the first time the particle leaves the control region.

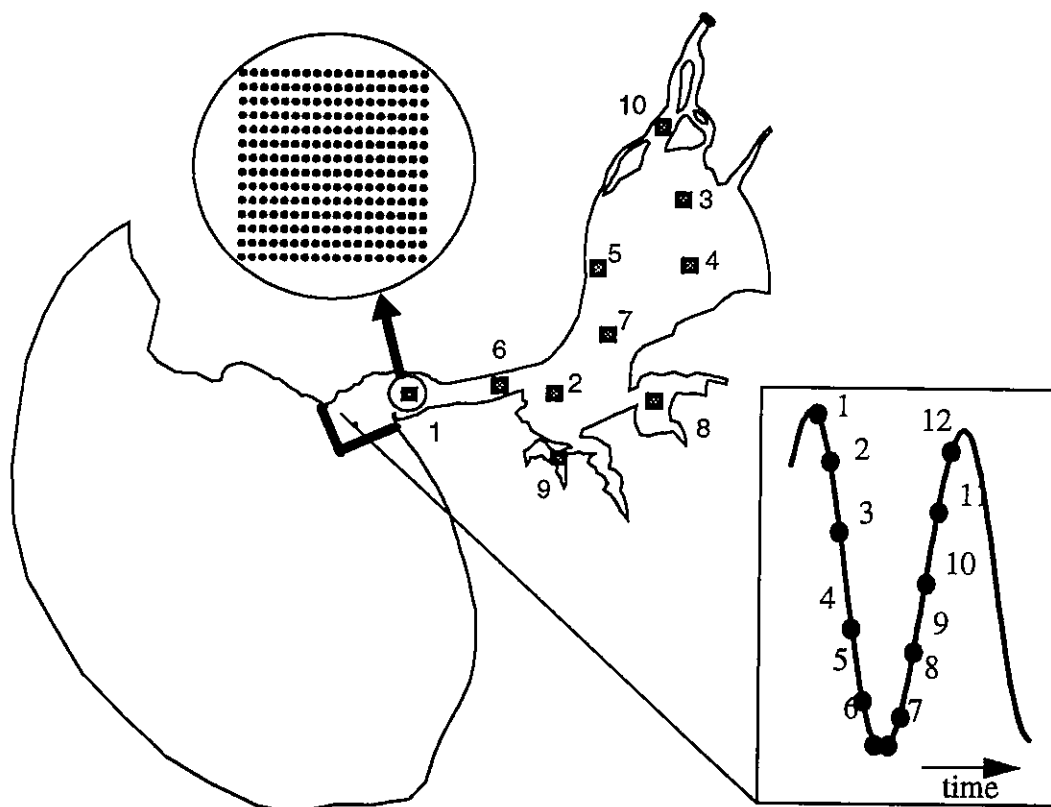


Figure 6.1 b) Definition of the control region, release regions and release times for the re-entrant tracer. Particles in each release are distributed in a $50 \times 50 \text{ m}^2$ grid, the coarsest distribution leading to converged statistics.

There are, of course, a multitude of important environmental issues for which the relevant RT is not represented directly by our two tracer types. An interesting example is the contamination of a biological species by exposure to toxic materials, with the relevant RT being the time the toxic material is actually inside the system. Using our methodology, this problem could be handled as the RT for the re-entrant tracer, minus the time outside the system. Another example are tracers (e.g., sediments) that deposit in the bottom to be eventually re-suspended at later times. Our methodology would require some significant adjustments for this case. Our goal here, though, is not to address all relevant cases, but to investigate whether new methodologies can provide more insight on the characterization of RTs in estuaries.

6.4 Accuracy analysis

Since RTs can be quite large for many systems, thus requiring long particle simulations, we must prevent error accumulation in the tracking of particles and hence on the evaluation of RTs. The accuracy of the proposed approach relies heavily on two factors: the accuracy of the tracking method and the quality of the driving flow field. In order to assess the reliability of our results, we look at the relative importance of each of these factors on RT calculations.

Our particle model uses the very accurate adaptive embedded 4th order Runge-Kutta tracking algorithm (Press et al., 1992). While sometimes computationally attractive, alternative methods are overall much less attractive. In particular, low order methods such as Euler tracking (Casulli and Cheng, 1992) have been shown to lead to very large closing errors in presence of complex flow fields, and semi-analytical methods (Pollock, 1988) cannot be applied when velocity components depend on nodal velocities in all coordinate directions, which is the case for flow fields generated by finite element models (Oliveira and Baptista, 1997).

For our method, tracking accuracy is controlled by the maximum allowed spatial error (ϵ). To select the appropriate ϵ , an experiment was set-up by releasing 2220 particles distributed throughout the Tagus estuary and following them for 10 M_2 tidal cycles, using a range of ϵ from 10^{-3} m (representative of values used in Eulerian-Lagrangian transport models, Wood and Baptista, 1995) to 10^{-7} m. Two sets of simulations were performed, using double and quadruple precision, and statistics of the distance between particle positions in the two sets of runs at each time step were calculated (Figure 6.2a). This analysis revealed that a very small ϵ is necessary to avoid fast error accumulation: for instance, for $\epsilon = 10^{-3}$ m and after only 5 days, average distances are of the order of 0.5 km.

Closing errors were then calculated by tracking backwards in time the final position for each particle. Statistics of the closing errors (defined as the distance between the release location and the backward tracked position) confirm that a very small ϵ is manda-

tory for a small closing error (Figure 6.2b). Therefore, we adopted $\epsilon = 10^{-7}$ m in our RT analysis.

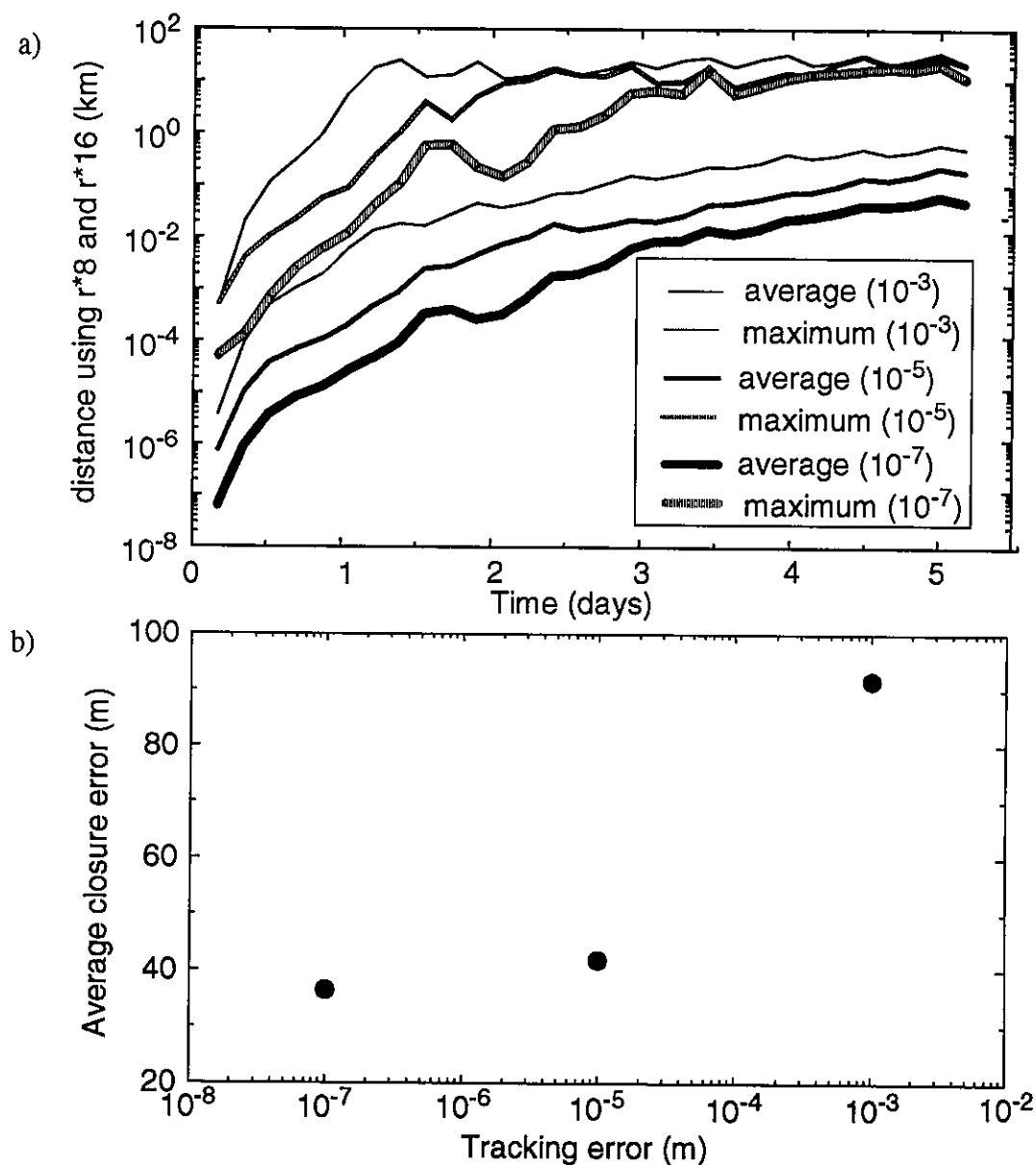


Figure 6.2 Effect of tracking accuracy: a) Statistics of distance between particle positions in real*8 and real*16 runs, for 10 M_2 cycles. b) Closing errors.

The effect of the accuracy of the flow field on RT calculations is more complex to evaluate as several factors are involved: the physics being included in the flow simulation (e.g. exclusion of some physical processes, choice of dimensionality of the models, topological simplification of the domain) and numerical aspects (e.g., grid refinement, calibra-

tion coefficients). Rather than presenting an exhaustive analysis of the effect of each accuracy factor, our goal here is to illustrate that the accuracy of RT calculations depends significantly on the quality of the driving flow field, and therefore, caution must be exercised on practical applications of the proposed concept. In this context, we look at the effect of advection and of the use of two levels of grid refinement. Flow simulations for this analysis, as well as all other flow fields used in this paper, were generated using ADCIRC (Luettich et al., 1991), a time-domain, finite element generalized wave continuity equation model.

First, we examine the effect of excluding momentum advection from the flow simulation on RT calculations for both tracers. For the re-entrant tracer, we compare the RT for 320 particles released close to the mouth of the Tagus estuary (where advection plays a major role, Fortunato et al., 1997), driven either by a fully non-linear flow field or by a contrasting flow field without advection. Histograms of RTs for both runs reveal that the difference is quite significant (Figure 6.3). For the once-through tracer, we extended this analysis for a larger area and calculated RTs for particles spread from the mouth to the end of the channel, separated by 50m, driven by the same flow fields. Maps of RTs reveal that distinct forcings lead to considerably different results (Figure 6.4a-b).

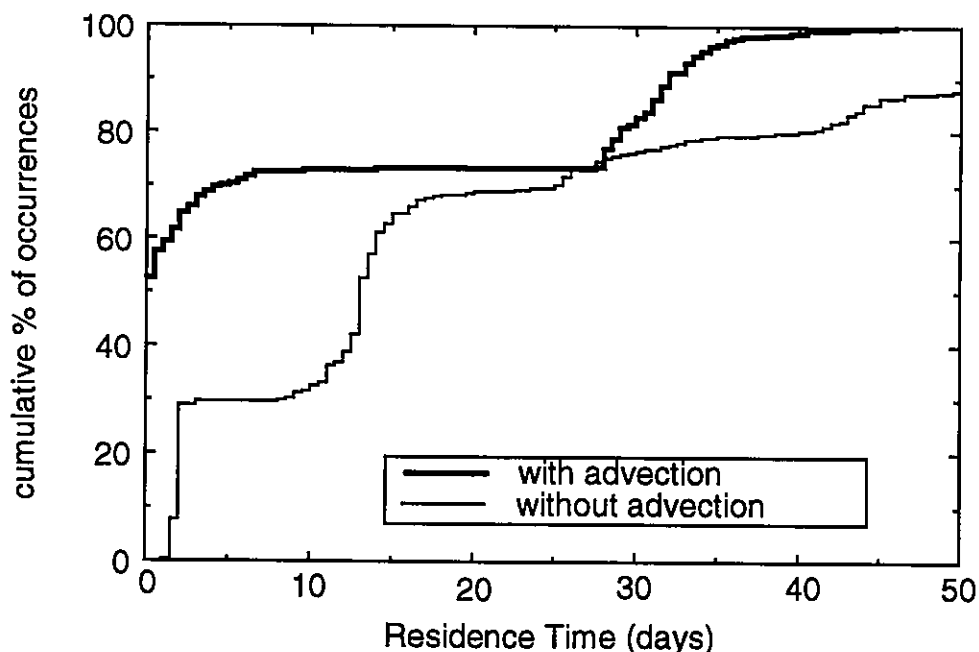


Figure 6.3 Accuracy analysis - effect of advection for the re-entrant tracer

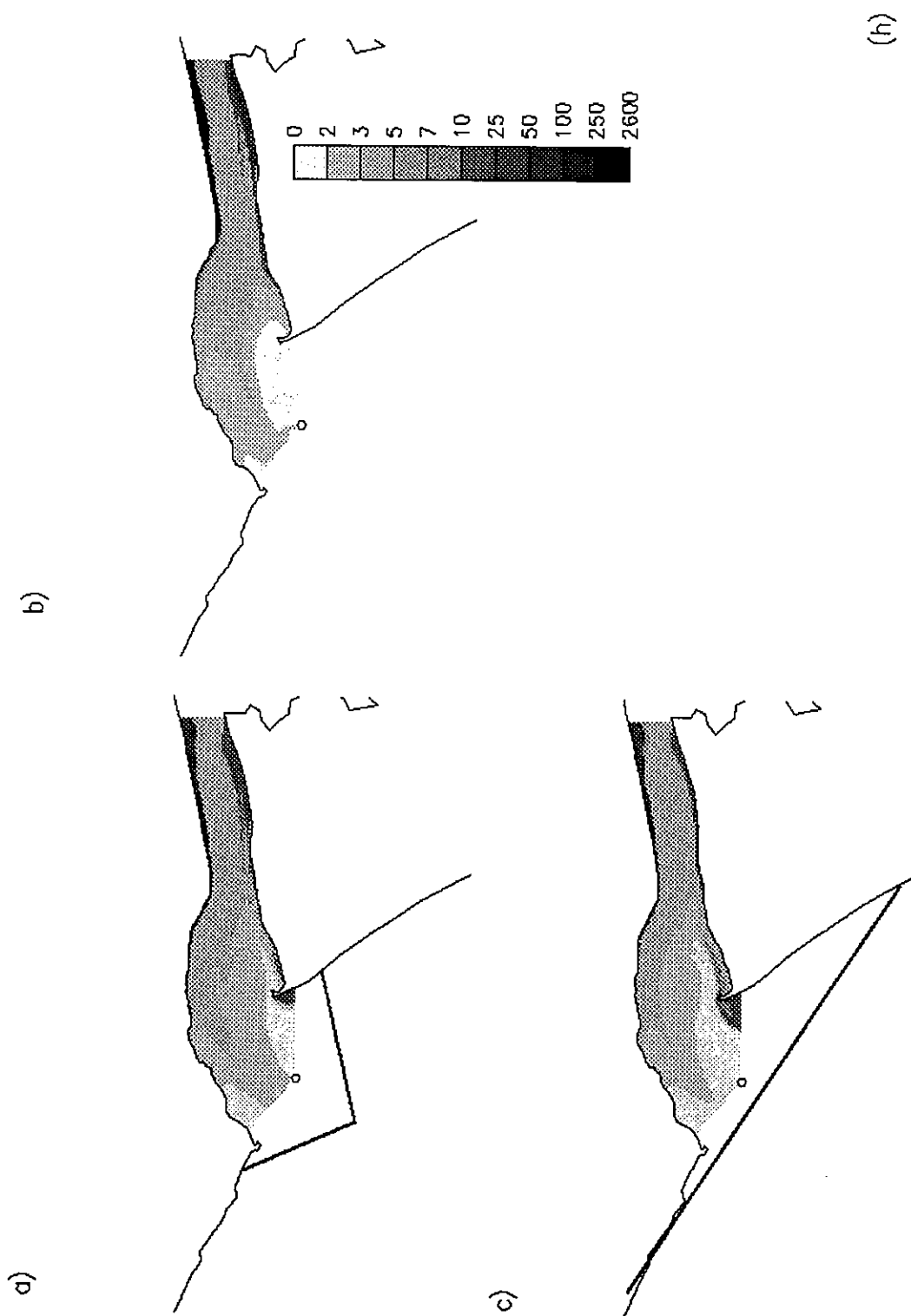


Figure 6.4 Accuracy analysis - effect of advection and the shape of the control region: a) reference control region, with advection. b) reference control region, without advection. c) alternative control region.

Numerical aspects, such as grid refinement, can also have an important impact on RT calculations. We compare re-entrant RT for the same 320 particles for two grids: the first grid was used in the analysis of tides and currents reported in Fortunato et al. (1997) (where results were calibrated and validated with field data); the second grid was obtained from the first splitting into 4 all elements downstream of the control region (thus allowing a better resolution of flow patterns outside the estuary). Figure 6.5 shows that histograms of RTs for the two situations are quite different. This simplified analysis thus emphasizes that care is also necessary to prevent inaccurate results due to insufficient grid resolution, even when using grids that are sufficiently refined for other purposes. We expect that grid resolution will be a factor up to the point where all notable physical features are properly resolved.

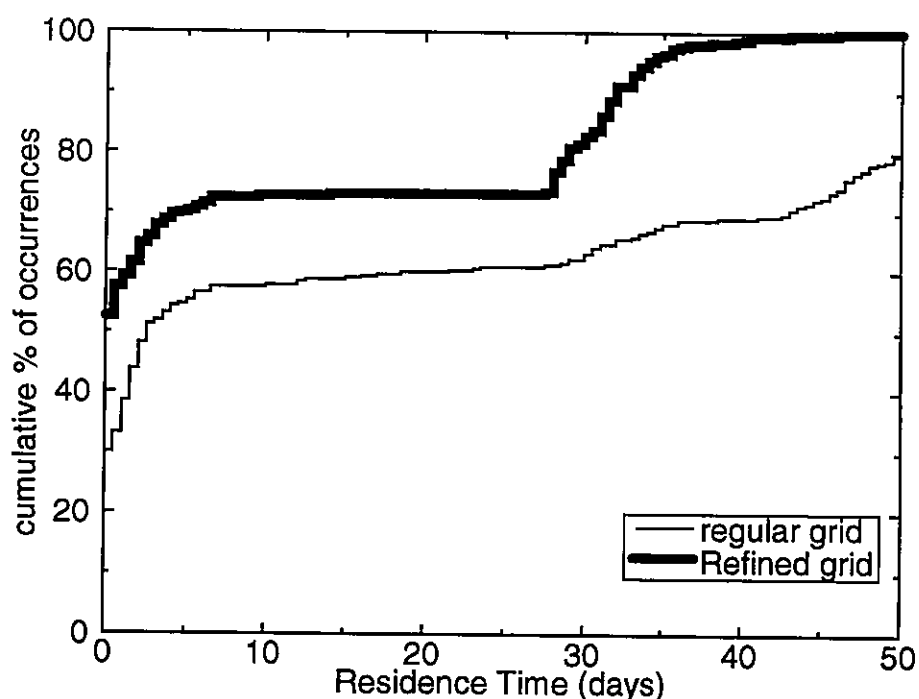


Figure 6.5 Accuracy analysis - effect of grid refinement for the re-entrant tracer.

For the once-through tracer, the shape of the downstream limit of the control region can potentially affect RT distributions (this should not affect re-entrant tracers, because RTs are much longer, and the effect of the shape of the control region is smoothed as the particles re-enter the system). To test the importance of this factor, we repeated the

calculations shown in Figure 6.4a, for a new limit of the control region (Figure 6.4c). Results show that the change in the shape of the control region only mildly affects particles located very close to the limit of the control region.

6.5 Diagnostic characterization of residence times

We now use particle models to characterize RTs in the Tagus estuary, whose circulation is simplified to the level described by a two-dimensional, depth-averaged, barotropic model (Fortunato et al., 1997). Our analysis is diagnostic and exploratory, and should not be regarded as an attempt to characterize RTs in the Tagus. In particular, we note that important processes such as inundation and baroclinic and wind forcings were not accounted for. Time variability of the river discharge was also neglected, which can affect residual velocities considerably and thus are expected to alter RTs.

Different approaches were used to characterize the distributions of the two types of tracers (re-entrant and once-through) considered in this analysis, as a result of their different nature. Therefore, results and discussion for the two tracers are held separately.

6.5.1 Re-entrant Tracer

6.5.1.1 Experiment Set-up

To assess the spatial variability of RTs, we identified 10 key regions with distinct flow characteristics. In each of these regions, with an area of approximately $1 \times 1 \text{ km}^2$, we released simultaneously, at selected times, an average of 400 particles, in $50 \times 50 \text{ m}^2$ grid arrangements (Figure 6.1b). RTs were computed for each particle, and associated statistics were determined within each region. In particular, we evaluated means and standard deviations, and, more meaningfully for the purpose of this study, we built histograms and cumulative histograms.

Dependence of RTs on release time within the tidal cycle was analyzed for both spring and neap tides. For all regions, twelve release times, one hour apart, were simulated

starting at high-water at Bugio (Figure 6.1b), for a spring tide and a river discharge of $4000 \text{ m}^3/\text{s}$. The influence of spring/neap cycles was then assessed for region 1 for the first release time, by repeating the simulation for a neap tide.

Spatial variability of RTs was analyzed by integrating the results for the twelve release times in each region, while time variability within the tidal cycle was assessed by integrating RTs for all regions in space, for each release time.

The dependence of RT distributions on river flow was analyzed by contrasting the minimum, mean and maximum monthly-averaged river discharges of 40, 400 and $4000 \text{ m}^3/\text{s}$, respectively. RT runs were then driven by these flow fields, for the first release time in all regions, and for all release times for region 1.

6.5.1.2 Spatial Variability of Residence Times

Histograms show that RTs vary strongly within each region (Figure 6.6a) and from region to region (Figure 6.7). The latter variation is expected, the need for its systematic illustration having originally motivated the present research. However, the strong variation within each region is less intuitive. The explanation lies in the fact that when particles are exchanged with the coastal ocean and re-enter the estuary at a later tidal cycle, they are effectively re-seeded in space and time.

A mechanism that is effective in dispersing particles originally released very close to each other is *chaotic stirring*. Chaotic stirring, generated by the interaction between tidal and residual flows and magnified by increasing ratios of tidal excursion over the characteristic length scale of residual eddies (Ridderinkhof and Loder, 1994), is common in estuaries and is very important at the mouth of the Tagus (Fortunato et al., 1997).

The strong variation within each release region prevents mean and standard deviation from being representative statistical indices for RTs (Figure 6.6a). Histograms (Figure 6.6b), while more complex for comparative analysis, synthesize information in a way that allows meaningful RT differentiation among regions and in time.

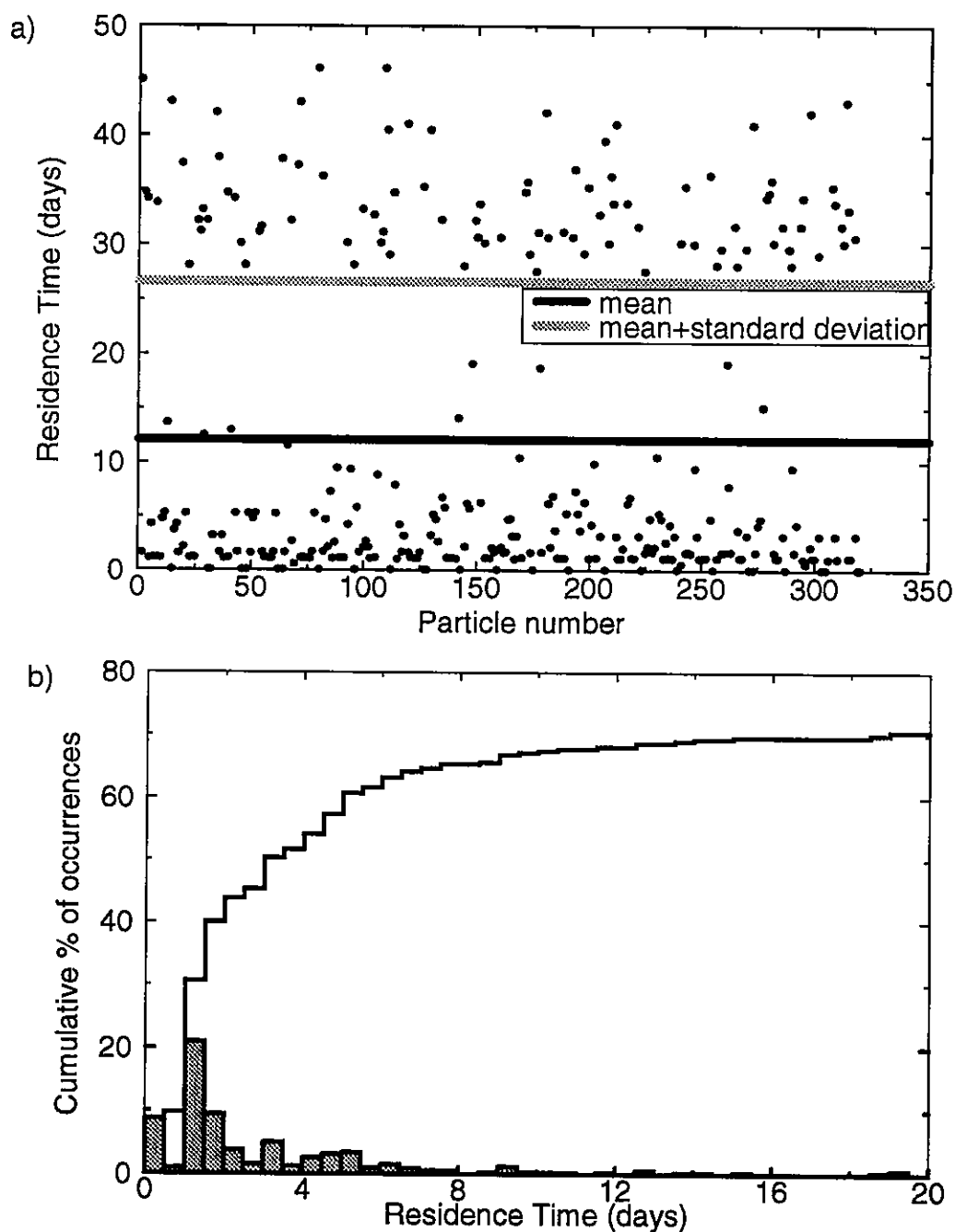


Figure 6.6 RTs for region 1 and release time 2 for the re-entrant tracer: a) Individual and statistics of RTs. b) Histogram and cumulative histogram of RTs.

Variability of RTs among different regions is closely related to the complexity of the circulation and of the geometry of the estuary, and to the location of the release region relative to the mouth. Several interesting patterns emerge from Figure 6.7: most particles released from regions close to the mouth (1, 2 and 6) leave the control region within the

first 2 days, with a considerable percentage effectively leaving in the first 12 hours. For the upper estuary regions (3,4 and 10), by contrast, it takes 2-3 days for any particle to actually leave the control region, and most particles take up to 6 days to be removed.

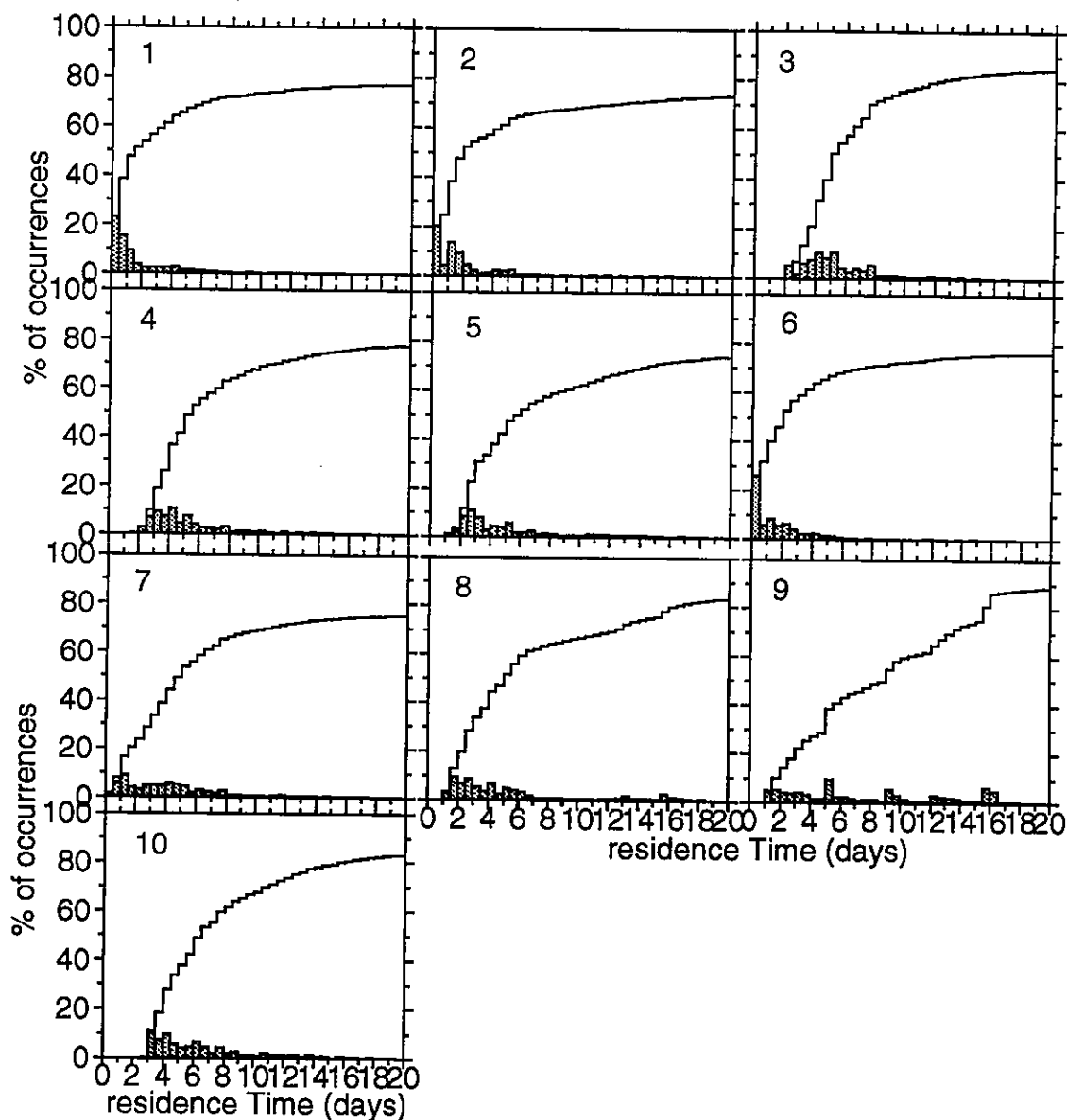


Figure 6.7 Variability of RT in space.

Particles released in lateral bays (e.g., region 9) show great diversity of behavior, translated into active particle removal occurring over a period of 15 days. This pattern can be explained by the large dispersion that occurs in these areas, as a result of exchanges between the lateral bays and the main estuary: some particles leave one bay and enter a

neighboring bay, thus taking a long time to leave the system, while other particles get into the main channel and quickly exit the control region. This behavior can be readily expected by examining the velocities in the lateral bays area (Figure 6.8), where strong spatial gradients are apparent throughout the tidal cycle.

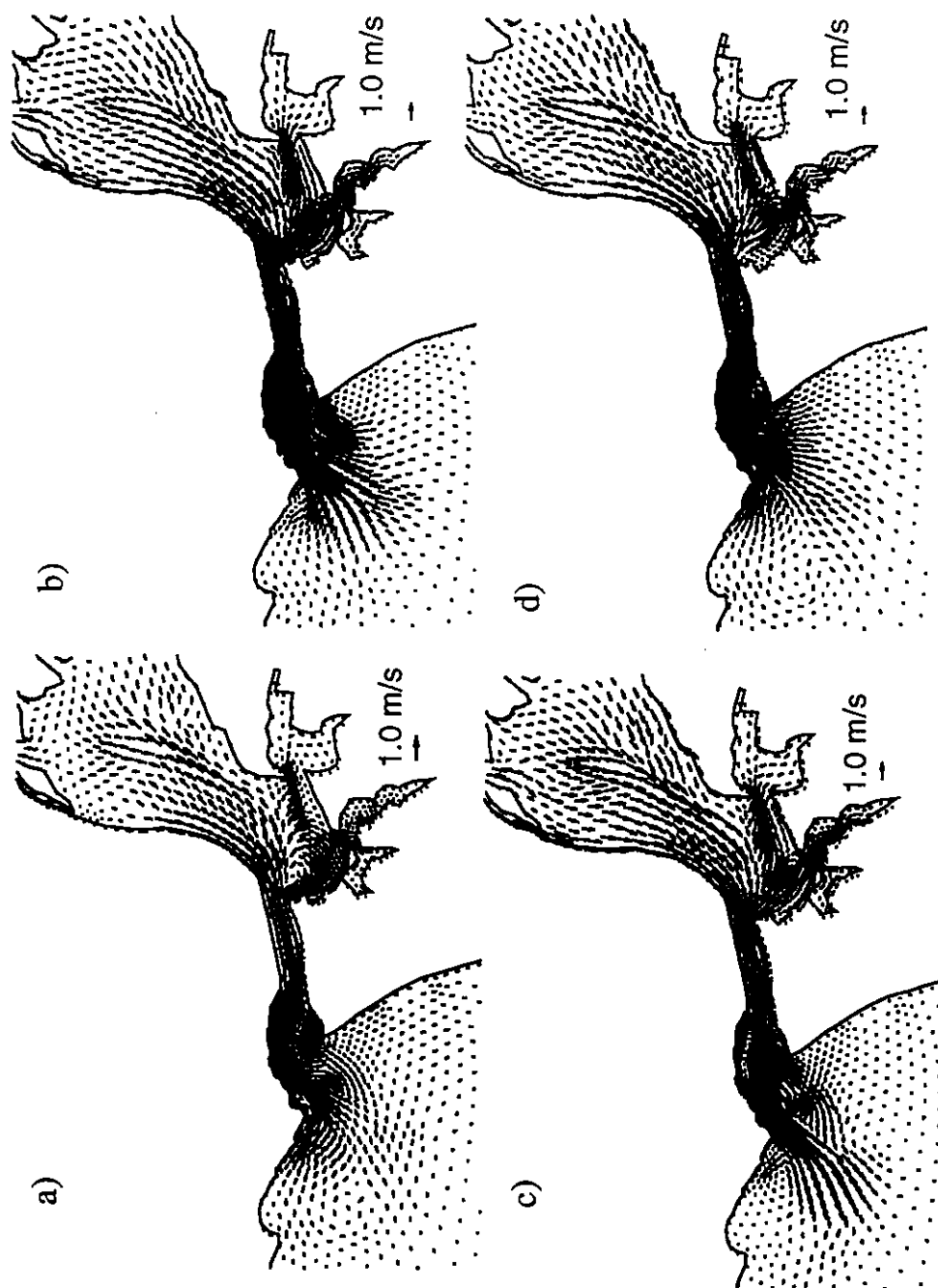


Figure 6.8 Snapshots of the forcing flow field for selected release times: a) release time 1. b) release time 4. c) release time 6. d) release time 11.

Our analysis also suggests that, in presence of strong exchanges either with the coastal ocean or with lateral bays, the effectiveness of attaching disposal strategies to particular locations and tidal stages can be substantially reduced for conservative and slow-decaying tracers, particularly when high percentage removal is required. This becomes apparent by observing, for instance, that different regions reach low removal percentages at very different times (Figure 6.7), while for all regions full removal requires essentially the same amount of time (about 45 days, not shown)

6.5.1.3 Influence of release time (within the tidal cycle and for spring/neap tides)

Within a tidal cycle, the time of release has noticeable influence on RT histograms for a specific region, in particular for regions near the mouth where early particle removal is more substantial (Figure 6.9a). Ebb is, as expected, the most effective release time for shorter RTs. The effect of release time within a tidal cycle becomes less significant for releases in the upper estuary, because an increasing number of particles tend to remain in the control region at least one full tidal cycle, allowing internal re-seeding from a tidal cycle to the next (Figure 6.9a).

Because of the complexity of the spatial and temporal patterns of circulation, the behavior of each region relative to release time within a tidal cycle is distinct, implying that the integrated behavior over all regions actually shows only very moderate dependence on release time (Figure 6.9b).

RTs also vary considerably with the tidal coefficient. Comparison of RTs for region 1 and release at high water, reveals that different cumulative histograms are obtained for neap and spring tides (Figure 6.10). Interestingly, larger tidal coefficients do not always lead to faster removal of particles. While not completely intuitive at first sight, this behavior is indeed logical: given the much larger tidal excursions of spring tides, particles are either removed quickly, or else re-seeded far upstream in the estuary, depending on the time of release within the tidal cycle.

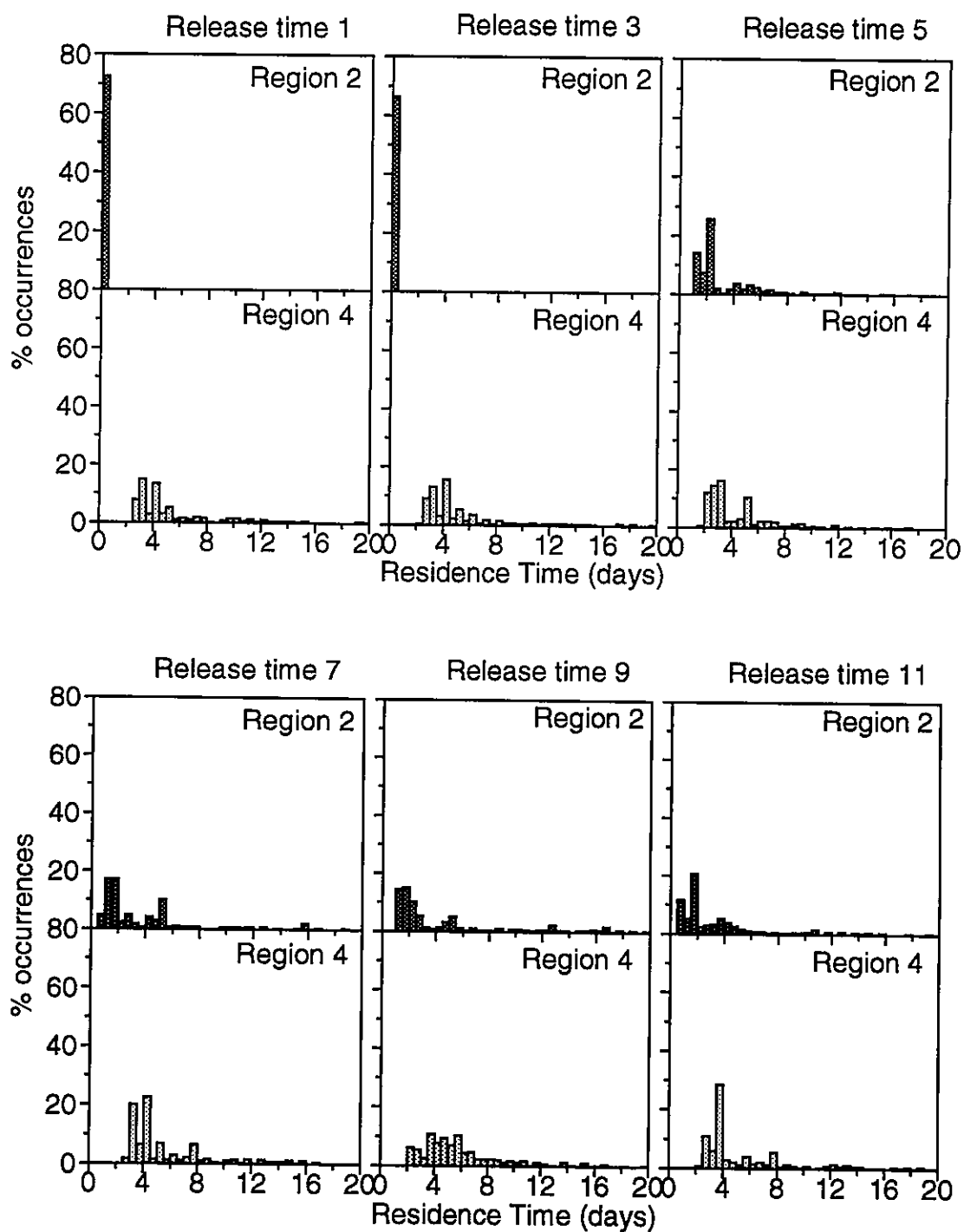


Figure 6.9 Variability of RT in time for every other release time. a) in region 2 and 4.

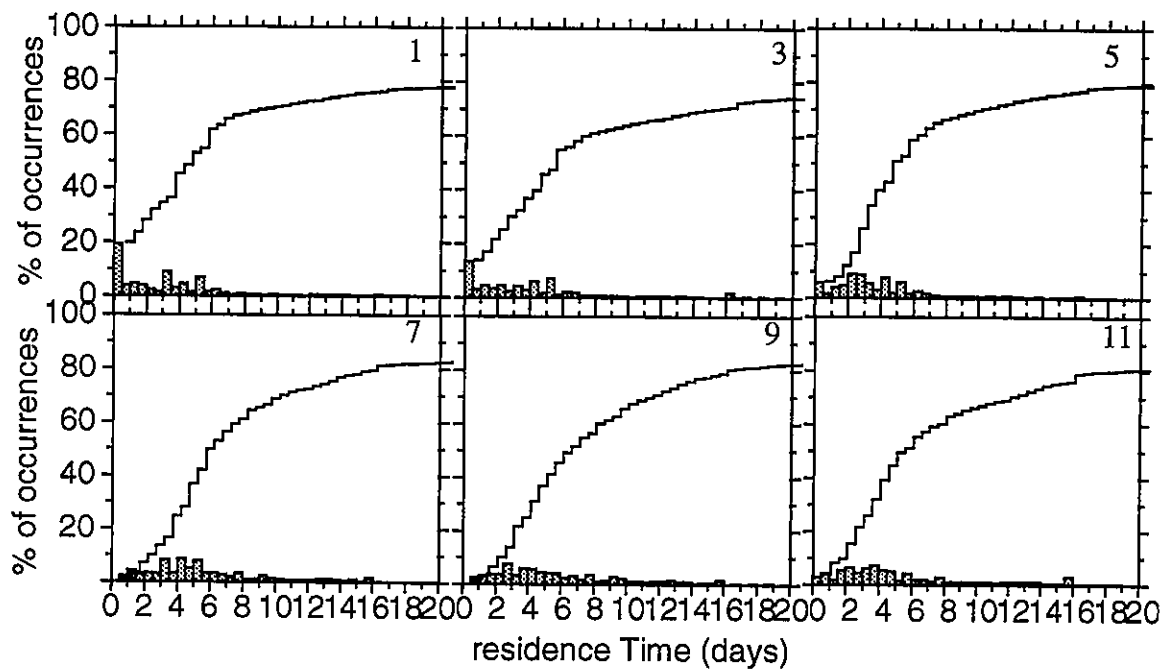


Figure 6.9 Variability of RT in time for every other release time. b) integrated over all regions.

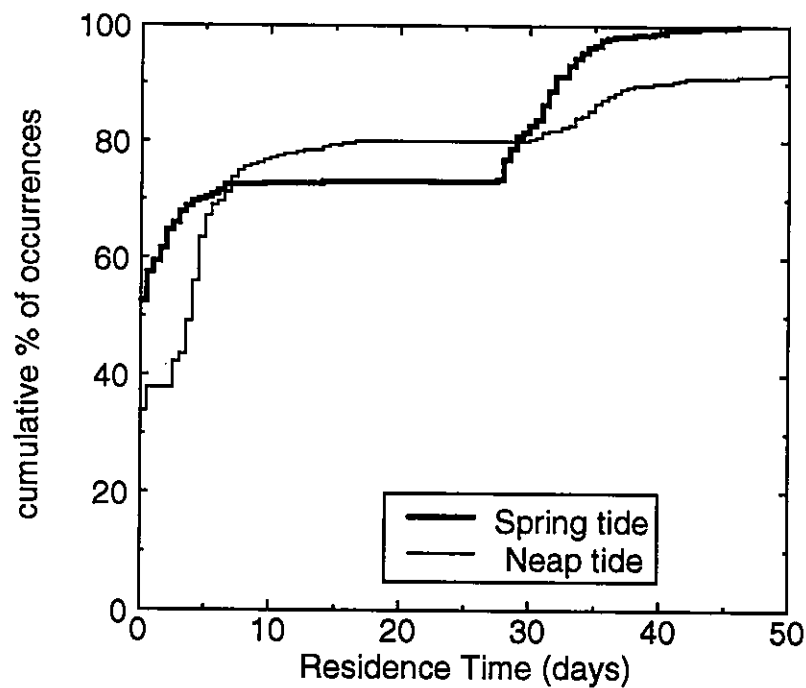


Figure 6.10 Histograms of RTs for region 1, release time 1, for a spring and a neap tides.

6.5.1.4 Influence of river flow

Large river discharges are expected to lead to smaller RTs. Our results generally support these expectations (Figures 6.11a and 6.11c). However they also show that the influence of river discharge depends on both the location and time of release, and that *locally* RTs may, due to the complexity of tide/river interaction, be higher for larger rather than for smaller river discharges (Figures 6.11b and 6.11d).

The observed deviations from an inverse relationship between river flow and RTs can have important consequences from an ecological view point. For instance, after a rain storm event that brings pollutants into the estuary by run-off, the increase in river flow would be expected to accelerate the estuary's clean-up; our results suggest that this may not happen in some areas and actually a longer period may be necessary to remove the pollutant from the system.

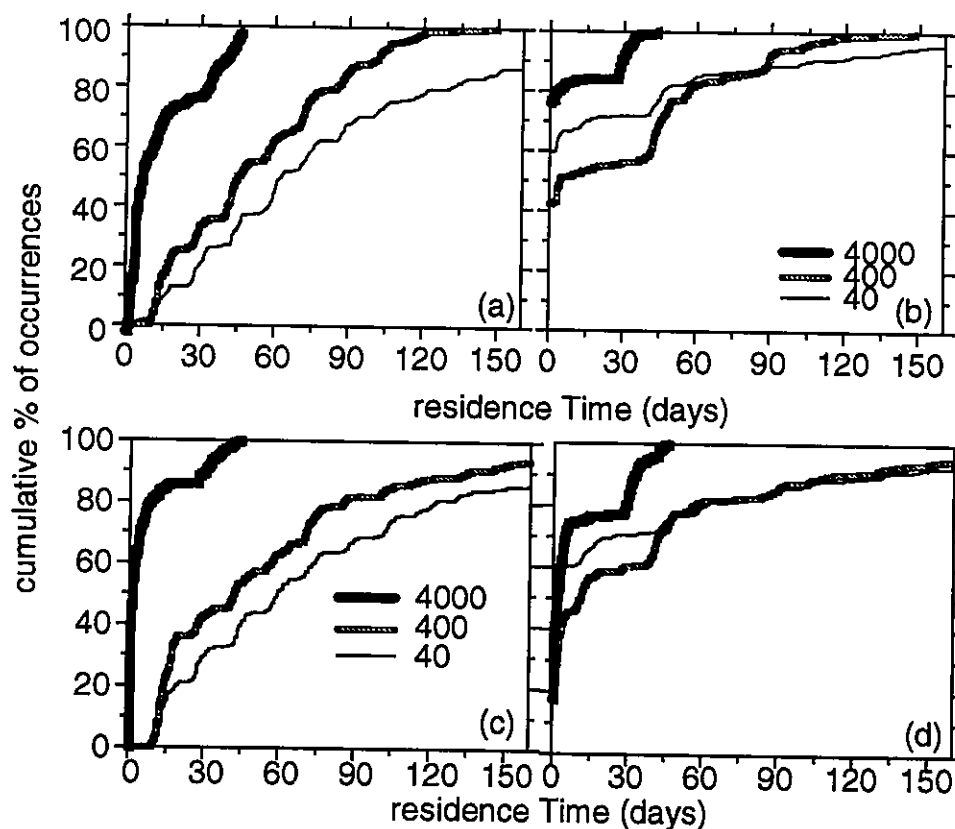


Figure 6.11 Histograms of RTs for a river flow of 40, 400 and 4000 m³/s. a) release time 1, for region 5. b) release time 1, for region 6. c) region 1, for release time 8. d) region 1, for release time 12.

6.5.1.5 Integral analysis

We now analyze the extent to which particle tracking can be used to describe the global flushing properties of an estuary, and contrast our method with traditional “single-number” approaches based on equation (6.2). We start by integrating RTs for all release times at all regions into a single histogram (Figure 6.12), for river discharges of 400 and 4000 m³/s. We then ran a transport model (Baptista et al., 1984) to estimate the average salinity necessary for calculating the RT with equation (6.2). The model was run for 50 days, imposing zero salinity at the upstream boundary and 36‰ at the ocean boundary, and forced by the same flow simulations that we used in our particle-tracking simulations (forced by river discharges of 400 and 4000 m³/s, respectively). The average, volume-weighted salinities were then computed using the last 30 days of simulation. The volume of the estuary was calculated for mean sea level, using the finite element grid of the transport simulations. The use of these values in equation (6.2) leads to a RT of 4.5 days for a river discharge of 4000 m³/s (which is remarkably close to the histogram median of 4.8 days) and a RT of 20.1 days, for a river discharge of 400 m³/s (in contrast to the histogram median of 41.3 days).

RTs based on particle tracking and transport simulations, as described above, were mapped against results of an independent analysis of RT based on the use of equation (6.2) with actual salinity data (reported in Martins et al. (1984)). While we were not looking for a rigorous direct comparison, it is reassuring to observe that both order of magnitude and trends are quite consistent (Figure 6.13).

We conclude from the above discussion that particle tracking followed by histogram analysis provides considerably more information than evaluation of RTs based on equation (6.2), while retaining the potential for simplicity required by comparative studies among estuaries (e.g., through the use of medians).

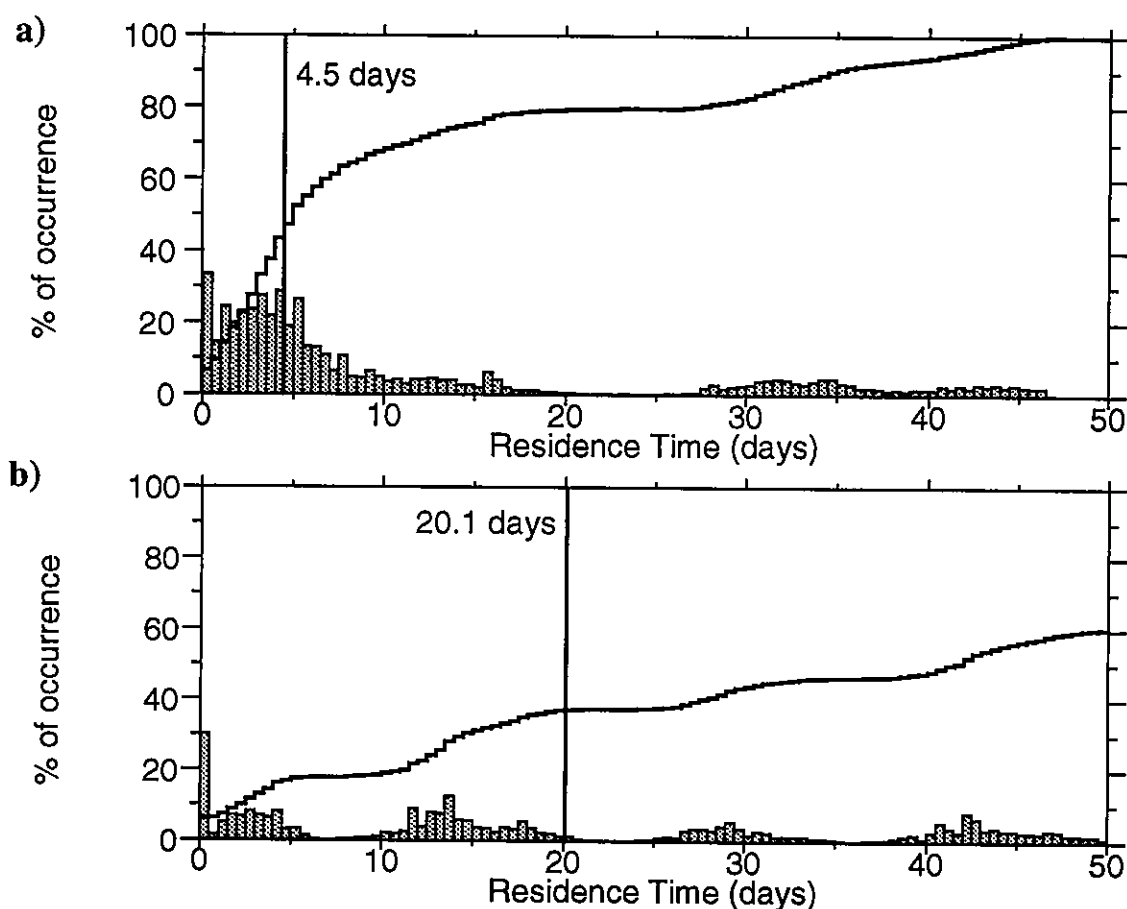


Figure 6.12 Comparison of “single number” RT and histogram calculated with RT results at all release times and all regions. a) 4000 m³/s. b) 400 m³/s. Histograms are multiplied by 5.

6.5.2 Once-through Tracer

6.5.2.1 Experiment set-up

RTs for once-through tracers were initially conceived in the same manner described in the previous section. Early analysis of the results suggested, however, that spatial variation was considerably smoother, prompting us to modify the experimental design. The 50 m grid was extended over the entire domain (rather than over the 10 chosen regions) and post-processing was preferentially deterministic (maps of isolines of RT) rather than statistical. The upper limit on particle location was constrained by the proximity of the upstream boundary, as particles could not be followed or re-introduced, after

leaving the computational domain by the upstream boundary. A narrower range of environmental conditions was analyzed, because our emphasis was placed on the understanding of the spatial variability and the effect of the release time. To make the computational problem manageable, the effect of the release time was further restricted to the channel region, using the same twelve release times used in the re-entrant tracer analysis.

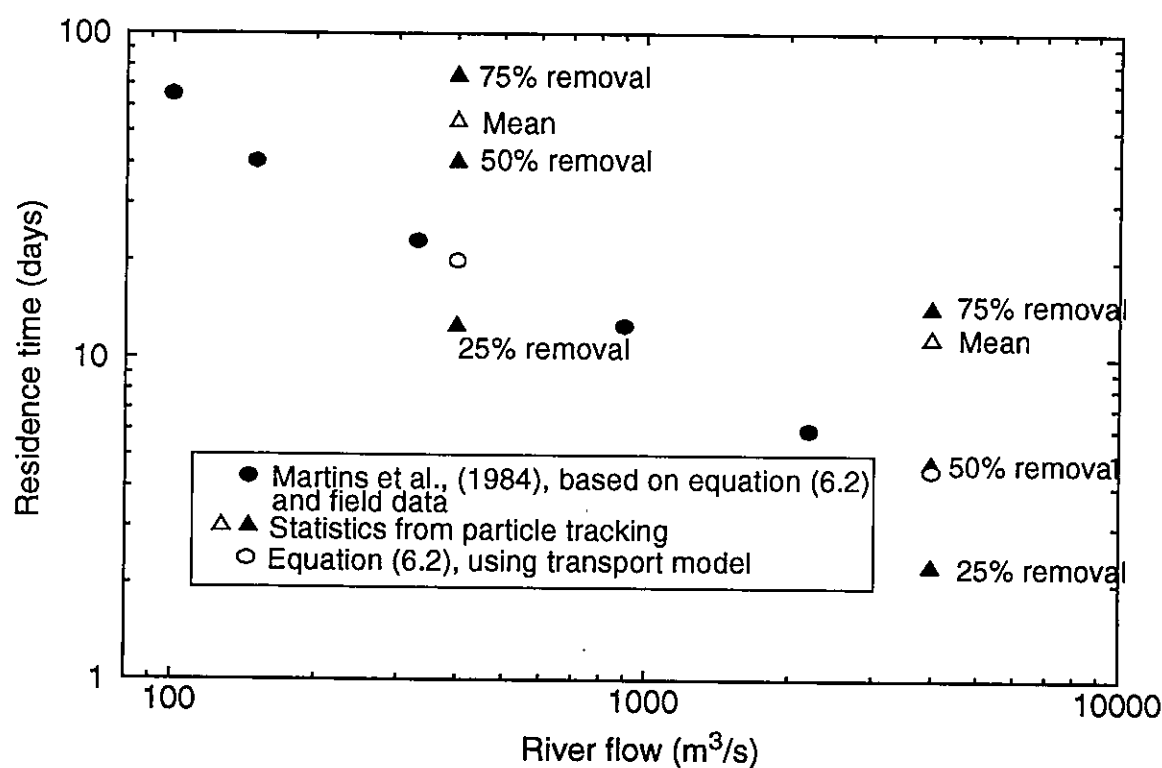


Figure 6.13 RTs versus river flow for integral approach using salinity data (adapted from Martins et al. (1984)) and transport model, and statistics of integrated particle model results (calculated with RTs from all release times and all regions).

6.5.2.2 Spatial Variability of Residence Times

Like for re-entrant tracers, spatial variability of RTs is strong. However, unlike for re-entrant tracers, this variability is fairly smooth, which translates into meaningful maps of RT isolines. The estuary-wide map of RTs for release time 1 (immediately prior to ebb), reveals several expected features (Figure 6.14): larger RTs occur for particles released in the tidal flats and in areas with strong geometric constraints (e.g., lateral bays); shorter RTs are obtained for the region close to the mouth, especially for particles released in the main channel.

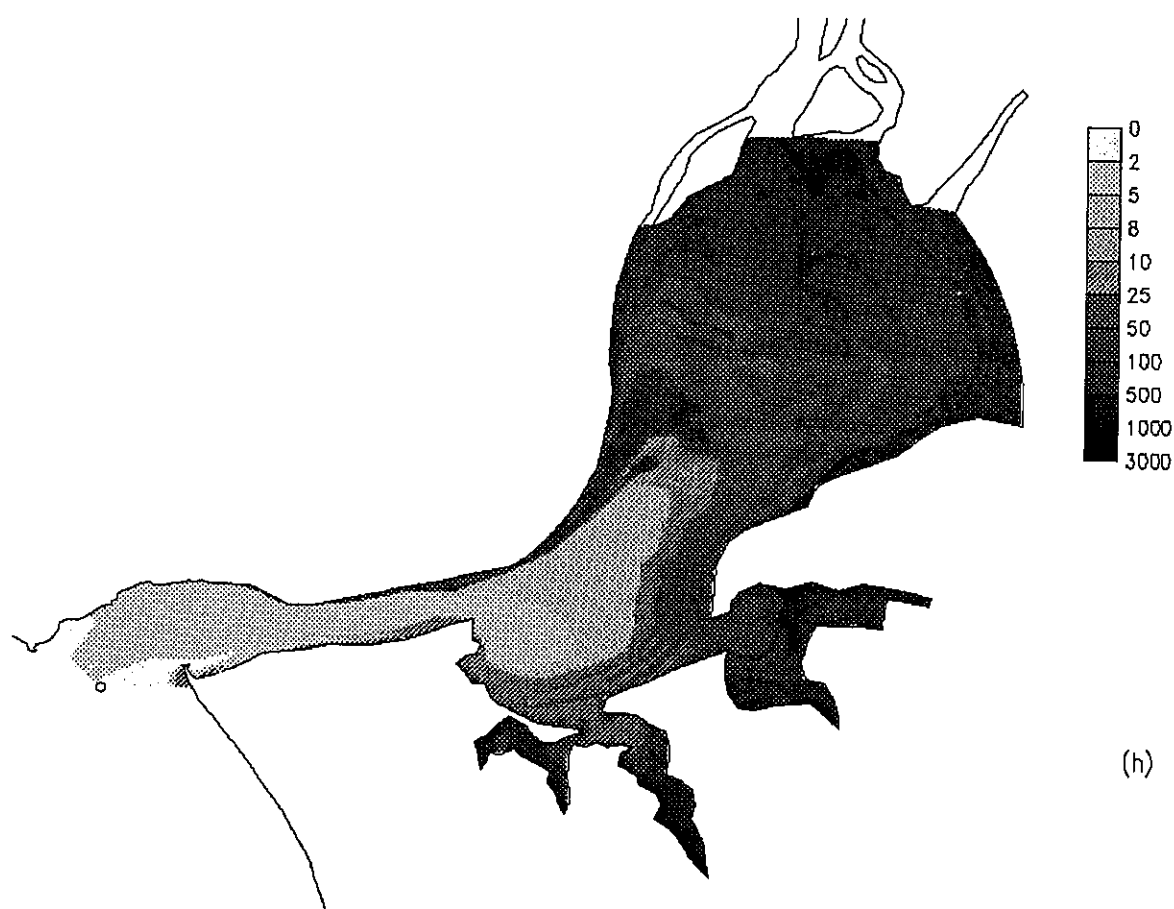


Figure 6.14 Map of RT for the whole estuary at release time 1.

Interesting RT patterns (Figure 6.14) are often associated with the presence of eddies in the complex circulation in the Tagus. In particular, the eddy north of the bays of Seixal and Montijo (Figure 6.8a) is clearly correlated with the fast removal of particles released in that region (e.g., see form of the isolines of 5 and 8 days immediately upstream of the entrance channel).

Differential propagation of tides is also clearly reflected on RTs. For instance, the mouth of the estuary is marked by significant phase differences between tides in the northern and southern margins and tides in the main channel, which map well into local RT isoline patterns (e.g., see light color tip on the RTs downstream of the main channel, Figure 6.15d-g).

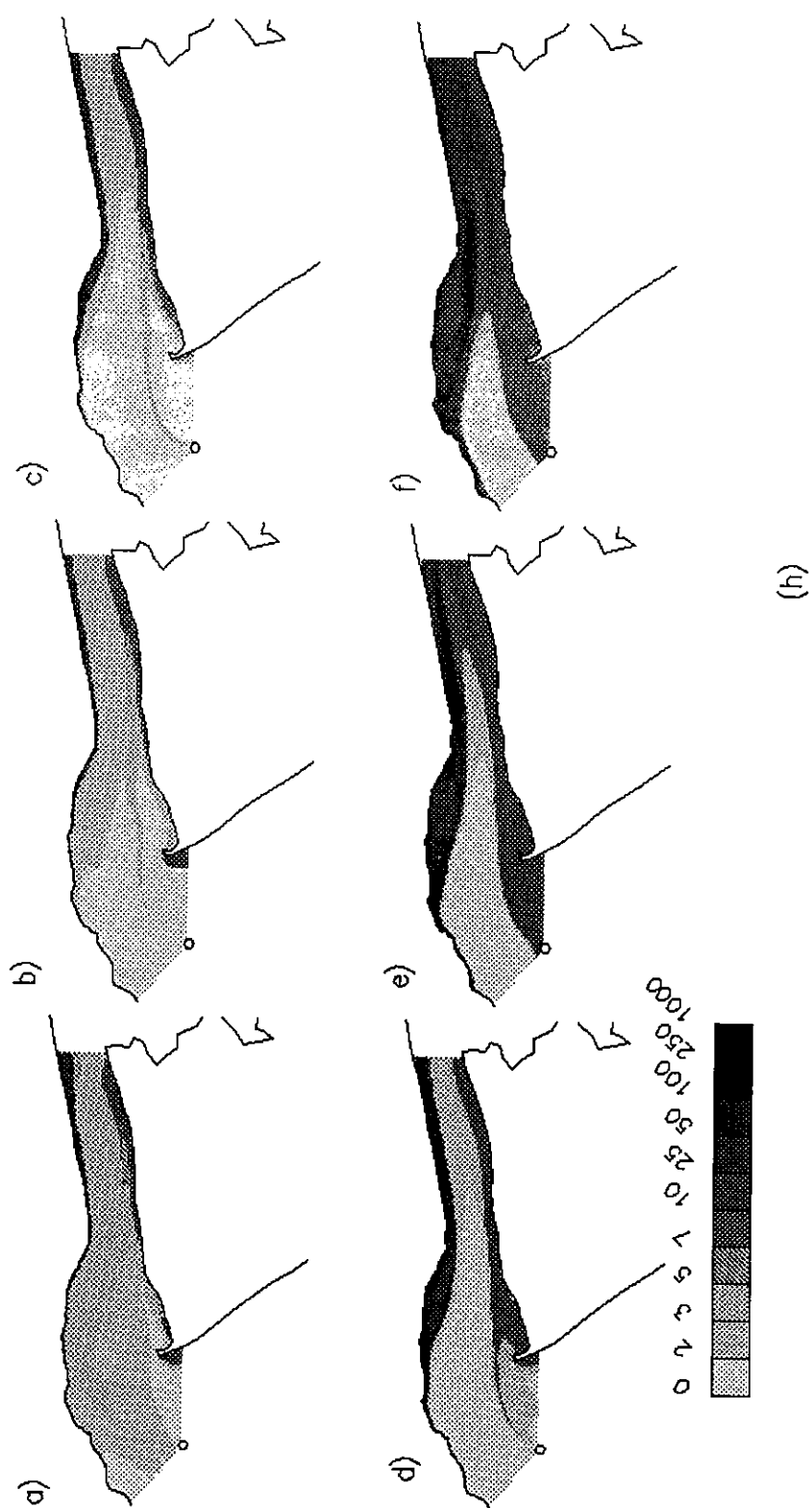


Figure 6.15 Maps of RT for the channel region: a) release time 1; b) release time 2; c) release time 3; d) release time 4; e) release time 5; f) release time 6.

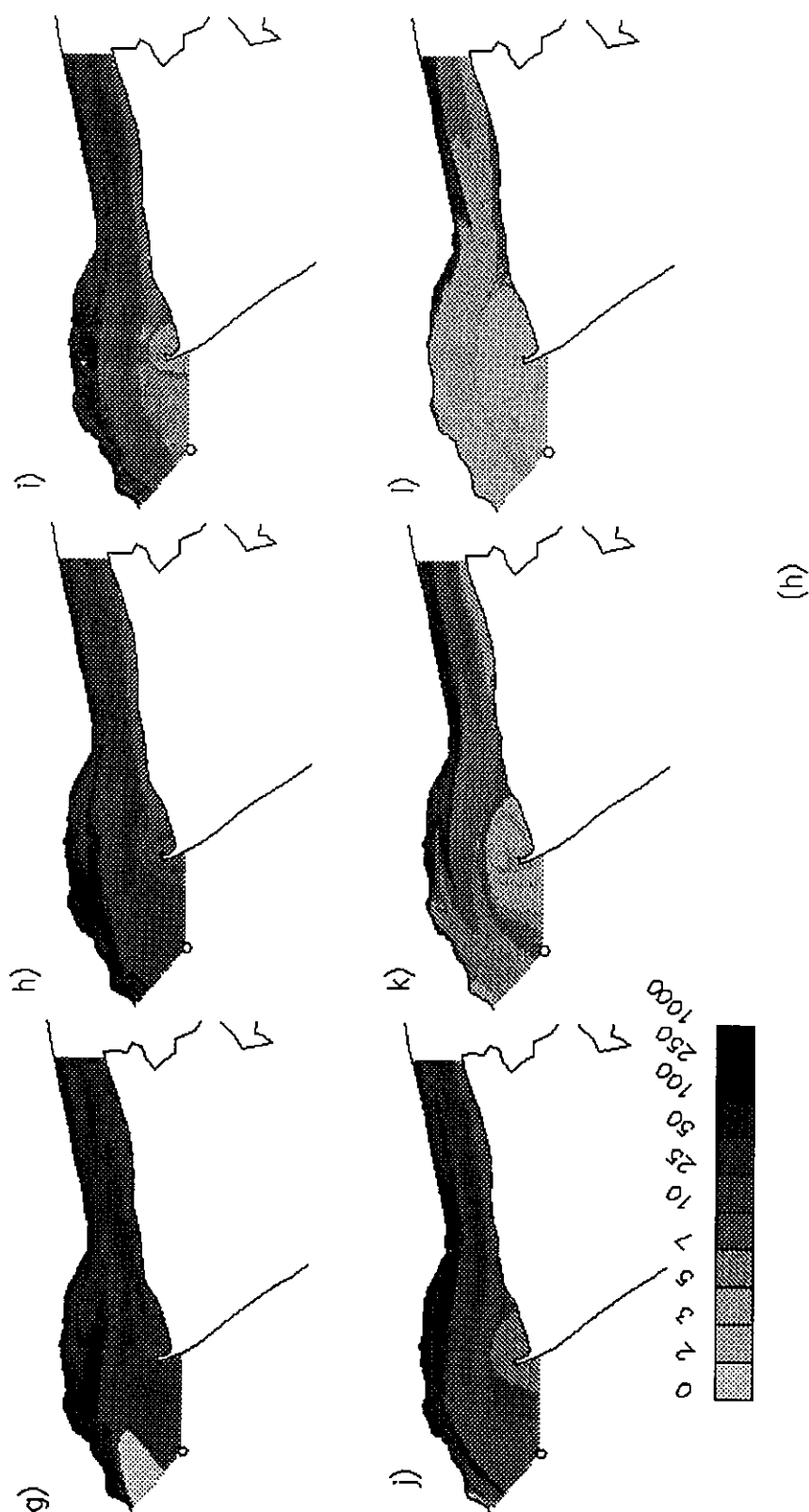


Figure 6.15 Maps of RT for the channel region: g) release time 7; h) release time 8; i) release time 9; j) release time 10; k) release time 11; l) release time 12.

6.5.2.3 Influence of release time

The influence of release time is stronger for once-through tracers than for re-entrant tracers. This influence is shown clearly on Figure 6.15. In particular: (i) larger RTs are found for flood releases (e.g., Figure 6.15g) than for ebb releases (Figures 6.15b); and (ii) the time of formation and destruction of eddies is clearly imprinted in the sequence of RT maps corresponding to the various release times.

RT means and standard deviations (Figure 6.16) are of the same order of magnitude, thus revealing a strong time variability. However, statistically aggregated patterns are not as clearly flow-dependent as patterns for individual release times. Noteworthy is the fact that overall spatial patterns are similar for both RT means and standard deviations: areas with larger means, have larger standard deviations, and areas with smaller means also have smaller standard deviations. This appears consistent with the fact that longer RTs allow for more effective dispersal of particles, i.e., significant re-seeding within the estuary from one tide to the next, hence leading to increasing variability of RTs among particles.

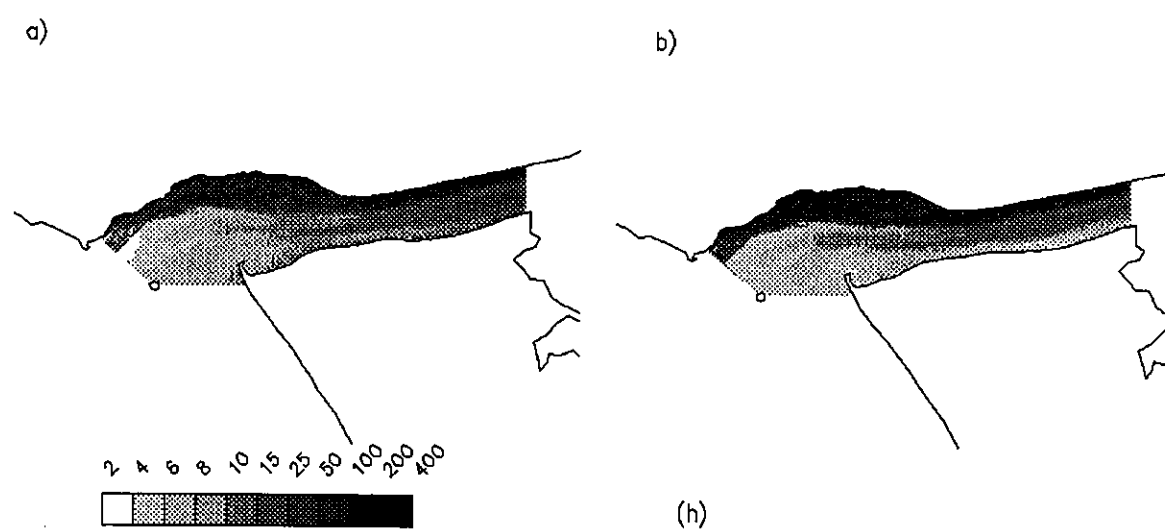


Figure 6.16 Maps of RT statistics. a) mean. b) standard deviation.

6.6 Conclusions

Our analysis provides conceptual insights on the spatial and temporal variability of residence times in estuaries. In particular:

- The spatial distribution of RT in an estuary is fairly smooth prior to exchanges with the coastal ocean. Chaotic stirring in this exchange destroys the smoothness (Figure 6.6), leading to spatial variability that is not interpretable except in a statistically aggregate sense (Figures 6.7 and 6.9);
- Regions of distinct geometry/flow regime tend to behave as “units” with regard to RTs. Hence, even if a single residence time rarely characterizes a whole estuary appropriately, the notion of RT for distinct sub-units appears quite valuable;
- The time of release over the tidal cycle is an important control for RTs prior to exchange with the coastal ocean (Figure 6.15). Once the exchange takes place, the importance of this factor is considerably reduced (Figure 6.9);
- While increasing river discharges tend to reduce RTs (Figure 6.11a and c), factors such as exchange with the coastal ocean may lead locally to counter-intuitive opposite behavior (Figure 6.11b and d).

A common thread in the above remarks is that the complexity of the characterization of residence time increases dramatically once exchanges with the coastal ocean take place. An implication is that different methods may have to be used depending on whether this exchange is included in the definition of RT. For instance, deployment of one or a small number of drifters is meaningless if coastal exchanges are to be accounted for, given the larger number of devices that would be required for a statistical smoothing.

With regard to the use of numerical particle tracking methods for the analysis of residence times, we conclude that:

- these methods are excellent tools for conceptualization and diagnostic analysis; quantitatively, though, they are only as good as the supporting flow fields;

- the accuracy of the tracking algorithm should be extremely high to avoid important errors, in particular if chaotic stirring is a factor; the use of low accuracy algorithms is strongly discouraged even for conceptual analysis;
- these methods extend the applicability of the concept of RT as defined by integral methods, to a broader range of situations that do not require scaling with regard to a main riverine source.

References

- Baptista, A.M., E.E. Adams, and K.D. Stolzenbach, 1984. *Eulerian- Lagrangian analysis of pollutant transport in shallow water*, Technical Report no. 296, MIT R.M. Parsons Laboratory, Cambridge.
- Casulli, V. and R.T. Cheng, 1992. Semi-implicit finite difference methods for three-dimensional shallow water flow, *International Journal for Numerical Methods in Fluids*, 15(6): 629-648.
- Delesalle, B. and A. Sournia, 1992. Residence Time of Water and Phytoplankton Biomass in Coral Reef Lagoons, *Continental Shelf Research*, 12(7/8): 939-949.
- Dimou, K., and E.E. Adams, 1989. 2-D Particle Tracking Model for Estuary Mixing, in *Estuarine and Coastal Modeling*, M.L. Spaulding (editor), American Society of Civil Engineers, 472-481.
- Fairbridge, R.W., 1980. The estuary: its definition and geodynamic cycle, in *Chemistry and Biogeochemistry of Estuaries*, E. Olausson and I. Cato (editors), John Wiley and Sons, New York, 1-36.
- Foreman, M.G.G., A.M. Baptista and R.A. Walters, 1992. Tidal Model Studies of Particle Trajectories Around a Shallow Coastal Bank, *Atmosphere-Ocean*, 30(1): 43-69.
- Fortunato, A.B., A.M. Baptista and R.A. Luettich, Jr., 1997. A Three-Dimensional Model of Tidal Currents at the Mouth of the Tagus Estuary (Portugal), *Continental Shelf Research* (in press).
- Hofmann, E.E., K.S. Hedstrom, J.R. Moisan, D.B. Haidvogel and D.L. Mackas, 1991. Use of Simulated Drifter Tracks to Investigate General Transport Patterns and Residence Times in the Coastal Transition Zone, *Journal of Geophysical Research*, 96(C8): 15,041-15,052.

- Jay, D., 1994. Residence Times, Box Models and Shear Fluxes in Tidal Channel Flows, in *Changes in Fluxes in Estuaries*, K.R. Dyer and R.J. Orth, (editors), Olsen and Olsen, Fredensborg, Denmark, 3-12.
- Jay, D., W.R. Geyer and D.R. Montgomery, 1995. An Ecological Approach to Estuarine Classification, in *Estuarine Synthesis*, J. Hobbie (editor), Scientific Committee on the Problems of the Environment, (submitted).
- Luetlich, Jr., R.A., J.J. Westerink and N.W. Sheffner, 1991. *ADCIRC: An Advanced Three-Dimensional Circulation Model for Shelves, Coasts and Estuaries. Report 1: Theory and Methodology of ADCIRC-2DDI and ADCIRC-3DL*. Department of the Army, US Army Corps of Engineers,
- Martins, M.C.S., J.G. Ferreira, T. Calvão and H. Figueiredo, 1984. Nutrientes no Estuário do Tejo - Comparação da situação em Caudais Médios e em Cheia, com Destaque para Alterações na Qualidade da Água, in *Proceedings do I Simpósio Luso-Brasileiro de Engenharia Sanitária e Ambiental*, Associação Portuguesa de Recursos Hídricos, Lisboa, Portugal, (in Portuguese), n.p.
- Officer, C.B., 1980. Box Models Revisited, in *Estuarine and Wetland Processes*, Hamilton and MacDonald (editors), Plenum Press, New York, 65-114.
- Officer, C.B. and D.R. Kester, 1991. On Estimating the Non-Advective Tidal Exchanges and Advective Gravitational Circulation Exchanges in an Estuary, *Estuarine, Coastal and Shelf Science*, 32(1): 99-103.
- Oliveira, A. and A.M. Baptista, 1997. The role of tracking on Eulerian-Lagrangian solutions of the transport equation, *Advances in Water Resources*, (in press).
- Pilson, M.E., 1985. On the Residence Time of Water in Narragansett Bay, *Estuaries*, 8(1): 2-14.
- Pollock, D.W., 1988. Semianalytical computation of path lines for finite difference models, *Groundwater*, 26(6): 743-750.
- Press, W.H., W.T. Teukolsky, Vetterling and B.P. Flannery, 1992. *Numerical Recipes in Fortran*, Cambridge University Press, New York, 704-716.
- Pritchard, D. W., 1967. Observation of Circulation in Coastal Plain Estuaries, in *Estuaries*, G.H. Lauff (editor), American Association for the Advancement of Science, Publ. 83, Washington, DC, 3-5.

- Ridderinkhof, H. and J.W. Loder, 1994. Lagrangian Characterization of Circulation over Submarine Banks with Application to the Outer Gulf of Maine, *Journal of Physical Oceanography*, 24(6): 1184-1200.
- Salomon, J.C. and M. Pommepuy, 1990. Mathematical Model of Bacterial Contamination of the Morlaix Estuary (France), *Water Research*, 24(8), 983-994.
- Signell, R.P. and W.R. Geyer, 1990. Numerical Simulation of Tidal Dispersion Around a Coastal Headland, in *Coastal and Estuarine Studies: Residual Currents and Long-Term Transport*, 38, R.T. Cheng (editor), American Geophysical Union, Springer-Verlag Publications, Washington, D.C., 210-222.
- Takeoka, H., 1984. Fundamental concepts of exchange and transport time scales in a coastal sea, *Continental Shelf Research*, 3(3): 311-326.
- Van de Kreeke, J., 1988. Dispersion in Shallow Estuaries, in *Hydrodynamics of Estuaries: Estuarine Physics*. Vol. 1, B. Kjerfve (editor), CRC Press Inc, Boca Raton, FL, 28-38.
- Wood, T.M. and A.M. Baptista, 1995. Diagnostic Modeling of Trace Metal Partitioning in South San Francisco Bay, *Limnology and Oceanography*, 40(2), 345-358.
- Wu, J. and I.K. Tsanis, 1994. Pollutant Transport and Residence Time in a Distorted Scale Model and a Numerical Model, *Journal of Hydraulic Research*, 32(4): 583-598.
- Zimmerman, J.T.F, 1988. Estuarine Residence Times, in *Hydrodynamics of Estuaries: Estuarine Physics*. Vol. 1, B. Kjerfve, (editor), CRC Press Inc, Boca Raton, FL, 76-84.

CHAPTER 7

Final Considerations

7.1 Major Contributions

The primary goal of this thesis was to enhance transport modeling in estuarine and coastal systems using Eulerian-Lagrangian methods (ELMs). In spite of ELM's attractive numerical properties, including ability to withstand large Courant numbers, their Lagrangian treatment of advection creates the potential for mass and overall accuracy errors.

Our work (Chapters 2 to 5) analyzes systematically the influence of main sources of errors (non-conservative forcing flow fields, the tracking of the characteristic lines and the evaluation of integrals at the feet of the characteristic lines) on the mass conservation, overall accuracy and stability of ELM transport simulations. To achieve mass conservative, stable and accurate ELM transport simulations in coastal systems, we propose guidelines and solutions to address each source of errors (Chapters 2 to 5), in combination with techniques that extend to two dimensions the flexibility and accuracy of the methods proposed in Oliveira (1994). Specific contributions include:

- We show (Chapter 3) that, in the presence of complex flows, large tracking errors are generated if low-order tracking methods are used (Table 3.4). Tracking errors generate important transport mass errors (Figure 3.4) and severely affect the overall accuracy. Important phase errors appear in presence of inexact tracking, as well as excessive positive and negative numerical diffusion, which in combination with highly-accurate ELMs can lead to an unstable

behaviour (Figure 3.11). Our work recommends thus, the use of accuracy controlled, high order methods in estuarine and coastal simulations.

- We propose and implement a new 2D ELM formulation that targets both mass conservation and overall accuracy, while keeping the flexibility of finite element domain discretization. This new method combines finite volume concepts on a finite element framework and uses a flexible and unconditionally stable quadrature integration at the feet of the characteristic lines (subdivision quadrature integration control volume finite element ELMs, Chapter 2 and Appendix). Distinct numbers of quadrature points can be used in different regions of the domain, which allow for accurate peaks and small negative concentrations.
- We show that errors associated with the evaluation of the integrals at the feet of the characteristic lines are particularly severe in presence of complex flow fields, in particular for quadratic element based formulations, but they can be eliminated with increasing grid refinement (Figure 5.4). A combination of control volume finite element concepts based on linear elements, and subdivision quadrature integration is also effective to reduce integration errors both in simple tests and in a complex estuary (Chapters 2 and 5). This combination leads to substantially better mass balance than traditional quadratic interpolation finite element ELMs while keeping the good overall accuracy and stability of the 1D formulations analyzed in Oliveira (1994) (Figures 5.4 and 5.14). Our work recommends thus, subdivision quadrature control volume finite element methods for multi-dimensional ELM transport simulations of complex systems.
- We show that flow mass errors are the primary concern for ELM coastal applications since current solutions for the transport simulation are powerless to mitigate their effect without jeopardizing the overall accuracy (Chapter 5). We also show that grid refinement on the flow simulations is inadequate to eliminate these errors (Chapter 4).
- We identify bathymetry and geometry complexity, which are common features of estuarine and coastal regions, as the main generators of flow mass errors

(Chapter 4). We show that flow mass errors lead to strong mass imbalances in ELM transport simulations, which can not be eliminated with grid refinement (Chapters 2 and 5). The use of conservative forms of the transport equation (based on the total derivative of the concentration or the total mass in the water column) is also strongly discouraged for coastal systems, since they lead to an unstable behaviour (Chapter 5, Figure 5.18), although they generate mass conservative solutions for simple test cases (Chapter 2, Figure 2.5). Our analysis identifies, thus, conservative flow fields as mandatory for mass conservative ELM transport simulations in estuarine and coastal systems (Chapter 5).

Our secondary goal was to take advantage of the improved numerical techniques to deepen our understanding of coastal systems. The need to quantify the variability of residence times, which is necessary to address many ecological problems that occur locally or result from local physical processes, has been broadly identified, but seldom investigated.

We explore the use of numerical particle methods for diagnostic characterization of the spatial and temporal variability of estuarine residence times of conservative tracers (Chapter 6), as a first step towards a comprehensive analysis of residence times of complex environmental tracers using numerical models. Specific contributions include:

- we propose a new methodology that illustrates the importance of local analysis of residence times (Figure 6.14) and provides an alternative, synthetic yet detailed, approach to the traditional bulk analysis of residence times (Figure 6.12); the proposed methodology extends the applicability of residence time analysis to a broader range of systems that include multiple river inputs and non-point sources, and to systems without river forcing.
- we show that the accuracy of residence times (and all other calculations based on particle tracking) is, however, limited by the quality of the forcing flow field (Figures 6.3 to 6.5), thus reinforcing the diagnostic nature of this type of analysis for most environmental problems.

Overall, this work established the potential of numerical particle models to characterize diagnostically residence times distributions in estuaries and coasts and provided

guidelines and requirements for mass conservative and globally accurate applications of Eulerian-Lagrangian methods. Specifically, we found that:

- accuracy-controlled, high-order tracking methods should be used to avoid mass and overall accuracy errors, and potential for instabilities;
- fine grids and quadrature control volume finite element ELMs should be used to avoid both mass and overall accuracy errors;
- conservative forms of the transport equation should not be used in traditional ELM frameworks (e.g., based on the total derivative of the concentration or the total mass in the water column) because they either introduce overall accuracy errors or lead to instabilities;
- mass conservative flow fields are mandatory to guarantee mass balance of ELM transport simulations.

7.2 Directions for future research

As pointed out in Chapter 1, much remains to be done in the numerical modeling of water quality for estuaries and coasts. A significant concern is related to the quantification of parameters that characterize complex chemical and biological processes, either due to the necessary data being often scarce or due to our limited understanding of the basic processes. In spite of the importance of this problem, the influence of the numerical properties of the models on our modeling ability should not be underestimated, in particular as we move towards more complex problems and simulations on the scale of several years or decades (Cerco and Cole, 1992).

Eulerian-Lagrangian methods offer several advantages for estuarine water quality modeling as they provide an unprecedented flexibility in the coupling of processes with distinct time scales and an efficient framework for long term simulations, since they allow for the use of large time steps. The work presented herein raised some questions regarding the application of ELMs to estuarine modeling that should be pursued in future research. The most important questions are related to the extension of the methods proposed herein to

three-dimensional models and to systems with extensive tidal flats, and, for residence times, the extension to non-conservative tracers. In the next subsections we examine conceptually the effects of each of these problems on mass and accuracy of ELMs, and on the evaluation of residence times.

7.2.1 Mass conservation in flow and transport models

The impact of non-conservative flow fields on ELM transport simulations addressed in Chapter 5 can be further aggravated if tidal flats are taken into account on the flow simulations or if three-dimensional flow models are used. Both two-dimensional finite element flow models with inundation and fully three-dimensional finite element flow models are still in an “development stage” (Westerink and Gray, 1990, Luettich and Westerink, 1995, Beck and Baptista, 1997), and therefore mass conservation is, in general, overshadowed by other accuracy concerns.

7.2.1.1 Influence of inundation

Tidal flats are important features of many estuaries, having a relevant role both from the physical (e.g., they slow down tidal propagation) and the ecological perspectives (e.g, they are often breeding grounds for many species). Accounting for inundation in flow models is, however, a complex problem (Luettich and Westerink, 1995). Excessive computational cost associated with spatially deforming grids and numerical noise generated when grid elements change from “wet” to “dry” on fixed grid methods are some of the operational problems often found (Luettich and Westerink, 1995).

Flow models accounting for tidal flats can also generate important local flow mass errors, in particular at the interface between wet and dry elements (Luettich and Westerink, 1995, Janin, 1995). Several approaches have been proposed to reduce these errors (e.g. element-based wetting/drying methods have been shown to preserve mass better than nodal-based approaches - Luettich and Westerink, 1995), but important errors remain. Similarly to other flow mass errors, tidal flats-induced mass imbalances have the potential to generate mass errors in ELM transport simulations. To illustrate this effect, we examine the flow and

transport mass errors in a Gauss plume simulation in the Tagus estuary, forced by two flow fields, one that accounts for inundation and another that raises all tidal flats to dry level (Fortunato et al., 1997a). Cumulative nodal fractions of maximum local flow mass errors (scaled at each time step by the volume of water) for both cases confirm that tidal flats considerably increase the mass imbalances in the flow simulations (Figure 7.1a). These additional flow mass errors lead to larger transport mass errors (Figure 7.1b).

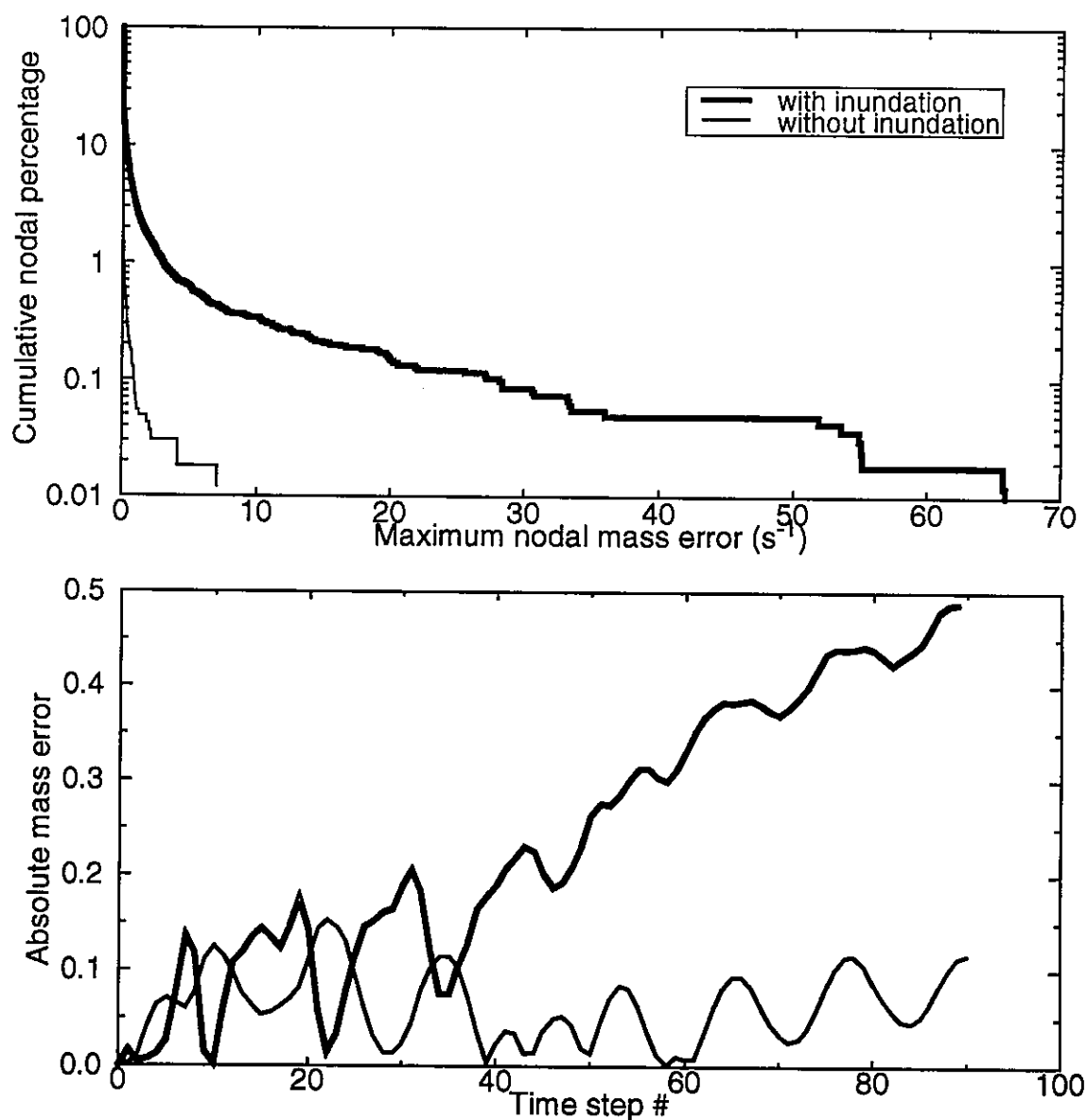


Figure 7.1 Mass errors in flow and transport simulations in the Tagus estuary, with and without inundation: a) cumulative nodal fractions of maximum flow mass errors (mass errors are calculated with equation (4.2), but the scaling was done using the elemental volume at each time step). b) transport mass errors for a Gauss plume released in the upper Tagus estuary ('dry' nodes are not included in the computations).

Solutions for mass conservation of ELM transport simulations with inundation should be addressed directly in the flow models, as we recommended in Chapter 5 for problems neglecting tidal flats. Since current flow models accounting for inundation do not appear to be inherently conservative, the use of a-posteriori corrections on the flow fields may be the best solution to prevent serious mass problems in ELM transport simulations in complex coastal systems.

7.2.1.2 Influence of the vertical dimension

Three dimensional simulations present yet another source of flow mass errors that is expected to affect ELM transport mass conservation. The continuity equation, which is used to compute the vertical velocities, is a first order differential equation that requires a single boundary condition. However, vertical velocities are generally available at the surface and the bottom of the water column, thus providing two boundary conditions. Two main approaches have been proposed to address this problem, by using one boundary condition to solve the equation and use the other for error calculation and posterior redistribution in the water column (Fortunato, 1996) or by using the vertical derivative of the continuity equation, which requires two boundary conditions (Lynch and Naimie, 1993). However, both approaches target overall accuracy, not specifically mass conservation.

Two different approaches were proposed recently with the purpose of improving mass conservation: Mucino et al. (1994) proposed a least square approach for the solution of the continuity equation, which retains both boundary conditions while keeping the continuity equation; Janin (1995) uses a staggered grid for the vertical velocities, thus increasing the number of unknowns by one. Preliminary comparisons for simple tests for the methods proposed by Lynch and Naimie (1993) and Mucino et al. (1994) show that mass conservation is improved by an order of magnitude when the least square approach is used (Mucino et al., 1994). However, a systematic analysis involving real systems has not been done yet. Also, it is necessary to assess the influence of these flow mass errors on transport simulations.

7.2.2 Overall accuracy of ELMs

Although a very large effort has been dedicated to the accuracy of ELMs (e.g., Baptista, 1987, Yeh et al., 1992, Healy and Russell, 1993, Oliveira and Baptista, 1995), new concerns arise with the extension to systems with tidal flats and the inclusion of the vertical dimension. The approximations used in flow models to handle tidal flats can be both a source of mass and accuracy errors. For instance, tracer's mass can be left behind during a basin's drainage, when a flow element is considered dry (e.g., elevation below a specified value) and the velocity is set to zero.

7.2.2.1 Three-dimensional finite element ELMs

Although several three-dimensional finite element ELM transport models have been developed recently (Dimou, 1992, Janin, 1995, King and DeGeorge, 1996), a generalized application of these models for coastal water systems has not been observed. The major reason for this apparent lack of popularity may be the large computational effort associated with 3D finite element transport models. Unlike most 3D finite element flow models, which decouple the vertical and horizontal dimensions, explicitly recognizing the different scales associated with each direction, three-dimensional transport models traditionally use fully three-dimensional finite elements, which are very computationally intensive. Since an accurate representation of the horizontal direction requires in general a large number of nodes for coastal systems, the number of vertical nodes is then limited by computational constraints, leading to coarse representations of the vertical processes.

Although the fast growth in computing power could potentially overcome resolution constraints in the near future, the extension of flow models' decoupling strategy to ELM transport models appears attractive. By separating the horizontal and vertical dimensions, transport models take explicitly into account the different scales involved in each direction, and become computationally more efficient. More importantly, the decoupling allows for an increasing flexibility for the vertical discretization. The use of unstructured grids in the vertical dimension, which is starting to be used in flow models (Localized Sigma Coordinates - LSC, Fortunato and Baptista, 1994) is also appealing for transport simulations: for

instance, the sharp gradients of density near a pycnocline, whose position changes strongly in space and time (Fortunato et al., 1997b), suggest that a fine grid is needed locally for accurate results.

The decoupling of the horizontal and vertical directions in the 3D transport equation can be easily obtained by splitting the concentration, c , as a sum of a depth-averaged part, \bar{c} , and a deviation from this mean, c' . We start with the non-conservative 3D transport equation in sigma-coordinates (Dimou, 1992):

$$\frac{\partial}{\partial t}(c) + u\frac{\partial}{\partial r}(c) + v\frac{\partial}{\partial s}(c) + \theta\frac{\partial}{\partial \sigma}(c) = \frac{\partial}{\partial \sigma}\left(\frac{D_{zz}\partial c}{H^2\partial \sigma}\right) + DifHor \quad (7.1)$$

where (u, v, θ) are the velocity components in the systems of coordinates (r, s, σ) , H is the total water depth, D_{zz} is the vertical diffusion coefficient and $DifHor$ are the horizontal diffusion terms. The concentration is now split as (Baptista, personal communication):

$$c = \bar{c} + c' \quad (7.2)$$

Substituting equation (7.2) into equation (7.1), and evaluating the horizontal diffusion terms with the depth-averaged concentration (since they are in general used for smoothness only), we get:

$$\begin{aligned} & \frac{\partial}{\partial t}(c') + u\frac{\partial}{\partial r}(c') + v\frac{\partial}{\partial s}(c') + \theta\frac{\partial}{\partial \sigma}(c') - \frac{\partial}{\partial \sigma}\left(\frac{D_{zz}\partial}{H^2\partial \sigma}(c')\right) = \\ & \frac{\partial \bar{c}}{\partial t} + u\frac{\partial \bar{c}}{\partial r} + v\frac{\partial \bar{c}}{\partial s} + \frac{\partial}{\partial r}\left(D_{rr}\frac{\partial \bar{c}}{\partial r}\right) + \frac{\partial}{\partial s}\left(D_{ss}\frac{\partial \bar{c}}{\partial s}\right) + \frac{\partial}{\partial r}\left(D_{rs}\frac{\partial \bar{c}}{\partial s}\right) \end{aligned} \quad (7.3)$$

If horizontal diffusion terms are treated explicitly, equation (7.3) becomes a one-dimensional equation in the vertical, forced by the depth-averaged, two-dimensional transport equation (advection only) and horizontal diffusion:

$$\begin{aligned} \frac{Dc'}{Dt} - \frac{\partial}{\partial \sigma} \left(\frac{D_{zz}}{H^2} \frac{\partial}{\partial \sigma} (c') \right) &= \frac{D^* \bar{c}}{Dt} + \\ \frac{\partial}{\partial r} \left(D_{rr} \frac{\partial}{\partial r} (\bar{c}) \right) + \frac{\partial}{\partial s} \left(D_{ss} \frac{\partial}{\partial s} (\bar{c}) \right) + \frac{\partial}{\partial r} \left(D_{rs} \frac{\partial}{\partial s} (\bar{c}) \right) \end{aligned} \quad (7.4)$$

where D/Dt and D^*/Dt represent the total derivative in three and two dimensions, respectively. The procedure will thus be, to solve the two-dimensional transport equation first, using for instance the model described in the Appendix, and then use the depth-averaged concentration to force a one dimensional ELM model (with three-dimensional tracking) that solves equation (7.4).

Extension of the subdivision quadrature integration control volume finite element method described in the Appendix, to solve equation (7.4) is straightforward. Each vertical can be discretized independently with one dimensional finite elements, and equation (7.4) is then integrated in the control volume defined by the mid-distance between vertical nodes (Figure 7.2).

The evaluation of the integrals at the feet of the characteristic lines can be obtained by subdividing the two three-dimensional straight lines that connect the feet of the characteristic lines of the corners of the control volume and the foot of the nodal characteristic line, into a user-specified number of subdivision points. However, accuracy errors can arise both from assuming the integration line at the feet of the characteristic lines to be a straight line, and from the interpolation of the concentration between verticals. The use of grid refinement, though, is expected to eliminate these errors.

The decoupling approach to CVFE- ELM transport models proposed herein is expected to reduce considerably the computational cost associated with traditional 3D finite element models without jeopardizing their overall accuracy, and increase their flexibility to allow for a straightforward implementation of unstructured grids in the vertical and of quadrature integration finite volume methods. However, a detailed analysis of mass conservation is necessary since a three-dimensional control through finite volumes is not applied due to the decoupling of the vertical and horizontal dimensions.

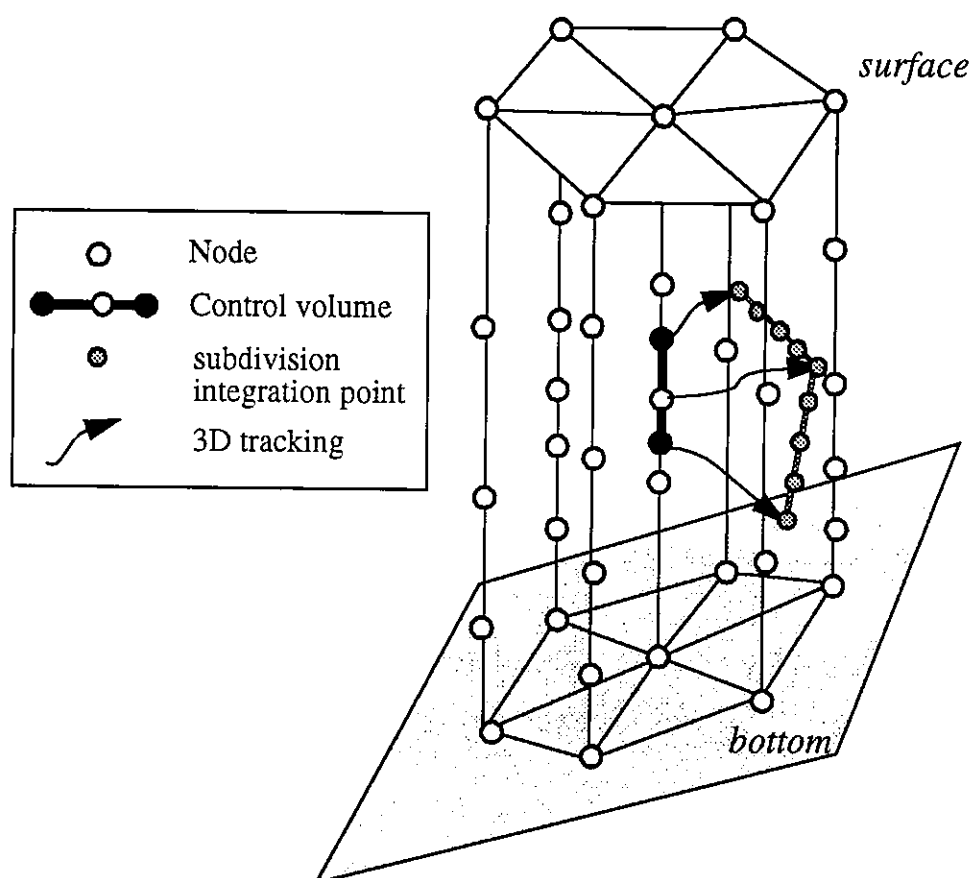


Figure 7.2 Domain discretization, control volume definition and subdivision quadrature integration

7.2.2.2 Adaptive grids

The flexibility provided by the above 3D formulation becomes particularly relevant since strategies in domain discretization are changing, not only in the vertical dimension, but in a broader sense. The traditional use of time-independent, single grid for flow and transport simulations is becoming obsolete and limiting in our modeling ability due to computational constraints. As seen in chapters 2 and 5, the accuracy of ELM simulations is strongly dependent on grid refinement. Since for many problems (e.g. localized spills), the concentrations are very small or null in the majority of the domain and the location of the plume varies strongly in time, the use of adaptive grids may be necessary to provide the necessary resolution at an affordable computational cost. In addition, the use of a single grid for flow and transport simulations is not likely to be an acceptable solution in the future, as criteria for optimal grids for flow and transport simulations are rather distinct (Baptista,

1993).

Adaptive grids have been successfully used for the transport equation, both by automatically refining the grid (*h-methods*) or by redistributing the nodes (*r-methods*). Distinction between the many approaches is generally based on the error measure used to control the grid adaptation and on the grid generation based on the error measure distribution in the domain (Oden and Demkowicz, 1987, Baehmann et al., 1988, Zegeling, 1996). For ELM-based methods, several adaptive grid techniques have been proposed, which either refine the grid on the advection part (Yeh et al., 1992, Demkowitz and Oden, 1986) or on solution of diffusion (Dahle et al., 1990). Several questions remain to be addressed, such as the extension of locally adaptive ELM models to three-dimensions, the computational cost associated with the use of adaptive grids and the potential for mass and accuracy errors that result from interpolating concentrations and velocities when using different grids in the flow and transport simulations.

7.2.3 Diagnostic modeling of residence times

Residence times of contaminants and environmental tracers can have an immediate effect on short-lived species and generate important changes on the life of longer lived species. Since contact time between species and tracers happens on a localized scale, estimates of residence time need to be defined locally too. In chapter 6, we proposed a new methodology to evaluate diagnostically temporal and spatial distributions of residence times that takes advantage of the flexibility of numerical particle models. The conceptual approach was then tested for conservative tracers using a two dimensional model of the Tagus estuary that did not account for inundation.

Extension of the conservative tracer's residence time approach to more complex tests that include tidal flats and the vertical dimension, presents no conceptual difficulty, the additional requirements being on the flow simulations. To illustrate this point, we repeated the residence time simulations for the re-entrant tracer released in region 4 (Chapter 6), forced by two 2D flow simulations of the Tagus estuary: one accounts for inundation, while the other neglects it (Fortunato et al., 1997a). Comparison of residence times for total par-

ticle flushing for the two simulations (Figure 7.3) emphasizes the dependence of residence times calculations on flow simulations that accurately represent the physical processes.

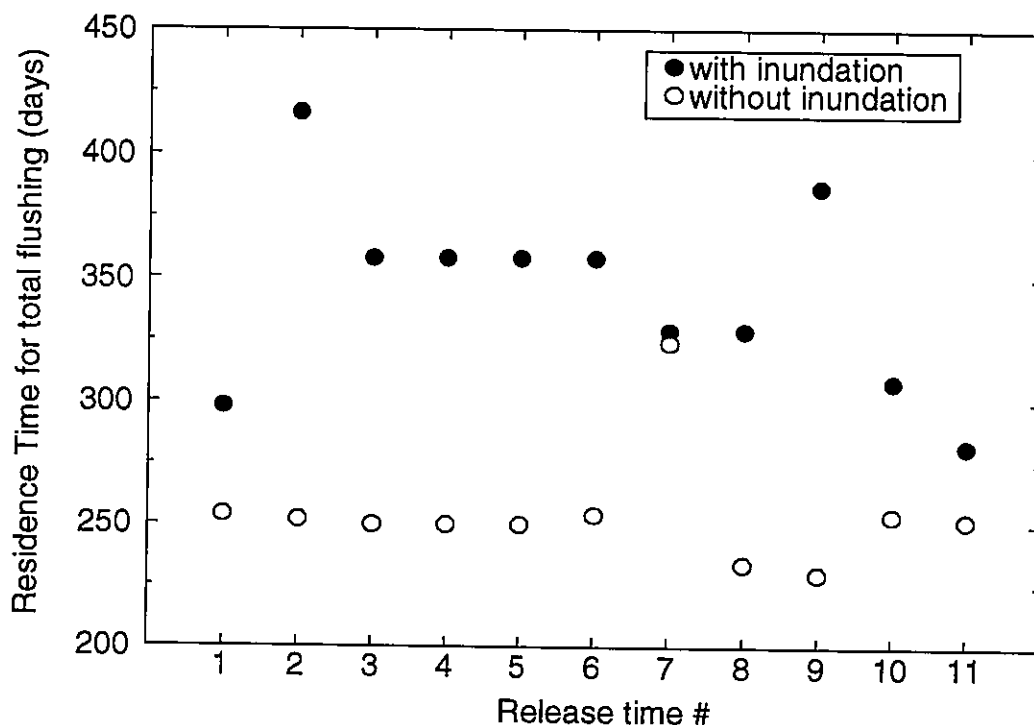


Figure 7.3 Residence times for the re-entrant tracer in region 4 (Figure 6.1b), using particle simulations forced by two flow fields that differ on the handling of the tidal flats.

Evaluation of residence times for non-conservative tracers is a more complex problem. In presence of transformation processes, particle models require the mapping of each particle's mass into the computational grid at each transformation time step, increasing the complexity and computational cost. In addition, the tracking of particles for long periods involves a considerable number of sequential calculations, which requires very strict closing errors to guarantee the accuracy of residence time calculations.

While particle models are an attractive alternative for simple residence time problems, transport (i.e. concentration-based) models provide the general framework in which both the residence times of complex non-conservative and conservative tracers can be analyzed. Moreover, comparison of residence time evaluated with transport models and field data becomes simpler, thus providing additional robustness to residence time calculations based on numerical models. In particular, ELM transport models are an attractive choice

due to their flexibility in incorporating processes with distinct time scales and in dealing simultaneously with several interacting tracers.

However, new difficulties arise. On the one hand, the accuracy of the residence times calculations is expected to depend on the accuracy and mass conservation of the transport simulations, thus requiring the use of fine grids and conservative forcing flow fields in the transport simulations. On the other hand, the definition of residence times becomes less straightforward. Several definitions of residence times have been proposed for transport model based analysis such as: 1) the time to reduce the initial mass by a factor of $1/e$ ("e-folding" approach, Becker and Bjork, 1996), 2) the time to remove $x\%$ of the pollutant's mass in the domain (Wu and Tsanis, 1994), which has the full pollutant's removal ($x = 100$) as one particular case, and 3) the time to reduce the maximum concentration to $y\%$ of the initial peak value (Wu and Tsanis, 1994).

Given the multitude of different environmental problems to which residence times can be useful, a single definition of residence time is clearly insufficient. Operational definitions, tailor-made to address specific problems, appear to be the best approach.

References

- Baptista, A.M., 1987. *Solution of Advection-Dominated Transport by Eulerian-Lagrangian Methods using the Backwards Method of Characteristics*, Ph.D. Dissertation, Massachusetts Institute of Technology, Cambridge.
- Baptista, A.M., 1993. Coupling Flow and Transport Models for Highly Resolved Grids, *SIAM Conference in Mathematical and Computational Issues in Geosciences*, Houston, Texas, [abstract only].
- Baehmann P.L., M.S. Shephard and J.E. Flaherty, 1988. Adaptive Analysis for Automated Finite Element Modeling, in *6th Conference on the Mathematics of Finite Elements and Applications*, J.R. Whiteman (editor), Academic Press.
- Beck, B.C. and A.M. Baptista, 1997. WET2: An Eulerian-Lagrangian Shallow Water FEM Model, in *Proceedings of the International Workshop on Long-Wave Runup Models*, H. Yeh et al. (editors), 265-271.
- Becker, P. and G. Bjork, 1996. Residence Times in the upper Artic Ocean, *Journal of Geo-*

- physical Research*, 101(C2): 28,377-28,396.
- Cerco, C.F. and T.M. Cole, 1992. Thirty Year Simulation of Chesapeake Bay Eutrophication, in *Estuarine and Coastal Modeling*, M. L. Spaulding et al. (editors), American Society of Civil Engineers, 116-126.
- Dahle, H.K., M.S. Espedal, R.E. Ewing and O. Saevareid, 1990. Characteristic Adaptive Subdomain Methods for Reservoir Flow Problems, *Numerical Methods for Partial Differential Equations*, 6(4): 279-309.
- Demkowicz, L. and J.T. Oden, 1986. An Adaptive Characteristic Petrov-Galerkin Finite Element Method for Convection-Dominated Linear and Non-linear Parabolic Problems in Two Space Variables, *Computer Methods in Applied Mechanics and Engineering*, 55(1/2): 63-87.
- Dimou, K., 1992. *3-D Hybrid Eulerian-Lagrangian / Particle Tracking Model for Simulating Mass Transport in Coastal Water Bodies*, Ph.D. Dissertation, Massachusetts Institute of Technology, Cambridge.
- Fortunato, A.B., 1996. *Three-Dimensional Modeling of Coastal Flows Using Unstructured Grids*, Ph.D. Dissertation, Oregon Graduate Institute of Science and Technology, Portland.
- Fortunato, A.B. and A.M. Baptista, 1994. Localized Sigma Coordinates for the Vertical Structure of Hydrodynamic Models, in *Estuarine and Coastal Modeling III*, M.L. Spaulding et al. (editors), American Society of Civil Engineers, 323-335.
- Fortunato, A.B., A. Oliveira and A.M. Baptista, 1997a. On the effect of tidal flats on the hydrodynamics of the Tagus estuary, *Oceanologica Acta*, (submitted).
- Fortunato, A.B., A. Oliveira and A.M. Baptista, 1997b. Finite Element Modeling of Flow and Transport in Coastal Waters, in *Proceedings of the 5th Encontro Nacional de Mecânica Computacional*, Guimarães, Portugal, (in press).
- Healy, R.W. and T.F. Russell, 1993. A Finite-Volume Eulerian-Lagrangian Localized Adjoint Method for Solution of the Advection-Dispersion Equation, *Water Resources Research*, 29(7): 2399-2413.
- Janin, J.M., 1995. *Conservativité et Positivité dans un module de transport de scalaire écrit en éléments finis - Application à Telemac-3D*, Rapport HE-42/95/054/A, Département Laboratoire National d'Hydraulique, Châtou, France.

- King, I.P. and J.F. DeGeorge, 1996, Multidimensional modeling of Water Quality using the Finite Element Method, in *Proceedings of the 4th International Conference on Estuarine and Coastal Modeling*, M.L. Spaulding and R.T. Cheng (editors), American Society of Civil Engineers, 340-354.
- Luetlich, Jr., R.A. and J.J. Westerink, 1995. *Implementation and Testing of Elemental Flooding and Drying in the ADCIRC Hydrodynamic Model, Final Contractors Report*, Contract No. DACW39-94-M-5869, Coastal Engineering Research Center, Waterways Experiment Station, US Army Corps of Engineers, Vicksburg, MS 39180.
- Lynch, D.R. and C.E. Naimie, 1993. The M2 Tide and Its Residual on the Outer Banks of the Gulf of Maine, *Journal of Physical Oceanography*, 23(10): 2222-2253.
- Mucino, J.C., W.G. Gray and M.G.G. Foreman, 1994. Calculation of Vertical Velocity in a 3D Model Using a Least Squares Approach, in *Proceedings of the 10th International Conference on Computational Methods in Water Resources*, A. Peters et al. (editors), Kluwer Academic Publishers, 1105-1112.
- Oden, J.T. and L. Demkowicz, 1987. Advances in Adaptive Improvements: A survey of Adaptive Finite Element Methods in Computational Mechanics, in *State of the Art Surveys in Computational Mechanics*, A.K. Noor (editor), American Society of Mechanical Engineers, 441-467.
- Oliveira, A., 1994. *A comparison of Eulerian-Lagrangian Methods for the Solution of the Transport Equation*, M.Sc. Thesis, Oregon Graduate Institute of Science and Technology, Portland.
- Oliveira, A. and A.M. Baptista, 1995. A comparison of integration and interpolation Eulerian-Lagrangian methods, *International Journal for Numerical Methods in Fluids*, 21(3), 183-204.
- Westerink, J.J. and W.G. Gray, 1990. Progress in Surface Water Modeling, *Reviews in Geophysics*, supplement, 210-217.
- Wu, J. and I.K. Tsanis, 1994. Pollutant Transport and Residence Time in a distorted scale model and a numerical model, *Journal of Hydraulic Research*, 32(4); 583-598.
- Yeh, G.T., J.R. Chang and T.E. Short, 1992. An exact peak capturing and oscillation-free scheme to solve advection-dispersion transport equations, *Water Resources Research*, 28(11), 2937-2951.
- Zegeling, P.A., 1996. Numerical solution of advection-dispersion models using dynamically-moving adaptive grids, in *Proceedings of the 11th International Conference on Computational Methods in Water Resources*, A.A. Aldama et al. (editors), 593-602.

APPENDIX

VELA, User's manual for a Two-Dimensional Depth-Averaged Transport and Particle Model

A.1 Introduction

This Appendix describes the formulation and application of *VELA* (Oliveira and Baptista, 1997b). *VELA* (Variations on Eulerian-Lagrangian Analysis) is a two-dimensional model that accommodates both a mass transport mode (*VELAconc*) and a particle transport mode (*VELApart*). *VELAconc* solves the advection-diffusion equation for several control volume finite element Eulerian-Lagrangian formulations, while *VELApart* uses the tracking module of *VELAconc* to solve the advection equation for individual, passive, non-reactive particles.

The main characteristics of the model are as follows:

1. *VELAconc*:

- uses node-centered finite volume concepts while keeping the flexibility of finite elements in geometry representation as well as variable definition;
- allows the use of either the concentration (c) or the total mass in the water column (cH) as variables transported along the characteristic lines;
- for formulations transporting c along the characteristic lines, the model allows the use of the conservative or the non-conservative forms of the transport equation;

- integrals at the feet of the characteristic lines are evaluate by a subdivision-quadrature integration method, with a user-specified number of quadrature points;
- evaluation of integrals involving quantities at the feet of the characteristic lines can be performed at the time step where concentrations are being calculated or at the previous time step;
- uses an accuracy-controlled adaptive, embedded 4th order Runge-Kutta method for the solution of advection;
- uses 3-node triangular finite elements.

2. *VELA*part:

- uses an accuracy-controlled adaptive, embedded 4th order Runge-Kutta method;
- allows for both forward and backward tracking;
- calculates residence times for two types of non-reactive tracers, which differ on the definition of permanence inside the estuary;
- compensates for inaccuracies in the flow field at closed boundaries by using the tangential velocity only.

This appendix includes four sections besides this **Introduction**. **Model Description** presents the several formulations of *VELAconc* and the various options of *VELA*part. In **Input and Output Files Structure**, we present the input and output files format for both the mass transport and particle transport modes. **Examples of Application** uses two tests to illustrate the use of *VELAconc* and *VELA*part.

A.2 Model Description

A.2.1 Transport model

The tracer transport equation is obtained by averaging the instantaneous mass conservation equation over the time scales of turbulence (e.g. Baptista and Adams, 1986):

$$\frac{\partial c}{\partial t} + \frac{\partial}{\partial x_i}(u_i c) = \frac{\partial}{\partial x_i} \left(D_{i,j} \frac{\partial c}{\partial x_j} \right) + S \quad i, j = 1, 2, 3 \quad (\text{A.1})$$

Assuming that the tracer is well mixed in the water column and integrating equation (A.1) over depth, we obtain the conservative, depth-averaged transport equation:

$$\frac{\partial}{\partial t}(cH) + \frac{\partial}{\partial x_i}(Hu_i c) = \frac{\partial}{\partial x_i} \left(D_{ij} H \frac{\partial c}{\partial x_j} \right) + SH \quad i, j = 1, 2 \quad (\text{A.2})$$

where c is the concentration, t is time, x_i are the space coordinates, u_i is the velocity along direction i , D_{ij} is the diffusion tensor, H is the total depth (defined as the sum of the elevation, η and the water depth, h) and S is a source/sink.

Distinct formulations can now be obtained, depending on the choice of variable to be transported along the characteristic lines. In VELA, either the concentration (c) or the total concentration (cH) can be used. While surface water ELM models use c -based formulations, motivation for development of a cH formulation arises from its similarity to the equation solved in ELLAMs (Celia et al., 1990, Healy and Russell, 1993, Binning and Celia, 1996). ELLAMs are becoming very popular methods for subsurface transport, due to the excellent properties of accuracy and mass conservation obtained in simple tests (Celia et al., 1990, Healy and Russell, 1993, Binning and Celia, 1996).

A.2.1.1 c formulations

Equation (A.2) must now be rearranged to isolate the total derivative of c . Expanding the left hand side of (A.2) and dividing by H , we get:

$$\frac{Dc}{Dt} + c \left(\frac{1}{H} \frac{DH}{Dt} + \frac{\partial}{\partial x_i}(u_i) \right) = \frac{1}{H} \frac{\partial}{\partial x_i} \left(D_{ij} H \frac{\partial c}{\partial x_j} \right) + S \quad (\text{A.3})$$

where the second term in the *LHS* of (A.3) is the flow continuity equation multiplied by c/H .

Eulerian-Lagrangian concepts are now used to handle each term with an appropriate technique. Equation (A.3) is divided into three simpler equations:

$$u_i = \frac{dx_i}{dt} \quad (\text{A.4})$$

$$\frac{Dc}{Dt} = K_1 c \quad (\text{A.5})$$

$$\frac{Dc}{Dt} = K_2 c + \frac{1}{H} \frac{\partial}{\partial x_i} \left(D_{ij} H \frac{\partial c}{\partial x_j} \right) + S \quad (\text{A.6})$$

The second term on the LHS of equation (A.3), which contains the flow continuity equation, is neglected in most traditional ELM models (e.g., see Baptista et al., 1984, Cheng et al., 1984). However, when flow mass balance is not preserved numerically, the continuity equation term is effectively different from zero. In *VELA*, this term can also be neglected by making $K_1 = K_2 = 0$ (non-conservative c formulation) or it can be incorporated in equations (A.5) and (A.6) (conservative c formulations). Two approaches can be used to evaluate the continuity equation term: a *mixed approach*, where the first part is evaluated along the characteristic lines and the second part is evaluated in the diffusion time steps:

$$K_1 = -\frac{\partial u_i}{\partial x_i} \quad K_2 = -\frac{1}{H} \frac{DH}{Dt} = -\frac{D(\ln H)}{Dt} \quad (\text{A.7})$$

and a *Lagrangian approach*, where the whole term is evaluated along the characteristic lines:

$$K_1 = -\frac{D(\ln H)}{Dt} - \frac{\partial}{\partial x_i} (u_i) \quad K_2 = 0 \quad (\text{A.8})$$

The use of the logarithmic form of equations (A.7) and (A.8) avoids the need for an approximation of the $1/H$ factor along the characteristic lines.

Equation (A.4) is solved by the backward method of characteristics using an adaptive, embedded 4th order Runge-Kutta method (Press et al., 1992). Selection of a highly-accurate tracking technique, though computationally intensive, is necessary to prevent the generation of both mass and overall accuracy errors (Oliveira and Baptista, 1997a). Equation (A.5) is solved with an α -method along the characteristic lines (Wood and Baptista, 1993).

We extend the basic concepts presented in Healy and Russell (1993) to two-dimensional problems with unstructured grids: equation (A.6) is solved by node-centered finite volumes, while using a finite element framework to define concentrations, depth and velocity within each element. We selected node-centered finite volumes for their superior accuracy (Morton, 1991).

Following Baptista et al. (1984), equations (A.5) and (A.6) are discretized in time with an α -method:

$$\frac{c^{m+1} - c^m}{\Delta t'} = \alpha K_1^{m+1} c^{m+1} + (1 - \alpha) K_1^m c^m \quad (\text{A.9})$$

$$\begin{aligned} \frac{c^{n+1} - c^\xi}{\Delta t} &= \alpha \frac{1}{H} \frac{\partial}{\partial x_i} (D_{ij} H \frac{\partial c}{\partial x_j}) + K_2 c^{n+1} + \\ &(1 - \alpha) \left[\frac{1}{H} \frac{\partial}{\partial x_i} (D_{ij} H \frac{\partial c}{\partial x_j}) + K_2 c \right]^\xi + S^\xi \end{aligned} \quad (\text{A.10})$$

where ξ denotes the feet of the characteristic lines at time n , Δt is the time step between time instants $n+1$ and n , and $m+1$ and m denote intermediate time instants, separated by the sub-time step $\Delta t'$, between times $n+1$ and n . Equation (A.10) is then integrated in the node-centered control volume, a space-time volume defined at time $n+1$ by the area of influence (Voronoi polygon) of a node, and at ξ by the feet of the characteristic lines of the corners of the Voronoi polygon (Figure A.1). Concentration, depth and velocity are still defined inside each element by linear shape functions:

$$c(t_n, x, y) = \sum_{m=1}^3 c_m^n \phi_m \quad (\text{A.11})$$

where ϕ_m are the area-coordinates shape functions:

$$\begin{bmatrix} \phi_1 \\ \phi_2 \\ \phi_3 \end{bmatrix} = \frac{1}{2A} \begin{bmatrix} x_2 y_3 - x_3 y_2 & y_2 - y_3 & x_3 - x_2 \\ x_3 y_1 - x_1 y_3 & y_3 - y_1 & x_1 - x_3 \\ x_1 y_2 - x_2 y_1 & y_1 - y_2 & x_2 - x_1 \end{bmatrix} \begin{bmatrix} 1 \\ x \\ y \end{bmatrix} \quad (\text{A.12})$$

where (x_m, y_m) are the coordinates of nodes that define the element which contains a generic point of coordinates (x, y) at time t_n , and A is the element area.

Since the shape functions are linear, second derivatives cannot be directly evaluated. The diffusion term is evaluated by approximating $1/H$ by its average on the control volume, followed by application of the Green's theorem:

$$\int_{\Omega_{cv}} \frac{1}{H} \frac{\partial}{\partial x_i} (D_{ij} H \frac{\partial c}{\partial x_j}) d\Omega_{cv} = \frac{1}{\bar{H}} \int_{\Omega_{cv}} \frac{\partial}{\partial x_i} D_{ij} H \frac{\partial c}{\partial x_j} d\Omega_{cv} = \frac{1}{\bar{H}_T} \int_{\Gamma} (D_{ij} H \frac{\partial c}{\partial x_j}) \cdot \vec{n} d\Gamma \quad (\text{A.13})$$

where Ω_{cv} is the control volume, \bar{H} is the average depth in the control volume, Γ is the boundary of Ω_{cv} and \vec{n} is the outward unit normal on Γ .

Integration of equation (A.10) leads to:

$$\begin{aligned} \int_{\Omega_{cv}} c^{n+1} d\Omega_{cv} - \frac{\alpha \Delta t}{H} \int_{\Gamma} (D_{ij} H \frac{\partial c}{\partial x_j}) \cdot \vec{n} \Big|^{n+1} d\Gamma + \alpha \Delta t \int_{\Omega_{cv}} K_1 c^{n+1} d\Omega_{cv} = \\ \int_{\Omega_{cv}} c^{\xi} d\Omega_{cv} + \int_{\Omega_{cv}} S^{\xi} d\Omega_{cv} - \frac{(1-\alpha)\Delta t}{H} \int_{\Gamma} (D_{ij} H \frac{\partial c}{\partial x_j}) \cdot \vec{n} \Big|_{\xi}^{\xi} d\Gamma - (1-\alpha)\Delta t \int_{\Omega_{cv}} K_1 c^{\xi} d\Omega_{cv} \end{aligned} \quad (\text{A.14})$$

The area integrals at time $n+1$ are evaluated analytically in each quadrangle (dashed area in Figure A.1). The area integrals at the feet of the characteristic lines are evaluated by subdivision quadrature: each triangle formed by the foot of the nodal charac-

teristic line and two sequential corners of the tracked image of the Voronoi polygon (Figure A.2a) is divided in a user-specified number of sub-triangles (Figure A.2b). Concentrations and depths are interpolated at each sub-triangle corner and then assumed linear within each sub-triangle (dashed area in Figure A.2c). Subdivision quadrature integration extends the quadrature described in Healy and Russell (1993) to an area of integration supported by the feet of the characteristic lines.

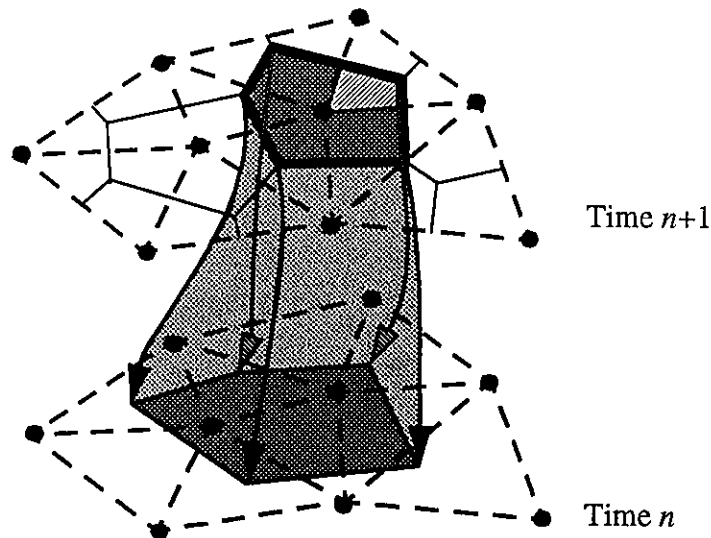


Figure A.1 Control volume (shaded area in space and time), area of influence (Voronoi polygon, dark shaded area) and integration quadrangle at time $n+1$ (dashed area).

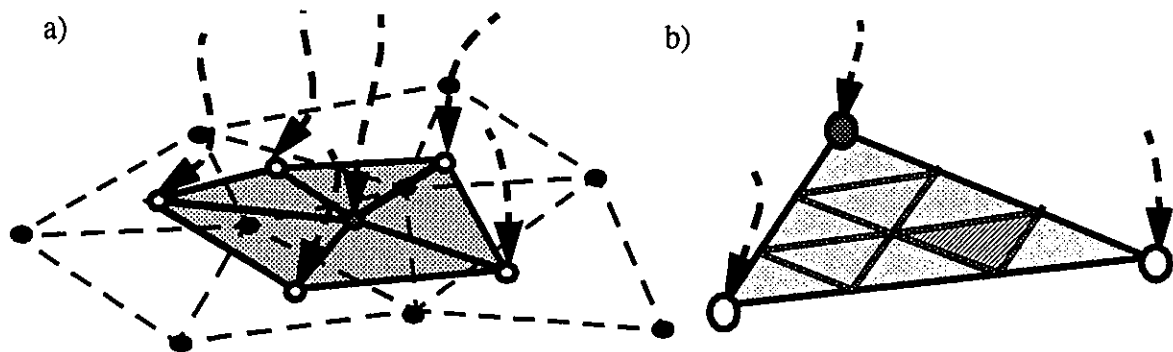


Figure A.2 a) integration area at the feet of the characteristic lines. b) subdivision of each triangle into sub-triangles: illustrated for 3 subdivision levels.

The continuity equation term (equations (A.7) and (A.8)) requires the evaluation of spatial gradients of velocity. Since tracking sub-time steps vary for each point, this term

is approximated by the gradients of velocity along the nodal characteristic line. A similar approach was used for terms involving the total depth in equation (A.8). For the Lagrangian approach, time discretization of equation (A.5) between two tracking sub-time steps becomes:

$$\begin{aligned} & \frac{c^{m+1} - c^m}{\Delta t'} + \alpha c \left. \frac{\partial u_i}{\partial x_i} \right|^{m+1} + (1 - \alpha) c \left. \frac{\partial u_i}{\partial x_i} \right|^{m+1} + \\ & (\alpha c^{m+1} + (1 - \alpha) c^m) \frac{(\ln H^{m+1} - \ln H^m)}{\Delta t'} = 0 \end{aligned} \quad (\text{A.15})$$

Integration in the control volume leads to:

$$\begin{aligned} & \int_{\Omega_{cv}} c^{m+1} d\Omega_{cv} + \alpha (\overline{\ln H^{m+1}} - \overline{\ln H^m}) \int_{\Omega_{cv}} c^{m+1} d\Omega_{cv} + \alpha \overline{\frac{\partial u_i^{m+1}}{\partial x_i}} \int_{\Omega_{cv}} \Delta t' c^{m+1} d\Omega_{cv} + \\ & (1 - \alpha) \overline{\frac{\partial u_i^m}{\partial x_i}} \int_{\Omega_{cv}} \Delta t' c^m d\Omega_{cv} - \int_{\Omega_{cv}} c^m d\Omega_{cv} + (1 - \alpha) (\overline{\ln H^{m+1}} - \overline{\ln H^m}) \int_{\Omega_{cv}} c^m d\Omega_{cv} = 0 \end{aligned} \quad (\text{A.16})$$

where the overbar indicates quantities averaged over the control volume.

Combining equation (A.15) for all intermediate sub-time steps leads to:

$$c^{n+1} = c^\xi \prod_{i=1}^{n \text{ track steps}} \frac{\left(1 - (1 - \alpha) \left(\Delta t'_i \left(\frac{\partial u_j}{\partial x_j} \right)^i + \overline{(\ln H)^{i+1}} - \overline{(\ln H)^i} \right) \right)}{\left(1 + \alpha \left(\Delta t'_i \left(\frac{\partial u_j}{\partial x_j} \right)^{i+1} + \overline{(\ln H)^{i+1}} - \overline{(\ln H)^i} \right) \right)} \quad (\text{A.17})$$

For consistency, K_1 in the mixed approach (equation (A.7)), is evaluated using the gradients of depth at the head and feet of the nodal characteristic line.

The time step and the region where *RHS* integrals of equation (A.14) are evaluated provides yet another distinction in ELM models with space-time weighting functions. *RHS* integrals can be evaluated directly at the feet of the characteristic lines (Celia et al.,

1990) or else at the head of the characteristic lines, by forward tracking (Healy and Russell, 1993). Both approaches are implemented in *VELA*, and their numerical properties are compared in Chapter 2.

The above model description applies to both integration at the feet or head of the characteristic lines. For integrals evaluated at the head of the characteristic lines ($n+1$), the subdivision triangles at ξ are mapped to $n+1$ (Figure A.3). The use of mapping, rather than forward-tracking as suggested by Healy and Russell (1993), is justified by both computational cost restrictions, as high-accuracy tracking is a computationally intensive task, and to avoid oscillations. For 8 subdivision levels, which was deemed accurate for transport simulations in the Tagus estuary (Chapter 5), the forward-tracking proposed by Healy and Russell (1993) would increase the tracking computational cost by a factor of 64. More importantly, quadrature integration based on forward tracking of large numbers of points leads to oscillations due to the relative deformation of pathways of neighboring integration points (Healy and Russell, 1993). In presence of complex flows, this deformation can be very large, leading to large accumulation of mass in some control volumes, and quasi-depletion of neighboring areas, thus potentially leading to very severe oscillations. This effect is illustrated in the forward tracking of the quadrature points for a 5-level subdivision in the Tagus estuary's complex flow, for a time step of one hour (Figure A.4).

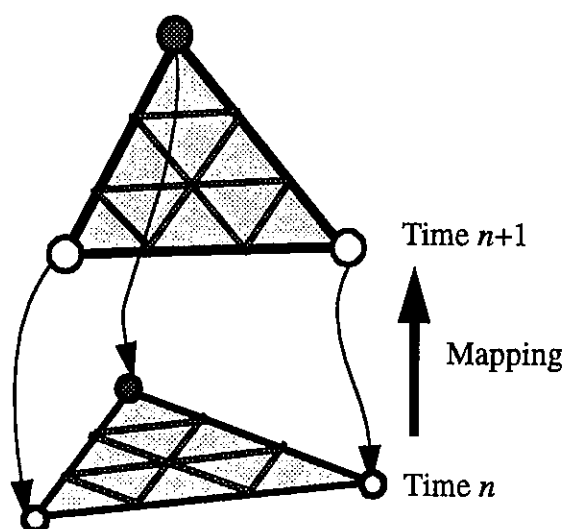


Figure A.3 Mapping of subdivision triangles from time step n to time step $n+1$.

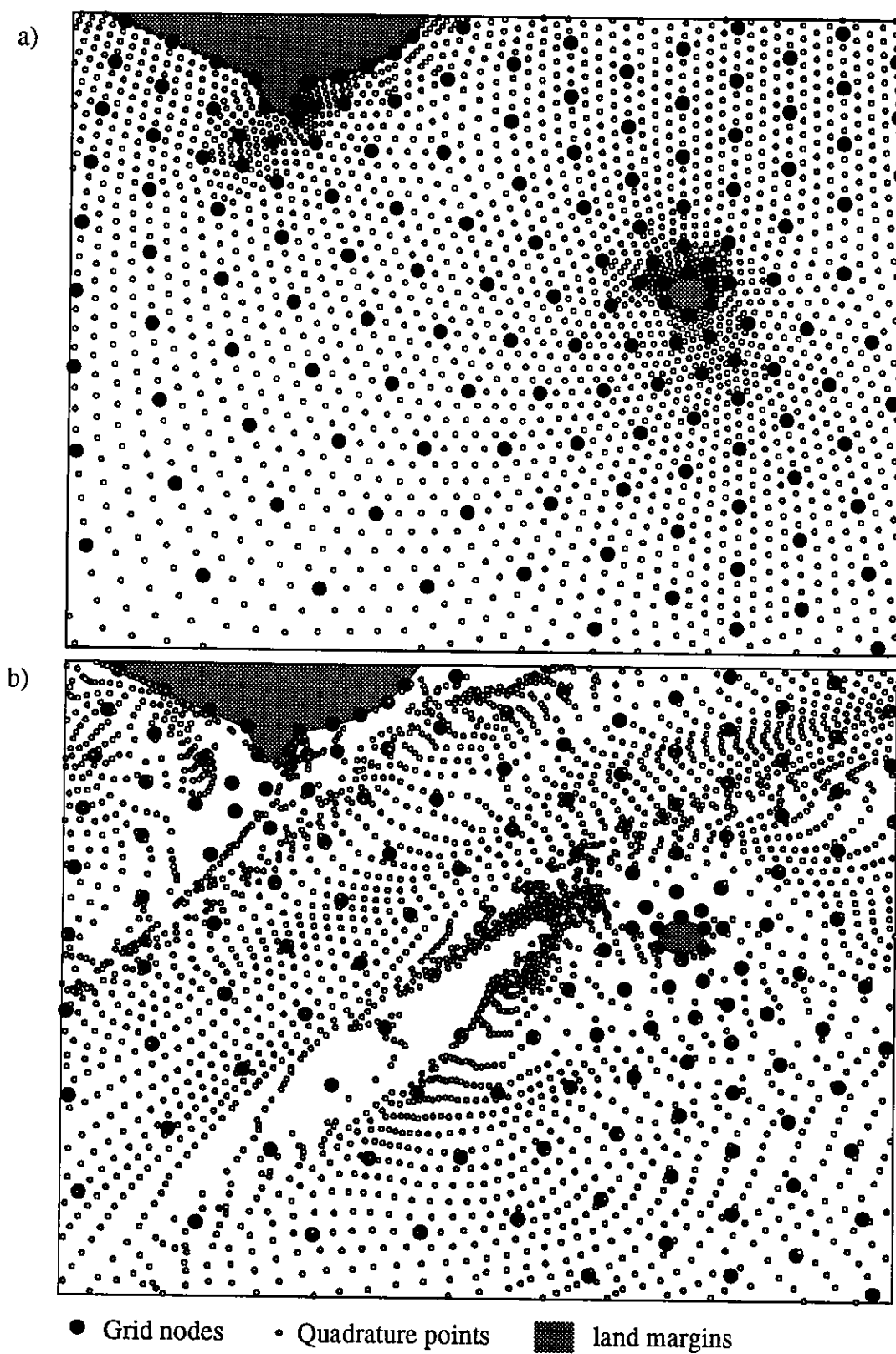


Figure A.4 Forward tracking of quadrature integration points for 5 subdivision levels at the mouth the Tagus estuary: a) initial positions; b) after 1 hour.

A.2.1.2 cH formulation

Equation (A.2) is rearranged to isolate the total derivative of cH . Expanding the left hand side of (A.2), we get:

$$\frac{D(cH)}{Dt} + cH \frac{\partial u_i}{\partial x_i} = \frac{\partial}{\partial x_i} \left(D_{ij} H \frac{\partial c}{\partial x_j} \right) \quad (\text{A.18})$$

Unlike for c formulations, the velocity gradient term cannot be neglected since it does not contain the full continuity equation, and therefore it is non-zero even for conservative flows. Similarly to c -formulations, equation (A.18) is divided into three simpler equations, the velocity gradient term being treated in Lagrangian form, along the characteristic lines:

$$u_i = \frac{dx_i}{dt} \quad (\text{A.19})$$

$$\frac{D(cH)}{Dt} = cH \left(- \frac{\partial}{\partial x_i} (u_i) \right) \quad (\text{A.20})$$

$$\frac{D(cH)}{Dt} = \frac{\partial}{\partial x_i} \left(D_{ij} H \frac{\partial c}{\partial x_j} \right) \quad (\text{A.21})$$

Equations (A.19) and (A.20) are treated similarly to equations (A.5) and (A.6). The velocity gradient term is approximated by the gradients along the nodal characteristic lines, since tracking sub-time steps vary for each point. Time discretization of equation (A.20) between two tracking sub-time steps becomes:

$$(cH)^{m+1} - (cH)^m + \alpha (\Delta t') \frac{\partial u_i^{m+1}}{\partial x_i} (cH)^{m+1} + (1 - \alpha) (\Delta t') \frac{\partial u_i^m}{\partial x_i} (cH)^m = 0 \quad (\text{A.22})$$

Integration in the control volume leads to:

A.2.1.2 cH formulation

Equation (A.2) is rearranged to isolate the total derivative of cH . Expanding the left hand side of (A.2), we get:

$$\frac{D(cH)}{Dt} + cH \frac{\partial u_i}{\partial x_i} = \frac{\partial}{\partial x_i} \left(D_{ij} H \frac{\partial c}{\partial x_j} \right) \quad (\text{A.18})$$

Unlike for c formulations, the velocity gradient term cannot be neglected since it does not contain the full continuity equation, and therefore it is non-zero even for conservative flows. Similarly to c -formulations, equation (A.18) is divided into three simpler equations, the velocity gradient term being treated in Lagrangian form, along the characteristic lines:

$$u_i = \frac{dx_i}{dt} \quad (\text{A.19})$$

$$\frac{D(cH)}{Dt} = cH \left(- \frac{\partial}{\partial x_i} (u_i) \right) \quad (\text{A.20})$$

$$\frac{D(cH)}{Dt} = \frac{\partial}{\partial x_i} \left(D_{ij} H \frac{\partial c}{\partial x_j} \right) \quad (\text{A.21})$$

Equations (A.19) and (A.20) are treated similarly to equations (A.5) and (A.6). The velocity gradient term is approximated by the gradients along the nodal characteristic lines, since tracking sub-time steps vary for each point. Time discretization of equation (A.20) between two tracking sub-time steps becomes:

$$(cH)^{m+1} - (cH)^m + \alpha (\Delta t') \frac{\partial u_i^{m+1}}{\partial x_i} (cH)^{m+1} + (1 - \alpha) (\Delta t') \frac{\partial u_i^m}{\partial x_i} (cH)^m = 0 \quad (\text{A.22})$$

Integration in the control volume leads to:

$$\frac{dx_i}{dt} = u_i \quad (\text{A.26})$$

Equation (A.26) is solved by an adaptive, embedded 4th order Runge-Kutta method (Press et al., 1992), which combines user-controlled high accuracy with computational efficiency. The general form of a Runge-Kutta algorithm is:

$$x(t^n) = x(t^{n+1}) + \Delta t \sum_{j=1}^q a_j k_j \quad (\text{A.27})$$

with $k_j = u \left(t^{n+1} + c_j \Delta t, x(t^{n+1}) + \Delta t \sum_{m=1}^{j-1} b_{jm} k_m \right)$

where q defines the order of the method, and the choice of coefficients a_j , b_{jm} and c_j determines the specific RK method. We use those proposed in Press et al. (1992) (Table A.1).

The time step for the RK tracking is dynamically adjusted to meet a user-specified criterion. This adaptive control has been shown to be extremely important for coastal systems (Oliveira and Baptista, 1997a) because it allows an automatic adjustment of the tracking to the local complexity of the flow field. For the method used herein, the time step is adjusted by comparison between the 5th order and the embedded 4th order truncation error, which leads to a more efficient algorithm than the traditional RK methods based on step-doubling (e.g., Baptista et al., 1984). The selected set of constants have also been shown to improve the accuracy of the original adaptive embedded RK.

Since *VELA* will in general be forced by flow fields generated from numerical circulation models, errors in the flow simulations can introduce errors in the particles' trajectories. Among these sources of errors are the non-zero normal velocities at closed boundaries, which may tend to move particles out of the domain. To avoid this problem, *VELA* moves the particles that reach a closed boundary using only the tangential component of the velocity.

Table A.1 Runge-Kutta coefficients

i	c _i	b _{ij}					a _i
1							37/378
2	1/5	1/5					0
3	3/10	3/40	9/40				250/621
4	3/5	3/10	-9/10	6/5			125/594
5	1	-11/54	5/2	-70/27	35/27		0
6	7/8	1631/ 55296	175/512	575/ 13824	44275/ 110592	253/4096	512/1771
	j =	1	2	3	4	5	

Tracking errors in *VELApart* simulations can be estimated inside the model through an evaluation of closure errors. These errors, evaluated by forward tracking particles for a certain period and then backward tracking to the initial time, are defined as:

$$\varepsilon_c = \frac{\sqrt{(x_f - x_r)^2 + (y_f - y_r)^2}}{D_{aver}} \quad (\text{A.28})$$

where f and r denote final and release locations and D_{aver} is the equivalent diameter of the averaged visited element during the tracking.

The main motivation for the development of *VELApart* is the evaluation of residence times using particles as conservative tracers. Particles trajectories have been used for many purposes in coastal systems, such as estimation of Lagrangian velocities (Foreman et al., 1992) and mixing (Salomon and Pommepuy, 1990), and understanding the chaotic properties of a system (Fortunato et al., 1997). The success of these applications prompted us to extend the analysis proposed in Hofmann et al (1991) to estuarine systems. Two main approaches can be used in *VELApart*, depending on the tracer's properties.

Estuarine residence time are estimated using large numbers of particles, that represent parcels of water driven exclusively by advection. Residence times for each particle are calculated on the basis of their permanence on a control region, which represent the

“limits” of the estuary (Figure A.5). Different tracers can be obtained depending on the definition of permanence. *VELA* allows for two contrasting cases: re-entrant and once-through tracers. For re-entrant tracers, particles are allowed to move in and out of the control region with tides and the residence time is the time for the particle to leave the control region without returning on a later phase of the tide or on a later tidal cycle (Figure A.5). Once-through tracers represent materials whose properties are considerably changed when outside the control region, and thus individual residence times are defined as the first time the particle leaves the control region (Figure A.5).

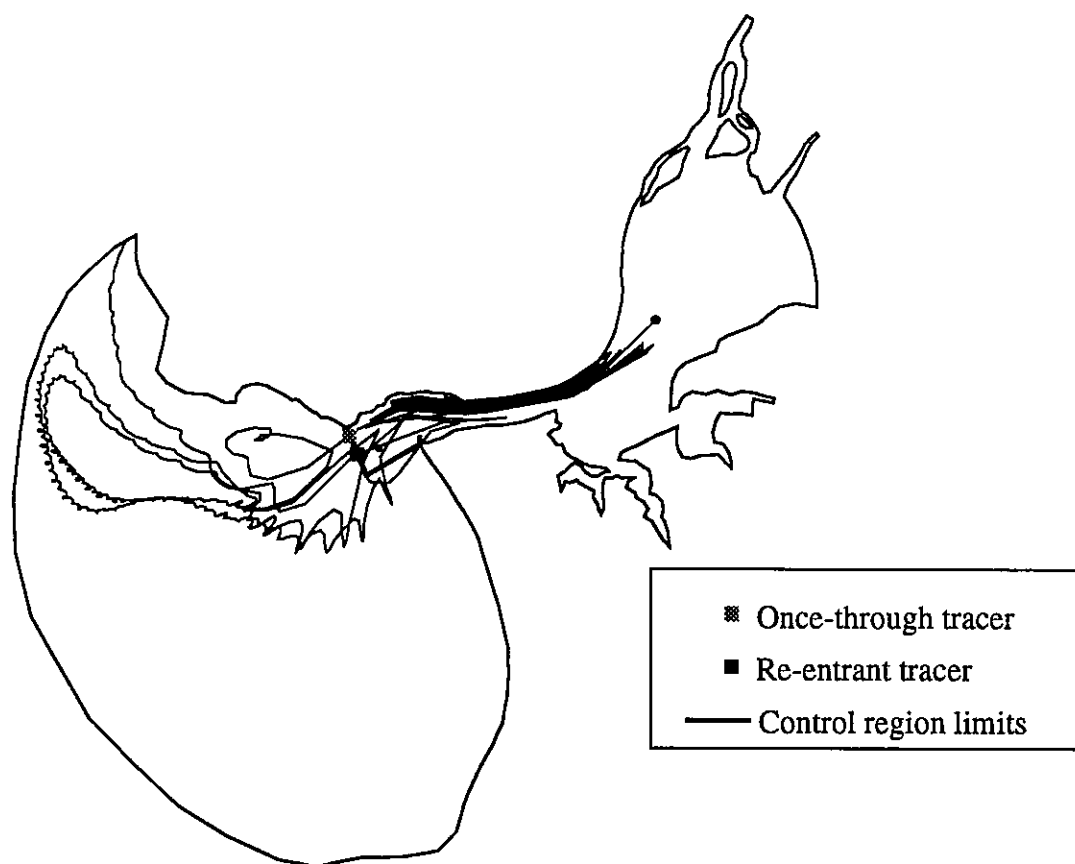


Figure A.5 Control region for a Tagus estuary simulation and example of residence time calculation for a re-entrant and once-through tracer.

A.3 Input Files Structure

To run *VELA* type:

```
vela casefXX casetYY [casepZZ]
```

The meaning of the parameters is as follows:

- *casef* is the case name for flow files (character*5).
- *XX* is the case number for flow files (10-99).
- *caset* is the case name for transport files (character*5).
- *YY* is the case number for transport files (10-99).
- *casep* is the case name for particle files (character*5).
- *ZZ* is the case number for particle files (10-99).

Typing simply “vela” will write out information on how to run the model to the screen.

The following input files are needed to run *VELA* in **particle transport mode**:

- *caset.grd* (transport grid file);
- *casetYY.par* (parameter file);
- *casetYY.bcs* (boundary information file);
- *casefXX.tct* (flow field file);
- *casepZZ.bpt* (particle initial location file).

For residence times calculations, an extra file is required:

- *casepZZ.pts* (estuary limits file).

The following input files are needed to run *VELA* in **mass transport mode**:

- *caset.grd* (transport grid file);
- *casetYY.par* (parameter file);
- *casetYY.bcs* (boundary information file);
- *casefXX.tct* (flow field file);

- *casepYY.cn0* (concentration initial conditions file).

If sources are present, an extra file is required:

- *casetYY.cns* (input source file).

A.3.1 Transport Grid File

This file can be generated by GREDIT (grid format). Extension must be “.grd” and the format is:

- File identifier
- *n_elem, n_nodes*: number of elements and number of nodes of the transport grid.

For each node ($i = 1, n_nodes$):

- *node_number, nodes(i,1), nodes(i,2), h_t(i)*; cartesian coordinates (x,y) and depth at each transport node.

For each element ($i = 1, n_elem$):

- *element_number, 3, elem(i,j); j=1, 3*: element number, number of nodes in this element, nodes that define this element.

A.3.2 Parameter File

This file must have “.par” extension and the format is:

For the **particle mode**:

- File identifier.
- *flag_model, flag_grid, flag_vel*: transport/particle mode (0/1), flow grid =/ <>transport grid (0/1 - not available in current version), flow field type (1 - frequency domain; 2 - time domain, not available in current version).
- *n_time_steps, dt_dif, init_time*: number of time steps, time step (seconds), initial time (seconds).

- *typ_output, first_out, last_out, skip_out*: ascii/binary output (0/1 - not available in current version), first and last step to output, number of steps to skip in the output files (only ascii format).
- *eps, dt_track_min*: tracking criterion (in meters, we suggest 10^{-7} m for residence time simulations), minimum tracking time step (in seconds).
- *flag_tracer*: type of particle run:
 - 0 - tracks the particles forward, saving the pathways at all time steps
 - 1 - tracks the particles forward and backward and then calculates the closing error.
 - 2 - tracks the particles forward and calculates the residence time (saves the initial and final position of the particles).

For the **concentration mode**:

- File identifier.
- *flag_model, flag_grid, flag_vel*: transport/particle mode (0/1), flow grid =/ <>transport grid (0/1 - not available in current version), flow field type (1 - frequency domain; 2 - time domain, not available in current version).
- *n_time_steps, dt_dif, init_time*: number of time steps, time step (seconds), initial time (seconds).
- *typ_output, first_out, last_out, skip_out*: ascii/binary output (0/1 - not available in current version), first and last step to output, number of steps to skip in the output files.
- *eps, dt_track_min*: tracking criterion (in meters, we suggest 10^{-3} m for transport simulations), minimum tracking time step (in seconds).
- *flag_form, flag_int, flag_cont*: cH/c formulation(1/2), integration performed at feet of characteristic lines/at time step where concentrations are being calculated (2/1), include/exclude the continuity equation term (1/0).

- *save_last*: creates a warm-start concentration file for model re-starting, in *cn0* format (0/1 = No/Yes)
- *flag_ini_cond*: initial conditions specified in the whole domain/specified only at the boundaries (0/1).
- *flag_solver*: direct/iterative solver (0/1, direct solver not available in current version).
- *flag_diff*, *alpha*, *dxx*, *dyy*, *dxy*: include/exclude diffusion processes (1/0), α -method coefficient (current version uses a fully-implicit formulation - 1), components of diffusion matrix along x, y and cross-term.
- *n_react*: number of reaction processes.

For each reaction ($i = 1, n_react$):

- *flag_decay(i)*, *k_react(i)*, *dt_react(i)*; reaction coefficient dependency (not available in current version), reaction coefficient, time step for reaction.
- *n_source*: includes sources according to the time dependency. For *n_source* greater or equal to 1, an additional input file (*casetYY.cns*) is required.
 - 0 - no sources are included;
 - 1 - time independent source, specified in the *casetYY.cns* file;
 - 2 - time dependent source, with the source definition at each diffusion time step defined in the *casetYY.cns* file.

A.3.3 Boundary Conditions File

This file must have “.bcs” extension and can be generated by first creating the “bound.tmp” file in the ADCIRC interface (using “define/edit boundaries” in the circulation version) and then running the pre-processor “cr_bcs”.

The format is:

- File identifier.

- ***n_bound***: total number of boundaries.

For each boundary ($i = 1, n_bound$):

- ***bound(i,0)***, ***type_bound(i)***: number of points in boundary i , type of boundary for boundary i .

The options for ***type_bound*** are:

10 - ocean/river boundary;

20 - land boundary.

For every node of boundary i ($k = 1, bound(i,0)$):

- ***bound(i,k)***, ***bc(i,k)***: boundary node number, concentration at boundary node $bound(i,k)$.

A.3.4 Flow field File

Frequency domain (TEA-NL format, Westerink et al., 1988): This file must have “.tct” extension and the format is:

- File identifier.

- ***n_freq***: number of frequencies

For each frequency ($i = 1, n_freq$):

- ***freq(i)***, ***flag_freq***: frequency i , flag that indicates if the frequency was/was not used (1/0).

- ***freq_name***: frequency name

For each node of the flow grid ($k = 1, n_nodes$):

- *node_number, elev_amp(k,i),elev_ph(k,i)*: node number, elevation amplitude at node k, elevation phase at node k

For each node of the flow grid ($k = 1, n_nodes$):

- *node_number, velx_amp(k,i),velx_ph(k,i), vely_amp(k,i), vely_ph(k,i)*: node number, x-velocity amplitude at node k, x-velocity phase at node k, y-velocity amplitude at node k, y-velocity phase at node k

A.3.5 Particle initial position File

This file can be generated by GREDIT (build points format). Extension must be “.bpt” and the format is:

- File identifier.
- *n_part*: number of particles.

For each particle ($i = 1, n_part$):

- *particle_number, x_part(i), y_part(i)*: particle number, x and y coordinates of particle i.

A.3.6 Estuary limits File

This file must have “.pts” extension and the format is:

- File identifier.
- *n_lines*: number of estuary limit lines.

For each limit line ($i = 1, n_lines$):

- *n_limit(i)*: number of points in limit line i.

For each point k in limit line i ($k = 1, n_limit(i)$):

- *particle_number, x_limit(i,k), y_limit(i,k)*: particle number, x and y coordinates of point k

Suggestion: If using one estuary limit only, it's convenient to generate the file using GREDIT in build points format and then add line 2.

A.3.7 Concentration initial conditions File

Extension of this file must be “.cn0” and the format is:

- *init_time*: initial time for simulation (note: this value overrides the initial time specified in the parameter file)

For each node ($i = 1, n_nodes$):

- *i, c(i)*: node number, initial concentration.

Note: this file has the same format as the output concentration file. Therefore it can be visualized inside XMVIS in the ELA interface.

A.3.8 Source File

Extension of this file must be “.cns” and the format is:

- For *n_source* equal to 1:

- *init_time_sour*: initial time for source (note: in the current version, this value must be the same as *init_time*)

For each node ($i = 1, n_nodes$):

- *i, c_sour(i)*: node number, source concentration.

- For *n_source* equal to 2:

For each diffusion time step:

- *time_sour*: time for source (note: in the current version, this value must coincide with the simulation times)

For each node ($i = 1, n_nodes$):

- *i, c_sour(i)*: node number, source concentration.

NOTE: this file has the same format as the output concentration file. Therefore it can be verified inside XMVIS in the ELA interface.

A.4 Output Files Structure

A.4.1 Particle transport mode

VELApart generates the following output files:

- *casepZZ.pth* (particle pathways): if residence times (*flag_tracer* equal to 2) are being calculated, only the initial and final particle positions are saved. If *flag_tracer* is equal to zero or one then the particle pathways are saved at the time steps specified by *first_out*, *last_out*, *skip_out* in the parameter file. The file format is:

- File identifier.

- *n_time_steps+1*: number of time steps + 1 (initial conditions);

- *init_time, n_part*: initial time, number of particles;

For each particle ($i = 1, n_part$):

- *x_part_ini(i), y_part_ini(i), particle_number*: x- and y-initial coordinates, particle number;

For each time step:

- *time, n_part*: time (in seconds), number of particles

For each particle(i):

- *x_part(i), y_part(i), particle_number, particle_number*: x- and y- coordinates at time t, particle number, particle number;

Only for residence times calculations:

- *casepZZ.rtm* (residence times for each particle). The format is (build-points format for GREDIT):

- File identifier.

- *n_part*: number of particles.

For each particle (i = 1, n_part):

- *particle_number, x_part(i), y_part(i), res_time(i)*: particle number, x- and y-coordinates of the initial location of particle i, residence time (in hours). *Note*: When the residence time cannot be calculated for a particle, then a code is assigned in its place:

code = - 8888 - The total time of simulation is not enough to remove a particle from the estuary.

code = - 9999 - The particle left through an upstream boundary.

- *run.description*: summary of run's inputs

A.4.2 Mass transport mode

VELAconc mode generates the following output files:

- *casepYY.cnc* (concentration field for each time step). The format is:

For each time step:

- *time*: time

For each node ($i = 1, n_nodes$):

- $i, c(i)$: node number, initial concentration.

Note: this file can be visualized inside XMVIS in the ELA interface.

- **caseYY.mas** (model mass divided by initial mass for each time step. If sources are present, source mass is added to the initial mass at each time step for the scaling). The format is:

For each node ($i = 1, n_nodes$):

- $i, mass(i)$: time step number, scaled mass.

- **caseYY.max** (maximum nodal concentration for each time step). The format is:

For each node ($i = 1, n_nodes$):

- $i, max(i)$: time step number, maximum nodal concentration.

- **caseYY.min** (minimum nodal concentration for each time step). The format is:

For each node ($i = 1, n_nodes$):

- $i, min(i)$: time step number, minimum nodal concentration.

- **run.description**: summary of run's inputs

A.5 Examples of Application

Two examples of application are presented in this section, to illustrate the use of *VELAconc* and *VELApart*. The first test was selected from the reference problems of the Convection-Diffusion forum and consists of a Gauss plume advected in a stationary, rotating flow field. An analytical solution is given in Baptista et al. (1995). The second test illustrates the evaluation of residence times in a real estuary (Tagus estuary, Portugal). The input files are presented, along with selected results. Due to the extent of some input

files, only representative lines are given.

A.5.1 Pure convection of a rotating Gauss hill

A.5.1.1 Definition of the Test

This test consists of a Gauss hill advected in a stationary rotating flow field with constant depth (Figure A.6). The standard deviation and maximum concentration of the plume were taken as 600 m and 1, respectively. A grid with nodal spacing of 200 m was used, leading to a dimensionless standard deviation of 3. A time step of 50 s was chosen, which leads to maximum Courant numbers of 1.8.

The evaluation of the integrals at the feet of the characteristic lines was done using 8 subdivisions levels.

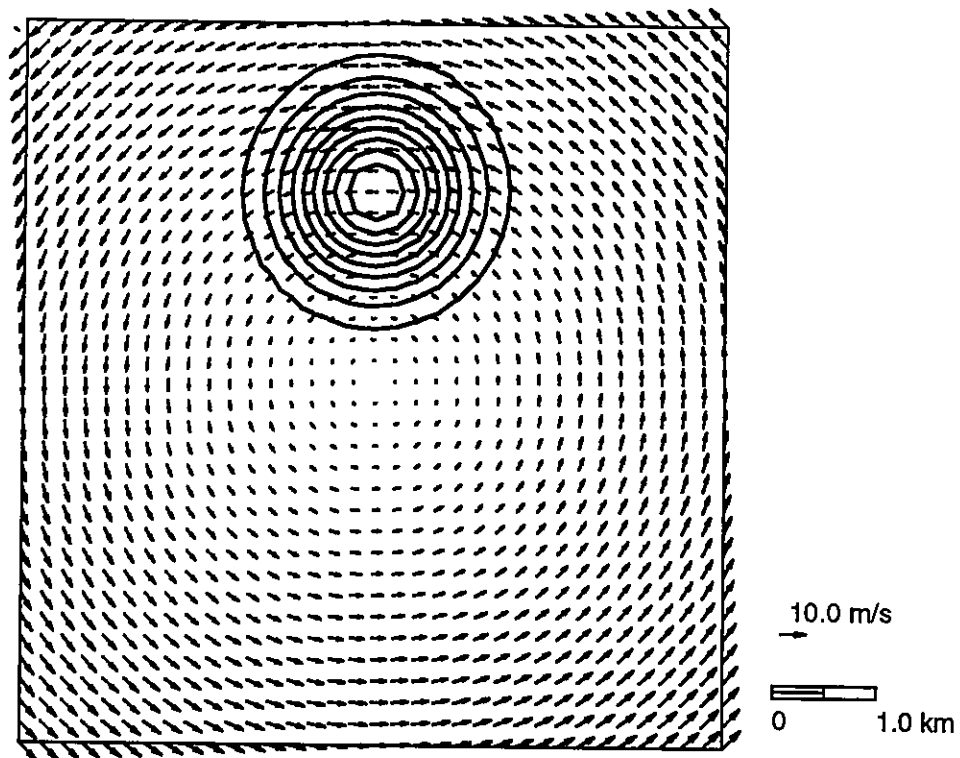


Figure A.6 Geometry and forcings of the test case.

A.5.1.2 Input files

Grid file

```

grid file
2312 1225
1 -3200.000000 -3400.000000 10.000
2 -3200.000000 -3200.000000 10.000
3 -3400.000000 -3400.000000 10.000
4 -3400.000000 -3200.000000 10.000
5 -3000.000000 -3400.000000 10.000
6 -3000.000000 -3200.000000 10.000
7 -2800.000000 -3400.000000 10.000
8 -2800.000000 -3200.000000 10.000
9 -2600.000000 -3400.000000 10.000
10 -2600.000000 -3200.000000 10.000
... similar lines for nodes 11 to 1209...
1210 400.000000 3400.000000 10.000
1211 600.000000 3400.000000 10.000
1212 800.000000 3400.000000 10.000
1213 1000.000000 3400.000000 10.000
1214 1200.000000 3400.000000 10.000
1215 1400.000000 3400.000000 10.000
1216 1600.000000 3400.000000 10.000
1217 1800.000000 3400.000000 10.000
1218 2000.000000 3400.000000 10.000
1219 2200.000000 3400.000000 10.000
1220 2400.000000 3400.000000 10.000
1221 2600.000000 3400.000000 10.000
1222 2800.000000 3400.000000 10.000
1223 3000.000000 3400.000000 10.000
1224 3200.000000 3400.000000 10.000
1225 3400.000000 3400.000000 10.000
1 3 1 2 3
2 3 3 2 4
3 3 5 6 1
4 3 1 6 2
5 3 7 8 5
6 3 5 8 6
7 3 9 10 7
8 3 7 10 8
9 3 11 12 9
10 3 9 12 10
... similar for elements 11 to 2299...
2300 3 1183 1219 1218
2301 3 1185 1220 1184
2302 3 1184 1220 1219
2303 3 1186 1221 1185
2304 3 1185 1221 1220
2305 3 1187 1222 1186
2306 3 1186 1222 1221
2307 3 1188 1223 1187
2308 3 1187 1223 1222
2309 3 1189 1224 1188
2310 3 1188 1224 1223
2311 3 1190 1225 1189
2312 3 1189 1225 1224

```

Parameter file

```

parameter file
0 0 1
50 50 0.0
0 1 50 0
0.001 0.0001
2 1 0
0
0
1
0 0 0 0 0
0
0

```

Initial conditions file

```

0.0000
1 3.259844063933274E-023
2 5.542399897347204E-022
3 5.211830412010481E-024
4 8.861174882599904E-023
5 1.824519181833949E-022
6 3.102054800100854E-021
7 9.137872601482542E-022
8 1.553624749378962E-020
9 4.095310376420597E-021
10 6.962863058698410E-020
... similar for nodes 11 to 1209...
1210 2.287346491123891E-002
1211 1.732585203587509E-002
1212 1.174362845702137E-002
1213 7.122870715457228E-003
1214 3.865920139472808E-003
1215 1.877568335762843E-003
1216 8.159878350721483E-004
1217 3.173340493287281E-004
1218 1.104319447771196E-004
1219 3.438886362675382E-005
1220 9.582657960536534E-006
1221 2.389456928417124E-006
1222 5.331599071054882E-007
1223 1.064537141107602E-007
1224 1.901994297910288E-008
1225 3.040903653949218E-009

```

Boundary conditions file

```

Boundary conditions file
1
137 10
1192 0.0
1157 0.0
1122 0.0
1087 0.0
1052 0.0
1017 0.0
982 0.0
947 0.0

```


912 0.0
 877 0.0
 842 0.0
 807 0.0
 772 0.0
 737 0.0
 702 0.0
 667 0.0
 632 0.0
 597 0.0
 562 0.0
 527 0.0
 492 0.0
 457 0.0
 422 0.0
 387 0.0
 352 0.0
 317 0.0
 282 0.0 ... similar for other boundary nodes...

Flow field file

flow field file
 1
 0.000000000E+00 1
 frequency name
 1 .0 .0
 2 .0 .0
 3 .0 .0
 4 .0 .0
 5 .0 .0
 6 .0 .0
 7 .0 .0
 8 .0 .0
 9 .0 .0
 10 .0 .0
 ... similar for nodes 11 to 1209...
 1210 .0 .0
 1211 .0 .0
 1212 .0 .0
 1213 .0 .0
 1214 .0 .0
 1215 .0 .0
 1216 .0 .0
 1217 .0 .0
 1218 .0 .0
 1219 .0 .0
 1220 .0 .0
 1221 .0 .0
 1222 .0 .0
 1223 .0 .0
 1224 .0 .0
 1225 .0 .0
 1 7.12094334 .0 -6.70206432 .0
 2 6.70206432 .0 -6.70206432 .0
 3 7.12094334 .0 -7.12094334 .0
 4 6.70206432 .0 -7.12094334 .0
 5 7.12094334 .0 -6.2831853 .0
 6 6.70206432 .0 -6.2831853 .0

```

7 7.12094334 .0 -5.86430628 .0
8 6.70206432 .0 -5.86430628 .0
9 7.12094334 .0 -5.44542726 .0
... similar for nodes 10 to 1209 ...
1210 -7.12094334 .0 .837758039 .0
1211 -7.12094334 .0 1.25663706 .0
1212 -7.12094334 .0 1.67551608 .0
1213 -7.12094334 .0 2.0943951 .0
1214 -7.12094334 .0 2.51327412 .0
1215 -7.12094334 .0 2.93215314 .0
1216 -7.12094334 .0 3.35103216 .0
1217 -7.12094334 .0 3.76991118 .0
1218 -7.12094334 .0 4.1887902 .0
1219 -7.12094334 .0 4.60766922 .0
1220 -7.12094334 .0 5.02654824 .0
1221 -7.12094334 .0 5.44542726 .0
1222 -7.12094334 .0 5.86430628 .0
1223 -7.12094334 .0 6.2831853 .0
1224 -7.12094334 .0 6.70206432 .0
1225 -7.12094334 .0 7.12094334 .0

```

A.5.1.3 Results

VELAconc was run for 50 time steps. The final concentrations are shown in Figure A.7, against the analytical solution. Time series of mass and peak errors, and maximum negative concentrations are shown in Figure A.8.

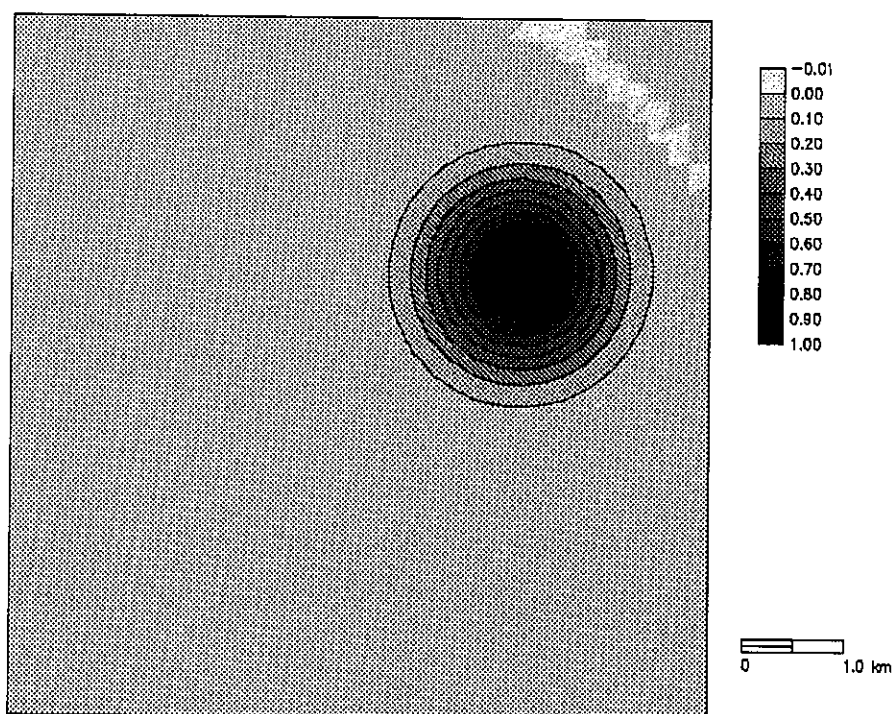


Figure A.7 Concentrations after 50 time steps: analytical solution and model represented by lines and filled isolines, respectively.

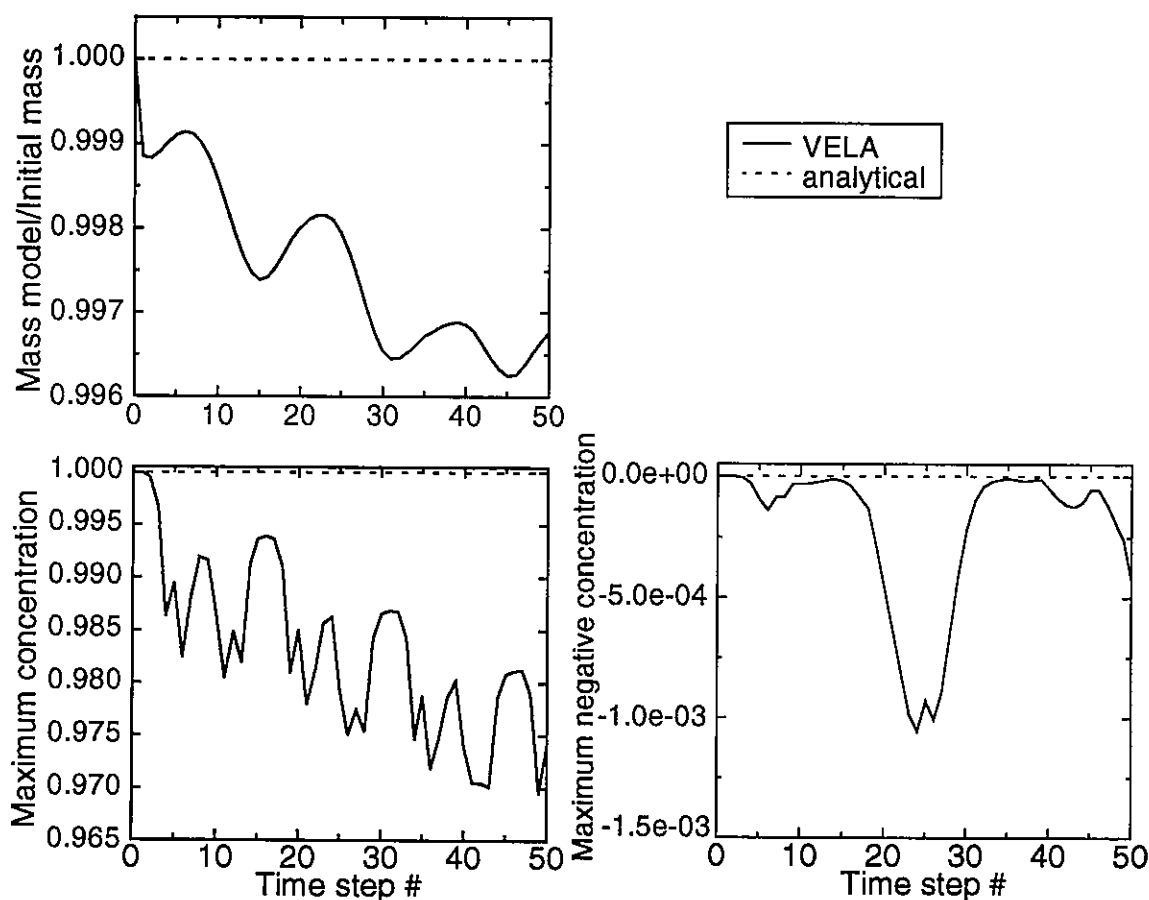


Figure A.8 Error measures a) mass error; b) peak error; c) negative concentrations.

A.5.2 Residence Times in the Tagus estuary

A.5.2.1 Definition of the Test

This test illustrates the use of *VELA*part for residence time calculations for re-entrant tracers in the Tagus estuary. Four hundred particles, placed in a $1 \times 1 \text{ km}^2$ square area, were released in the upper estuary. These particles were then followed until leaving the control region without returning in a later phase of the tide or in a later tidal cycle (Figure A.9).

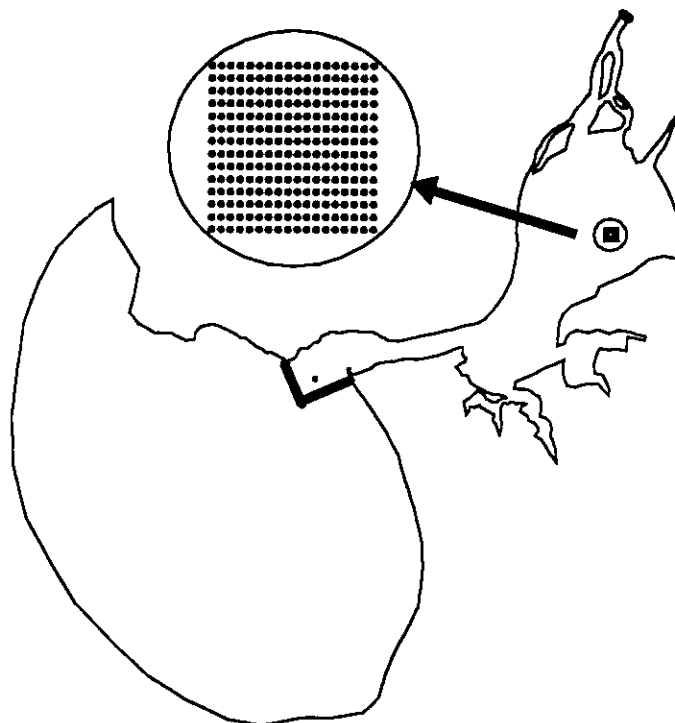


Figure A.9 Tagus estuary: limits of control region (thick line) and particle release area (square).

A.5.2.2 Input files

Grid file

```

grid file
4136 2336
1 114219.899668 194103.690224 12.839
2 114209.583856 193612.486194 15.869
3 113676.408658 193725.857960 15.202
4 114808.139800 194033.158839 13.681
5 113709.915593 194104.196990 2.500
6 114723.238422 194553.048055 11.627
7 114192.231936 194592.848925 9.006
8 114128.477423 193077.418056 17.267
9 114833.619801 193439.249700 13.720
10 113591.907244 193292.638777 18.477
... similar for nodes 11 to 2324...
2325 80008.360930 201285.535757 30.906
2326 80733.777918 201002.165131 24.400
2327 80932.428039 201644.837550 19.692
2328 78234.039616 202770.474725 48.479
2329 79169.021085 202454.448501 41.198
2330 80109.315261 202148.598885 22.536
2331 80651.587800 202836.526291 10.560
  
```

```

2332 79061.967077 203497.041948 43.850
2333 79916.709410 203087.527269 25.987
2334 80651.587800 203629.145080 18.880
2335 79856.777438 203959.402908 35.525
2336 80651.587800 204421.763869 27.200
1 3 2238 2221 2223
2 3 2238 2220 2221
3 3 2223 2201 2202
4 3 2237 2218 2219
5 3 2220 2197 2221
6 3 2219 2193 2194
7 3 2223 2221 2201
8 3 2194 2151 2195
9 3 2195 2152 2196
10 3 2194 2193 2151
... similar for elements 11 to 4124...
4125 3 1321 1349 1317
4126 3 1351 1380 1349
4127 3 1349 1350 1317
4128 3 1380 1381 1349
4129 3 1349 1381 1350
4130 3 1380 1412 1381
4131 3 1381 1382 1350
4132 3 1412 1413 1381
4133 3 1381 1413 1382
4134 3 1412 1439 1413
4135 3 1413 1439 1414
4136 3 1413 1414 1382

```

Parameter file

```

parameter file
1 0 1
3670 6001.61 30691100
0 1 3670 3669
0.0000001 0.001
2

```

Boundary conditions file

```

boundary file
9
41 10
2336 0.000000000000000000E+00
2335 0.000000000000000000E+00
2332 0.000000000000000000E+00
2328 0.000000000000000000E+00
2322 0.000000000000000000E+00
2314 0.000000000000000000E+00
2303 0.000000000000000000E+00
2291 0.000000000000000000E+00
2278 0.000000000000000000E+00
2265 0.000000000000000000E+00
2252 0.000000000000000000E+00
2240 0.000000000000000000E+00
2224 0.000000000000000000E+00
2204 0.000000000000000000E+00
2176 0.000000000000000000E+00
2175 0.000000000000000000E+00

```

```

2174 0.0000000000000000E+00
2173 0.0000000000000000E+00
2172 0.0000000000000000E+00
2171 0.0000000000000000E+00
2170 0.0000000000000000E+00
2169 0.0000000000000000E+00
2168 0.0000000000000000E+00
2167 0.0000000000000000E+00
2166 0.0000000000000000E+00
2165 0.0000000000000000E+00
2164 0.0000000000000000E+00
2163 0.0000000000000000E+00
2162 0.0000000000000000E+00
2203 0.0000000000000000E+00
2202 0.0000000000000000E+00
2223 0.0000000000000000E+00
2238 0.0000000000000000E+00
2220 0.0000000000000000E+00
2196 0.0000000000000000E+00
2195 0.0000000000000000E+00
2194 0.0000000000000000E+00
2219 0.0000000000000000E+00
2237 0.0000000000000000E+00
2236 0.0000000000000000E+00
2235 0.0000000000000000E+00
... similar for other boundaries ...

```

Flow field file

```

flow field file
11 0.0000000000E+00    2336
0.0000000000E+00    1
first frequency name
1 -0.2075687237E-01  0.0000000000E+00
2 -0.1657026820E-01  0.0000000000E+00
3 -0.2320783399E-01  0.0000000000E+00
4 -0.1327257324E-01  0.0000000000E+00
5 -0.2440908737E-01  0.0000000000E+00
6 -0.1309218071E-01  0.0000000000E+00
7 -0.2004690096E-01  0.0000000000E+00
8 -0.1285841689E-01  0.0000000000E+00
9 -0.1063171402E-01  0.0000000000E+00
10 -0.1761811413E-01  0.0000000000E+00
.. similar for nodes 11 to 2324
2325 -0.1389788958E-03  0.0000000000E+00
2326 -0.3703748371E-04  0.0000000000E+00
2327 -0.3580012126E-02  0.0000000000E+00
2328  0.6891610838E-06  0.0000000000E+00
2329 -0.1777085825E-02  0.0000000000E+00
2330 -0.4772981629E-02  0.0000000000E+00
2331 -0.8729958907E-02  0.0000000000E+00
2332  0.6891610838E-06  0.0000000000E+00
2333 -0.3775769146E-02  0.0000000000E+00
2334 -0.3115240252E-02  0.0000000000E+00
2335  0.6891610838E-06  0.0000000000E+00
2336  0.6891610838E-06  0.0000000000E+00
1 -0.2334944159E-01  0.0000000000E+00 -0.4299813136E-01  0.0000000000E+00
2  0.1770299114E-01  0.0000000000E+00 -0.5182888359E-02  0.0000000000E+00
3  0.3045633622E-01  0.0000000000E+00 -0.2187309228E-01  0.0000000000E+00

```

```

4 0.2476593852E-01 0.0000000000E+00 0.7210186217E-02 0.0000000000E+00
5 0.4469876643E-02 0.0000000000E+00 0.3735412378E-02 0.0000000000E+00
6 -0.4263207316E-01 0.0000000000E+00 -0.4725186620E-02 0.0000000000E+00
7 -0.7414373755E-01 0.0000000000E+00 -0.7700137049E-01 0.0000000000E+00
8 0.3316208720E-01 0.0000000000E+00 0.1511773909E-02 0.0000000000E+00
9 0.3380955011E-01 0.0000000000E+00 0.7646098733E-02 0.0000000000E+00
10 0.1114794426E-01 0.0000000000E+00 -0.2089447714E-01 0.0000000000E+00
... similar for nodes 11 to 2324...
2325 -0.2278575860E-01 0.0000000000E+00 -0.2296859175 0.0000000000E+00
2326 0.2242803015E-01 0.0000000000E+00 -0.1004378572 0.0000000000E+00
2327 0.6825609505E-01 0.0000000000E+00 -0.1650042385 0.0000000000E+00
2328 -0.2471389994E-01 0.0000000000E+00 -0.3948475420 0.0000000000E+00
2329 -0.2726250514E-01 0.0000000000E+00 -0.3877602518 0.0000000000E+00
2330 -0.3408936551E-02 0.0000000000E+00 -0.3661419153 0.0000000000E+00
2331 0.5831384659E-01 0.0000000000E+00 -0.4120155275 0.0000000000E+00
2332 -0.1891175751E-02 0.0000000000E+00 -0.3469337821 0.0000000000E+00
2333 -0.3747133166E-01 0.0000000000E+00 -0.4107960165 0.0000000000E+00
2334 0.0000000000E+00 0.0000000000E+00 -0.4012108445 0.0000000000E+00
2335 -0.3436143324E-01 0.0000000000E+00 -0.3221359253 0.0000000000E+00
2336 0.0000000000E+00 0.0000000000E+00 -0.3306802809 0.0000000000E+00
... similar for the other ten frequencies...

```

Particle initial position file

```

particle position file
400
1 124503.978033 201060.889481
2 124503.978033 201110.889481
3 124503.978033 201160.889481
4 124503.978033 201210.889481
5 124503.978033 201260.889481
6 124503.978033 201310.889481
7 124503.978033 201360.889481
8 124503.978033 201410.889481
9 124503.978033 201460.889481
10 124503.978033 201510.889481
... similar for particles 11 to 389...
390 125503.978033 201510.889481
391 125503.978033 201560.889481
392 125503.978033 201610.889481
393 125503.978033 201660.889481
394 125503.978033 201710.889481
395 125503.978033 201760.889481
396 125503.978033 201810.889481
397 125503.978033 201860.889481
398 125503.978033 201910.889481
399 125503.978033 201960.889481
400 125503.978033 201960.889481

```

Control region limits file

```

control region definition
1
3
1 95475.947649 191162.330311 1.000000
2 96943.337950 186387.207168 1.000000
3 103044.592363 187619.497012 1.000000

```

A.5.2.3 Results

Particles' residence times and their integrated histogram analysis are shown in Figure A.10.

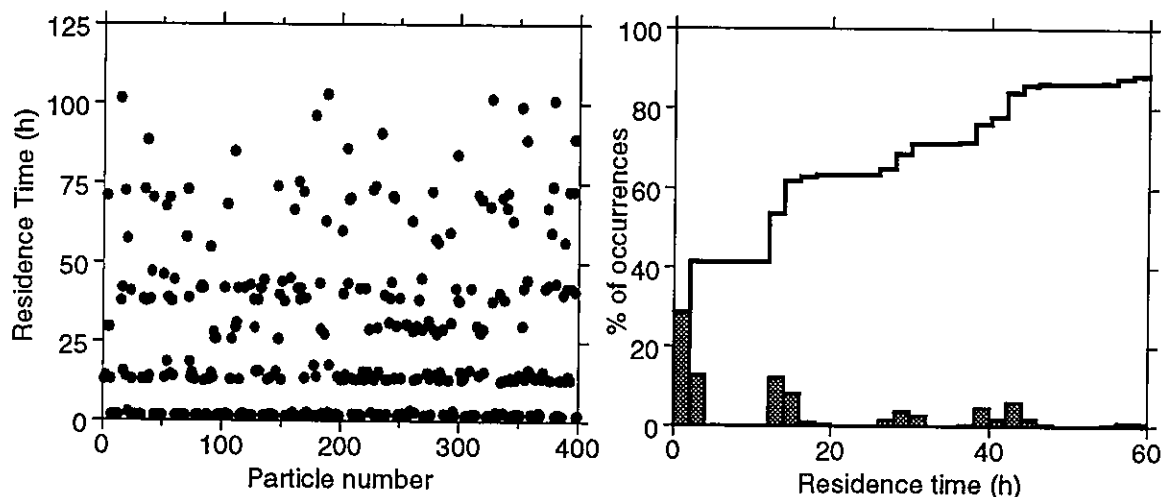


Figure A.10 Residence times in the Tagus estuary: individual residence times and histogram analysis.

References

- Baptista, A.M., E.E. Adams and K.D. Stolzenbach, 1984. *Eulerian-Lagrangian analysis of pollutant transport in shallow water*, Technical Report no.296, MIT R.M. Parsons, Cambridge.
- Baptista, A.M. and E.E. Adams, 1986. Ocean Dispersion Modeling, in *Complex Flow Phenomena and Modeling*, Encyclopedia of Fluid Mechanics, N.P. Chermisinoff (editor), Gulf Publishing Company, 6: 865-895.
- Baptista, A.M., E.E. Adams and P. Gresho, 1995. Benchmarks for the Transport Equation: the Convection-Diffusion Forum and Beyond, in *Quantitative Skill Assessment for Coastal Ocean Models*, D. Lynch et al. (editors), American Geophysical Union Estuarine/Coastal Monograph, 47: 241-268.
- Binning, P. and M.A. Celia, 1996. A finite volume Eulerian-Lagrangian localized Adjoint method for solution of the contaminant transport equations in two-dimensional multiphase flow systems, *Water Resources Research*, 32(1): 103-114.

- Celia, M.A., T.F. Russell, I. Herrera, R.E. Ewing, 1990. An Eulerian-Lagrangian Localized Adjoint Method for the Advection-Diffusion Equation, *Advances in Water Resources*, 13(4): 187-206.
- Cheng, R.T., V. Casulli and S.N. Milford, 1984. Eulerian-Lagrangian Solution of the Convection-Dispersion Equation in Natural Coordinates, *Water Resources Research*, 20(7): 944-952.
- Foreman, M.G.G., A.M. Baptista and R.A. Walters, 1992. Tidal Model Studies of Particle Trajectories Around a Shallow Coastal Bank, *Atmosphere-Ocean*, 30(1): 43-69.
- Fortunato, A.B., A.M. Baptista and R.A. Luettich, Jr., 1997. A Three-Dimensional Model of Tidal Currents at the Mouth of the Tagus Estuary (Portugal), *Continental Shelf Research* (in press).
- Healy, R.W. and T.F. Russell, 1993. A Finite-Volume Eulerian-Lagrangian Localized Adjoint Method for Solution of the Advection-Dispersion Equation, *Water Resources Research*, 29(7), 2399-2413.
- Hofmann, E.E., K.S. Hedstrom, J.R. Moisan, D.B. Haidvogel and D.L. Mackas, 1991. Use of Simulated Drifters Tracks to Investigate General Transport Patterns and Residence Times in the Coastal Transition Zone, *Journal of Geophysical Research*, 96(C8): 15,041-15,052.
- Morton, K.W., 1991. Finite Volume Methods and Their Analysis, in *Proceedings of the 7th Conference on the Mathematics of Finite Elements and Applications*, Academic Press, 189-214.
- Oliveira, A. and A.M. Baptista, 1997a. On the Role of Tracking on Eulerian-Lagrangian Solutions of the Transport Equation, *Advances in Water Resources*, (in press).
- Oliveira, A. and A.M. Baptista, 1997b. VELA User's Manual. A Two-Dimensional Depth-Averaged Transport and Particle Model, (in preparation).
- Press, W.H., S.A. Teukolsky, W.T. Vetterling and B.P. Flannery, 1992. *Numerical Recipes in Fortran*, Cambridge University Press, 704-716.
- Salomon, J.C. and M. Pompepuy, 1990. Mathematical Model of Bacterial Contamination of the Morlaix Estuary (France), *Water Research*, 24(8): 983-994.
- Westerink, J.J., J.J. Connor, K.D. Stolzenbach, 1988. A Frequency-Time Domain Finite Element Model for Tidal Circulation Based on The Least-Square Harmonic Analysis Method, *International Journal for Numerical Methods in Fluids*, 8(7): 813-843.

Wood, T.M. and A.M. Baptista, 1993. A Model for Diagnostic Analysis of Estuarine Geochemistry, *Water Resources Research*, 29(1): 51-71.

VITAE

The author was born on March 10th, 1967, in Lisbon (Portugal). She entered Instituto Superior Técnico (Lisbon) in October, 1985, and she received her Bachelor of Science degree in Civil Engineering in September, 1990. She then worked for one year at the Estuaries Division of the Laboratório Nacional de Engenharia Civil.

The author came to the Oregon Graduate Institute of Science and Technology in September 1991, and was awarded her Master of Science degree in Environmental Science and Engineering in January, 1994. She started the Ph.D. program in February, 1994 and received her Ph.D. in October, 1997.

Publications

- Oliveira, A. 1994. *A comparison of Eulerian-Lagrangian Methods for the Solution of the Transport Equation*, M.Sc. thesis, Oregon Graduate Institute of Science and Technology, Portland, Oregon.
- Oliveira, A. and A.M. Baptista, 1994. Integration ELMs or Interpolation ELMs?, in *Proceedings of the 10th International Conference on Computational Methods in Water Resources*, A. Peters et al. (editors), Kluwer Academic Publishers, 2: 1045-1052.
- Oliveira, A. and A.M. Baptista, 1995. A comparison of integration and interpolation Eulerian-Lagrangian methods, *International Journal for Numerical Methods in Fluids*, 21(3): 183-204.
- Fortunato, A.B., A. Oliveira and A.M. Baptista, 1996. Marés e Correntes Residuais no Estuário do Tejo, in *3^o Congresso da Água*, Associação Portuguesa de Recursos Hídricos, 2: 435-445.
- Oliveira, A. and A.M. Baptista, 1996. Diagnostic analysis of estuarine residence times, in *Proceedings of the 11th International Conference on Computational Methods in Water Resources*, A.A. Aldama et al., (editors), Computational Mechanics Publications, 2: 355-362.

- Oliveira A., A.M. Baptista and A.B. Fortunato, 1997. Análise Diagnóstica de Tempos de Residência em Estuários, in *Seminário Sobre Lagunas Costeiras e Ilhas-Barreira da Zona Costeira de Portugal*, Associação EUROCOAST-Portugal, Aveiro, Portugal, n.p.
- Oliveira, A. and A.M. Baptista, 1997. On the Role of Tracking on Eulerian-Lagrangian Solutions of the Transport Equation, *Advances in Water Resources*, (in press).
- Oliveira, A. and A.M. Baptista, 1997. Diagnostic Modeling of Residence Times in Estuaries, *Water Resources Research*, 33(8):1935-1946.
- Fortunato, A.B., A. Oliveira and A.M. Baptista, 1997. On the effect of tidal flats on the hydrodynamics of the Tagus estuary, *Oceanologica Acta*, (in review).
- Fortunato, A.B., J.B. Fernandes, G.A. Santos, A. Oliveira and M.A. Santos, 1997. A tool for visualizing flow and transport in the Tagus estuary, *Netherlands Journal of Aquatic Ecology*, (submitted).
- Fortunato, A.B., A. Oliveira and A.M. Baptista, 1997. Finite Element Modeling of Flow and Transport in Coastal Waters, in *Proceedings of the 5th Encontro Nacional de Mecânica Computacional*, Guimarães, Portugal, (in press).